

**FACTORS INFLUENCING
THE MECHANICAL BEHAVIOUR
OF
SMALL DEVICES SUCH AS STENTS**

Carine Gachon M.Eng.

July 2003

Submitted for the degree of
Doctor of Philosophy.



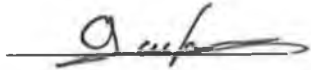
GMIT

GALWAY-MAYO INSTITUTE OF TECHNOLOGY
INSTITIÚID TEICNEOLAÍOCHTA NA GAILLIMHE-MAIGH EÓ

Submitted to: GMIT and HETAC
Research carried out at: The School of Engineering, GMIT
Research Director: Dr. Patrick Delassus

DECLARATION

I hereby declare that the work presented in this thesis is my own and that it has not been used to obtain a degree in this institute or elsewhere.

A handwritten signature in black ink, appearing to read 'Carine Gachon', written over a horizontal line.

Carine Gachon

To my fiancé Niall

FACTORS INFLUENCING THE MECHANICAL BEHAVIOUR OF SMALL DEVICES SUCH AS STENTS

Author : Carine Gachon

A coronary stent is a mechanical device designed to open arteries that have been occluded. The manufacturing of stents involves the laser cutting of specific designs in stainless steel tubes. In order to determine factors influencing the mechanical behaviour of stents, tensile tests were performed on struts laser-cut in tubes used for the manufacturing of stents. The hardening curves obtained show that the yield stress and Young's Modulus increase when the width of the struts decreases, until a limit is reached where they start decreasing again; the breaking point varies inversely. To confirm the results a three-point bending test was conducted. Because the struts are cut in a tube, the resulting geometry makes it difficult to predict the mechanical behaviour. A model using Finite Element Analysis (F.E.A.) was therefore created and the mechanical behaviour identified by comparing the experimental results and the F.E.A. prediction. The hardening curves obtained confirm the conclusions reached in tension. In order to understand the phenomenon, the accuracy of laser cutting was investigated. An F.E.A. was conducted, showing that the inaccuracy of laser cutting can only explain the strain at breaking decreasing with the width. The geometry of the specimen being discarded, the microstructure was examined in order to understand the mechanical behaviour. The Heat Affected Zone (H.A.Z.) resulting from laser cutting was first observed. It was found that the size of the H.A.Z. is negligible when considering wide struts but becomes significant when dealing with struts smaller than a millimetre. Consequently, the strut behaves like a sandwich material partly explaining the experimental results. However, according to the sandwich theory, the yield stress, Young's Modulus and strain at breaking should be linear functions of the width which is not the case. Therefore, another factor has to be considered. The number of grains in the width was then investigated and shown to explain the other part of the experimental results. In conclusion, the number of grains in the width and the H.A.Z. both influence the mechanical behaviour of the struts.

PUBLISHED WORK ASSOCIATED WITH THIS THESIS

C. Gachon, P. Delassus, P. McHugh, "Influence of the manufacturing path on the mechanical behaviour of medical devices such as stents", ACTA of Bioengineering and Biomechanics, Volume 4, Supplement 1, 2002.

C. Gachon, P. Delassus, P. McHugh, "Accuracy of laser-cutting and its influence on the mechanical behaviour of stents", Proceedings of S.P.I.E., Opto-Ireland, Volume 4876-4877, 2002.

C. Gachon, P. Delassus, "Influence of the size effect on the mechanical behaviour of stents", Proceedings of the Third International Congress on Biomaterials, Biomat03, Havana, Cuba, 2003.

C. Gachon, P. Delassus, "Influence of the dimensions on the mechanical behaviour of stents", Proceedings of the Twentieth International Manufacturing Conference IMC-20, Cork Institute of Technology, 2003.

FUNDING

The research described in this thesis was funded by Abbot Ireland and Enterprise Ireland.

ACKNOWLEDGEMENTS

There are many people who I would like to thank for having contributed in some way to the development of this thesis. Firstly thanks to Dr. Patrick Delassus for all the help, specially in the last few months, advice and supports and for giving me the opportunity to come to Ireland.

Thanks to John Kelly and all the Abbot staff that I had the opportunity to work with.

Thanks to Peter McHugh for his advice and for always pointing me in the right direction

Thanks to everybody who helped in my practical work:

In G.M.I.T, John Noone and all in the workshop, Sam and Jessy in the School of Sciences, and everybody in the chemistry lab. In NCBES, Liam Brennan. In the Department of Material Sciences and Technology, U.L., Ken Stanton and Gerard Dolan.

To everybody working in the lab and specially Aurora, Jean-Philippe and Laurentiu, thanks for providing company and support, and raising a smile on bad days.

Again, thanks to my parents for being who you are. I would not have gone so far without your support and encouragement.

Thanks to the O Doherty family for making me feel part of your family when I was missing mine so dearly.

Finally, thanks to Niall for being here all along. You provided me with motivation, moral support and great help . I could not have done it without you.

TABLE OF CONTENT

INTRODUCTION..... 1

CHAPTER 1 : LITERATURE REVIEW..... 5

I FROM CORONARY ARTERY DISEASE TO STENTS 5

 I.1 ANATOMY OF THE HEART..... 5

 I.2 CORONARY ARTERY DISEASE 6

 I.3 UNBLOCKING CORONARY ARTERIES..... 7

 I.3.1 PTCA 7

 I.3.2 Atherectomy 10

 I.3.3 Coronary stents 11

 I.4 REVIEW OF STENTS 12

 I.4.1 The Maass Double Helix Spiral Stent..... 12

 I.4.2 Nitinol Stent..... 12

 I.4.3 Palmaz-Schatz Stent..... 13

 I.4.4 Gianturco-Roubin Stent..... 13

 I.4.5 Strecker Stent 14

 I.4.6 Gianturco Stent..... 14

 I.4.7 Wallstent..... 15

 I.5 ABBOT VASCULAR DEVICES 15

 I.5.1 Biodivysio SV OTW..... 15

 I.5.2 Biodivysio OC OTW 17

II MATERIAL AND MANUFACTURING PROCESSES..... 18

II.1 STAINLESS STEEL 18

 II.1.1 Introduction..... 18

 II.1.2 Stainless Steel 18

 II.1.3 Austenitic stainless steels..... 18

 II.1.4 316L 19

 II.1.5 316L Hollow Bar 19

II.2 MANUFACTURING PROCESSES..... 20

 II.2.1 Laser cutting..... 20

 II.2.2 Electro-polishing..... 21

 II.2.3 Annealing 21

III MECHANICAL BEHAVIOUR	26
III.1 HARDENING CURVE.....	26
III.1.1 Introduction.....	26
III.1.2 Elasticity	26
III.1.3 Elastic limit or Yield stress.....	27
III.1.4 Plastic flow	28
III.1.5 Hardening.....	28
III.2 MULTIAXIAL PLASTICITY CRITERIA	30
III.2.1 Introduction.....	30
III.2.2 Hardening Criteria.....	31
III.2.3 Isotropic criteria.....	31
III.2.4 Anisotropic criteria.....	32
III.3 LARGE DEFORMATION PLASTICITY.....	32
III.3.1 Deformation Gradient	32
III.3.2 Polar Decomposition.....	33
III.3.3 Measure of Deformation.....	34
III.3.4 Stress	37
III.4 STRAIN GRADIENT PLASTICITY	37
III.4.1 Introduction	37
III.4.2 Low-Order Gradient Plasticity Model	38
III.5 MICROSTRUCTURE.....	39
III.5.1 Introduction.....	39
III.5.2 Movement of dislocations	40
III.5.3 Effect of the grain size on the Yield stress	42
III.5.4 Fracture	44
III.5.5 Manufacturing process influence on the microstructure.....	48
IV EXPERIMENTAL METHODS	49
IV.1 TENSILE TEST.....	49
IV.1.1 Introduction	49
IV.1.2 Standards.....	49
IV.1.3 Methods of strain measurement	50
IV.1.4 Engineering stress and strain.....	51
IV.1.5 True stress and Strain.....	52
IV.1.6 Hardening curve.....	53
IV.2 BENDING TEST.....	54
IV.2.1 Introduction	54
IV.2.2 Standards.....	55

IV.2.3 Shearing forces	55
IV.2.4 Bending Moments	56
IV.2.5 Centroid and moments of inertia	56
IV.2.6 Stress in elasticity.....	57
IV.2.7 Deflection of beam in elasticity	58
IV.2.8 Strain in elasticity.....	58
IV.2.9 Yield stress and plasticity	58
V METALLOGRAPHY	59
V.1 STANDARDS.....	59
V.2 SAMPLE PREPARATION	59
V.3 GRAIN SIZE MEASUREMENTS.....	60
V.4 SCANNING ELECTRON MICROSCOPE	62
CHAPTER 2 : CONTEXT OF THE STUDY.....	63
I INTRODUCTION	63
II PROBLEM ENCOUNTERED.....	63
II.1 INTRODUCTION.....	63
II.2 EXPERIMENTATION.....	63
II.3 CONSEQUENCE.....	68
III STRESS DISTRIBUTION IN THE STENT	68
III.1 INTRODUCTION	68
III.2 F.E.A MODELLING.....	68
III.2.1 Crimping	69
III.2.2 Crimping tool removal and artery introduction.....	70
III.2.3 Expansion of the stent.....	70
III.2.4 Analysis of the stress distribution	71
IV CONCLUSION.....	72
CHAPTER 3 : TENSILE BEHAVIOUR.....	73
I INTRODUCTION.....	73
II EXPERIMENTATION	73
II.1 EQUIPMENT	73
II.2 MEASUREMENTS.....	74
II.3 SPECIMEN DESIGN	77
II.4 VALIDATION OF THE TEST	78
II.4.1 Conditions for validity :	78
II.4.2 Method of validation	79

II.4.3 Breaking point	79
II.4.4 Uniformity of the stress along the strut.....	82
II.5 POSITIONING OF THE SPECIMEN	82
II.5.1 Manipulation of the specimen	82
II.5.2 Specimen positioning.....	83
II.6 ACCURACY OF LASER CUTTING.....	84
II.6.1 Observation:.....	84
II.6.2 Influence of the trapezoidal shape on the yield stress.....	86
II.6.3 Potential solutions for improving the accuracy of laser-cutting.....	87
III DATA PROCESSING	90
IV INFLUENCE OF THE WIDTH.....	94
IV.1 INTRODUCTION.....	94
IV.2 EXPERIMENTAL RESULTS	94
IV.3 COMPARISON BETWEEN DIFFERENT BATCHES	97
V INFLUENCE OF THE MANUFACTURING PATH.....	100
V.1 INTRODUCTION	100
V.2 EXPERIMENTAL RESULTS FOR ELECTRO-POLISHED SPECIMENS	100
V.3 INFLUENCE OF ELECTRO-POLISHING.....	101
V.4 EXPERIMENTAL RESULTS FOR ANNEALED SPECIMENS.....	104
V.5 INFLUENCE OF ANNEALING.....	105
VI INFLUENCE OF THE TRAPEZOIDAL SHAPE OF THE STRUTS ON THEIR MECHANICAL BEHAVIOUR	107
VI.1 INFLUENCE OF THE TRAPEZOIDAL SHAPE ON THE YIELD STRESS.....	107
VI.2 INFLUENCE OF THE TRAPEZOIDAL SHAPE ON THE BREAKING POINT.....	108
VII CONCLUSION.....	110
 CHAPTER 4 : BENDING BEHAVIOUR.....	111
I INTRODUCTION.....	111
II EXPERIMENTATION.....	112
II.1 TEST DEVELOPED FOR THE MICRO TENSILE TESTER	112
II.2 DYNAMIC MECHANICAL ANALYSER.....	115
II.3 MEASUREMENTS.....	116
II.4 SPECIMEN DESIGN	119
II.5 POSITIONING OF THE SPECIMEN	120
II.6 VALIDATION OF THE TEST	121
III INVERSE IDENTIFICATION.....	124

IV INFLUENCE OF THE WIDTH.....	134
IV.1 INTRODUCTION.....	134
IV.2 EXPERIMENTAL RESULTS FOR BATCH 0.....	134
IV.3 TENSILE VERSUS BENDING BEHAVIOUR FOR BATCH 0.....	135
IV.4 EXPERIMENTAL RESULTS FOR BATCH 2.....	137
IV.5 TENSILE VERSUS BENDING BEHAVIOUR FOR BATCH 2.....	137
IV.6 COMPARISON BETWEEN BATCHES.....	138
V INFLUENCE OF THE MANUFACTURING PATH.....	140
V.1 INTRODUCTION.....	140
V.2 RESULTS FOR ELECTRO-POLISHED SPECIMENS.....	140
V.3 TENSILE VERSUS BENDING BEHAVIOUR.....	141
V.4 INFLUENCE OF ELECTRO-POLISHING IN BENDING.....	141
V.5 RESULTS FOR ANNEALED SPECIMENS.....	142
V.6 TENSILE VERSUS BENDING BEHAVIOUR.....	142
V.7 INFLUENCE OF ANNEALING IN BENDING.....	143
VI CONCLUSION.....	144
CHAPTER 5 : MICROSTRUCTURE ANALYSIS.....	145
I INTRODUCTION.....	145
II EXPERIMENTATION.....	146
II.1 ETCHING.....	146
II.1.1 Chemical Etching.....	147
II.1.2 Electro-etching.....	149
II.2 IMAGE CAPTURE.....	151
II.2.1 Scanning Electron Microscope.....	151
II.2.2 Stereomicroscope linked to a computer.....	156
III INFLUENCE OF THE HEAT AFFECTED ZONE.....	157
III.1 INTRODUCTION.....	157
III.2 MICROSCOPE USED.....	158
III.3 WIDTH OF THE H.A.Z.....	158
III.4 COMPARISON BETWEEN DIFFERENT BATCHES.....	161
III.5 INFLUENCE OF THE MANUFACTURING PROCESSES ON THE H.A.Z.....	162
III.5.1 Electro-polishing.....	162
III.5.2 Annealing.....	165
III.6 CONCLUSION.....	166
IV GRAIN SIZE.....	166
IV.1 INTRODUCTION.....	166

Table of Content

IV.2 COMPARISON BETWEEN BATCHES.....	167
IV.3 INFLUENCE OF THE MANUFACTURING PATH.....	169
IV.3.1 Electro-polishing.....	169
IV.3.2 Annealing.....	170
IV.4 CONCLUSION.....	170
V NUMBER OF GRAINS IN THE WIDTH.....	171
V.1 INTRODUCTION.....	171
V.2 ONE GRAIN IN THE WIDTH.....	171
V.3 FEW GRAINS IN THE WIDTH.....	173
V.4 CONCLUSION.....	173
VI CONCLUSION.....	174
CONCLUSION.....	176
REFERENCES.....	180
APPENDIX I	
APPENDIX II	
APPENDIX III	
APPENDIX IV	
APPENDIX V	
APPENDIX VI	

LIST OF FIGURES

Fig.1.1 Heart and Arteries.	5
Fig.1.2 Artery occluded by a build up of fat.	6
Fig.1.3 Angioplasty procedure.	9
Fig.1.4 Stent inserted in an artery.	11
Fig.1.5 Maass Double Helix Spiral.	12
Fig.1.6 BiodivYsio SV OTW.	15
Fig.1.7 Design of a fully expanded stent.	16
Fig.1.8 Biodivysio SV OTW specifications.	16
Fig.1.9 BiodivYsio OC OTW.	17
Fig.1.10 Biodivysio OC OTW specifications.	17
Fig.1.11 Face centres cubic structure.	18
Fig.1.12 Laser Cutting Technique.	20
Fig.1.13 Starcut laser stent cutter	21
Fig.1.14 Iron-carbon phase diagram.	22
Fig.1.15 Body-centre cubic structure.	23
Fig.1.16 Iron Carbon phase diagram showing the different annealing zone.	24
Fig.1.17 Hardening Curve of (a) a ductile material, (b) a brittle material.	26
Fig.1.18 Mohr circle.	27
Fig.1.19 Yield stress is the stress above which irreversible deformations appears.	27
Fig.1.20 Nominal Stress-Strain Curve and True Stress-Strain Curve.	29
Fig.1.21 Elastic domain in terms of normal and shear stresses.	30
Fig.1.22 Transformation diagram.	32
Fig.1.23 R transformation opposed to an RU transformation.	34
Fig.1.24 Grains and grain boundaries.	39
Fig.1.25 Edge dislocation and burgers vector.	40
Fig.1.26 Screw dislocation.	41
Fig.1.27 Climb.	41
Fig.1.28 Dislocation pile up.	42
Fig.1.29 Hall-Petch effect.	43
Fig.1.30 Influence of the grain boundaries on the Hall Petch effect.	44
Fig.1.31 Ductile fracture.	45
Fig.1.32 Intergranular fracture of a brittle material.	46
Fig.1.33 Yield stress increasing when grain size decreases and strain at breaking decreasing .	47
Fig.1.34 Tenile test specimen design.	49
Fig.1.35 Measurement of the proof stress.	53

Fig.1.36 Ultimate tensile strength.	54
Fig.1.37 Three-Point bending.	54
Fig.1.38 Shearing force diagram for the three-point bending test.	55
Fig.1.39 Bending moments diagram for a three-point bending test.	56
Fig.1.40 Cross section area of a beam.	56
Fig.1.41 Stress versus position in the thickness of the beam.	57
Fig.2.1 3D drawings of the laser-cut stent B.	64
Fig.2.2 Expansion of the stent inside the artery.	64
Fig.2.3 Pressure valve plugged to the catheter, balloon, stent system.	65
Fig.2.4 Stent mounted on the measurement apparatus.	65
Fig.2.5 Stent crimped around balloon and catheter.	66
Fig.2.6 Extremities of the stent expand first.	66
Fig.2.7 Stent fully deployed.	66
Fig.2.8 Expansion of the diameter along the stent for different pressures.	67
Fig.2.9 Observation of the longitudinal expansion.	67
Fig.2.10 (a) Z-Stent design, (b) one loop of the design.	68
Fig.2.11 Crimping of the stent against the balloon.	69
Fig.2.12 Removal of the crimping tool and introduction of the artery.	70
Fig.2.13 Deployment of the stent.	70
Fig.2.14 Stent coming in contact with the artery.	71
Fig.2.15 Drawing showing the two nodes further analysed.	71
Fig.2.16 Stress in the direction X for two opposite nodes on the strut.	72
Fig.3.1 Micro tensile tester.	74
Fig.3.2 Computer linked to the tensile tester.	74
Fig.3.3 Input of the speed and criteria to end the test.	75
Fig.3.4 Input of the measurement frequency.	75
Fig.3.5 The computer reads the load and extension and plot the curve instantaneously.	76
Fig.3.6 A text file containing the data is created.	77
Fig.3.7 (a) 3D drawing of the specimen, (b) detail of the fillets.	78
Fig.3.8 Strain-stress curve used for F.E.A analyses.	79
Fig.3.9 Stress distribution in the direction Z.	80
Fig.3.10 Stress distribution in the direction X.	81
Fig.3.11 Stress distribution in the direction Y.	81
Fig.3.12 Stiffening bars have been added to the specimen design.	82
Fig.3.13 Experimental results for four specimens of the same size.	83
Fig.3.14 Interval of confidence versus strain.	83
Fig.3.15 Width measured along the length of the struts for different strut widths.	84

Fig.3.16 F.E.A model of the strut.	86
Fig.3.17 Hardening curves obtained for different width increases along the strut.	86
Fig.3.18 Laser-cutting process.	87
Fig.3.19 Improvement of the support of the tube.	88
Fig.3.20 Expansion of the material due to the heat generated by the laser beam.	88
Fig.3.21 Shape obtained by alternating the cuts.	89
Fig.3.22 True stress versus true strain curve.	91
Fig.3.23 Curves obtained for four different specimens 0.0412 mm wide.	92
Fig.3.24 Interval of confidence versus strain for 0.0412 mm struts.	92
Fig.3.25 Hardening curves and average obtained for 0.78 mm.	93
Fig.3.26 The width of the strut varies from 0.05 mm to 0.8 mm.	94
Fig.3.27 Hardening curves obtained by tensile tests of seven different widths.	95
Fig.3.28 Zoom of the yield stress area.	96
Fig.3.29 Hardening curves for batch 1 and zoom on the yield stress area.	97
Fig.3.30 Hardening curves for batch 2 and zoom on the yield stress area.	98
Fig.3.31 Yield stress versus width of the strut for three different batches.	98
Fig.3.32 Strain at breaking versus width of the strut for three different batches.	99
Fig.3.33 Young's Modulus versus the width of the strut for three different batches.	99
Fig.3.34 Hardening curves for polished specimens and zoom on the yield stress area.	101
Fig.3.35 Yield stress versus the width of the struts before and after electro-polishing.	102
Fig.3.36 Strain at breaking versus the width of the struts before and after electro-polishing.	102
Fig.3.37 Maximum stress versus strain at breaking point before and after electro-polishing.	103
Fig.3.38 Young's Modulus versus the width of the struts before and after electro-polishing.	103
Fig.3.39 Hardening curves for annealed specimens and zoom on the yield stress area.	104
Fig.3.40 Yield stress versus the width of the strut before and after annealing.	105
Fig.3.41 Strain at breaking versus the width of the strut before and after annealing.	105
Fig.3.42 Maximum stress versus strain at breaking point before and after annealing.	106
Fig.3.43 Young's Modulus versus the width of the struts before and after annealing.	116
Fig.3.44 Comparison between experiment and F.E.A..	117
Fig.3.45 F.E.A representation of the necking at ht smaller extremity of the strut.	108
Fig.3.46 Stress vs. time at three different points along the strut.	109
Fig.3.47 Strain vs. Time at three different points along the strut.	109
Fig.4.1 Bending apparatus developed for the micro-tensile tester.	112
Fig.4.2 The apparatus is designed to (a) clamp the specimens or just (b) support them.	113
Fig.4.3 The supports move when rotating the wheel.	113
Fig.4.4 Force versus deflection curves obtained from bending a specimen clamped at both extremities.	114

Fig.4.5 F.E.A simulation of the strut before bending (a), after bending (b).	114
Fig.4.6 Picture of the Dynamic Mechanical Analyser DMA in NCBES, NUIGalway.	115
Fig.4.7 Three-points bending apparatus	116
Fig.4.8 Computer linked to the DMA.	116
Fig.4.9 Input of the speed and criteria to end the test.	117
Fig.4.10 The software plots the stress and strain versus time for basic geometries.	118
Fig.4.11 Universal Analysis converts the DMA file into a text file readable by Excel.	118
Fig.4.12 Text file created by Universal Analysis.	119
Fig.4.13 Strut bending under the weight of the left over part of tubes.	119
Fig.4.14 View from the top of the apparatus.	120
Fig.4.15 Force versus deflection curves obtained for four specimens of the same size.	120
Fig.4.16 Interval of confidence versus deflection.	121
Fig.4.17 Modelling of the test.	122
Fig.4.18 Displacement applied at the centre node on top of the strut.	122
Fig.4.19 Von Misses Equivalent Stress.	123
Fig.4.20 Equivalent plastic strain.	124
Fig.4.21 Flow chart of the inverse identification method.	125
Fig.4.22 Displacement applied.	126
Fig.4.23 The node selected is the one where the displacement was applied.	126
Fig.4.24 Force versus displacement on the Y axis (deflection of the beam).	127
Fig.4.25 The data are probed (yellow spots on the curve).	127
Fig.4.26 The struts tilt on their side when they are higher than wide.	128
Fig.4.27 Comparison between F.E.A results, computed using tensile test results, and experimental results.	129
Fig.4.28 Parameters used for the inverse identification.	129
Fig.4.29 Graph showing the results obtained after modifying the material.	130
Fig.4.30 Curves obtained for 0.5 mm wide struts.	131
Fig.4.31 Curves obtained for 0.3 mm wide struts.	131
Fig.4.32 Curves obtained for 0.2 mm wide struts.	132
Fig.4.33 Curves obtained for 0.1 mm wide struts.	133
Fig.4.34 Hardening curves obtained for batch 0.	135
Fig.4.35 Yield stress versus the width of the strut in tension and bending.	135
Fig.4.36 % increase of the yield stress from tension to bending versus the width of the strut for batch 0.	136
Fig.4.37 Young's Modulus versus the width of the strut in tension and bending.	136
Fig.4.38 Hardening curves obtained for batch 2.	137
Fig.4.39 Yield stress versus the width of the strut in tension and bending for batch 2.	137

Fig.4.40 Young's Modulus versus width of the strut in tension and bending for batch 2.	138
Fig.4.41 Yield stress versus width of the struts for batch 0 and 2.	138
Fig.4.42 % increase of the yield stress from tension to bending versus the width of the strut for batch 0 and batch 2.	139
Fig.4.43 Young's Modulus versus width of the struts for batch 0 and 2.	139
Fig.4.44 Hardening curves obtained for electro-polished struts.	140
Fig.4.45 Yield stress versus width for electro-polished struts in tension and bending.	141
Fig.4.46 Yield stress versus width of the strut before and after electro-polishing.	141
Fig.4.47 Hardening curves obtained for annealed struts.	142
Fig.4.48 Yield stress versus width of the strut in tension and bending for annealed strut.	142
Fig.4.49 Yield stress versus the width of the strut before and after annealing.	143
Fig.4.50 Load versus deflection curves before and after annealing.	143
Fig.5.1 X200 Grain boundaries visible after etching.	146
Fig.5.2 (a) Immersion of the sample, (b) swabbing.	147
Fig.5.3 X200 Over-etched sample.	147
Fig.5.4 (a) X1000 Etched grain boundaries, (b) X500 Grains getting etched as well as the grain boundaries.	148
Fig.5.5 X500 (a) Colours of the grains getting darker, (b) Sample over-etched.	148
Fig.5.6 Electro-etching apparatus.	149
Fig.5.7 (a) preparation of the solution, (b) apparatus immersed in the solution.	150
Fig.5.8 Apparatus connected to a power supply.	150
Fig.5.9 X200 Etch obtained by electro-etching.	151
Fig.5.10 SEM LEICA 430.	152
Fig.5.11 Diagram of the path followed by the electrons before striking the sample.	152
Fig.5.12 Reactions occurring when the beam strikes the sample.	153
Fig.5.13 Sample prepared for SEM examination.	153
Fig.5.14 Sample screwed inside the air-tight chamber.	154
Fig.5.15 X2500 SEM picture showing the cup shape characteristic of ductile fracture.	154
Fig.5.16 X3000 SEM picture of a chemically etched strut.	155
Fig.5.17 X5000 SEM picture of an electro-etched strut.	155
Fig.5.18 Stereomicroscope equipped with a digital camera linked to a computer.	156
Fig.5.19 Software used for image capture.	156
Fig.5.20 X2500 SEM picture of a laser cut strut compared to a sandwich material.	157
Fig.5.21 (a) X2500 SEM picture of a 0.07 mm strut, (b) X500 Stereomicroscope picture of the same strut.	158
Fig.5.22 (a) X1250 0.07 mm strut, (b) X500 0.1 mm strut.	158
Fig.5.23 Hall-Petch Effect and assumption made concerning the grain sizes.	159

Fig.5.24 Yield stress of the strut versus relative volume of the H.A.Z.	159
Fig.5.25 (a) Increase of the yield when the width decreases and (b) Increase of the strain at breaking point with the width of the strut.	160
Fig.5.26 Young's Modulus increases when the width of the strut decreases.	160
Fig.5.27 X2500 SEM pictures of 0.07 mm struts cut in (a) batch 0, (b) batch 1, (c) Batch 2.	161
Fig.5.28 X1000 (a)cut before electro-polishing, (b)cut after electro-polishing.	162
Fig.5.29 X3000 Grains structure of an electro-polished strut.	163
Fig.5.30 Yield stress versus the width of the struts before and after electro-polishing.	163
Fig.5.31 (a)X2500 S.E.M picture of an electro-polished 0.07 mm strut , (b) X200 stereomicroscope picture of a 0.05 mm strut.	164
Fig.5.32 (a) Width of the strut versus position along the strut, (b) close up on the 0.05 mm strut.	164
Fig.5.33 (a) X2500 SEM picture of a 0.07 mm annealed strut, (b) X200 Stereomicroscope picture of the same strut.	165
Fig.5.34 Yield stress versus true strain before and after annealing.	165
Fig.5.35 FCC structure.	166
Fig.5.36 Grain count.	167
Fig.5.37 Yield stress versus width of the strut.	168
Fig.5.38 X100 Electro-polished 0.0309 mm strut.	169
Fig.5.39 X200 (a) annealed 0.05 mm strut, (b) annealed 0.07 mm strut.	170
Fig.5.40 Sketch of a pile of crystals representing the strut.	170
Fig.5.41 Orientation of the slip planes.	171
Fig.5.42 Mohr circle.	172
Fig.5.43 Hardening curves of annealed struts in tension.	172
Fig.5.44 Summary of the factors influencing the mechanical behaviour of the struts.	175
Fig.I.1 Supplier's Specifications of the 316L tube.	I.1
Fig.II.1 Hand belt grinder.	II.5
Fig.II.2 (a) Hardener, (b) Epoxy resin.	II.12
Fig.II.3 (a) strut glued on the bottom of the cup, (b) resin poured in the cup, (c) resin after curing, (d) sample ready for polishing.	II.13
Fig.II.4 (a) Metaserv 2000 Grinder Polisher, (b) manual grinding.	II.14
Fig.II.5 Carbide Grinding Paper 600 grit.	II.15
Fig.II.6 Meiji stereomicroscope.	II.15
Fig.II.7 X200 Scratches resulting from rough grinding.	II.16
Fig.II.8 (a) Ultrapad, (b) Metadi Diamond Suspension 9 μm .	II.16
Fig.II.9 Structure of the Ultrapad.	II.17
Fig.II.10 X200 Surface obtained after grinding with a 9 μm diamond suspension.	II.17

Fig.II.11 (a) Trident cloth, (b) Metadi 3 μm diamond suspension, (c) close-up on the structure of the Trident cloth.	II.18
Fig.II.12 X 200 Surface obtained after grinding with a 3 μm diamond suspension.	II.18
Fig.II.13 (a) Microcloth, (b) Mastermet, (c) Microcloth structure.	II.19
Fig.II.14 X200 Surface obtained after polishing.	II.19
Fig.III.1 S.E.M mechanism.	III.1
Fig.III.2 Specimen interaction.	III.2
Fig.IV.1 Tensile Batch 0 0.05 mm wide laser-cut struts.	IV.1
Fig.IV.2 Tensile Batch 0 0.07 mm wide laser-cut struts.	IV.1
Fig.IV.3 Tensile Batch 0 0.1 mm wide laser-cut struts.	IV.1
Fig.IV.4 Tensile Batch 0 0.2 mm wide laser-cut struts.	IV.2
Fig.IV.5 Tensile Batch 0 0.3 mm wide laser-cut struts.	IV.2
Fig.IV.6 Tensile Batch 0 0.5 mm wide laser-cut struts.	IV.2
Fig.IV.7 Tensile Batch 1 0.06 mm laser-cut wide struts.	IV.3
Fig.IV.8 Tensile Batch 1 0.07 mm laser-cut wide struts.	IV.3
Fig.IV.9 Tensile Batch 1 0.11 mm wide laser-cut struts.	IV.3
Fig.IV.10 Tensile Batch 1 0.49 mm wide laser-cut struts.	IV.4
Fig.IV.11 Tensile Batch 1 0.80 mm wide laser-cut struts.	IV.4
Fig.IV.12 Tensile Batch 2 0.05 mm wide laser-cut struts.	IV.4
Fig.IV.13 Tensile Batch 2 0.08 mm wide laser-cut struts.	IV.5
Fig.IV.14 Tensile Batch 2 0.2 mm wide laser-cut struts.	IV.5
Fig.IV.15 Tensile Batch 2 0.58 mm wide laser-cut struts.	IV.5
Fig.IV.16 Tensile Batch 2 0.75 mm wide laser cut struts.	IV.6
Fig.IV.17 Tensile Batch 0 0.02 mm electro-polished struts.	IV.6
Fig.IV.18 Tensile Batch 0 0.07 mm electro-polished struts.	IV.6
Fig.IV.19 Tensile Batch 0 0.07 mm electro-polished struts.	IV.7
Fig.IV.20 Tensile Batch 0 0.17 mm electro-polished struts.	IV.7
Fig.IV.21 Tensile Batch 0 0.27 mm electro-polished struts.	IV.7
Fig.IV.22 Tensile Batch 0 0.46 mm electro-polished struts.	IV.8
Fig.IV.23 Tensile Batch 0 0.75 mm electro-polished struts.	IV.8
Fig.IV.24 Tensile Batch 0 0.05 mm annealed struts.	IV.8
Fig.IV.25 Tensile Batch 0 0.07 mm annealed struts.	IV.9
Fig.IV.26 Tensile Batch 0 0.10 mm annealed struts.	IV.9
Fig.IV.27 Tensile Batch 0 0.30 mm annealed struts.	IV.9
Fig.IV.28 Tensile Batch 0 0.80 mm annealed struts.	IV.10
Fig.V.1 Bending Batch 2 0.12 mm laser-cut struts.	V.1
Fig.V.2 Bending Batch 2 0.20 mm laser-cut struts.	V.1

Fig.V.3 Bending Batch 2 0.39 mm laser-cut struts.	V.1
Fig.V.4 Bending Batch 2 0.58 mm laser-cut struts.	V.2
Fig.V.5 Bending Batch 2 0.75 mm laser-cut struts.	V.2
Fig.V.6 Bending Batch 0 electro-polished 0.17 mm laser-cut struts.	V.2
Fig.V.7 Bending Batch 0 electro-polished 0.27 mm struts.	V.3
Fig.V.8 Bending Batch 0 electro-polished 0.46 mm struts.	V.3
Fig.V.9 Bending Batch 0 electro-polished 0.75 mm struts.	V.3
Fig.V.10 Bending Batch 0 0.1 mm annealed struts.	V.4
Fig.V.11 Bending Batch 0 0.3 mm annealed struts.	V.4
Fig.V.12 Bending Batch 0 0.5 mm annealed struts.	V.4
Fig.V.13 Bending Batch 0 0.8 mm annealed struts.	V.5
Fig.VI.1 Batch 0 0.07 mm struts (a) X200, (b) X500.	VI.1
Fig.VI.2 Batch 0 SEM 0.07 mm laser-cut (a) X1250, (a) 2500.	VI.1
Fig.VI.3 Batch 0 0.1 mm struts (a) X200, (b) X500.	VI.1
Fig.VI.4 Batch 0 0.3 mm struts (a)X200, (b)x500.	VI.2
Fig.VI.5 Batch 0 0.5 mm struts (a) X500, (b) SEM X1250.	VI.2
Fig.VI.6 Batch 0 0.8 mm struts (a) X500,(b) X1000.	VI.2
Fig.VI.7 Batch 0 0.8 mm struts SEM (a) X2500 (b) X800.	VI.3
Fig.VI.8 Batch 1 0.07 mm (a) X100, (b) X200.	VI.3
Fig.VI.9 Batch 1 0.07 mm (a) X500, (b)X100.	VI.3
Fig.VI.10 Batch 1 0.07 mm struts SEM X2500.	VI.4
Fig.VI.11 Batch 1 0.5 mm struts (a) X100, (b) X200.	VI.4
Fig.VI.12 Batch 2 0.05 mm struts (a) X100, (b) X1000.	VI.4
Fig.VI.13 Batch 2 0.07 mm struts (a)X200, (b) SEM X2500.	VI.5
Fig.VI.14 Batch 2 0.1 mm struts (a) X200, (b) X500.	VI.5
Fig.VI.15 Batch 2 0.2 mm struts (a) X500, (b) X200.	VI.5
Fig.VI.16 Batch 2 0.4 mm struts (a) X200, (b) X100.	VI.6
Fig.VI.17 Batch 2 0.8 mm struts (a) X100, (b) X200.	VI.6
Fig.VI.18 Batch 0 0.8 mm electro-polished strut (a) X200, (b) X100.	VI.6
Fig.VI.19 Batch 0 0.05 mm annealed struts (a) X100, (b) X200.	VI.7
Fig.VI.20 Batch 0 0.07 mm annealed struts SEM (a) X1250, (b) X2500.	VI.7
Fig.VI.21 Batch 0 0.8 mm annealed struts (a) X100, (b) X200.	VI.7

LIST OF TABLES

Table 1.1.	Chemical Composition	19
Table 1.2.	Mechanical Properties	19
Table 1.3.	ASTM standards concerning tensile tests.	49
Table 1.4.	ASTM standard concerning Bending tests.	55
Table 1.5.	ASTM standard relating to metallographic practice.	59
Table 3.1.	Table analysing the inaccuracy of laser-cutting of struts.	85
Table 3.2.	Example of table obtained using experimental results.	91
Table 3.3.	Yield stress and breaking point for each width.	96
Table 3.4.	Mean intercept length and number of grains/mm for each of the batches.	97
Table 3.5.	Width of the struts after electro-polishing compared to their width before.	100
Table 4.1.	Material identified from tensile test results.	128
Table 4.2.	Modified material properties	130
Table 4.3.	Material properties identified for 0.3 mm wide struts.	132
Table 4.4.	Material identified for 0.2 mm wide struts.	133
Table 4.5.	Material identified for 0.1 mm wide struts.	133
Table II.1.	Common chemical etchants.	II.11
Table II.2.	Common electro-chemical etchants.	II.12

INTRODUCTION

BACKGROUND FOR THE STUDY

A build-up of cholesterol and calcium occasionally occludes coronary arteries and consequently, not enough oxygenated blood is carried to the muscle. The heart muscle not getting enough blood to meet its demands results in chest pain. Total occlusion of the artery leads to a heart attack.

One way to re-open the artery is to inflate a balloon within the narrowed section of the vessel. The inflated balloon opens-up the occluded artery by splitting and compressing the plaque and slightly stretching the wall of the artery. However, this method is not always successful, the artery may collapse during the procedure and, even once the procedure has been completed, vessels may shrink and return to their pre-operative diameter. To prevent the artery from collapsing, stents were developed.

A coronary stent is a simple mechanical device designed to open occluded arteries and prevent them from collapsing. The stent is a round, spring-like, stainless steel device that provides mechanical support to the wall of the artery. Stents are laser-cut in tubes, then crimped around a balloon catheter. Once the balloon and stent are positioned in the artery, the balloon is inflated, leading to the expansion of the stent. The balloon is then removed and the stent is left to provide support to the artery wall. It is therefore exposed to the pulsations of the artery. The stent is a permanent implant. After a few weeks it is covered with cells and becomes part of the blood vessel wall.

In its lifetime, the stent is subjected to crimping, expansion and pulsations of the artery. It is therefore of great importance to perfectly understand and control the mechanical behaviour of stents in order to guarantee the safety of the patient.

Observation of the stent deployment have shown that the stent does not expand uniformly, either in the longitudinal or radial direction. In reality, the first parts in contact

with the artery are the extremities of the stent. As the balloon continues to inflate, the middle of the stent expands leading to a longitudinal displacement of its extremities. This type of uncontrolled expansions leads to artery scarring and is another motivation for studying the mechanical behaviour of stents.

When studying the mechanical behaviour of a device two aspects have to be considered: the design adopted and the material used. The mechanical behaviour of the geometry can be studied using experimentation and Finite Element Analysis. However, the material properties have to be determined prior to the F.E.A. in order to obtain reliable results.

A perfect control of the expansion of the stent, means a perfect knowledge of the yield stress and hardening rule of the material. The strain at breaking is also of prime importance in order to prevent cracks and fracture.

OBJECTIVES OF THE PROJECT

For general applications, when using stainless steel, the mechanical properties of the material are given by the supplier and are independent of the geometry. However, we intend to show that when dealing with such small devices the material mechanical behaviour is a function of the size of the device and the manufacturing path followed.

Because the specimen had to be representative of the stent struts, a specimen has to be designed specially for this study.

The influence of the size and the manufacturing processes (electro-polishing and annealing) on the mechanical behaviour of the specimens has, then, to be identified. Both tensile and bending behaviour have to be studied.

Finally, the microstructure has to be studied in order to explain the results found.

ORGANISATION OF THE WORK

This work is organised into five chapters.

Chapter 1 supplies a literature review necessary to follow this work, with :

- an introduction to stents,
- the known properties of the material used and a description of the manufacturing processes utilised,
- a theoretical background on elasto-plastic behaviour,
- a background on the different test methods used in this work,
- a review of metallographic techniques.

Chapter 2 describes the context of the study by presenting:

- an experiment performed to observe the non-uniform deployment of the stent,
- a Finite Element Analysis of the different steps followed by the stent.

Chapter 3 presents a tensile test conducted on struts laser-cut in tubes used for the manufacturing of stents. The following points are developed :

- the apparatus used is described and the design of the specimen tested is presented. The specimen is laser cut in a tube, therefore the accuracy of the cut and its implication are studied as well as possible improvements of the process,
- the influence of the size of the specimen on the tensile behaviour is analysed using experimental results,
- stents being electro-polished after laser-cutting, the influence of this manufacturing process on the mechanical behaviour of the specimens is tested,
- finally, the influence of annealing on the mechanical behaviour is analysed since it is sometimes included in the manufacturing of stents.

Chapter 4 presents a bending test conducted on specimens originally having the same design as the ones used for the tensile test. The following points are developed :

- an apparatus designed for a three-point bending test is presented but shown to be inadequate for this study,

- the apparatus eventually used is, then, described as well as alterations made to the specimen design : the tensile test specimens are used after removing the parts of tube left-over after laser cutting,
- the method for the inverse identification of the mechanical properties of the struts is explained,
- As in Chapter 3, the influence of the width and the mechanical processes is studied,
- Tensile and bending behaviour are compared.

Chapter 5 presents the different steps followed to examine the specimens microstructure and explains the results found in Chapter 3 and 4.

- a procedure for the preparation of the samples was developed and is presented.
- pictures of the grain structure are observed to study the possible influence of the Heat Affected Zone resulting from laser cutting,
- and finally, the role of the number of grains in the width of the strut is studied.

CHAPTER 1 : LITERATURE REVIEW

I FROM CORONARY ARTERY DISEASE TO STENTS

I.1 ANATOMY OF THE HEART [web 1]

The heart is a muscular organ composed of four chambers: two upper chambers called atria and two lower chambers called ventricles. These four chambers pump blood through the body in a rhythmic pattern with the help of the four valves in the heart. The movement of blood through the body can be felt at the wrist or neck and is known as the pulse. Although the heart is full of blood, it cannot receive oxygen and nutrients from the blood inside the chambers. The heart muscle must rely on the arteries on the surface of the heart to nourish it and keep it working properly. These surface arteries are known as the coronary arteries. Fig.1.1 shows the heart and the arteries.

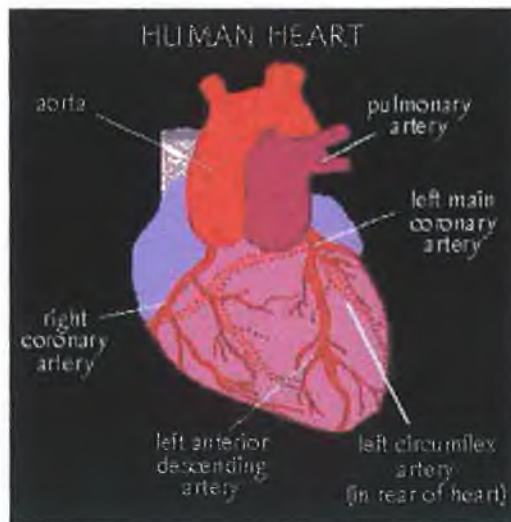


Fig.1.1 Heart and arteries.

There are three main coronary arteries: the right coronary artery, the left anterior descending coronary artery and the circumflex coronary artery.

These three arteries branch into thousands of small arteries like a tree trunk breaks into branches, bringing oxygen and nutrients to the heart muscle cells.

I.2 CORONARY ARTERY DISEASE

Occasionally, these arteries become narrowed due to a build-up of fat (Fig.1.2), cholesterol and calcium and cannot carry enough oxygenated blood to the muscle.

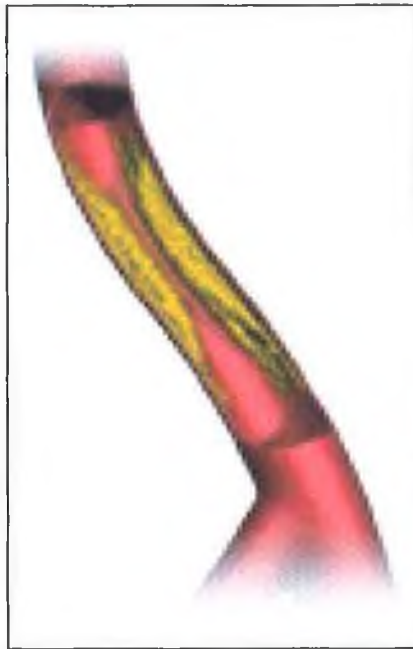


Fig.1.2 Artery occluded by a build up of fat.

The term "coronary artery disease" refers to any abnormal condition of the coronary arteries that interferes with the delivery of an adequate supply of blood to the heart muscle. More than 95 percent of all coronary artery disease is due to atherosclerosis (cholesterol and calcium deposits).

When the heart muscle does not get enough oxygenated blood to meet its demands, it experiences a hunger for more oxygen. This hunger is felt by the patient as a painful tightening, pressure, or fullness in the chest called "angina pectoris". Total occlusion of a coronary artery leads to a heart attack (myocardial infarction).

Diagnosis of Coronary Artery Disease

If a physician suspects that someone has coronary artery disease or if they have symptoms of the disease, several tests are used to make a diagnosis. Initial tests may include an electrocardiogram (ECG) while the patient is resting, and again while they are walking, running on a treadmill or pedalling a stationary bicycle.

If this test indicates that the heart is not getting the oxygen it needs, cardiac catheterization, also called an angiography, may be performed.

By using a catheter to inject x-ray dye into the coronary arteries, x-ray movies of the coronary arteries can be obtained, allowing the doctor to see any narrowing of the coronary arteries and determine their severity.

Cardiac catheterization is also useful in diagnosing other disorders of the heart such as defective heart valves, muscle disease and other problems of the heart, lungs, and blood vessels.

I.3 UNBLOCKING CORONARY ARTERIES [WEB 2][WEB 3]

I.3.1 PTCA

Coronary artery disease remains the main cause of death and major disability in the western hemisphere. Several treatments have been developed in the last three decades. Coronary bypass surgery became available in 1969.

A method of unblocking the coronary arteries without the need of surgery was discovered in 1977 by Dr. Andreas Gruentzig in Switzerland. This method - percutaneous transluminal coronary angioplasty (PTCA) - has become rapidly accepted as an effective treatment of chest pain. PTCA, also called coronary angioplasty, is a technique used to widen the narrowing in coronary arteries without surgery.

Meaning of PTCA

- * Percutaneous means the procedure is performed through the skin.
- * Transluminal means the procedure is performed inside the artery.
- * Coronary identifies the artery being treated
- * Angioplasty is the technique used to widen the narrowing in coronary arteries.

The basic idea of PTCA is to position a small inflatable balloon on the end of a catheter within the narrowed section of the coronary artery. Inflation of the balloon catheter causes the balloon to push outward against the narrowing and surrounding wall of the coronary artery. This reduces the narrowing until it no longer interferes with blood flow to the heart muscle.

PTCA procedure

PTCA can be performed either through an artery in the groin (femoral approach) or through an artery in the arm (brachial approach). Most PTCAs are performed through a femoral approach.

Before starting PTCA, a local anesthetic is injected where the catheters will be inserted.

Inserting the Guiding Catheter

Groin/Femoral Approach

Catheter introduction into the groin first requires that an introducer sheath (short tube) be inserted into the femoral artery. Next, the doctor inserts a guiding catheter (long, flexible tube) into the introducer sheath and advances it through the aorta to where the coronary arteries branch off to the heart.

Arm/Brachial Approach

Catheter introduction into the arm first requires that a small incision be made at the inside of the elbow after local anesthesia has been given.

The guiding catheter is inserted directly into the artery through the small incision and advanced to where the coronary arteries branch off to the heart.

Injecting the Dye

After catheters are inserted, the doctor injects x-ray dye through the guiding catheter into the coronary artery to view the narrowing. The doctor watches this injection on an x-ray monitor.

Inserting and inflating the balloon

Fig.1.3 shows the different steps followed :

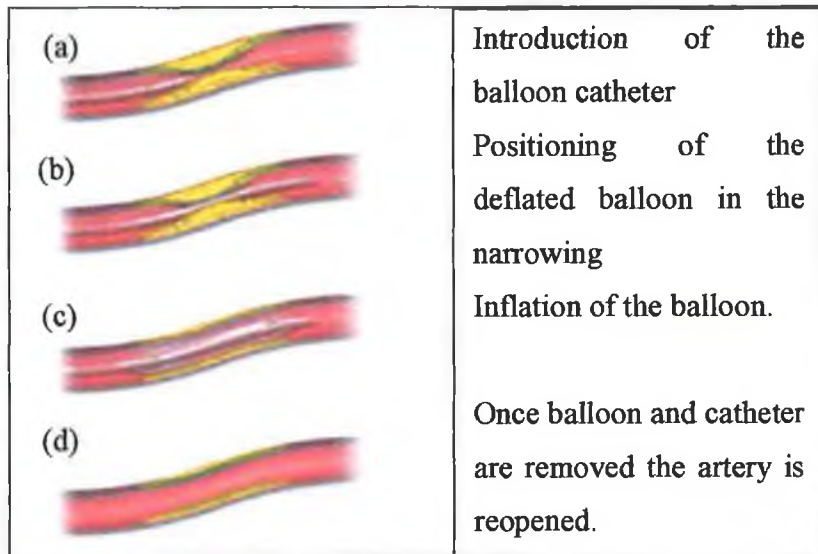


Fig.1.3 Angioplasty procedure.

- (a) The balloon catheter is passed through the guiding catheter to the origin of the artery where the narrowing is. A guide wire inside the balloon catheter is then advanced through the coronary artery until its tip is beyond the narrowing.
- (b) Next, the balloon catheter is moved over the guide wire until the balloon is within the narrowed segment. The balloon has special markers that can be seen with x-rays, so the doctor can check the position of the deflated balloon in the narrowing.
- (c) Once in position, the balloon is inflated. The inflated balloon opens up the narrowed artery by splitting and compressing the plaque and slightly stretching the wall of the artery. The balloon may be inflated and deflated several times during the angioplasty. Each balloon is made of special materials that allows it to inflate to a specific size. The doctor selects a balloon that will be about the same size as the artery. It is possible that the first balloon will be removed and other, larger balloons used if additional stretching is required.

- (d) When the plaque has been compressed and the artery has been opened sufficiently, the deflated balloon catheter is removed. X-rays of the artery shows the physician how much the blood flow has improved.

After the balloon catheter, guide wire and guiding catheter are removed, the introducer sheath may be secured and left in the groin for several hours or overnight if the PTCA was performed by the femoral approach.

If a brachial approach was used, the doctor closes the artery and incision, and bandages the arm.

Because angioplasty is a specialized form of cardiac catheterization, it shares many of the risks related to inserting a catheter in the arm or leg and passing it within the blood vessels of the heart. Angioplasty has the additional risk that the artery being treated may become more narrowed or even close off completely during the procedure. Should this occur, it may be possible to re-open the artery with a balloon catheter. Otherwise, immediate bypass surgery may be necessary to restore blood flow to the heart. There is also a possibility that it may not be possible to widen the narrowed arteries with a balloon catheter. If this happens, bypass surgery at a later date may be recommended.

I.3.2 Atherectomy

Directional coronary atherectomy (DCA) is a technique by which a catheter with a small, mechanically driven cutter shaves the plaque and stores it in a collection chamber. The plaque is then removed from the artery as the device is withdrawn.

Mechanical rotational atherectomy is a technique that uses a diamond-shaped burr that rotates and shaves the plaque into tiny particles, which then pass through the coronary circulation.

I.3.3 Coronary stents [1][2][3][4][5][6][7][8][9][web 4][web 5]

A coronary stent is a simple mechanical device designed to open closed coronary arteries. The stent (Fig.1.4) is a round, spring-like, stainless steel device that provides mechanical support to the wall of the artery.

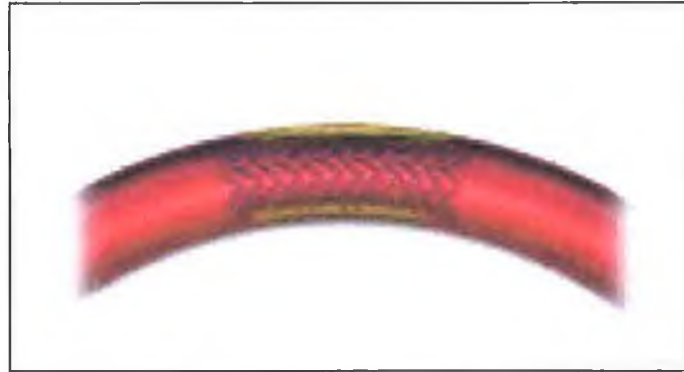


Fig.1.4 Stent inserted in an artery

The motivation for developing the coronary stent came from the fact that balloon angioplasty is not always one hundred percent successful. After an angioplasty procedure, vessels can experience restenosis and eventually return to their original pre-operative diameter. In as many as 10% of the procedures, the vessels may even collapse immediately. To prevent the vessels from shrinking, a stent is used.

Insertion of a coronary stent is very much like the procedure for Balloon angioplasty. The stent is placed around a balloon and is then positioned across the coronary lesion. The balloon is then inflated to position the stent. As the balloon inflates, the stent expands and compresses into the inner lining of the artery. There, the stent provides support to the artery wall. In two to three weeks, the stent is covered with cells and becomes a permanent part of the blood vessel wall.

I.4 REVIEW OF STENTS [1][WEB 3][WEB 5][WEB 7][WEB 8]

I.4.1 The Maass Double Helix Spiral Stent

The Maass Double Helix Spiral stent (Fig.1.5) was the first expandable prosthesis to be developed.

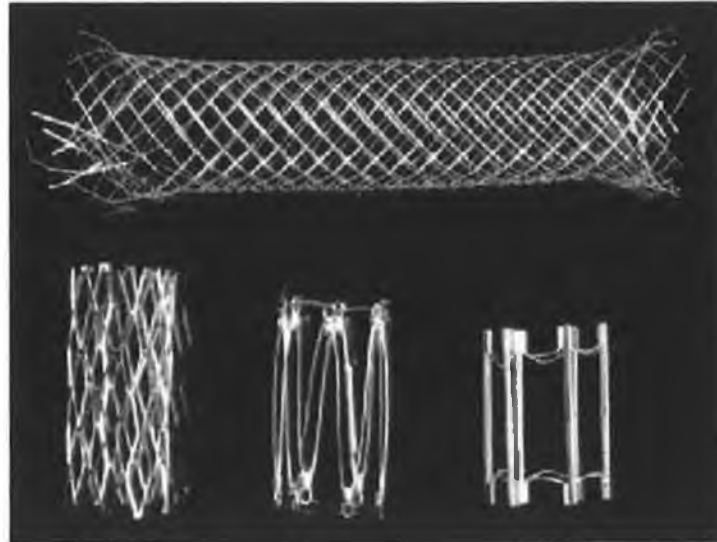


Fig.1.5 Maass Double Helix Spiral

Originally it had a diameter of up to thirty-five millimetres and was used for large vessels such as the aorta and vena cava. Although the stent had an excellent expansion ratio of 5:1, it still required a delivery system of seven millimetres in diameter. The system was too large to be delivered percutaneously. Therefore, smaller spirals were developed which had diameters of ten to fifteen millimetres.

I.4.2 Nitinol Stent

The first Nitinol stents were simultaneously applied by Dotter and Cragg in 1983 . They were made of a nickel titanium alloy which had the ability to memorize a helical shape if heated to 500 degrees Celsius and constrained to that form. The wire could be straightened if cooled to 0 degrees Celsius to allow introduction into an angiographic catheter. When the wire is introduced into the body and warmed to its transition temperature (ranging from 30 to 60 degrees celsius depending on the alloy) it coils into

its original helical shape. Dotter and Cragg performed successful implantations in canines, but this technique did not reach clinical applications because of two major problems. Difficulty occurred with the transcatheter introduction because of the length of wire necessary to form enough coils to sufficiently cover the stenotic region. Also the Nitinol coils caused significant intimal proliferation which is the rapid growth of the inner-most coat of the vessel. This causes the lumen to narrow.

I.4.3 Palmaz-Schatz Stent

The Palmaz-Schatz stent is specifically designed for use in the coronary arteries. It relies on an angioplasty balloon to dilate the stent to the correct diameter once it reaches the lesion site. This stent consists of two 7 mm slotted stainless steel tubes that are connected by a 1 mm central bridging strut. Unexpanded, the stent is only 1.6 mm in diameter.

Once the balloon is expanded, the stent has a large free space-to-metal ratio. The Palmaz-Schatz stent comes pre-mounted on its own stent delivery system. This consists of the two-segment stent crimped on an unexpanded balloon. Two markers are located on both ends of the balloon to make the stent location visible under fluoroscopy. A sheath covers the stent during delivery to keep the stent from coming into contact with and snagging the vessel walls. This stent has the advantages of reliable expansion, low profile, minimal metal surface area, and a rigid surface that will not slip.

I.4.4 Gianturco-Roubin Stent

The Gianturco-Roubin coronary stent is composed of a surgical stainless steel monofilament. The monofilament is folded in a series of loops and wrapped around a delivery balloon. It comes pre-mounted on the balloon and is slightly embedded into the balloon material to prevent slippage during delivery. Radiopaque bands are 1 to 2 mm from the ends of the stent to facilitate correct placement at the lesion site under fluoroscopy. A protective sheath that covers other stents is not required because its design does not cause the edges of the stent to snag or tear vessel walls. When the stent and delivery system are positioned in the correct location, the delivery balloon expands 0.5 mm greater than the stent size to allow for the slight recoil of the stent. It also helps embed the stent struts into the vessel walls.

I.4.5 Strecker Stent

The Strecker stent has several features that are not usually found in other stents. It can be compressed in the radial direction as well as the longitudinal direction. This is due to the knitting pattern of the single tantalum filament. It consists of loosely connected loops that allow the stent to have elastic properties. It is flexible in the compressed state as well as in the dilated state. These qualities allow the stent to be used in vessel sites in which the stent and catheter must pass through sharp curves or in vessels with kinks in them. This stent is also advantageous in deployment because it does not reduce in size longitudinally when dilated radially. This allows for more accurate placement because the longitudinal shortening does not have to be taken into consideration when placing the stent in the lesion site. This stent is loaded on a balloon catheter with the ends covered by silicon sleeves. These prevent the stent from slipping on the balloon during delivery. The tantalum knit is visible under roentgen fluoroscopy to allow for better visibility and placement at the lesion site. Once the correct position has been reached, the balloon is inflated and the silicon sleeves roll back off the ends of the stent to allow for full expansion. This stent has been used for successful implantations in the aorta, the aorta bifurcation, and the iliac, femoral, renal, and coronary arteries.

I.4.6 Gianturco Stent

The Gianturco Expandable Wire Stent is a self expanding stent mainly used in larger vessels, such as the vena cava, for benign or malignant obstructions. This rigid stent is commercially available in diameters between 15 and 40 mm. The size and rigidity of the stent has lead to specific design and implant considerations, such as implanting two stents connected by a wire strut with small barbs to prevent slippage. Once the stents have been introduced to the lesion site through a catheter, they expand and continue to dilate the stenosis during the first few days after placement. The expansion force depends on the calibre of the wire, the length of the stent, and the number and angles of the bends.

I.4.7 Wallstent

The Wallstent is used clinically in the coronary and peripheral arteries. It is made of stainless steel filaments woven in a criss-cross tubular pattern. It is highly flexible in the longitudinal direction. The Wallstent is compressed and contained on a delivery catheter by a doubled over membrane. To deploy the Wallstent, the outer membrane is retracted allowing the stent to be released. Once the stent is no longer constrained, it returns to its original size, which is 20-40% shorter than its compressed state. Balloon dilation can then be used to accelerate the rate of expansion to reach the maximum size faster.

I.5 ABBOT VASCULAR DEVICES [1][WEB 9]

I.5.1 Biodivysio SV OTW

This stent (Fig.1.6) is a specifically designed small vessel (SV) stent with a biocompatible coating.

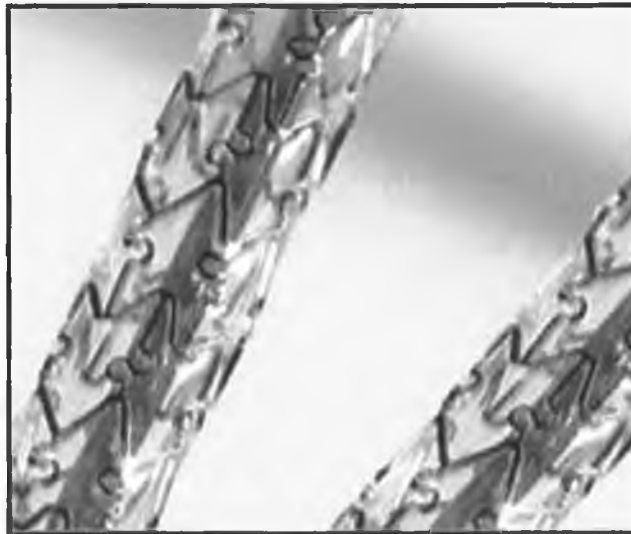


Fig.1.6 Biodivysio SV OTW.

Its main properties are: high radial strength and low recoil, excellent deliverability to access lesion sites, optimal balance of scaffolding and metal-to-artery ratio.

Fig.1.7 shows the design of a fully expanded stent.

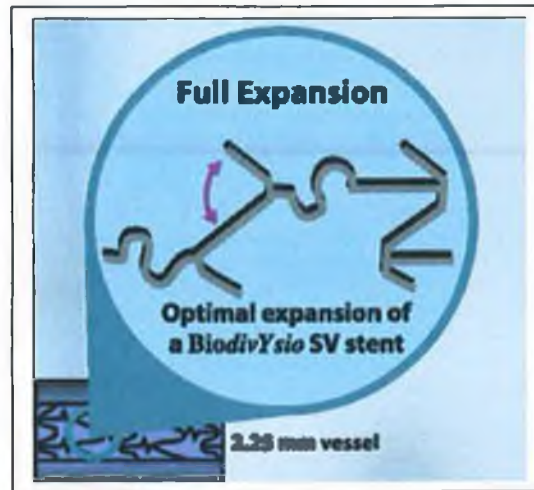


Fig.1.7 Design of a fully expanded stent.

Fig.1.8 gives the specifications of the stent.

Stent Specifications	
Stent Type:	Closed cell, tubular (1mm tube)
Stent Material:	316L Stainless Steel
Stent Coating:	Phosphorylcholine (PC Technology)
Strut Thickness:	0.0036"
Foreshortening*:	1.6%
Recoil*:	2.4%
Radiopacity:	Moderate
Max. Stent Diameter:	2.75mm
Inner Strut Diameter:	0.90mm or 0.035"
Max. Inner Strut Diameter:	2.00mm or 0.078"

*Biodivysio SV OTW Family Average.
*Data are on file at Abbott Vascular Devices.

Fig.1.8 Biodivysio SV OTW specifications.

The 316L tubes used for the manufacturing of the Biodivysio SV OTW, are the tubes used for the manufacturing of the specimens studied in this work.

I.5.2 Biodivysio OC OTW

The main properties of this stent (Fig.1.9) are excellent flexibility and low profiles for lesion access and optimised conformability (OC) to maintain the vessel original shape.

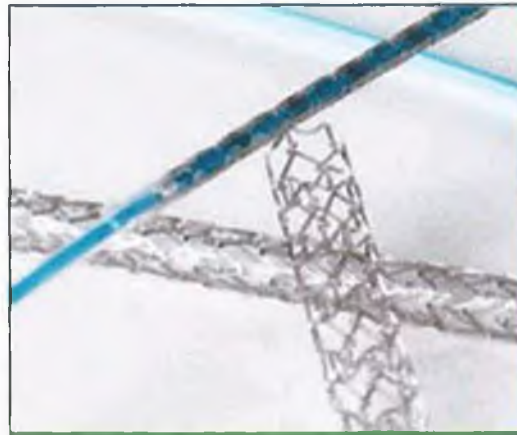


Fig.1.9 Biodivysio OC OTW.

Fig.1.10 shows the specifications of this stent.

Stent Specifications	
Stent Type:	Closed cell, tubular (1.6mm tube)
Stent Material:	316L Stainless Steel
Stent Coating:	Phosphorylcholine (PC Technology)
Strut Thickness:	0.0036"
Foreshortening*:	1.0%
Recoil*:	1.5%
Radiopacity:	Moderate
Max. Stent Diameter:	4.25mm
Inner Strut Diameter:	1.12mm or 0.044"
Max. Inner Strut Diameter:	2.70mm or 0.11"

*Biodivysio OC OTW Family Average.
*Data are on file at Abbott Vascular Devices.

Fig.1.10 Biodivysio OC OTW specifications.

II MATERIAL AND MANUFACTURING PROCESSES

II.1 STAINLESS STEEL [10][11][12]

II.1.1 Introduction

Stents are cut in hollow bars (tubes) of stainless steel; in order to show the influence of the dimensions and manufacturing path, it is important to know the characteristics of the material beforehand.

II.1.2 Stainless Steel

Stainless steels are iron-base alloys that contain a minimum of approximately 11% Cr, the amount needed to prevent the formation of rust in unpolluted atmospheres (hence the designation stainless).

II.1.3 Austenitic stainless steels

They constitute the largest stainless family in term of number of alloys and usage. They are nonmagnetic, and their structure is face centred cubic (Fig.1.11).

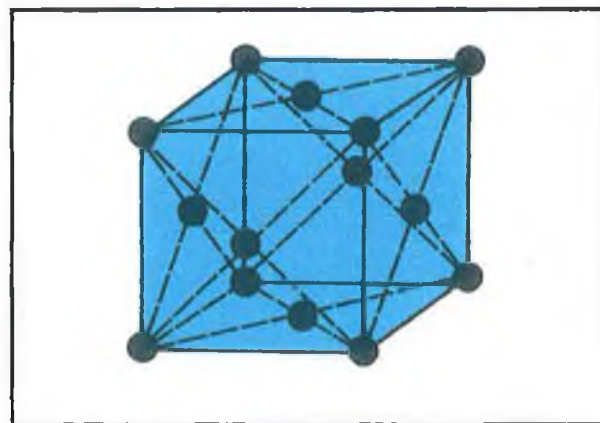


Fig.1.11 Face centres cubic structure.

They possess excellent ductility, formability, and toughness. In addition, they can be substantially hardened by cold work.

Although nickel is the chief element used to stabilise austenite, carbon and nitrogen are also used because they are readily soluble in the fcc structure. A wide range of corrosion resistance can be achieved by balancing the ferrite forming elements such as chromium and molybdenum, with austenite-forming elements.

II.1.4 316L [web 10][web 11]

The yield stresses of wrought austenitic stainless steels are rather modest and are comparable to those of mild steels (200 to 275 MPa). Their ultimate tensile stress is usually 520 to 760 MPa, and their elongation varies from 40% to 60%.

The addition of molybdenum in type 316L provides pitting resistance in phosphoric and acetic acids and diluted chloride solutions, as well as corrosion resistance in sulfurous acid.

II.1.5 316L Hollow Bar

The manufacturer receives hollow bars from the supplier. Each batch of hollow bars comes with a specification sheet (Appendix I). The following information was taken from these specification sheets.

Chemical Composition (%wt)

C	Si	Mn	P	S	Cr	Ni	Mo
max	max	max	max	max	max		
0.017	0.33	1.85	0.02	0.002	17.5	14.75	2.85

Table 1.1. Chemical Composition

Mechanical Properties

Proof Strength		Tensile strength	Elongation
R _{0.2%} (Mpa) min	R _{1%} (Mpa) min	R _m (Mpa)	A % min
220	250	515-690	49-57

Table 1.2. Mechanical Properties

Grain size

The ASTM grade given by the supplier is between 8 and 10. This corresponds to an average of 45 grains/mm for grade 8 and 90 for grade 10.

II.2 MANUFACTURING PROCESSES

II.2.1 Laser cutting [web 12][web 13]

Laser cutting offers a superior cut-edge quality with parallel sides and no burrs. The technology offers supreme flexibility, handling profiles from the simplest of components to shapes of almost limitless complexity.

As shown on Fig.1.12, a high-energy infra-red laser light beam is directed onto the material. A focusing lens is used to concentrate all of the energy onto a pin-point, causing rapid localised melting and partial vaporisation of the material. An assist gas, such as oxygen or nitrogen is then directed through a nozzle to expel the molten material. The position and power of the laser beam is precisely controlled by a computer.

Using Nitrogen as the assist gas prevents oxidation of the cut surface which is desirable when cutting stainless steel.

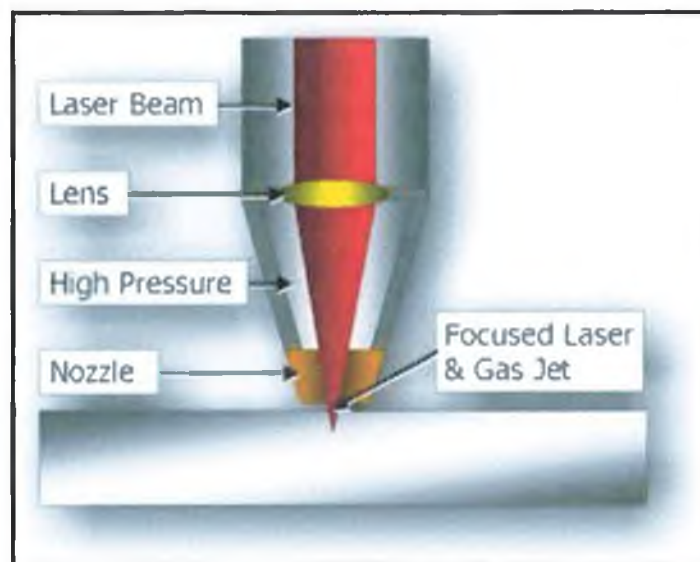


Fig.1.12 Laser Cutting Technique.

The machine used by Abbot to laser cut stents is a Rofin-Baasel Starcut laser stent cutter (Fig.1.13 next page)[web 14]. This machine is specially designed to cut extremely complex geometries from a thin-walled steel tube (1.0-10.0 mm diameter). The StarCut Laser delivers cut widths of less than 20 μm with nearly burr-free edge quality.



Fig.1.13 Starcut laser stent cutter

II.2.2 Electro-polishing [web 15][web 16]

Electro-polishing is widely used for cleaning fabricated stainless steel parts and in addition smooths and polishes the product surface. The development of a smoother, unstressed, and uncontaminated surface is a contribution to improved hygiene and cleanability. The ultimate benefits of electro-polishing are manifest by improved appearance, micro smoothness, corrosion resistance, cleanability, and resistance to further contamination and bacteria growth.

Electro-polishing is the process of smoothing a metal surface anodically in a concentrated acid or alkaline solution. With the application of electrical current, a film forms on the metal surface being treated, thus allowing metal ions to diffuse through the film. The high points of the surface roughness and also those burr areas, receive higher current density and are dissolved at a greater rate than the remainder of the surface. The result is a smoother, more uniform surface.

II.2.3 Annealing [10][13]

In order to understand heat treatments the iron-carbon phase diagram has to be introduced.

Iron-carbon phase diagram

The equilibrium iron-carbon phase diagram (Fig.1.14) shows the phases present at any composition and temperature.

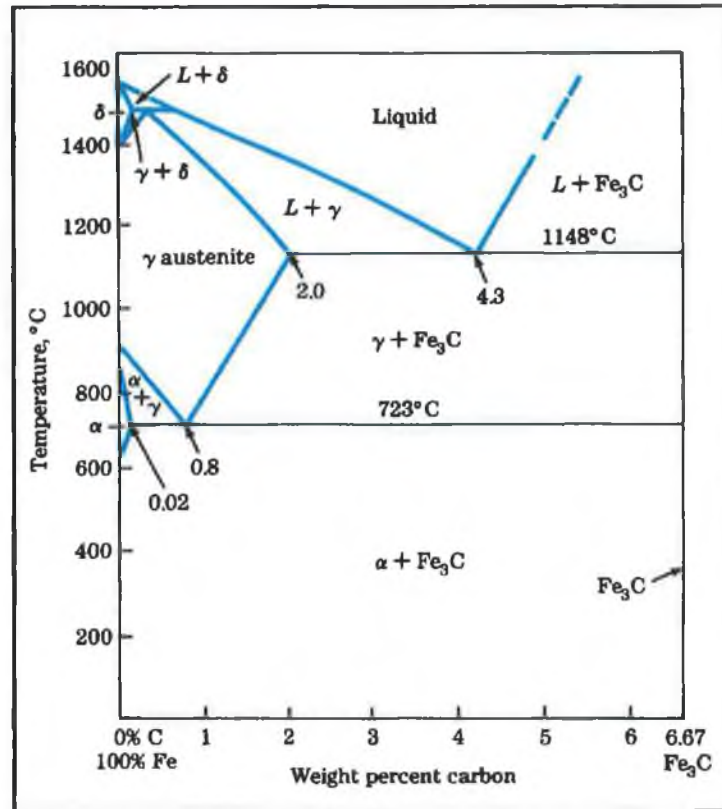


Fig.1.14 Iron-carbon phase diagram.

Phases

A phase is a homogeneous and physically distinct region of matter. In can be seen from Fig.1.14 that three phases can form on cooling (from the liquid) in the range of carbon compositions. These are austenite, ferrite + austenite, and ferrite + cementite.

Austenite

Austenite γ is a solid solution of carbon in iron and has a face-centred cubic (fcc) lattice structure (Fig.1.11). Austenite is the only phase that can transform into other phases on cooling. It is a phase that is stable at high temperatures but metastable (likely to transform to another phase) at lower temperatures. It exists when the steel is heated to temperatures

above 910°C and is stable on cooling to 727°C, as shown in the binary phase diagram (Fig.1.14). Austenite is a soft phase and is ductile.

Ferrite

As seen from the phase diagram previously, austenite transforms to ferrite (α). Ferrite has the body-centred cubic structure (Fig.1.15) which has no room for carbon. Ferrite nucleates at austenite grain boundaries and is softer than austenite. Because ferrite has a low solubility for carbon, the carbon is ejected from the lattice as the austenite transforms to ferrite and clumps together as carbides remaining separate from the ferrite.

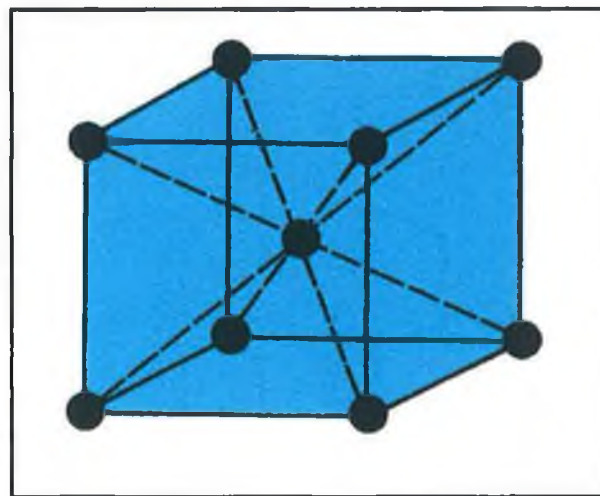


Fig.1.15 Body-centre cubic structure.

Cementite

The transformation of the face-centred lattice of austenite to the body-centred lattice of ferrite is hampered due to the presence of dissolved carbon in austenite. The austenite lattice has enough space to accommodate carbon atoms at the centres of unit cells but the body-centred lattice of ferrite has no such space. Therefore, almost all carbon precipitates from the austenite lattice as iron carbide (cementite).

Heat treatments processes such as annealing modify the phases present in the material.

Full annealing is the process of slowly raising the temperature about 50 °C (122 °F) above the line A_{C3} , in the case of Hypoeutectoid steels (steels with < 0.77% Carbon) and 50 °C (122 °F) above line A_{C1} , in the case of Hypereutectoid steels (steels with > 0.77% Carbon). (Fig.1.16)

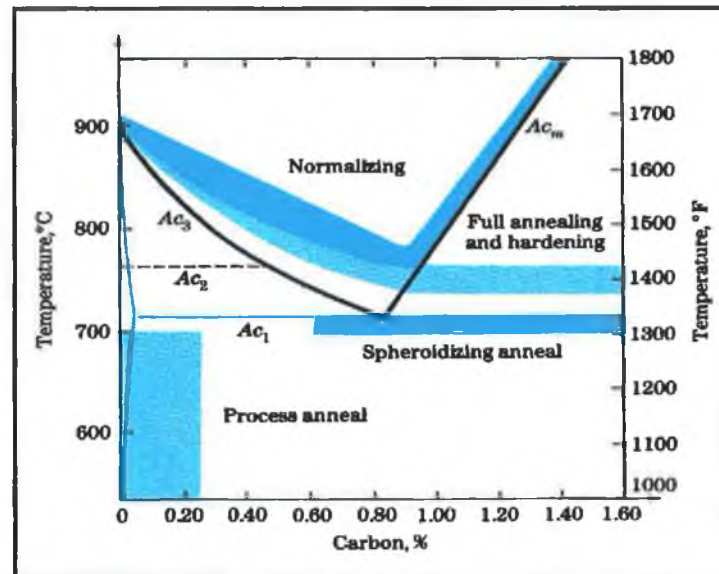


Fig.1.16 Iron Carbon phase diagram showing the different annealing zone.

It is held at this temperature for sufficient time for all the material to transform into Austenite or Austenite-Cementite as the case may be. It is then slowly cooled at the rate of about 20 °C/hr (60 °F/hr) in a furnace to about 50 °C (122 °F) into the Ferrite-Cementite range. At this point, it can be cooled in room temperature air with natural convection. The steel becomes soft and ductile.

Normalising is the process of raising the temperature to over 60 °C (140 °F), above line A_{C3} or line A_{CM} fully into the Austenite range. It is held at this temperature to fully convert the structure into Austenite, and then removed from the furnace and cooled at room temperature under natural convection. The resulting material is soft; the degree of softness depends on the actual ambient conditions of cooling. This process is considerably cheaper than full annealing since there is not the added cost of controlled furnace cooling.

The main difference between full annealing and normalizing is that fully annealed parts are uniform in softness (and machinability) throughout the entire part; since it is exposed to the controlled furnace cooling. In the case of the normalized part, depending on the geometry, the cooling is non-uniform resulting in non-uniform material properties across the part. This may not be desirable if further machining is desired, since it makes the machining job somewhat unpredictable. In such a case it is better to do full annealing.

Process Annealing is used to treat work-hardened parts made out of low-Carbon steels (< 0.25% Carbon). This allows the parts to be soft enough to undergo further cold working without fracturing. Process annealing is done by raising the temperature to just below the Ferrite-Austenite region, line A_{C1} on the diagram. This temperature is about 727 °C (1341 °F) so heating the part to about 700 °C (1292 °F) should suffice. The part is held at this temperature long enough to allow recrystallization of the ferrite phase, it is then cooled in still air. Since the material stays in the same phase through out the process, the only change that occurs is the size, shape and distribution of the grain structure. This process is cheaper than either full annealing or normalizing since the material is not heated to a very high temperature or cooled in a furnace.

Stress Relief Annealing is used to reduce residual stresses in large castings, welded parts and cold-formed parts. Such parts tend to have stresses due to thermal cycling or work hardening. Parts are heated to temperatures of up to 600 - 650 °C (1112 - 1202 °F), and held for an extended time (about 1 hour or more) and then slowly cooled in still air.

Note that the time held at the temperature and the cooling rate also influence the microstructure obtained.

The manufacturing processes presented above are the ones studied in this work.

III MECHANICAL BEHAVIOUR

III.1 HARDENING CURVE[10][14]

III.1.1 Introduction

Let us consider a uniaxial displacement applied to a material. If the stress (σ in Pa) is plotted as a function of the strain (ϵ), both measured in the same direction, the curve obtained is referred to as hardening curve. The hardening curve in tension completely characterises the uniaxial behaviour. Fig.1.17 gives two examples of hardening curves.

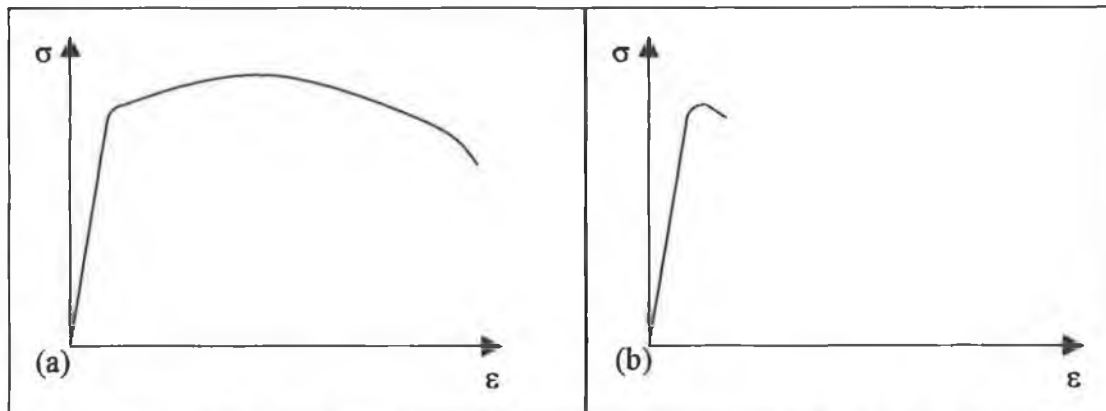


Fig.1.17 Hardening Curve of (a) a ductile material, (b) a brittle material.

III.1.2 Elasticity

Elastic deformation is a reversible phenomenon that occurs at atomic level. The observed macroscopic effect is the result of the variations in the interatomic spacing necessary to balance the external loads, and also of the reversible movements of dislocation (see III.5.1).

In elasticity σ_1 measured in the direction of the force applied is a linear function of ϵ_1 :

$$\sigma_1 = E.\epsilon_1 \quad (1.1.)$$

Where :

E is the Young Modulus

Consequently, the hardening curve allow the calculation of the Young Modulus in the direction of the stress applied.

If the stress is measured in another direction x at an angle θ from the main direction 1, σ_x is function of σ_1 , σ_2 and the shear stress τ_{12} as represented by the Mohr circle [15][16] [web 17] [web 18].

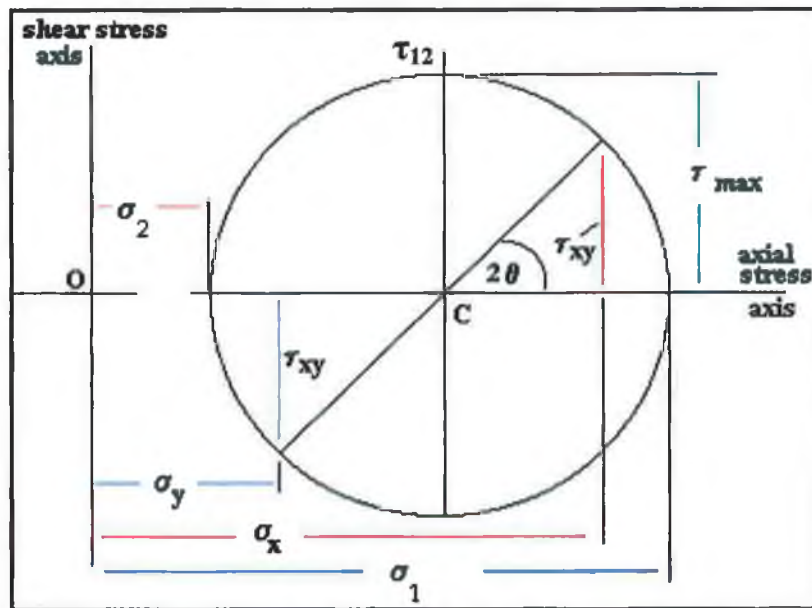


Fig.1.18 Mohr circle

III.1.3 Elastic limit or Yield stress

The yield stress σ_y is the stress above which irreversible deformations appear. (Fig.1.19).

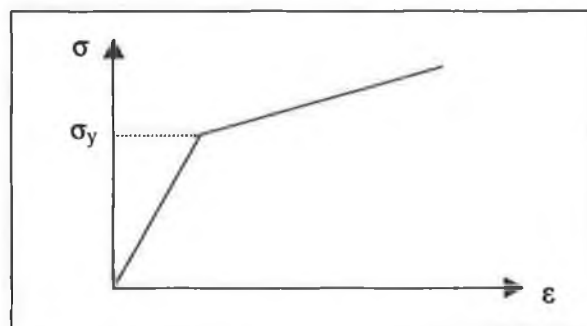


Fig.1.19 Yield stress is the stress above which irreversible deformations appears.

III.1.4 Plastic flow

The total strain may be partitioned or separated into the reversible or elastic strain and the irreversible or plastic strain.

$$\varepsilon = \varepsilon_e + \varepsilon_p \quad (1.2.)$$

Where :

ε_e is the elastic strain,

ε_p is the plastic strain.

A decoupled constitutive relations for ε_e and ε_p exists :

$$\begin{cases} \varepsilon_e = A(\sigma) \dots \dots \dots \forall \sigma \\ \varepsilon_p = g(\sigma) \dots \dots \dots |\sigma| \geq \sigma_y \\ \varepsilon_p = 0 \dots \dots \dots |\sigma| < \sigma_y \end{cases} \quad (1.3.)$$

A is a linear function of slope E. The plastic strain is equal to zero as long as the yield stress has not been reached, then is a function of the stress.

The relation is valid only in the case of continuous plastic flow.

Stainless steel is a strain rate sensitive material, however the deformations experienced by stents are quasi-static.

III.1.5 Hardening

Work hardening or hardening occurs when a metal is strained beyond the yield point. An increasing stress is required to produce additional plastic deformation and the metal apparently becomes stronger and more difficult to deform.

If true stress is plotted against true strain (see paragraph IV for true strain and true stress calculation), the rate of strain hardening tends to become almost uniform, that is, the curve becomes almost a straight line, as shown in Fig.1.20 (next page).

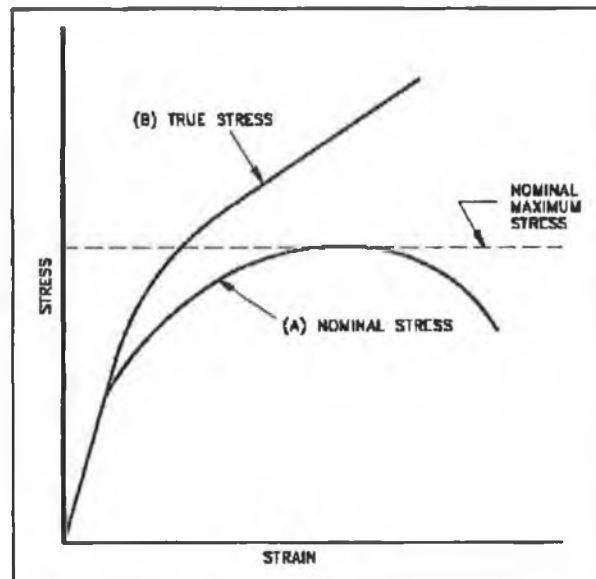


Fig.1.20 Nominal Stress-Strain Curve and True Stress-Strain Curve

The gradient of the straight part of the line is known as the strain hardening coefficient or work hardening coefficient, and is closely related to the shear modulus (about proportional). Therefore, a metal with a high shear modulus will have a high strain or work hardening coefficient (for example, molybdenum). Grain size will also influence strain hardening. A material with small grain size will strain harden more rapidly than the same material with a larger grain size. However, the effect only applies in the early stages of plastic deformation, and the influence disappears as the structure deforms and grain structure breaks down.

Work hardening reduces ductility, which increases the chances of brittle failure.

Work hardening can also be used to treat material. Prior work hardening (cold working) causes the treated material to have an apparently higher yield stress. Therefore, the metal is strengthened.

Perfect plastic flow without hardening corresponds to the case where the stress remains constant during the flow.

The hardening effect due to plastic flow manifests itself in two ways:

- The flow occurs only if the stress increases,
- The elastic limit increases during the flow.

For monotonic loading, the current limit of elasticity or the yield stress, is equal to the highest value of the stress previously attained.

Hardening model of an initially isotropic elastoplastic solid subjected to monotonic uniaxial loading is the following:

$$\sigma = \sigma_y + K_y \varepsilon_p^{1/M_y} \quad (1.4.)$$

K_y (Pa) and M_y are constants defining the hardening rule.

III.2 MULTIAXIAL PLASTICITY CRITERIA [14][17]

III.2.1 Introduction

The yield stress of uniaxial plasticity defines the elastic domain in the uniaxial stress space. The generalisation of this concept to the multiaxial case is the yield criterion. It defines in the stress space of three or six dimensions a domain within which any stress variation generates only variations of elastic strains.

For example, in a two dimensional space (tension-torsion), the curve obtained by plotting the normal stress σ_{11} and the corresponding tangential stress σ_{12} (shear stress) at plasticity thresholds defines the boundary of the elastic domain (yield criteria).

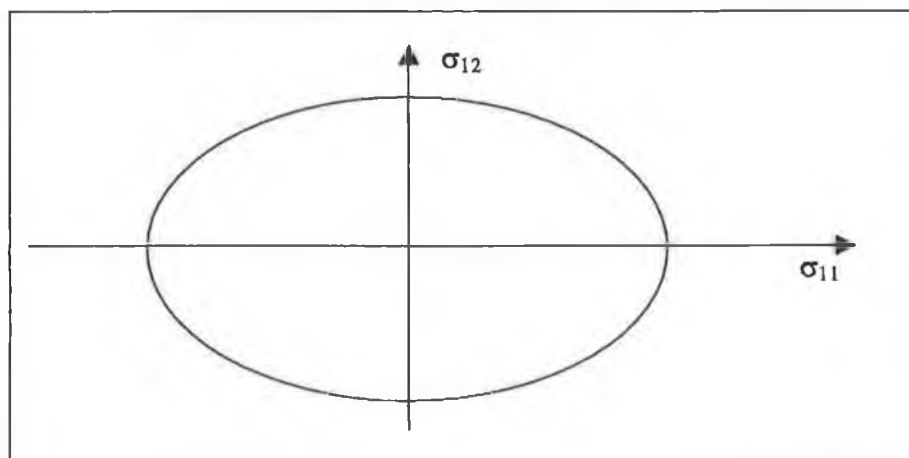


Fig.1.21 Elastic domain in terms of normal and shear stresses

III.2.2 Hardening Criteria

Two aspects are distinguished: one related to flow criteria and the other to hardening, i.e., the evolution of the criterion. The terms isotropic and anisotropic yield criteria are applicable to a given state (without modification of hardening). Hardening implies the idea of transformation. Isotropic hardening defines an homothetic transformation (dilatation of the criterion) whereas kinematic hardening defines a translation of the criterion. The transformation can also be combined isotropic-kinematic and finally anisotropic hardening defines an arbitrary transformation of the criterion. The following are different types of flow and hardening combination:

- Isotropic criterion-Isotropic hardening
- Isotropic criterion-Kinematic Hardening
- Anisotropic criterion-Isotropic hardening
- Anisotropic criterion-Kinematic hardening
- Isotropic criterion-Anisotropic hardening
- Anisotropic criterion-Anisotropic hardening

III.2.3 Isotropic criteria

These criteria correspond to isotropic-hardening states. The equation of the elastic domain boundary includes all the components of the stress tensor σ_{ii} (normal and shear stress in all directions) and a hardening variable σ_s which is a scalar variable in the case of isotropic hardening. The hardening variable is chosen to be the yield stress σ_y in simple tension.

The Von Mises Criterion

$$\frac{1}{\sqrt{2}} [(\sigma_{11} - \sigma_{22})^2 + (\sigma_{22} - \sigma_{33})^2 + (\sigma_{33} - \sigma_{11})^2 + 6(\sigma_{12}^2 + \sigma_{23}^2 + \sigma_{13}^2)]^{1/2} = \sigma_s \quad (1.5.)$$

The Tresca Criterion

$$\text{Sup}_{i \neq j} (|\sigma_i - \sigma_j|) = \sigma_s \quad (1.6.)$$

III.2.4 Anisotropic criteria

The Hill criterion [17]

The Hill criterion corresponds to a particular kind of anisotropy in which three planes of symmetry are conserved during hardening of the material. The intersection of these three planes are the principal axes of anisotropy.

$$F(\sigma_{11} - \sigma_{22})^2 + G(\sigma_{22} - \sigma_{33})^2 + H(\sigma_{33} - \sigma_{11})^2 + 2L\sigma_{12}^2 + 2M\sigma_{23}^2 + 2N\sigma_{13}^2 = 1 \quad (1.7.)$$

F, G, H, L, M, N are the six scalar parameters which characterise the state of anisotropic hardening. They may be determined with the help of three experiments in simple tension and three in simple shear.

The Tsai criterion [18]

The Tsai criterion allows for the eventual differences in tension and in compression.

In its most general form, it is expressed as the sum of a linear form and a quadratic form of the six stress components.

III.3 LARGE DEFORMATION PLASTICITY[17][19][20][21][22][WEB 19]

III.3.1 Deformation Gradient

Let S^0 be a body of volume V^0 in its initial configuration C^0 . In the current configuration C , at a time t , its volume is V . Let φ be the transformation which carries M^0 , a material point of the body in the initial configuration, to M (in the current configuration). X is the position vector of M^0 and x the position vector of M (Fig.1.22).

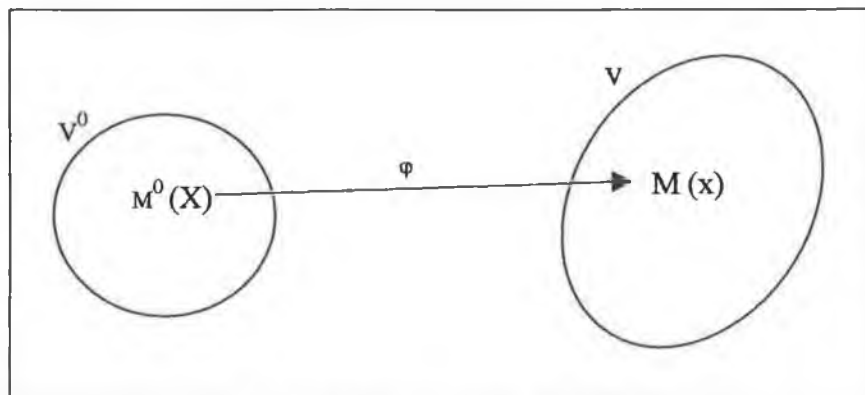


Fig.1.22 Transformation diagram.

x can be written as a function (φ) of X and t :

$$x = \varphi(X, t) \quad (1.8.)$$

The displacement vector u is defined by :

$$u = x - X \quad (1.9.)$$

The gradient F of the transformation φ in the vicinity of a point M is named deformation gradient and is given by:

$$F = \nabla_0 \varphi = \frac{\partial x}{\partial X} = 1 + \frac{\partial u}{\partial X} \quad (1.10.)$$

Where 1 is the unit second order tensor.

$$\det F = J > 0 \quad (1.11.)$$

J is the jacobian determinant of φ .

The right Cauchy-Green tensors C and the left Cauchy-Green tensors B are defined as following :

$$\begin{cases} C = F^T F = U^2 \\ B = F F^T = V^2 \end{cases} \quad (1.12.)$$

U and V are called the right and left stretch tensors.

III.3.2 Polar Decomposition

The polar decomposition of F is given by :

$$F = R U = V R \quad (1.13.)$$

U and V are symmetric and positive definite, R is a proper orthogonal tensor.

If the displacement is locally a rigid-body one, then we simply have $F=R$ (Fig.1.23).

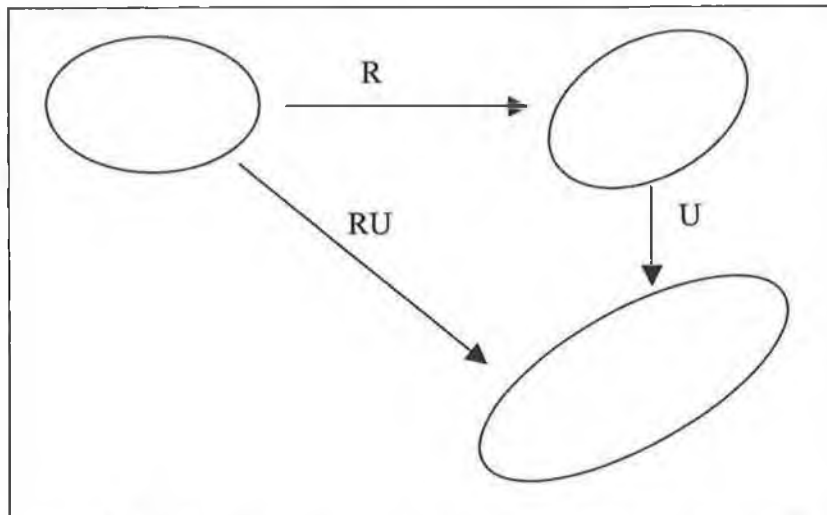


Fig.1.23 R transformation opposed to an RU transformation.

III.3.3 Measure of Deformation

A general measure of deformation was given by Hill, Ogden.

$$\begin{cases} E^{(m)} = \left(\frac{1}{m}\right)[U^m - 1] & \text{if } m \neq 0 \\ \ln U & \text{if } m = 0 \end{cases} \quad (1.14.)$$

The following ones are the most commonly used :

Green-Lagrange :

$$E^{(2)} = \left(\frac{1}{2}\right)[U^2 - 1] \quad \text{if } m=2 \quad (1.15.)$$

Almansi :

$$E^{(-2)} = \left(\frac{1}{2}\right)[I - U^{-2}] \text{ if } m = -2 \quad (1.16.)$$

Biot :

$$E^{(1)} = [U - I] \text{ if } m = 1 \quad (1.17.)$$

Hencky (true strain tensor)

$$E^{(0)} = \ln U \text{ if } m = 0 \quad (1.18.)$$

Deformation Rate Measure

The velocity field at time t is defined by :

$$v = \frac{\partial x}{\partial t} = \frac{\partial}{\partial t} \varphi(X, t) \quad (1.19.)$$

The velocity gradient L is defined by :

$$L = \frac{\partial v}{\partial x} = \frac{\partial v}{\partial X} \cdot \frac{\partial X}{\partial x} \quad (1.20.)$$

with :

$$\frac{\partial v}{\partial X} = \frac{\partial}{\partial t} \left(\frac{\partial x}{\partial X} \right) = \dot{F} \quad (1.21.)$$

So :

$$L = \dot{F}F^{-1} \text{ or } \dot{F} = LF \quad (1.22.)$$

Using differential calculus, we obtain :

$$\dot{C} = F^T \dot{F} + F^T F = F^T (L + L^T) F = 2F^T D F \quad (1.23.)$$

Where $D = \frac{1}{2}(L + L^T)$ is the deformation-rate tensor or stretching tensor.

An immediate corollary of the last result is :

$$\dot{\mathbf{E}} = \mathbf{F}^T \mathbf{D} \mathbf{F} \quad (1.24.)$$

A rigid-body motion is characterised by the right Cauchy-Green tensor field \mathbf{C} being constant in time (not necessarily equal to \mathbf{I} , since the initial configuration of the motion may be deformed with respect to the reference configuration), or, equivalently.

If $\mathbf{W} = \frac{1}{2}(\mathbf{L} - \mathbf{L}^T)$, then obviously $\mathbf{L} = \mathbf{D} + \mathbf{W}$. The antisymmetric tensor \mathbf{W} is called spin, vorticity or spinning tensor.

Area and Volume Deformation

Let $d\mathbf{S}^0$ be an infinitesimal area in the initial configuration, and $\mathbf{n}^0 d\mathbf{S}^0$ the oriented surface element corresponding.

Let $\mathbf{n} d\mathbf{S}$ be the oriented surface element in its current configuration, the Nanson formula allows to write :

$$\mathbf{n} d\mathbf{S} = \mathbf{J} \mathbf{F}^{-T} \mathbf{n}^0 d\mathbf{S}^0 \quad (1.25.)$$

Let dV^0 the infinitesimal volume in the initial configuration, and dV the infinitesimal volume in its current configuration.

The jacobian determinant has the important property of measuring the ratio between current and initial infinitesimal volumes.

$$dV = \mathbf{J} dV^0 \quad (1.26.)$$

If ρ and ρ^0 denote the mass density in the current and initial configurations, respectively, then conservation of mass in an infinitesimal volume requires $\rho dV = \rho^0 dV^0$, therefore :

$$\mathbf{J} = \frac{\rho^0}{\rho} \quad (1.27.)$$

III.3.4 Stress

The stress tensor is called the Cauchy stress and is noted T.

If df is the load, the stress tensor is defined by :

$$df = TndS \quad (1.28.)$$

Using the initial configuration, df is defined by :

$$df = Pn^0 dS^0 \quad (1.29.)$$

Where P the first Piola-Kirchhoff stress tensor, and :

$$P = JTF^{-T} \quad (1.30.)$$

If a load in the initial configuration df^0 is introduced, then :

$$df^0 = Sn^0 dS^0 \quad (1.34)$$

S is the second Piola-Kirchhoff stress tensor.

$$S = JF^{-1}TF^{-T} \quad (1.31.)$$

III.4 STRAIN GRADIENT PLASTICITY

III.4.1 Introduction [23][24][25][26][27][28][29][30]

Strain gradient plasticity theories have been introduced to extend continuum plasticity to the micron scale. Aifantis [31][32] has modified the constitutive model of classical plasticity by assuming that the actual flow stress is related to gradients of the equivalent plastic strain. Then, Fleck[33][34] and Hutchinson [35][36][37][38][39][40][41] have developed a theory of strain gradient plasticity. The theory is motivated from a microscopic view of plastic deformation that plasticity reflects a collective behaviour of many dislocations. When a material is deformed, dislocations are generated, moved and stored, and the storage causes the material to work harden. Dislocations become stored because they accumulate by trapping each other in a random way, or because they are required for compatible deformation of various parts of the materials. These are referred

as the statistically stored dislocations and geometrically necessary dislocations, respectively, and the latter are related to the strain gradient in a material. One or several length parameters have been introduced to scale strain gradients. These length parameters are assumed to depend on materials and microstructures and are to be determined by fitting microscale experiments. No explicit relations between these length parameters and the microstructures and mechanical properties of the material are given in these theories. Nevertheless, Fleck and Hutchinson estimates that, for ductile materials, the intrinsic material length associated with strain gradients is indeed on the order of microns.

The strain gradient plasticity theories of Fleck and Hutchinson as well as Gao and Al [42][43] correct some shortcomings of Aifantis' model, however, higher order strains and moment stresses are needed which make the plasticity theory rather complicated. From this motivation a modified gradient plasticity mode based on Aifantis' idea and Gao's flow stress formulation was introduced by Huang et al. [23][44][45][46]

III.4.2 Low-Order Gradient Plasticity Model

Both Aifantis [31] and Gao and Al.[42][43] assume that the flow stress depends upon strain gradients, that is the effective stress can be expressed as

$$\bar{\sigma} = \sigma_0 g[f(\bar{\varepsilon}), \nabla \bar{\varepsilon}, \nabla^2 \bar{\varepsilon}, \dots] \quad (1.32.)$$

σ_0 is a measure of initial yield stress in uniaxial tension and g is a dimensionless function describing material flow after yielding.

$\bar{\varepsilon}$ is the equivalent plastic strain :

$$\bar{\varepsilon} = \sqrt{2\varepsilon_{ij}\varepsilon_{ij}/3} \quad (1.33.)$$

For many ductile materials the function f can be written as

$$f(\bar{\varepsilon}) = \left(\frac{E\bar{\varepsilon}}{\sigma_0} \right)^N \quad (1.34.)$$

E denotes the Young's modulus and $N < 1$ the plastic work hardening exponent.

The actual flow stress is :

$$\bar{\sigma} = \sigma_0 \sqrt{f^2(\bar{\epsilon}) + l\chi} \quad (1.35.)$$

Where χ is a measurement of the strain gradient of the first order.

In general cases we assume $\chi = \|\nabla\bar{\epsilon}\|$, that is, the flow stress is related to the gradient of the equivalent plastic strain.

Chapter 4 will show that, due to the dimensions considered, the strain gradient is possibly one of the factors influencing the bending behaviour.

III.5 MICROSTRUCTURE [10][14][47][48]

III.5.1 Introduction

In order to explain the mechanical behaviour of a material, the microstructure of the material has to be studied.

Grains and grain boundaries [10]

After stable nuclei have been formed in a solidifying metal, these nuclei grow into crystals. In each solidifying crystal the atoms are arranged in an essentially regular pattern, but the orientation of each crystal varies. When solidification of the metal is completed, the crystals join together in different orientations and form crystal boundaries at which changes in orientation take place over a distance of a few atoms. Solidified metal containing many crystals is said to be polycrystalline. The crystals in the solidified metal are called grains, and the surfaces between them, grain boundaries (Fig.1.24).

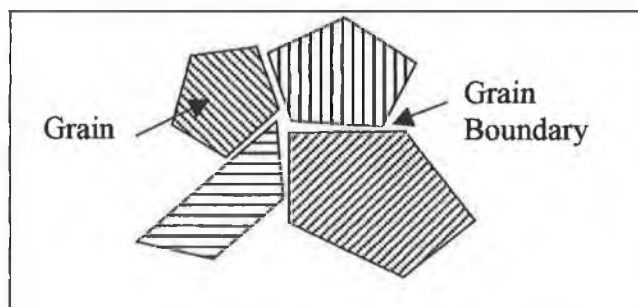


Fig.1.24 Grains and grain boundaries.

Dislocations [10][49][50][51][52][53][54]

Line imperfections, or dislocations, in crystalline solids are defects that cause lattice distortion centred on a line. Dislocations are created during solidification of crystalline solids. They are also formed by the permanent or plastic deformation of crystalline solids, by vacancy condensation, and by atomic mismatch in solid solutions. Plastic deformation within a grain requires the motion of dislocations.

III.5.2 Movement of dislocations [10][49][50]**Slip system**

Any given polycrystal will favour dislocation motion in particular crystallographically controlled direction. The plane in which the dislocation moves is called the slip plane, and the direction in which it moves is called the slip direction.

Burgers vector

The length of the dislocation of the crystal lattice caused by a single dislocation is known as the Burgers vector (Fig.1.25), and this will be constant for any one-slip system.

Critical Resolved Shear Stress

The Critical Resolved Shear Stress (CRSS) is the stress (as resolved onto the slip plane in the slip direction) needed to cause dislocation motion, i.e. break shortest bonds.

Edge dislocation

Edge dislocation movement results in part of the crystal moving perpendicular to the dislocation line.

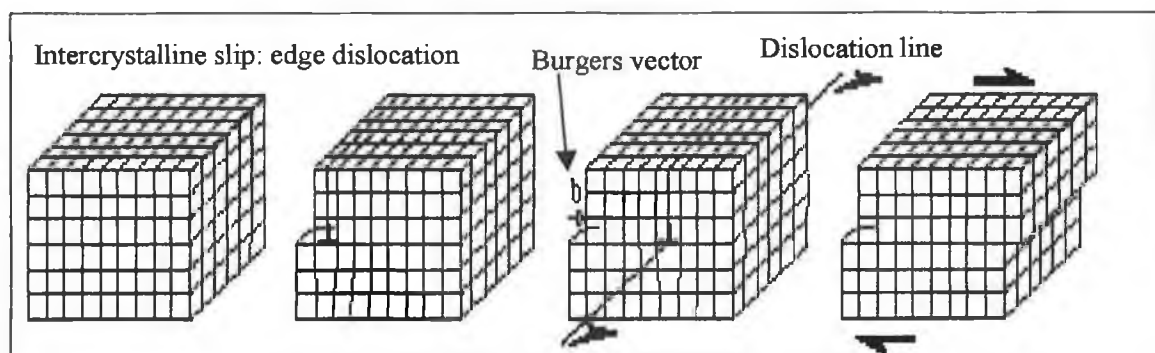


Fig.1.25 Edge dislocation and burgers vector.

Screw dislocation

Screw dislocation movement results in part of the crystal moving parallel to the dislocation line (Fig.1.26).

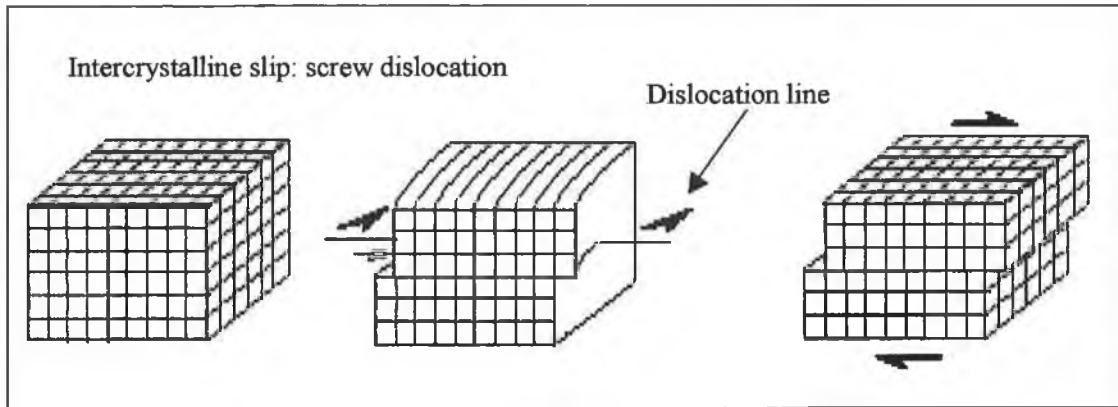


Fig.1.26 Screw dislocation.

Climb

Climb is a diffusive process whereby the dislocation line moves perpendicular to the dislocation line direction, but within the plane of the extra half-plane of atoms (Fig.1.27).

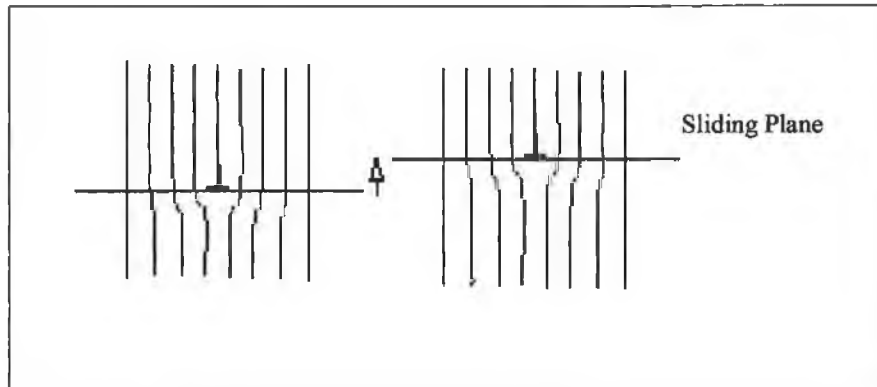


Fig.1.27 Climb.

III.5.3 Effect of the grain size on the Yield stress [55][56][57][58][59][60][61]

Dislocation pile-ups [49][50]

When a gliding dislocation encounters a large obstacle that it cannot pass, such as a grain boundary, it will stop, and dislocations emitted from the same source will pile up behind each other. The stress at the head of the pile-up will then increase until it reaches a critical value, at which point the stress concentration will be relieved by some form of plastic relaxation (Fig.1.28).

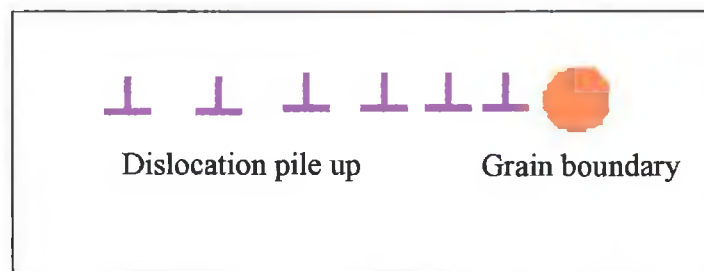


Fig.1.28 Dislocation pile up.

Hall-Petch Effect [20][50][57][62][63][64]

Pile-ups form at grain boundaries, and a critical stress is required to break through them. This gives rise to a strengthening of the material. However, the longer the pathway for the dislocations to build up, the larger the obstacle that can be overcome. This theory was developed by Hall[62] and Petch[63] and proves that the yield strength is related to the grain size. The yield strength of a polycrystalline material could be given by :

$$\sigma_{ys} = \sigma_i + k_y d^{-1/2} \quad (1.36.)$$

σ_{ys} = yield strength of polycrystalline sample

σ_i = overall resistance of lattice to dislocation movement

k_y = "locking parameter," which measure relative hardening contribution of grain boundaries

d = grain size

Fig.1.29 shows the yield stress versus grain size according to the Hall-Petch effect.

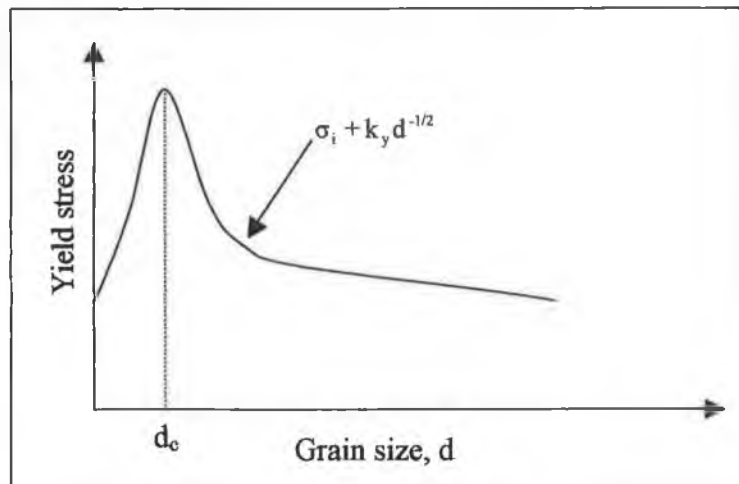


Fig.1.29 Hall-Petch effect.

Grain boundaries effect [56]

Higher hardening in the region adjacent to grain boundaries and triple point was recently confirmed by Gray et al.[65] studies. Going further, Murr and Hecker's [66] work shows how, as the applied stress increases, a work hardened layer along the grain boundaries is formed. Adams and King [67] have also measured this build-up of plastic deformation. Once this work hardened grain boundary layer is formed, the stress within the polycrystalline aggregate homogenise. Consequently when studying the stress distribution in grains, two regions have to be considered, the grain boundary as well as the centre of the grain.

This serves as a basis for the model developed by Meyers and Ashwoth [68], introducing a new definition of the yield stress.

$$\sigma_y = \sigma_{fg} + 8k_{MA} (\sigma_{f_{gb}} - \sigma_{fg}) d^{-1/2} - 16k_{MA}^2 (\sigma_{f_{gb}} - \sigma_{fg}) d^{-1} \quad (1.37.)$$

σ_{fg} = flow stress in the grain interiors

$\sigma_{f_{gb}}$ =flow stress in the grain boundary layers

k_{MA} = Meyers and Ashworth constant.

For large grain size the $d^{-1/2}$ term dominates and a Hall-Petch effect relationship is obtained (Fig.1.30). The Hall-Petch slope, k_{HP} , is equal to:

$$k_{HP} = 8 k_{MA} (\sigma_{f_{gb}} - \sigma_{f_g}) \quad (1.38.)$$

As the grain size is decreased, the d^{-1} term becomes progressively dominant, and the σ_y vs. d curve goes through a maximum. This occurs at $d_c = (4 k_{MA})^2$.

For values of $d < d_c$, it is assumed that the flow stress reaches a plateau and the grain-boundary effects dominate plastic flow.

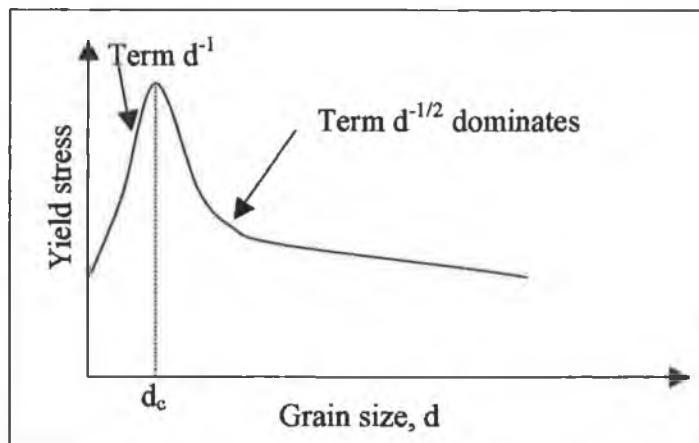


Fig.1.30 Influence of the grain boundaries on the Hall Petch effect.

This work will show that when dealing with small devices such as stents, the relative grain size (number of grains in the thickness) becomes the parameter influencing the mechanical behaviour.

III.5.4 Fracture

Ductile vs. Fragile [10][14][50][69][70][71][72][73][74][75]

Crack initiation and propagation are essential to fracture. The manner through which the crack propagates through the material gives great insight into the mode of fracture.

In ductile materials, the crack moves slowly and is accompanied by a large amount of plastic deformation. The crack will usually not extend unless an increased stress is applied.

The failure of many ductile materials can be attributed to cup and cone fracture:

- The specimen forms a neck (Fig.1.31 (a)), and cavities forms in the necked region (b),
- The cavities in the neck coalesce into a crack in the centre of the specimen (c) and propagate toward the surface in a direction perpendicular to the applied stress.
- When the crack nears the surface, the direction of the crack change to 45° to the tensile axis (d) and a cup-and-cone fracture results (e).

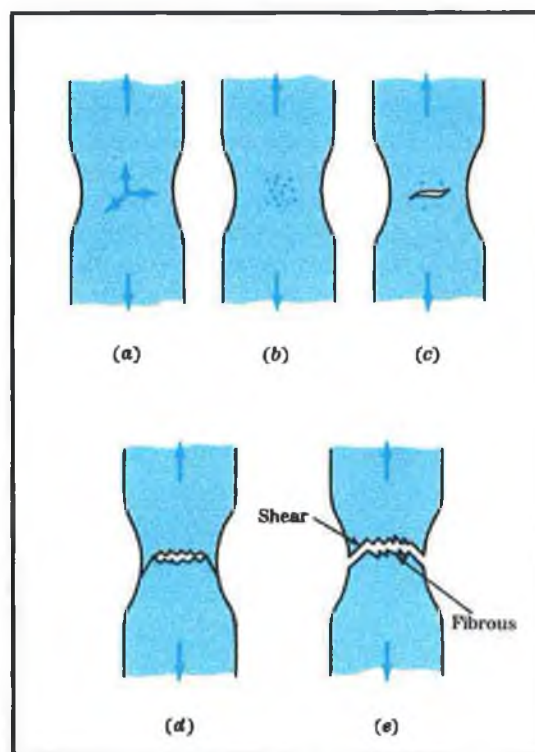


Fig.1.31 Ductile fracture.

In brittle fracture, the cracks run close to perpendicular to the applied stress. This perpendicular fracture leaves a relatively flat surface at the break. Besides having a nearly flat fracture surface, brittle materials usually contain a pattern on their fracture surfaces. Some brittle materials have lines and ridges beginning at the origin of the crack and spreading out across the crack surface.

The brittle fracture is described by atomic level bond breaking. There are two types of brittle fractures: Transgranular and intergranular. In transgranular fracture, the fracture travels through the grain of the material. The fracture changes direction from grain to grain due to the different lattice orientation of atoms in each grain. In other words, when the crack reaches a new grain, it may have to find a new path or plane of atoms to travel on because it is easier to change direction for the crack than it is to rip through. Cracks choose the path of least resistance. You can tell when a crack has changed in direction through the material, because you get a slightly bumpy crack surface. Intergranular fracture is the crack travelling along the grain boundaries, and not through the actual grains. Intergranular fracture usually occurs when the phase in the grain boundary is weak and brittle (i.e. Cementite in Iron's grain boundaries).

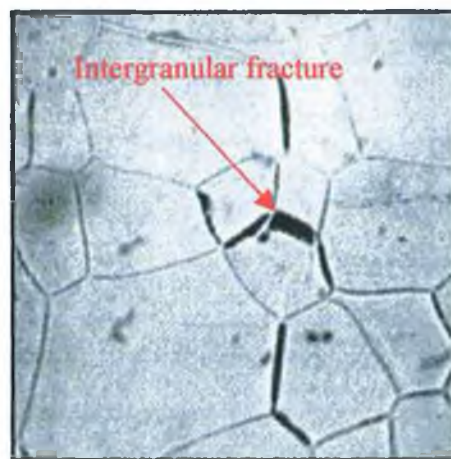


Fig.1.32 Intergranular fracture of a brittle material.

Ductile to Brittle Fracture Transition

- The first factor is temperature. Basically, at higher temperatures the yield strength is lowered and the fracture is more ductile in nature. On the opposite end, at lower temperatures the yield strength is greater and the fracture is more brittle in nature. Temperature determines the amount of brittle or ductile fracture that can occur in a material.

- Another factor, that determines the amount of brittle or ductile fracture that occurs in a material, is dislocation density. The higher the dislocation density, the more brittle the fracture will be in the material. The idea behind this theory is that plastic deformation comes from the movement of dislocations. As dislocations increase in a material due to stresses above the materials yield point, it becomes increasingly difficult for the dislocations to move because they pile into each other. So a material that already has a high dislocation density can only deform so much before it fractures in a brittle manner.

-The last factor is grain size. As grains get smaller in a material, the fracture becomes more brittle. This phenomena is due to the fact that, in smaller grains, dislocations have less space to move before they hit a grain boundary. When dislocations can not move very far before fracture, then plastic deformation decreases. Thus, the material fracture is more brittle. Thus, smaller grains mean higher yield stress and lower strain at breaking as shown on Fig.1.33.

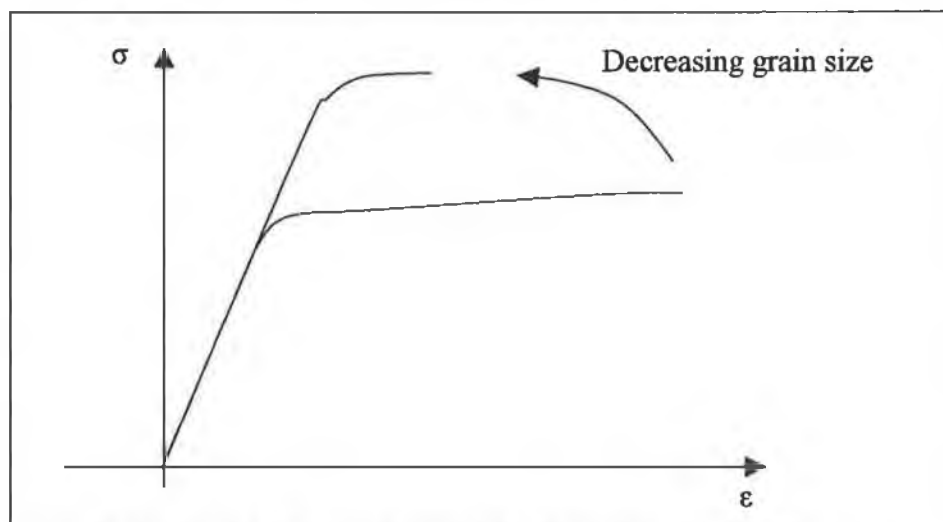


Fig.1.33 Yield stress increasing when grain size decreases and strain at breaking decreasing.

III.5.5 Manufacturing process influence on the microstructure

Laser-cutting and annealing are used in this work, therefore, their known effect on the microstructure is presented here.

Heat Affected Zone (H.A.Z) due to laser-cutting [76][77][78][79]

During laser cutting of steels a huge amount of energy is conducted into the workpiece and this results in changes in the material properties and the microstructure of the steel. A narrow zone exactly adjacent to the laser cut experiences changes in material properties. The changes occur either as grain refinement, or as precipitation of carbides (which are harmful for corrosion resistance properties of the steel) and other impurities such as sulfides and phosphides. This entire region which differs from the base material in properties can be defined as the heat affected zone.

The size of the heat affected zone is a function of the laser pulse duration and the material parameters such as thermal conductivity and specific heat. The heat affected zone will depend on the distance the heat is conducted within the material and varies with material and laser wavelength.

According to Sheng and Joshi [78][77], tests conducted on a 304 stainless steel show that heat affected zones can be as wide as 7 or 8 mm depending on the cutting power and velocity.

This work will show that the H.A.Z. is a factor influencing the mechanical behaviour.

Modifications due to annealing

The process used in this study is full annealing. Full annealing [10] consists of heating a material in its austenizing region and then cooling it down. This process changes the grain size and the structural components size of the material.

We have previously seen the effect of the grain size on the mechanical behaviour. D.Butorin and D.Gerasimov [80] have investigated the influence of structural components size. According to their study, the ability to strain cementite lamelli is primarily defined by their width. The thinner the carbides, the greater the strain they can withstand without formation of destroying cracks. Furthermore, with decreasing of cementite lamelli width the ferritic spacing size is also decreased, i.e. the amount of barriers for moving dislocations is increased, thus hardness and yield strength rise.

IV EXPERIMENTAL METHODS

IV.1 TENSILE TEST

IV.1.1 Introduction

The tensile test is performed by subjecting the specimen to a uniaxial deformation at constant speed. A sample is held rigidly between a fixed beam and a moving beam (the crosshead). A load cell (sensor) is used to measure the stress that builds up in the material as its length is increased by moving the crosshead. The change in the length (extension) of the sample as pulling proceeds is measured by the machine. The data obtained from this experiment are the force F and the elongation ΔL . The original gage length is known as L_0 and the original cross section as A .

IV.1.2 Standards

ASTM standards related to tensile testing [81] :

<u>E6</u>	Terminology Relating to Methods of Mechanical Testing
<u>E8</u>	Test Methods for Tension Testing of Metallic Materials
<u>E8M</u>	Test Methods for Tension Testing of Metallic Materials (Metric)
<u>A370</u>	Test Methods and Definitions for Mechanical Testing of Steel Products

Table 1.3. ASTM standards concerning tensile tests.

We wanted the specimen to represent the geometry of the stent struts, in order to use the results obtained for further modelling of the stent behaviour. Therefore, a specimen, laser cut in tubes used for the manufacturing of stents, was specially designed (Fig.1.34).

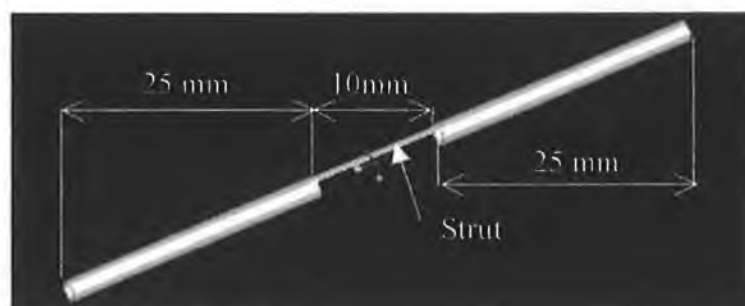


Fig.1.34 Tensile test specimen design.

IV.1.3 Methods of strain measurement

Conventional electrical resistance strain gages [82] [83]

Electrical resistance strain gages are very sensitive even for measuring deformations in composite materials. Strain measurement is based on the electrical resistance change of the gage bonded to the undergoing deformation.

Liquid metal strain gages [84]

Soft biological tissues or tire cord-rubber exhibit so little stiffness, due to their highly compliant matrix material, that conventional strain gages cannot be used to take quantitative strain measurement of them. Therefore, liquid metal strain gauges are used.

Geometric Moire [85]

Displacement and strains can be determined by putting two marks on a surface, measuring the length between them, then loading the body and measuring the length again. The difference between the two lengths gives the displacement, and the displacement divided by the initial length gives the strain. The technique is sometimes called the grid method. If the area is large it may be more convenient to take advantage of the fact that such arrays of dots or lines (called gratings), if regular, produce an interference pattern between the loaded and unloaded array. The pattern is called a moire pattern and is related to the surface displacements in an analysable way.

Birefringent coatings [82]

Birefringent or photoelastic coatings have been applied successfully to isotropic materials for several years. The method consists of bonding a thin sheet of photoelastic material to the surface of the specimen, such that the bonded interface is reflective. When the specimen is loaded, the surface strains are transmitted to the coating and produce a fringe pattern which is recorded and analysed by means of a reflection polariscope.

Holographic techniques [82]

Holography is an optical technique based on the optical interference produced by superposition of coherent light waves reflected from the object under consideration and those of a coherent reference beam. The laser is an ideal source of coherent monochromatic light.

Speckle interferometric technique [82]

Speckle interferometry makes use of the speckle pattern produced on the surface of an object illuminated by coherent light. It has many characteristics complementary to those of holographic interferometry.

Shearography [86]

Shearography is an interferometric method allowing full-field measurement of surface-displacement derivatives. The object to be tested is illuminated by a point source of coherent light. An image shearing camera produces a pair of laterally sheared images in the image plane ; hence, the method is named shearography. As the object is illuminated with coherent light, the two sheared images interfere with each other producing a random interference pattern commonly known as a speckle pattern. When the object is deformed, this speckle pattern is slightly modified. Superposition of the two speckle patterns by double exposure yields a fringe pattern depicting the derivatives of the surface displacements.

IV.1.4 Engineering stress and strain

Engineering stress

Using the force measured by the load cell and the cross section A the engineering stress may be calculated.

$$\sigma = \frac{F}{A} \quad (1.39.)$$

F : force (N)

A: cross section area (mm²)

Engineering strain

Using the original length l_0 and the extension Δl measured, the engineering strain ϵ may be calculated.

$$\epsilon = \frac{\Delta l}{l_0} \quad (1.40.)$$

ϵ : strain

Δl : extension in mm

l_0 : original length in mm

IV.1.5 True stress and Strain

Using the theory of large deformation plasticity (paragraph III.3)

$$F = \frac{l}{l_0} = 1 + \epsilon \quad (1.41.)$$

$$F^{-1} = \frac{1}{1 + \epsilon} = F^{-r} \quad (1.42.)$$

$$F = U \quad (1.43.)$$

Hence the true strain is :

$$\epsilon_T = \ln U = \ln(1 + \epsilon) \quad (1.44.)$$

The Jacobian :

$$J = \frac{dx}{dx_0} = 1 + \epsilon \quad (1.45.)$$

The second Piola Kirchof corresponds to the measured stress.

$$\sigma = S = T(1 + \epsilon) \left(\frac{1}{1 + \epsilon} \right) \left(\frac{1}{1 + \epsilon} \right) \quad (1.46.)$$

The Cauchy stress tensor or true stress is therefore :

$$\sigma_T = T = (1 + \epsilon) S = (1 + \epsilon) \sigma \quad (1.47.)$$

IV.1.6 Hardening curve

Once the true strain and true stress are calculated, the hardening curve is plotted.

Yield stress and proof stress

Detection of the yield stress presents an experimental problem since hardening curves do not often show a well-defined yield point. The yield stress is therefore replaced by a value known as proof stress. The proof stress is the stress that corresponds to the occurrence of a specified amount of permanent strain.

For quality control of materials, a conventional value of permanent strain equal to 0.2% is commonly used (Fig.1.35). If this value is too high a more refined conventional value of 0.02% permanent strain is often adopted.

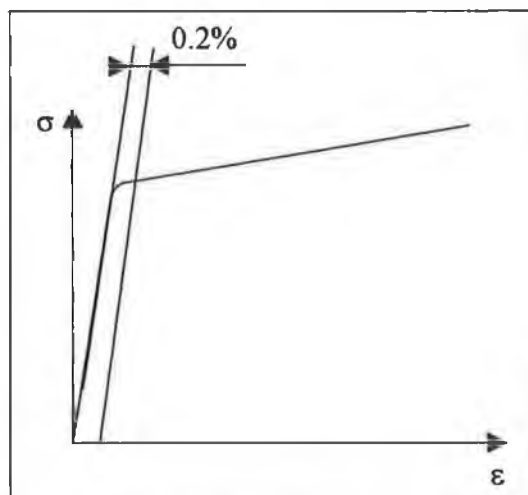


Fig.1.35 Measurement of the proof stress.

Ultimate tensile strength

The ultimate tensile strength is the maximum stress reached in the hardening curve (Fig.1.36).

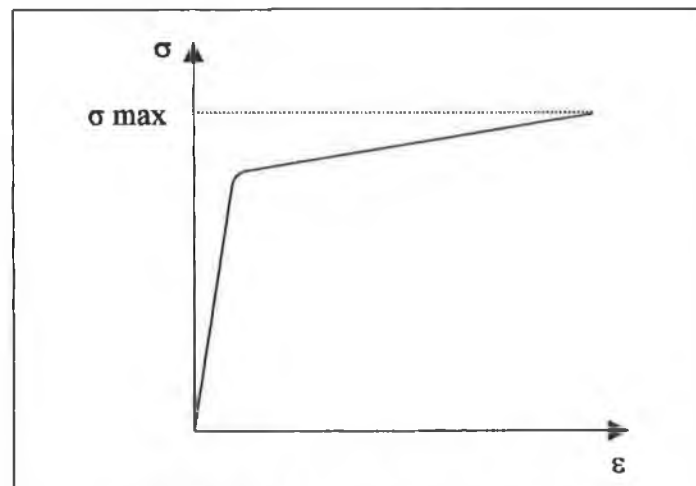


Fig.1.36 Ultimate tensile strength.

IV.2 BENDING TEST [87]

IV.2.1 Introduction

The bending test chosen is a three-point bending test. The specimen is supported at both its extremities and a load or displacement is applied at the centre of the beam.

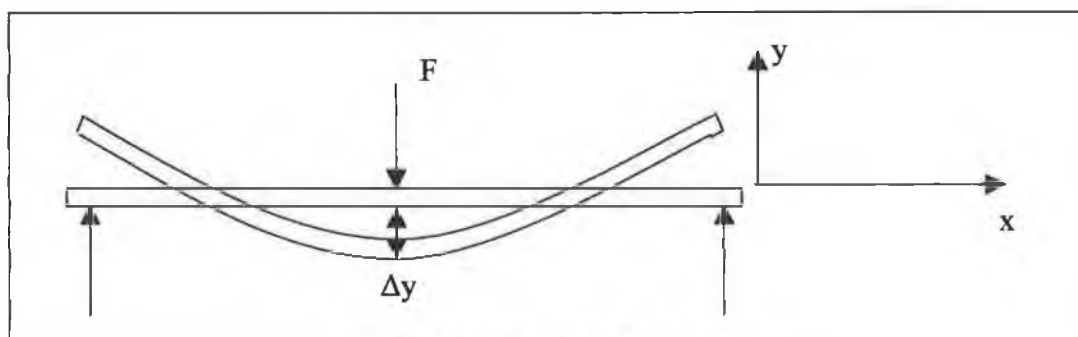


Fig.1.37 Three-Point bending.

The data obtained from this experiment are the force F (N) and the deflection Δy (mm) at the centre of the beam.

IV.2.2 Standards

ASTM standard relating to bending test [81] :

E290-97	a Standard Test Method for Bend Testing of Material for Ductility
---------	---

Table 1.4. ASTM standard concerning Bending tests.

Some studies [88][89][90][91][92][93] have been conducted to develop bending test methods adapted to micro-scale specimens. However, none of the methods described was applicable for this study.

In order to compare tensile and bending results, the tensile tests specimens were used for the bending test after removing the part of tube left over each side of the strut.

IV.2.3 Shearing forces [87]

Shearing forces are internal forces developed in the material of a beam to balance externally applied forces in order to secure equilibrium of all parts of the beam. The magnitude of the shearing force in any part of the beam is equal to the algebraic sum of all external forces acting to the left of the section of interest. Shearing forces are noted $V(N)$. Fig.1.38 shows the shearing force diagram for a three-point bending test.

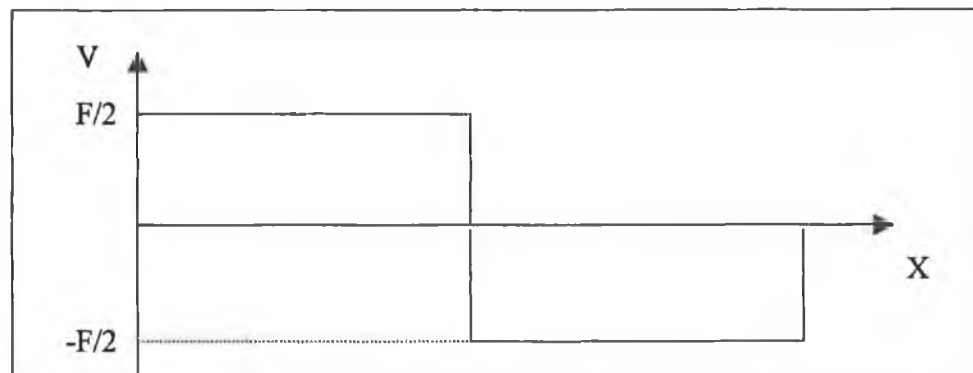


Fig.1.38 Shearing force diagram for tehtre-point bending test.

IV.2.4 Bending Moments [87]

Bending moments are internal moments developed in the material of a beam to balance the tendency for the external forces to cause rotation of any part of the beam. Bending moments are noted $M(\text{N.m})$

$$dM = Vdx \quad (1.48.)$$

Bending moments diagram for a three-point bending test is shown on Fig.1.39.

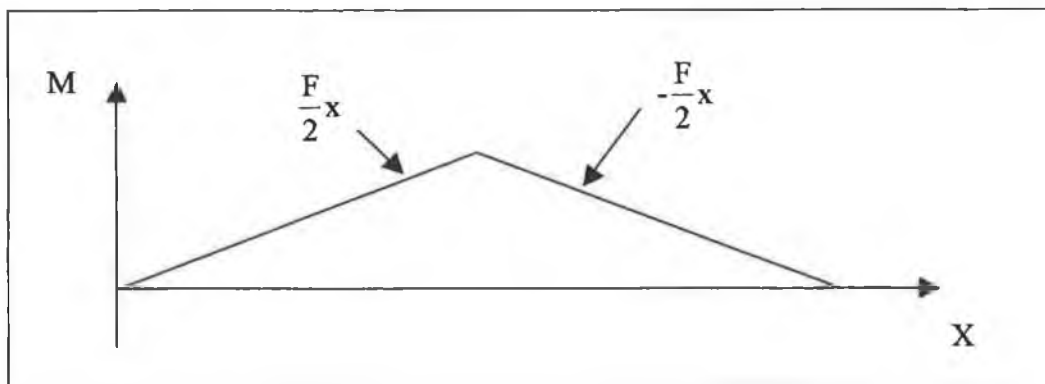


Fig.1.39 Bending moments diagram for a three-point bending test.

IV.2.5 Centroid and moments of inertia [87]

Let us consider the area shown on Fig.1.40.

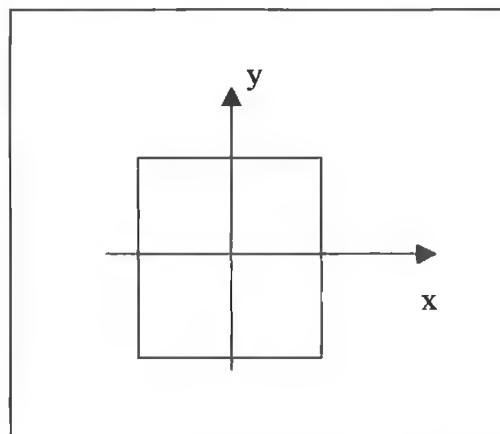


Fig.1.40 Cross section area of a beam.

The centroid of an area is the point about which the area could be balanced if it was supported from that point.

$$X = \frac{\int x ds}{\int ds} \quad (1.49.)$$

X = vector position of the centroid,

S = surface of beam section

The moment of inertia is an indication of the stiffness of the beam, that is, the resistance to deflection of the beam when carrying loads that tend to cause it to bend. The moment of inertia is noted I (mm^5).

$$I_x = \int y^2 ds \quad (1.50.)$$

IV.2.6 Stress in elasticity [87]

The stress at a distance y from the centroidal axis is given by :

$$\sigma = \frac{My}{I} \quad (1.51.)$$

y = distance from the centroidal axis of the beam to fibre.

σ = stress at a distance y from the centroidal axis.

The stress is not constant but linear across the thickness of the beam as represented on Fig.1.41.

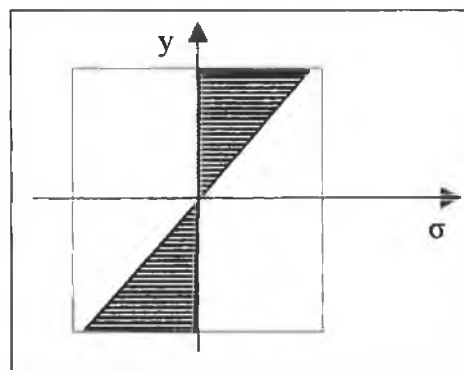


Fig.1.41 Stress versus position in the thickness of the beam.

IV.2.7 Deflection of beam in elasticity [87]

For a three-point bending test the deflection for an elastic deformation is :

$$\Delta y = \frac{-FL^3}{48EI} \quad (1.52.)$$

L = length of the beam

IV.2.8 Strain in elasticity.[87]

$$\varepsilon = \frac{y}{R} \quad (1.53.)$$

ε = strain

R = radius of curvature

$$R = \frac{4\Delta y^2 + L^2}{8\Delta y} \quad (1.54.)$$

IV.2.9 Yield stress and plasticity [17]

As seen on Fig.1.41, the stress is not constant in the thickness of the beam. Therefore, the outer fibres of the beam reach their yield stress first creating an elastic-plastic interface. The necessary condition of continuity between the plastic and elastic regions make the theory of plasticity in bending very complicated. In this work, a method for the inverse identification of the mechanical properties using Finite Element Analysis is therefore developed (see chapter 4 paragraph III)

V METALLOGRAPHY [94][95][96][97][98][99][100][WEB 20][WEB 21]

V.1 STANDARDS

ASTM standards relating directly to metallographic practice [81] :

E-3 Preparation of Metallographic Specimens
E-7 Standard Terminology Relating to Metallography
E-112 Standard Test Methods for Determining Average Grain Size
E-340 Macroetching Metals and Alloys
E-381 Standard Method of Macroetch Testing Steel Bars, Billets, Blooms, and Forgings
E-407 Microetching Metals and Alloys
E-562 Recommended Practice for Determining Volume Fraction by Systematic Point Count

Table 1.5. ASTM standard relating to metallographic practice.

V.2 SAMPLE PREPARATION [WEB 22][WEB 23]

The basic principles of abrasive polishing necessitate a sequence of operations which produces a distortion-free, polished surface capable of revealing the true microstructure. Equipment required to prepare an acceptable metallographic surface varies according to the tests required, materials to be processed, work volume, operating philosophy, and other considerations.

A typical preparation sequence includes:

Sectioning to produce a manageable size sample using either a conventional abrasive cutter or low speed saw.

Mounting to provide a safe means of holding the specimen and protect its edges from rounding. Compression moulding, with a mounting press, is used for rigid materials and

cold mounting is used for material that is delicate, hard to hold, or larger than normal size.

Rough Grinding to remove surface deposits or level irregular surfaces. Either belt or disc grinders may be used.

Fine Grinding to systematically abrade the specimen with a series of grits of decreasing coarseness. This operation may be performed on a manual fine grinder or rotating wheel. In some particularly demanding applications, the use of lapping with loose abrasive slurries may be necessary. This is particularly true for the preparation of extremely large specimens or when large numbers of smaller specimens must be prepared simultaneously.

Rough and Final Polishing to remove the remaining scratches and produce the smooth lustrous surface required for microscopic examination.

Etching to develop the microstructure not normally visible in the as-polished condition. Inclusion ratings and certain types of defect identification should be performed prior to application of the etchant. Two types of etching are commonly used: chemical etching and electrolytic etching.

Microscopy to observe, analyse, and record the true microstructure of the material.

More details about the different steps can be found in Appendix II.

V.3 GRAIN SIZE MEASUREMENTS

Grain size measurement is complicated by a number of factors. Firstly, the three-dimensional size of the grains is not constant and the sectioning plane will cut through the grains at random. Thus, on a cross-section, a range of sizes, none larger than the cross section of the largest grain sampled, are observed. Grain shape also varies, particularly as a function of grain size. In most cases, the grains observed on a polished cross-sectional plane exhibit a range of sizes around a central mean and individual measurements of grain areas, diameters, or intercept lengths exhibit a normal distribution. In the vast majority of cases, the mean value of the planar grain size is determined, rather than the distribution. Different product shapes, and different processing procedures, can produce a variety of non-equiaxed grain shapes. This, of course, does influence the ability to

measure the grain size. Grain size measurement is also complicated by the different types of grains that can be present in metals, although their fundamental shapes are the same. Three methods are commonly used for the measurement of the grains size.

The planimetric or Jeffries method

This method measures grain size in terms of the number of grains, N_A , visible on a cross section within a fixed area, the number per square inch at 100X, or the number per square millimetre at 1X. From this value, the average cross-sectional area A of the bisected grains can be computed. This is not an average of the maximum cross-sectional area of each grain because the sectioning plane does not intersect each grain at its maximum width. It is common practice to take the square root of A and call this the grain diameter, d , although this assumes that the cross sectional shape of the grains is a square, which it is not.

The Heyn intercept method

In this method, one or more lines are superimposed over the structure at a known magnification. The true line length is divided by the number of grains intercepted by the line. This gives the average length of the line within the intercepted grains. This average intercept length will be less than the average grain diameter but the two are interrelated. The intercept method yields a mean intercept length, L_3 ; its relationship to N_A , A , or d is not exceptionally well defined.

The ASTM grain size number

It is now common to express grain sizes in terms of a simple exponential equation:

$$n = 2^{G-1} \quad (1.55.)$$

where:

n = the number of grains per square inch at 100X magnification, and

G = the ASTM grain size number.

V.4 SCANNING ELECTRON MICROSCOPE [WEB 25][WEB 26]

A Scanning Electron Microscope (S.E.M) was used to observe the microstructure of the specimens. SEM has a higher magnification (as high as X300000) than an optical microscope.

An SEM can give a three dimensional picture of the sample as well as its atomic composition and structure. These properties are explained by the technology of the S.E.M described in Appendix III.

CHAPTER 2 : CONTEXT OF THE STUDY

I INTRODUCTION

As described in Chapter 1, stents are small medical devices laser-cut in tubes and implanted in arteries. It has been noted by surgeons and manufacturers that stents do not always expand as expected while being implanted in the arteries.

- In order to help in the understanding and solving of this problem, this chapter presents an experimental test conducted to observe the non-uniform expansion of the stent.

The aim of this study is to identify some of the factors influencing the mechanical behaviour of stents. When studying the mechanical behaviour of a device two aspects have to be considered: the design and the material.

- This study concentrates on the material, however this chapter contains a simplified Finite Element Analysis (F.E.A) of the stages leading to the implantation of the stent. This analysis was conducted to observe the stress distribution during the different steps and show that the bending behaviour is of prime importance for the manufacturer.

II PROBLEM ENCOUNTERED

II.1 INTRODUCTION

It has been observed by surgeons that the stent does not expand uniformly in the longitudinal and radial direction. This paragraph intends to identify experimentally the problem described and explain the possible consequence of this anomaly.

II.2 EXPERIMENTATION

Firstly, a brief description of the stages followed by the stent before implantation.

The stent is laser cut in a tube. Fig.2.1 shows two different views of a 3D drawing of the stent used for this experiment. All stents have similar designs, therefore the results of this experiment could also be obtained using any other balloon-expandable stent.



Fig.2.1 3D drawings of the laser-cut stent B [WEB 7].

The stent is then crimped around the balloon and catheter and packed ready to leave the manufacturer. During the procedure, the stent, balloon and catheter are first inserted in the artery, the balloon is then inflated, leading the stent to expand as shown on Fig.2.2.

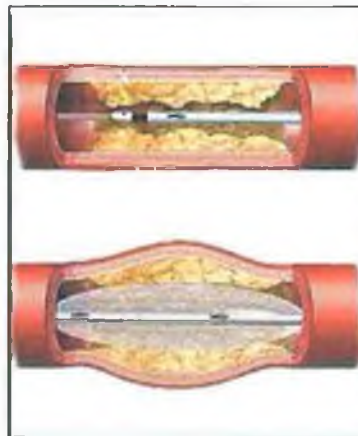


Fig.2.2 Expansion of the stent inside the artery.

The expansion is the part where a problem has been noticed and therefore needs to be studied.

In order to simulate the expansion, a pressure valve and a stent, balloon, catheter kit were used to reconstitute the expansion of the stent (Fig.2.3).

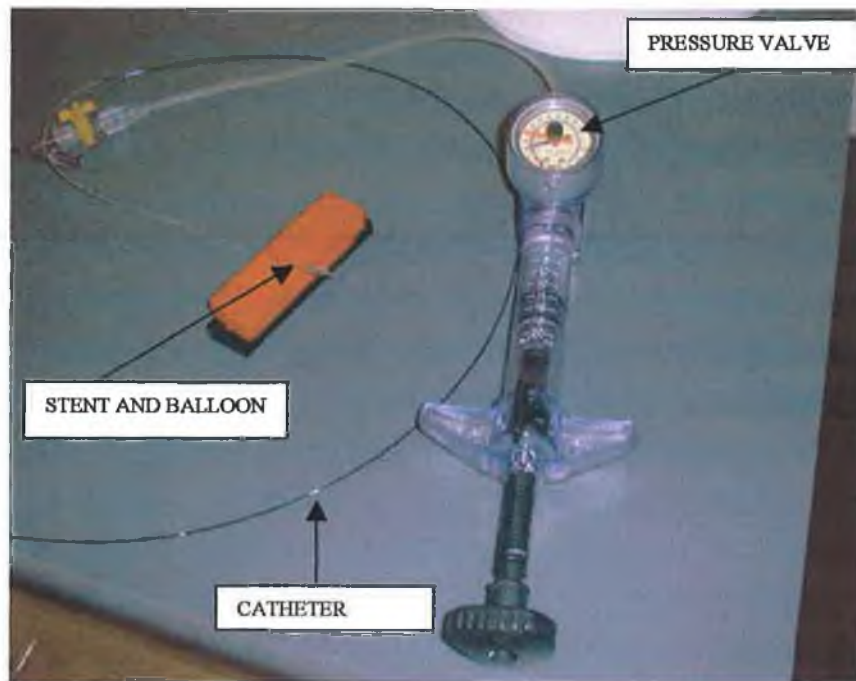


Fig.2.3 Pressure valve plugged to the catheter, balloon, stent system.

A projector was then used to measure the expansion of the balloon and stent at different pressures (Fig.2.4).

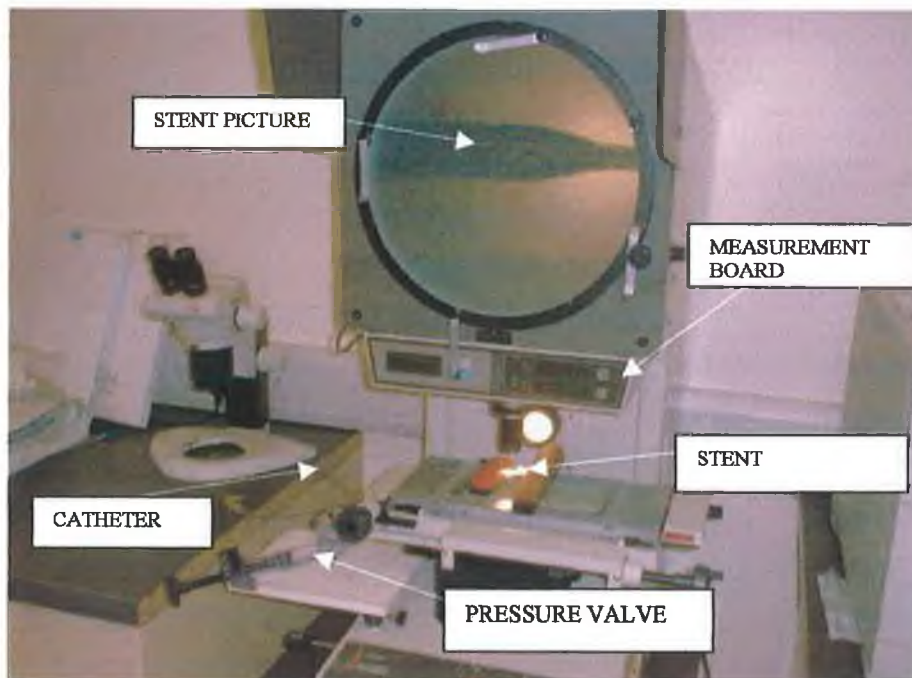


Fig.2.4 Stent mounted on the measurement apparatus.

The following pictures show the inflation of the balloon leading to the expansion of the stent. Fig.2.5 shows the stent crimped around the balloon and catheter.



Fig.2.5 Stent crimped around balloon and catheter.

The pressure valve is then progressively opened and Fig.2.6 shows the non-uniform expansion of the stent.

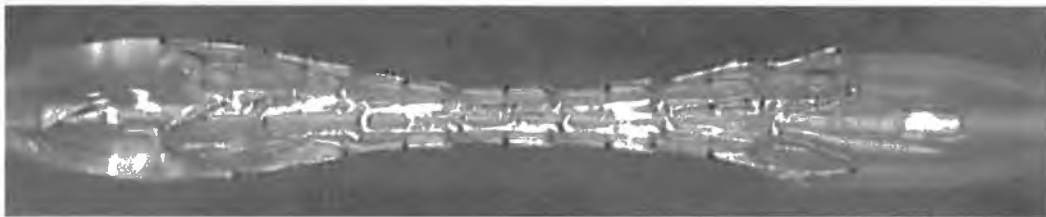


Fig.2.6 Extremities of the stent expand first.

The extremities of the stent expand first, therefore come in contact with the artery first. The pressure is increased and finally the stent is fully expanded as shown on Fig.2.7.

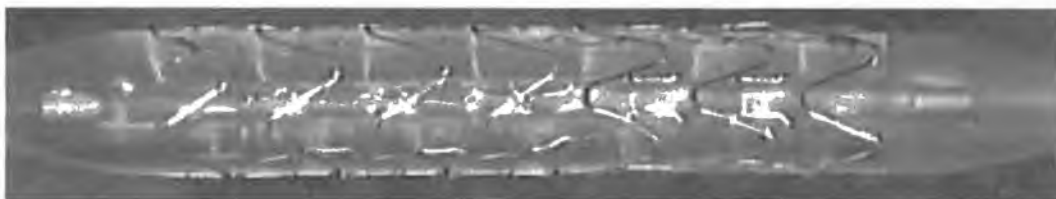


Fig.2.7 Stent fully deployed.

Fig.2.8 shows the expansion of the diameter along the stent at different pressures. It shows that the extremities expand first and the center of the stent does not start deploying before the extremities are fully expanded.

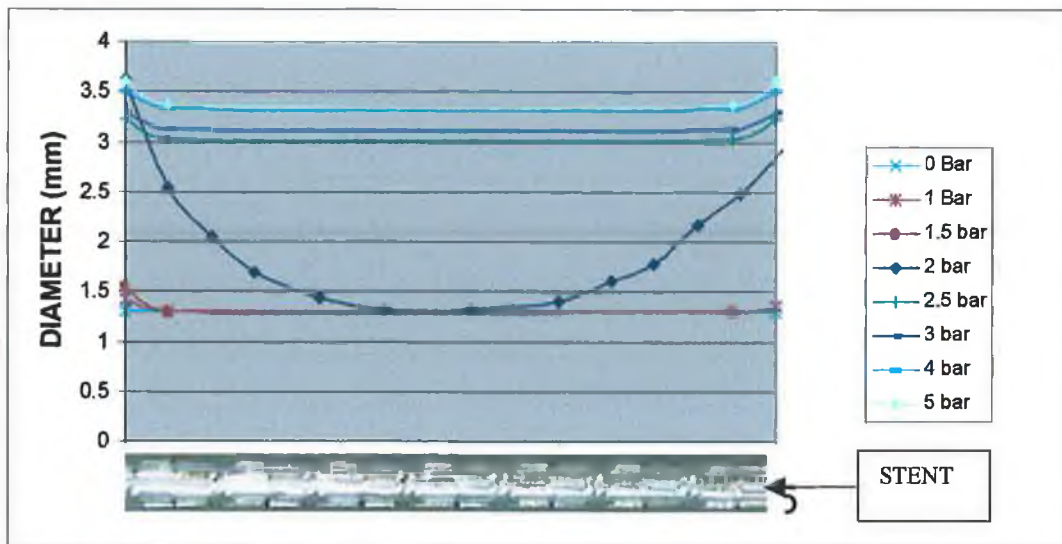


Fig.2.8 Expansion of the diameter along the stent for different pressures.

When the center of the stent finally expands, a longitudinal displacement of the extremities occurs. This displacement is not visible on Fig.2.8 but is noticeable when observing Fig.2.9. The two outside lines show that the two pictures are at the same scale since the two markers on the catheter are aligned. The two inside lines show the longitudinal expansion of the stent.

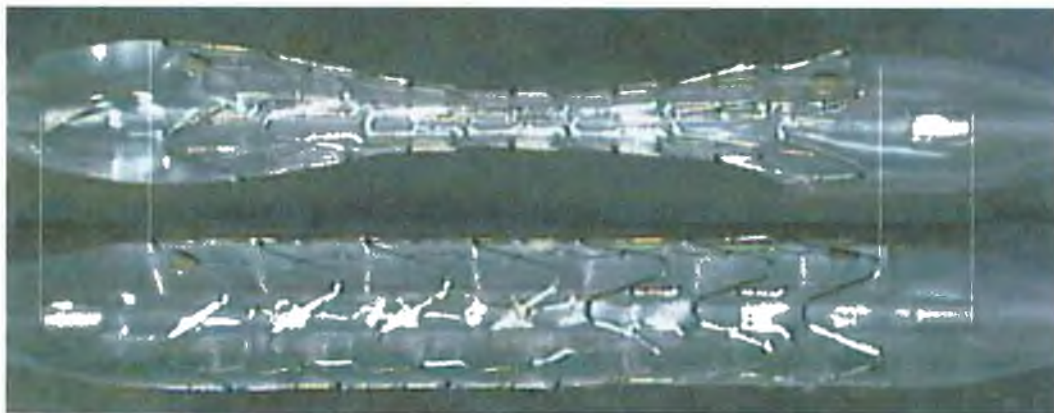


Fig.2.9 Observation of the longitudinal expansion.

During the expansion, all the struts constituting the stent are subjected to deformation. Therefore, a perfect knowledge of the struts mechanical behaviour is needed here in order to study the stent mechanical behaviour.

II.3 CONSEQUENCE

The extremities of the stent come first in contact with the artery. When the centre of the stent expands a radial and longitudinal pressure is created at the contact. A longitudinal displacement of the extremities occurs then leading to a scarring of the artery. Either balloon or stent might be at the origin of this occurrence. Both balloon and stent mechanical behaviours need therefore to be studied. This study concentrates on the stent.

III STRESS DISTRIBUTION IN THE STENT

III.1 INTRODUCTION

Modelling the different stages leading to the implantation of the stent is not the subject of this work, however a simplified modelling using MARC MENTAT was conducted here to analyse the distribution of stress in the stent and determine the mechanical properties necessary to optimise further modelling.

III.2 F.E.A MODELLING

To simplify the analysis, a simpler stent design was chosen (Fig.2.10(a)).

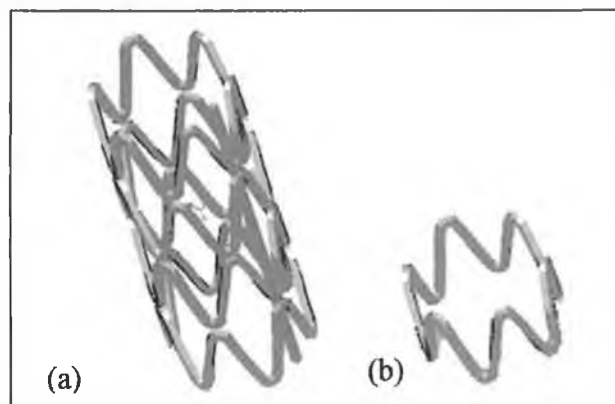


Fig.2.10 (a) Z-Stent design, (b) one loop of the design.

One loop of the stent, as shown in Fig.2.10(b), was modelled.

The loop being symmetrical only half of it was actually studied. 3D elasto-plastic brick elements were used.

III.2.1 Crimping

Fig.2.11 shows the crimping tool coming in contact with the stent, then crimping the stent against the balloon

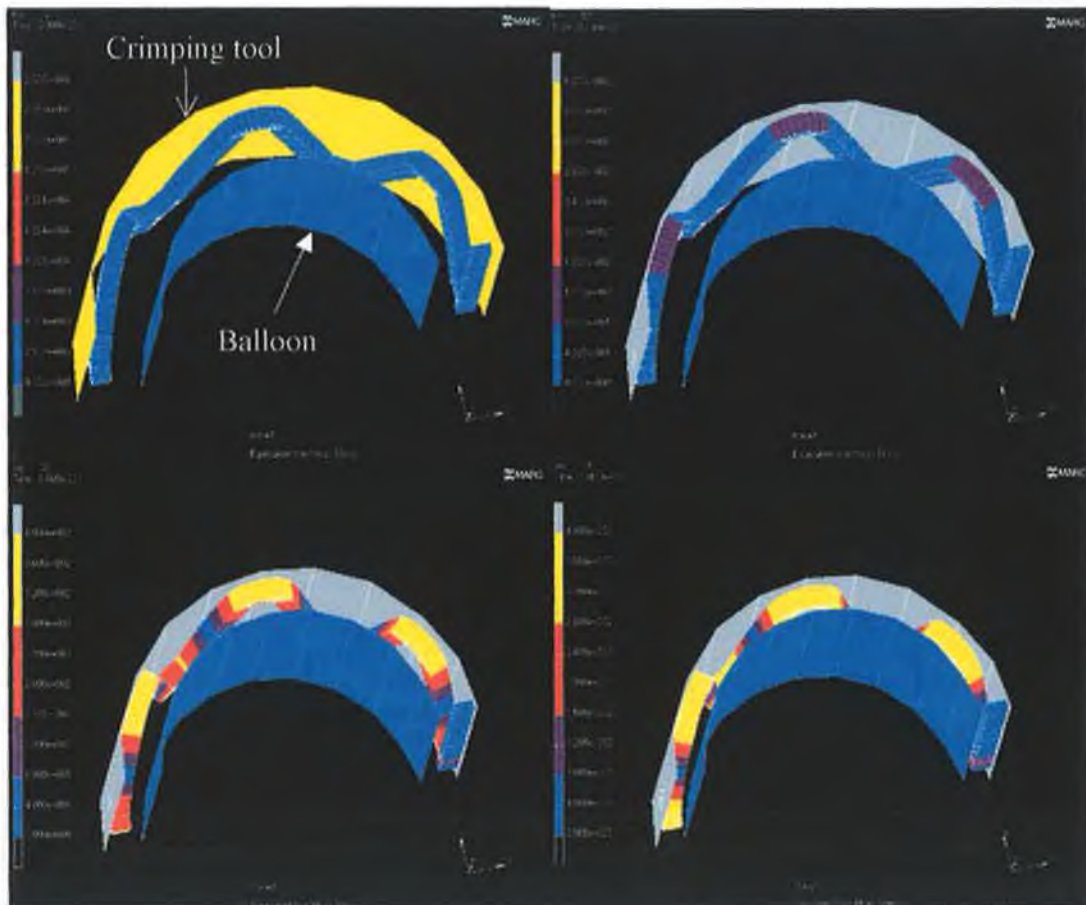


Fig.2.11 Crimping of the stent against the balloon.

The different colours show the distribution of the equivalent Von Misses Stress in the stent.

It can be noted that the maximum stress (yellow on the two last pictures) is observed in the elbow of the zigzag design.

III.2.2 Crimping tool removal and artery introduction

The crimping tool is then removed and a surface simulating the artery introduced as shown on Fig.2.12.

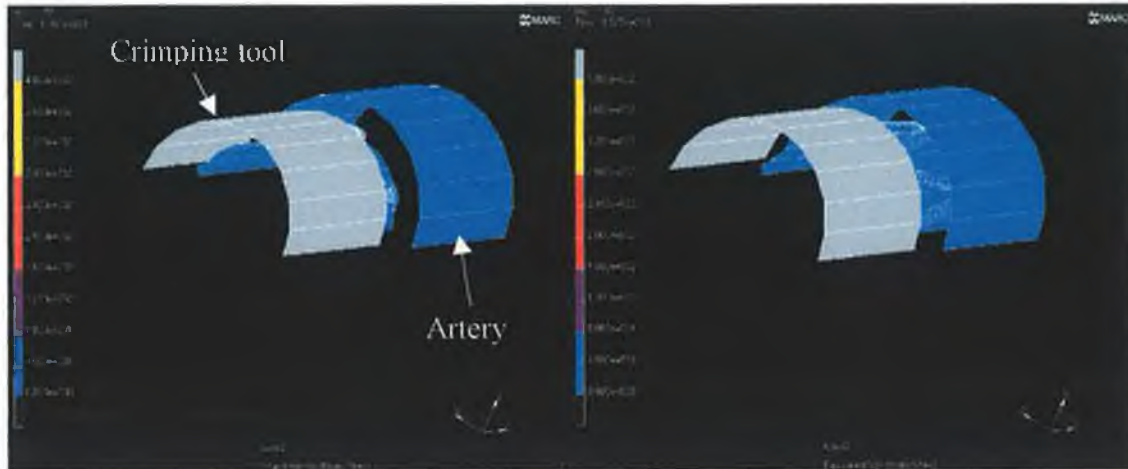


Fig.2.12 Removal of the crimping tool and introduction of the artery.

III.2.3 Expansion of the stent

The balloon simulated by the internal surface is then inflated leading the stent to deploy as shown on Fig.2.13.



Fig.2.13 Deployment of the stent.

Again the maximal Von Misses stress is observed at the elbows of the zig-zag design.

On Fig.2.14, the stent keeps deploying until coming in contact with the artery

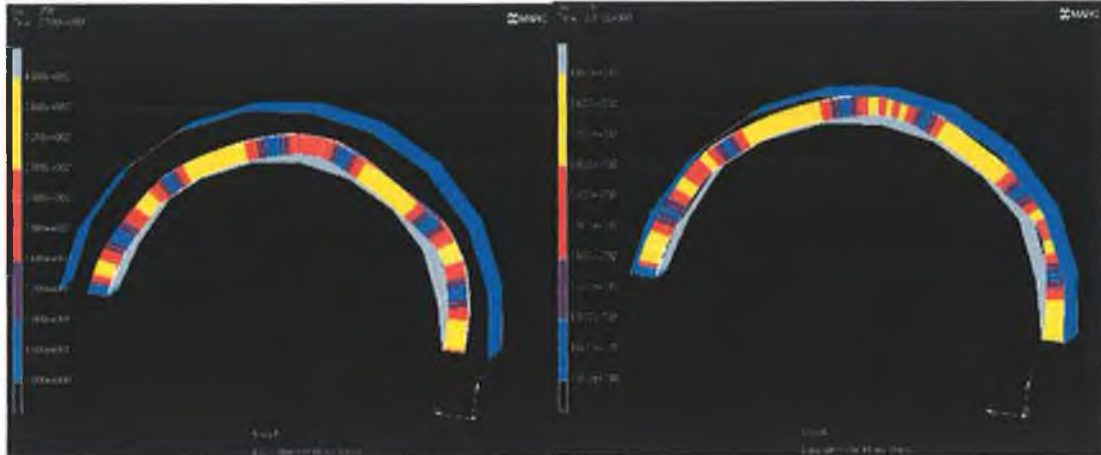


Fig.2.14 Stent coming in contact with the artery.

Again the maximal Von Misses stress (in yellow) is observed at the elbows.

III.2.4 Analysis of the stress distribution

The modelling of the different steps followed by the stent leading to its implantation showed that the maximal stress always occurs in the elbows of the zigzag. In order to investigate further, the stress at the two nodes, respectively at the top and bottom of one elbow (Fig.2.15), is analysed further.

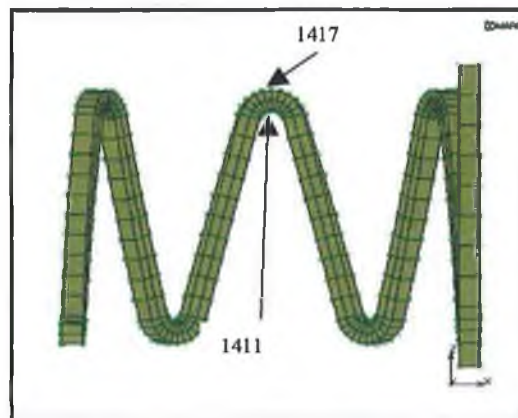


Fig.2.15 Drawing showing the two nodes further analysed.

Fig.2.16 shows the stress in the direction X (comp 11) of the nodes represented on Fig.2.15.

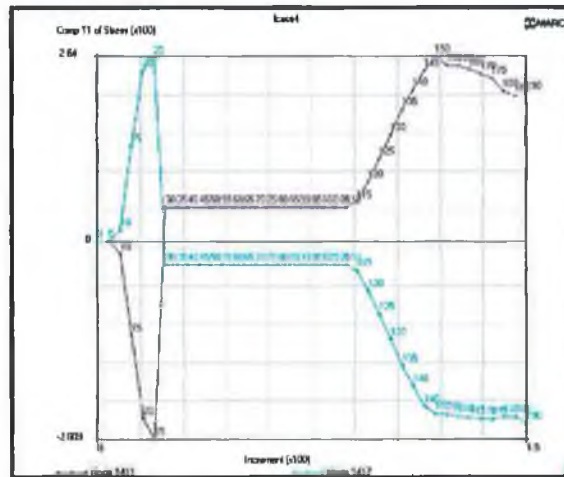


Fig.2.16 Stress in the direction X for two opposite nodes on the strut.

Fig.2.16 above, shows that during crimping the top node is in tension whereas the bottom one is in compression. Inversely, during expansion the top node is in compression whereas the bottom one is in tension. Therefore, in both situations, the elbow is bent. This make the study of the bending behaviour a primary concern of the manufacturer.

IV CONCLUSION

It has been shown that the stent does not expand uniformly. Its extremities expand first, the centre of the stent staying in place until the extremities come in contact with the artery. The centre then starts deploying, creating a radial and longitudinal pressure at the extremities. A longitudinal displacement of the extremities occurs then, scarring the artery. This occurrence was part of the motivation for this study. A better understanding of the mechanical behaviour of the device is necessary in order to solve this problem.

The mechanical behaviour of the material is the main concern of this work, nonetheless a simplified F.E.A. was conducted showing that the properties of the bending behaviour are the ones important for the manufacturer.

CHAPTER 3 : TENSILE BEHAVIOUR

I INTRODUCTION

Chapter 2 showed that the bending behaviour is the main interest of the manufacturer. However, it was decided to extend this work to both tensile and bending behaviour of the material in order that the results may be used for any other design of small devices. This chapter deals with the tensile behaviour and therefore the identification of the factors influencing this behaviour. The tensile test has been chosen here since it gives Young's Modulus and hardening rule in one of the main directions of the material.

- The apparatus used is described and the design of the specimen tested will be studied. The specimen is laser cut in a tube, therefore the accuracy of the cut and its implication will be analysed as well as possible improvements of the process.
- The influence of the size of the specimen on the tensile behaviour is analysed using experimental results.
- Stents being electro-polished after laser-cutting, the influence of this manufacturing process on the mechanical behaviour of the specimens is tested.
- Finally, the influence of annealing on the mechanical behaviour is analysed since it is sometimes included in the manufacturing of stents.

II EXPERIMENTATION

II.1 EQUIPMENT

The machine (see Fig.3.1) used in GMIT is an INSTRON micro tensile tester 5544 (capacity 2 KN). There are three load cells available : 10 N, 500 N and 2 kN.

The bottom grip is fixed, the top one imposes a displacement to the specimen.

The accuracy of the load cells is certified to be :

$\pm 0.4\%$ of reading down to 1/100 of the capacity of the load cell.

$\pm 0.5\%$ of reading down to 1/250 of the capacity of the load cell.



Fig.3.1 Micro tensile tester.

II.2 MEASUREMENTS

The tensile tester is linked to a computer (Fig.3.2) enabling the user to control the speed, and frequency of the measurements.



Fig.3.2 Computer linked to the tensile tester.

Rate of Deformation

The rate of deformation is controlled by the speed imposed to the head of the tensile tester (Fig.3.3). To determine the speed adequate for the test, specimens have been tested at different speeds varying from 0.1 mm/min and 2 mm/min. The study revealed that the speeds in this range do not influence the results and 1 mm/min was chosen.



Fig.3.3 Input of the speed and criteria to end the test.

Test stop

The software also allows the user to decide when the test stops (Fig.3.3). Here, the criteria chosen is the rate of load and the test stops when there is a drop in the load to less than 40% of the previous load.

Measurement frequency

The software allows the user to set the frequency of the measurements (Fig.3.4). Here, time and load have been selected. One record every second is adequate for the plastic behaviour but would not be enough for the elastic one. Therefore, data are also recorded every 5 N. For small specimen, where the maximum load is less than 10 N, the load value is reduced accordingly.

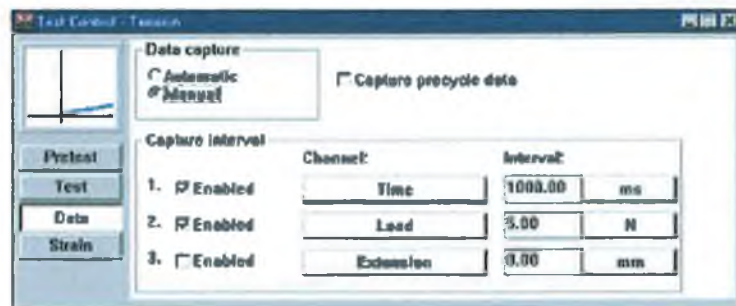


Fig.3.4 Input of the measurement frequency.

Data measured

Due to the size of the specimen, the use of strain gauges is not possible and the optical methods as described in chapter 1 were not available. However, the machine has been designed to measure small forces and displacement.

The machine measures the force and position of the head (load and extension on top of the screen in Fig.3.5).

When the specimen is positioned and secured in the grips, a load is created and needs to be reduced to zero by slowly moving the top grip. Once the load measured is back to zero, the extension is reset using the Reset Gauge Length button at the top of the screen.

The software plots simultaneously the force versus extension curve (Fig.3.5). More than one curve may be plotted on the same graph allowing an instantaneous comparison between hardening curves obtained from different specimen.

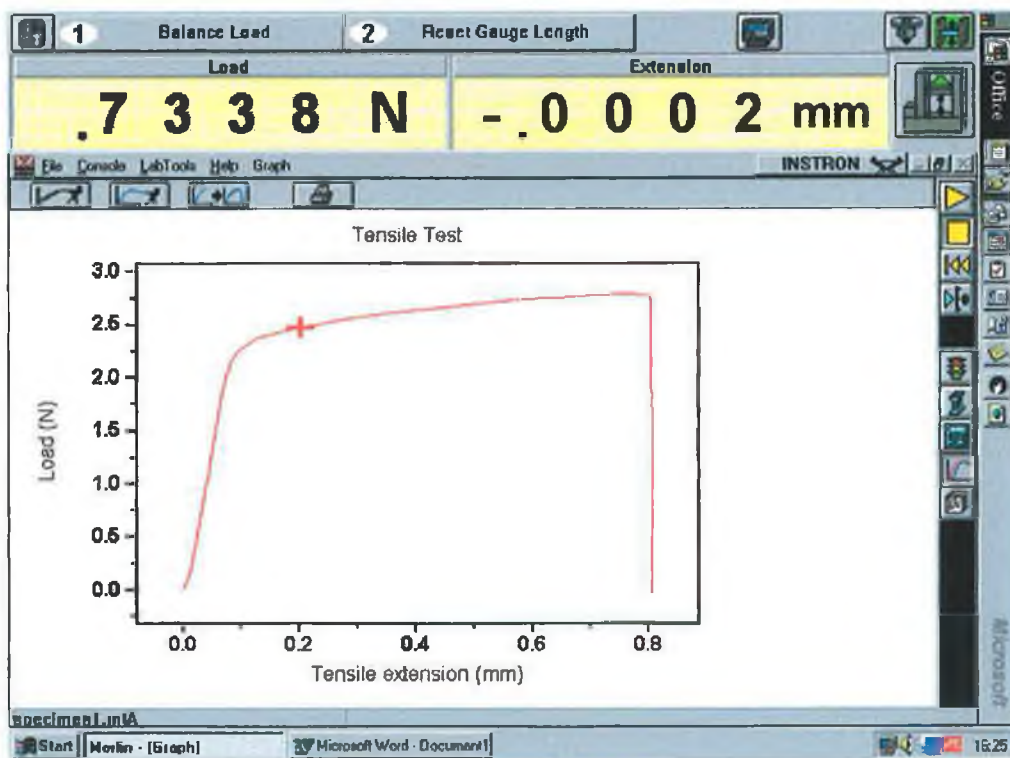


Fig.3.5 The computer reads the load and extension and plot the curve instantaneously.

The data measured are stored in a text file readable by Microsoft Excel (Fig.3.6).

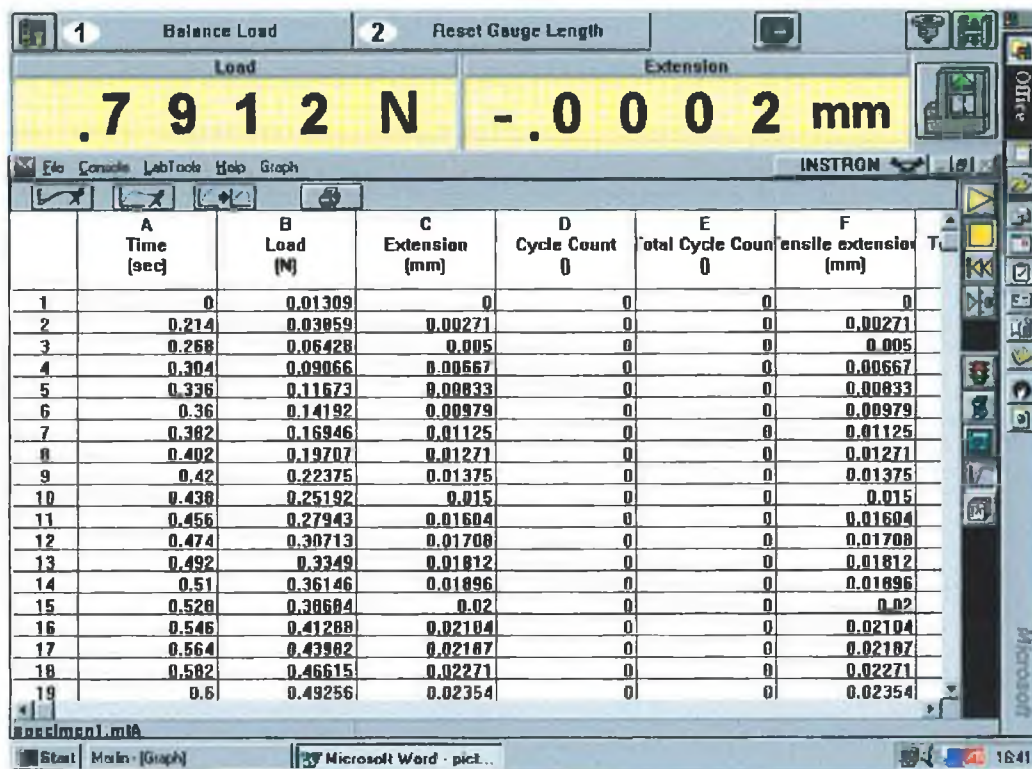


Fig.3.6 A text file containing the data is created.

II.3 SPECIMEN DESIGN

Standard specimens are not available for this scale. Hence, the specimen was designed to be representative of the stent geometry in order to use the results found when studying the mechanical behaviour of stents. The specimen is therefore cut in the same type of tube and its dimensions are similar to that of the stent.

Tubes dimensions

Internal diameter: 1.374 mm

External diameter: 1.557 mm

Specimen Design

The strut is laser cut in a tube. 25 mm of tube is left over each side of the strut (Fig.3.7 (a)) in order to position it in the grips. Fillets (Fig.3.7 (b)) are cut between the different parts in order to avoid stress concentration.

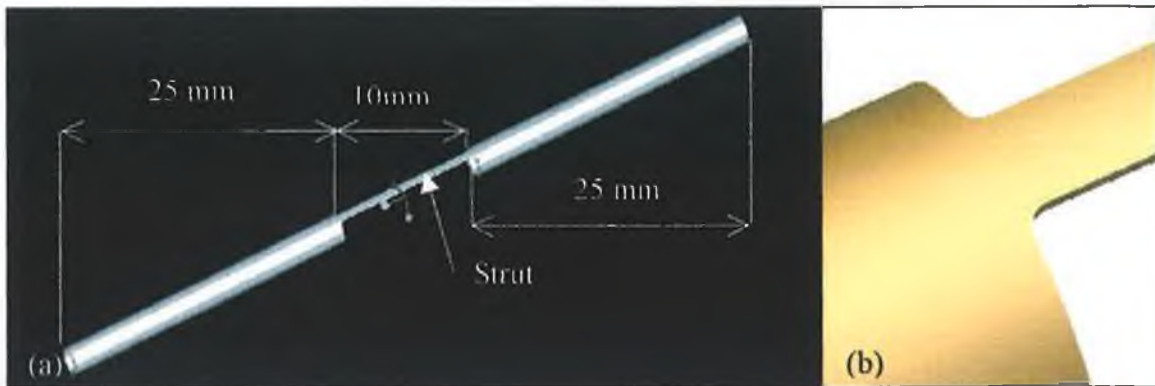


Fig.3.7 (a) 3D drawing of the specimen, (b) detail of the fillets.

II.4 VALIDATION OF THE TEST

In order to determine the tensile behaviour of the material, the hardening curve has to be plotted. As explained in chapter 1 paragraph III.1, the Young's Modulus, yield stress, maximal stress and strain at breaking point are determined from the hardening curve. Standard test specimens are either flat or round but here the specimens, being cut in a tube, are neither of these. Therefore, it is necessary to confirm that the values measured by the tensile tester are relevant to determine these data.

II.4.1 Conditions for validity :

- The rupture occurs along the strut and is not due to a stress concentration created at the junction between the strut and the tubes left over.
- The strain is uniform along the strut in order to consider representative the average strain calculated by dividing the increase in length by the original length.

The conditions for validity presented above are independent of the material used. Therefore, if the specimen design is shown to be valid for one material, it is valid for any material.

II.4.2 Method of validation

An F.E.A. was conducted to validate the design of the specimen before manufacturing. Because the mechanical behaviour of the stent material was not known at this stage, the following material, determined from a study previously conducted by the manufacturer on stainless steel 316L, has been used for this analysis:

Young's Modulus: 210000 Mpa,

Poisson's ratio: 0.3.

Fig.3.8 shows the hardening curve of the material.

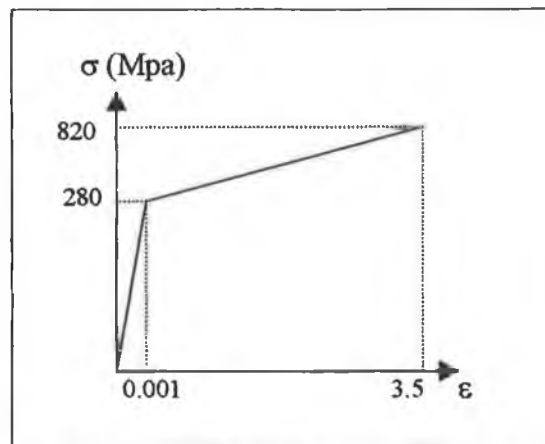


Fig.3.8 Strain-stress curve used for F.E.A analyses.

The characteristics of the material (Fig.3.8) are given here in order to be compared with the output of the F.E.A.

The specimen modelled was clamped at one end and displacement is applied at the other end. In a first approach, the dimensions of the specimen were considered to be accurate, therefore the strut was considered to be straight.

II.4.3 Breaking point

If there was a stress concentration at the junction between the tube and the strut, the fracture would occur there instead of along the strut. Therefore, the stress and strain calculated at breaking would not be representative of the material since force and displacement were measured along the strut and not at the real necking (no method was available to measure the stress and strain at the junction).

In order to predict where the specimen would break, Fig.3.9 shows the repartition of stress in the direction Z, which is the direction of the stress applied. Note that the maximal stress along the beam is 810 Mpa which is around the maximal stress of the material, therefore close to breaking point. This is important to study where breaking is going to occur. Fig.3.9 shows that there is no stress concentration at the junction between the tube and the strut in the direction Z. However, due to the geometry of the strut, the stress distribution in the two other directions has to be studied as well.

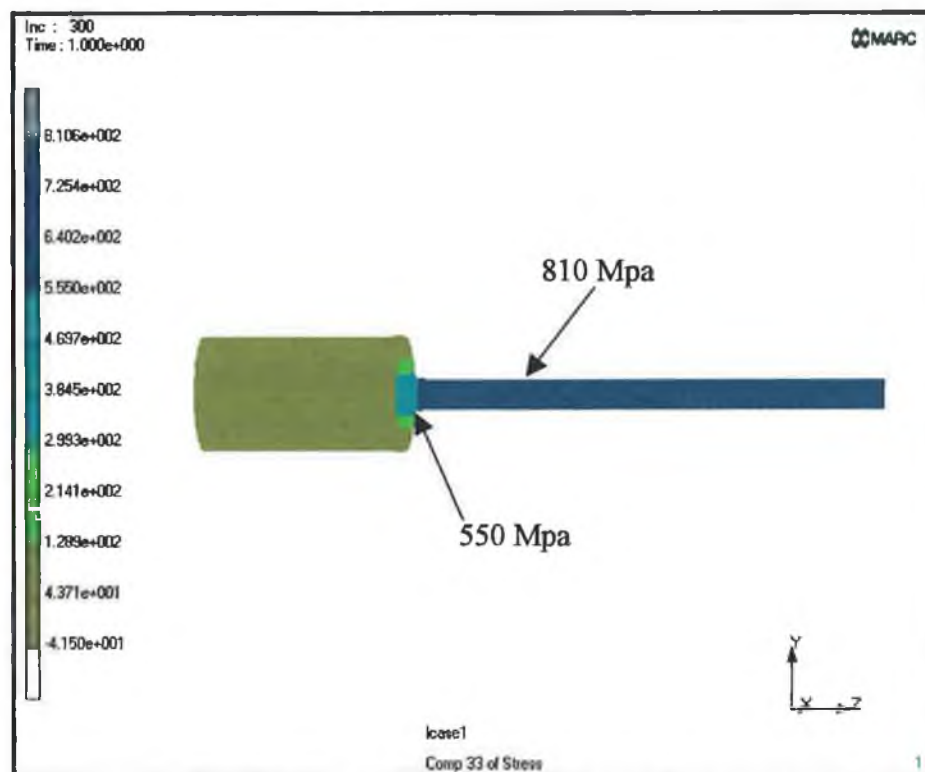


Fig.3.9 Stress distribution in the direction Z.

Fig.3.10 and Fig.3.11 present the stress repartition in direction X and Y respectively. A stress concentration is observed at the junction between the strut and the tube. In order to determine where the specimen breaks the three directions need to be considered. The Von Misses stress (Chapter 1, paragraph III.2.3) is an equivalent stress taking into account the three directions of the material. If the Von Misses stress is smaller at the junction than along the strut, it is assumed that the material breaks along the strut and not at the junction. Values read on Fig.3.9, Fig.3.10 and Fig.3.11 are used to calculate the Von

Misses stresses. The three directions studied being the main directions of the structure, the term $6(\sigma_{12}^2 + \sigma_{23}^2 + \sigma_{13}^2)$ is equal to zero.

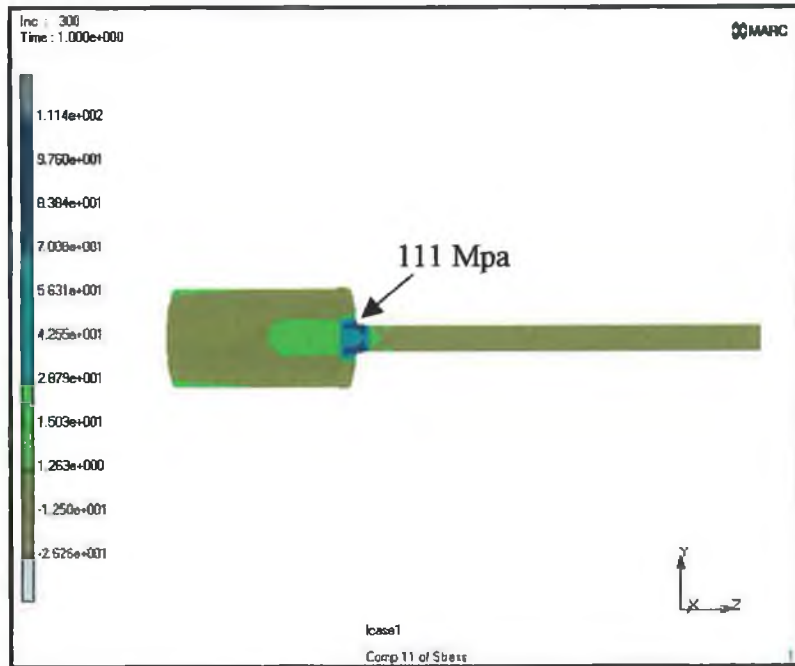


Fig.3.10 Stress distribution in the direction X.

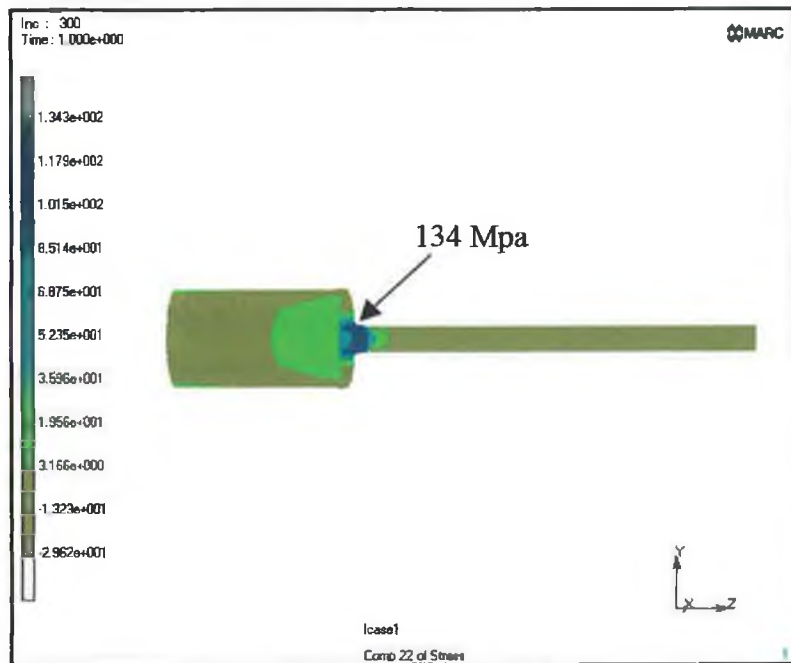


Fig.3.11 Stress distribution in the direction Y.

The maximum stress measured at the junction is 550 Mpa in the direction Z (direction 33), 111 Mpa in the direction X (direction 11) and 134 Mpa in the direction Y (direction 22). Therefore, the Von Misses stress is :

$$\sigma = \frac{1}{\sqrt{2}} \sqrt{(550 - 111)^2 + (134 - 111)^2 + (550 - 134)^2} = 428 \text{Mpa}$$

This is less than the stress observed along the strut in the direction Z, therefore the breaking occurs along the strut and not at the junction between the strut and tube.

II.4.4 Uniformity of the stress along the strut

In order to prove that the force and displacement measured are adequate to plot the stress versus strain curve, the strain has to be uniform along the beam. Indeed, the strain calculated is the average strain along the strut since it is calculated using the displacement, and original length of the strut. If the deformation is constant along the strut, the strain at any point is equal to the average strain but this is not true if the deformation is not constant along the strut. Consequently, the analysis could be erroneous if the strain is not uniform along the strut. Fig.3.9 shows that the stress is uniform, therefore the strain is uniform as well.

II.5 POSITIONING OF THE SPECIMEN

II.5.1 Manipulation of the specimen

Due to the small size of the specimens, there is a risk of bending them during manipulation. When cutting the specimen two bars have been left, as shown on Fig.3.12, avoiding any bending.

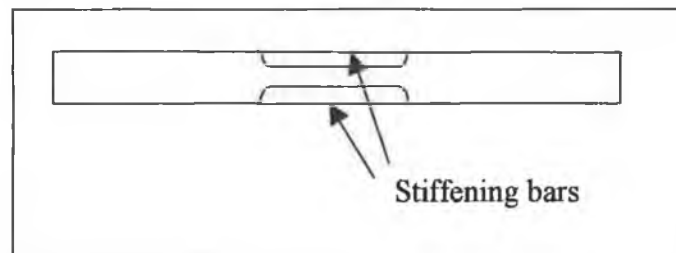


Fig.3.12 Stiffening bars have been added to the specimen design.

The stiffening bars are cut out once the specimen is secured between the grips.

II.5.2 Specimen positioning

The specimens are placed manually inside the grips provided by Instron. Incidentally, all specimens do not have exactly the same position. Fig.3.13 shows experimental hardening curves obtained for four specimens of the same size (laser-cut in the same batch) and the average of these curves. Fig.3.14 shows the interval of confidence versus true strain for the results presented in Fig.3.13.

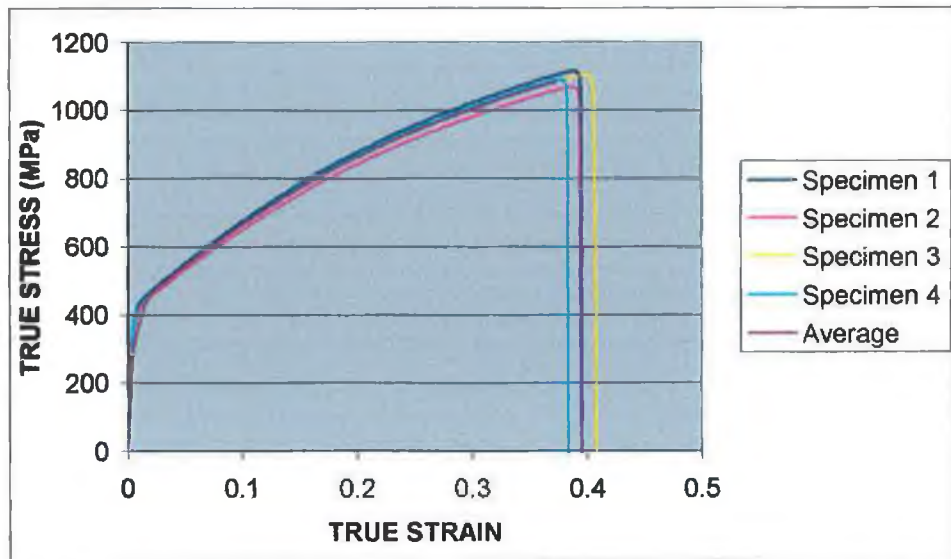


Fig.3.13 Experimental results for four specimens of the same size.

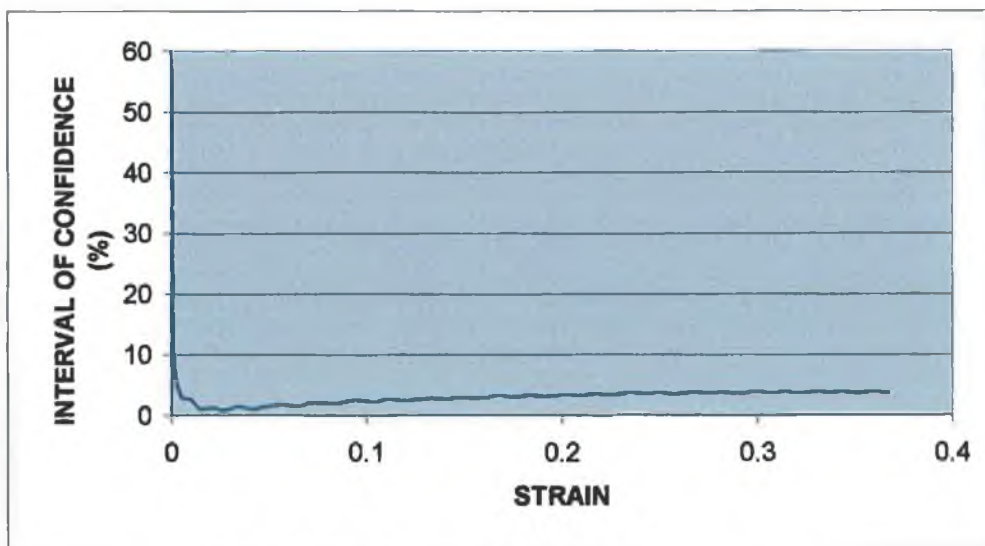


Fig.3.14 Interval of confidence versus strain.

Fig.3.14 shows that, under 0.001 mm, the interval of confidence is over 10 % and reaches 60% for the smallest true strain. This is in the elastic region (as shown in Fig.3.13), therefore the results are not repeatable enough to accurately calculate the Young's Modulus. However, as a first approach, the variation of the average Young's Modulus may be studied without considering its absolute value. A more accurate method, such as indentation [102], should be used to confirm the results. In the plastic region, the interval of confidence is less than 10%, therefore the curves are repeatable enough to study the plastic behaviour.

II.6 ACCURACY OF LASER CUTTING

The test and specimen design have been validated. The next step is to measure the laser-cut specimens in order to verify that the struts are straight and the dimensions are the ones required.

II.6.1 Observation:

Laser-cutting is recognised as being very accurate; however, a succession of straight beams laser-cut in the tubes used for the manufacturing of stents were measured and Fig.3.15 shows the profile of the struts for different width requested and Table 3.1 shows the values actually measured along the strut.

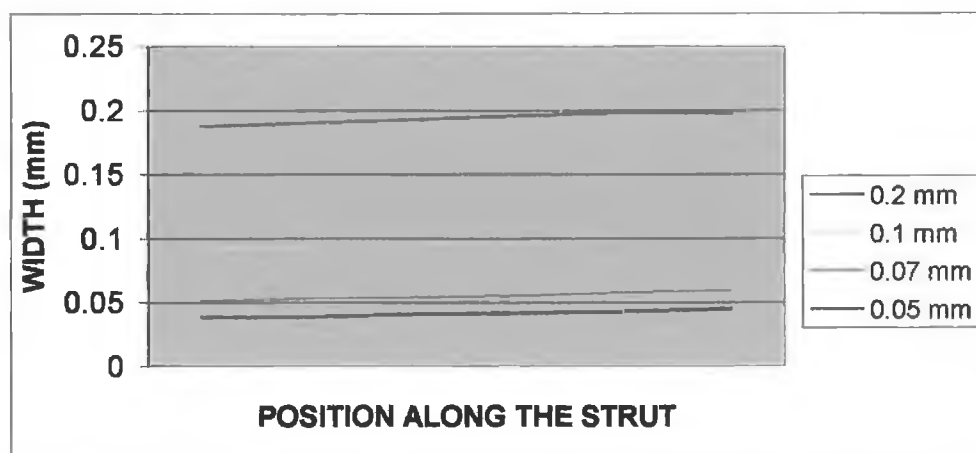


Fig.3.15 Width measured along the length of the struts for different strut widths.

Width Requested (mm)	0.05	0.07	0.1	0.2	0.3	0.5	0.8
Width along the length (mm)	0.0383	0.0513	0.0914	0.1877	0.2829	0.4835	0.7502
	0.0385	0.053	0.0936	0.1905	0.2841	0.486	0.7509
	0.0408	0.054	0.095	0.1928	0.2867	0.4871	0.752
	0.0414	0.0556	0.0968	0.1958	0.2897	0.4897	
	0.043	0.0578	0.0983	0.1984	0.2927	0.4927	
	0.045	0.0597	0.0988	0.1981	0.2947		
				0.2			
Standard Deviation	0.0026	0.0031	0.0029	0.0046	0.0047	0.0033	0.0009
Width Increase between smaller and larger side.	17%	16%	8%	6%	4%	2%	0%
Stress increase between larger and smaller extremities.	17%	16%	8%	6%	4%	2%	0%

Table 3.1. Table analysing the inaccuracy of laser-cutting of struts.

Fig.3.15 and Table 3.1 shows the following :

- 1- Some of the dimensions are far from the one requested. As an example, for a requested width of 0.0700 mm, the width obtained varies between 0.0513 mm and 0.0597 mm.
- 2- A difference in width between the two extremities of the beam is observed on both Fig.3.15 and Table 3.1. All struts represented on Fig.3.15 show a trapezoidal shape, resulting in a stress gradient along the beam. The stress gradients are calculated in Table 3.1.
- 3- The trapezoidal shape, hence the stress gradient, increases when the width of the beam decreases, (17% increase in size between the two extremities for the smaller specimens according to Table 3.1), and is negligible for the larger struts.

II.6.2 Influence of the trapezoidal shape on the yield stress

In order to study the influence of the trapezoidal shape of the specimen on the hardening curve, an F.E.A. has been conducted. A beam, representing the specimen, is clamped at its smaller extremity (0.050 mm) and a displacement is imposed to its larger one, (0.051 mm) as shown on Fig.3.16.

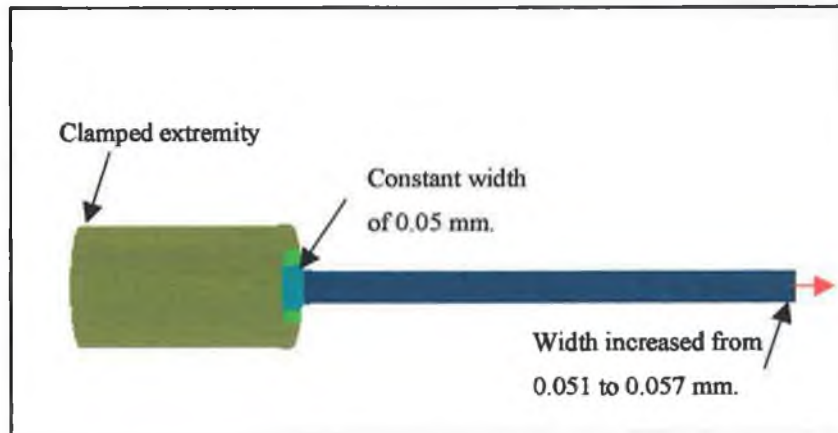


Fig.3.16 F.E.A model of the strut.

The stress at the larger extremity is plotted versus the global strain $\ln(L/L_0)$. The dimension of the larger extremity is then increased, (increasing the angle of the trapeze), and the same analysis is reproduced. Fig.3.17 shows the hardening curves obtained.

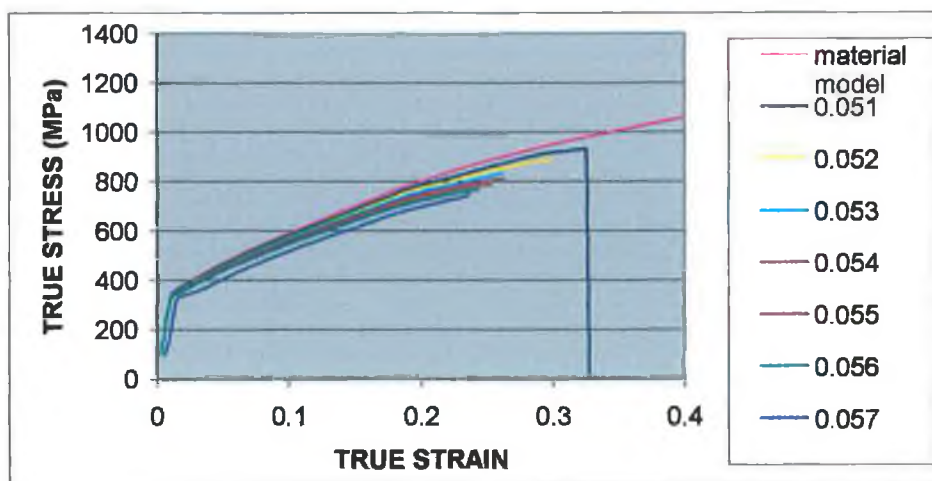


Fig.3.17 Hardening curves obtained for different width increases along the strut.

According to Fig.3.17, when the dimension of the larger extremity increases, the yield strength of the specimen decreases and the strain for a given stress increases.

II.6.3 Potential solutions for improving the accuracy of laser-cutting

To improve the cutting process, the cause of inaccuracy has to be identified. Therefore, the mechanism of laser cutting has to be studied in more detail.

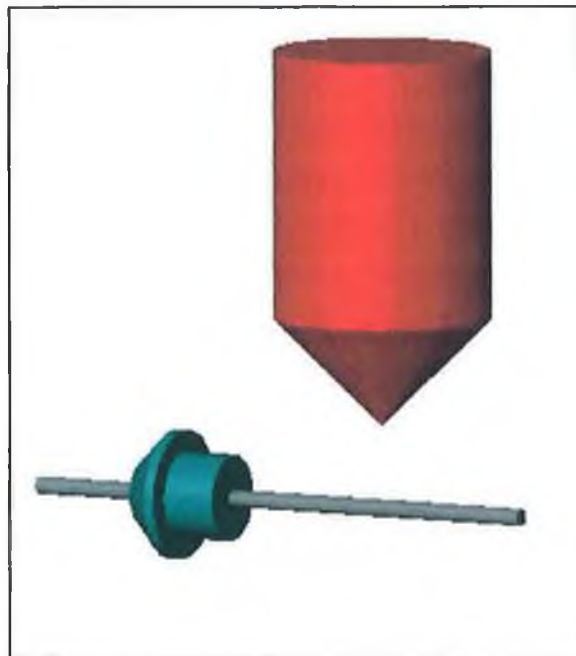


Fig.3.18 Laser-cutting process.

Fig.3.18 shows the laser in red, the exit of the machine (support of the specimen) in green and the tube in grey. The laser is fixed, the machine rotates and moves the tube back and forth.

Assumption 1

One assumption for the variation of the dimension along the strut could be the bending of the tube during the operation. Indeed, under the influence of its own weight and the heat produced by the laser, the tube tends to bend.

A new support was manufactured in order to support the tube while cutting (Fig.3.19). Specimens were cut and measured. The change in the width along the strut was still present. Another cause was then explored.

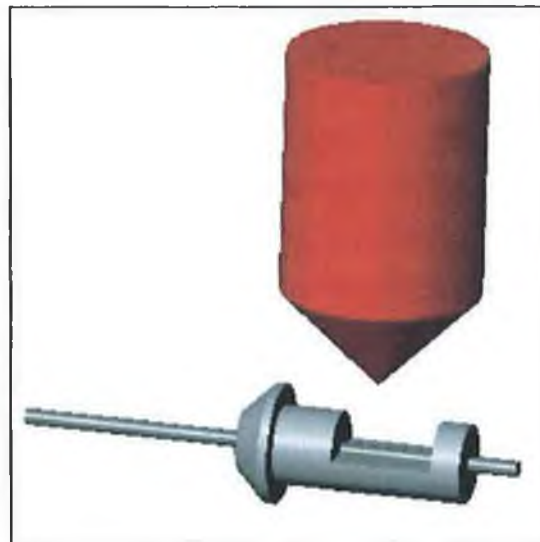


Fig.3.19 Improvement of the support of the tube.

Assumption 2

The laser generates an increase of the temperature and therefore an expansion of the material. The laser cut is straight but the material expands while being cut. When the material shrinks back to its original dimensions, the width of the strut decreases along the strut (Fig.3.20).

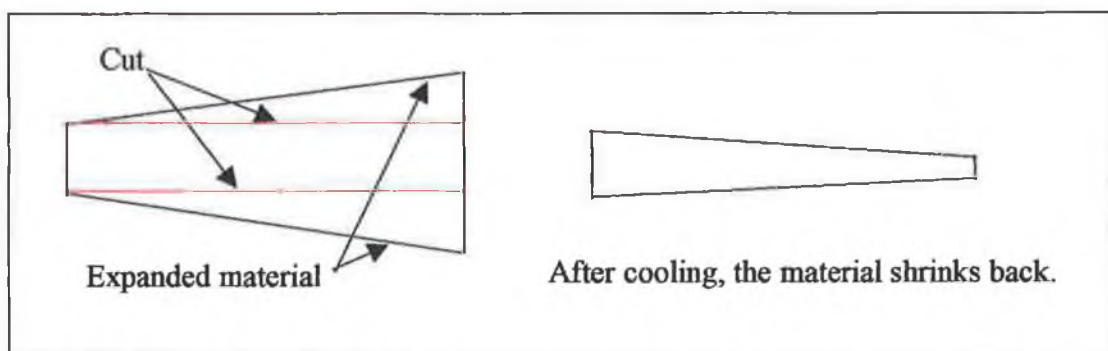


Fig.3.20 Expansion of the material due to the heat generated by the laser beam.

In order to stop this from happening, the power of the laser was reduced. Reducing the power means reducing the heat, therefore reducing the expansion. But with reduced the power, the laser does not go through the thickness of the tube and the cut has to be done in more than one step. However, the material melted by the first pass re-solidifies before the second pass. Consequently, the second pass re-melt the same quantity of material and no cut is possible.

Another approach is not to cut the full length of the strut in one go. By cutting a small length at a time, the material does not expand as much and the cut should be more regular.

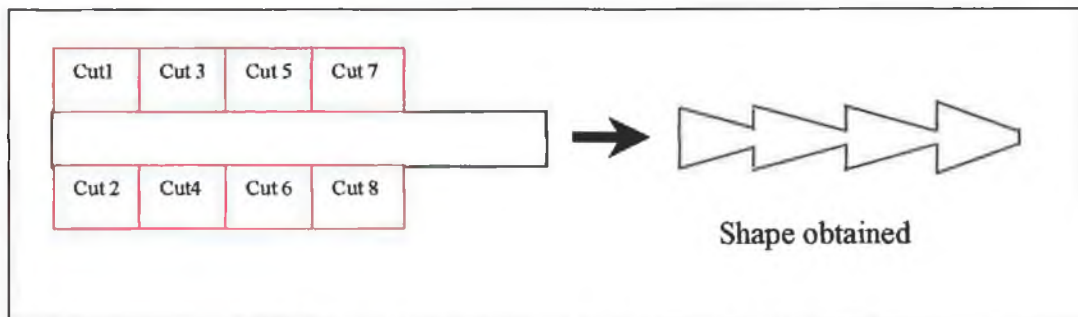


Fig.3.21 Shape obtained by alternating the cuts.

Fig.3.21 shows an exaggeration of the shape obtained. The material still expands along each cut. The solution seems to be to multiply the number of cuts and therefore reduce their length. The smaller the cut, the less time for the material to expand. But, this method would be time consuming and practically not feasible.

In conclusion, all the attempts to improve the accuracy of the cut have failed or were not feasible. Consequently, the influence of the specimen dimensions on the experimental results will have to be taken into consideration and studied in more detail.

III DATA PROCESSING

Force and displacement were measured. In order to plot the hardening curve, true strain and true stress have to be calculated (see chapter 1, paragraph IV.1 for more details on the formulae).

Engineering stress (σ in MPa)

$$\sigma = \frac{F}{A} \quad (3.1.)$$

F: load (N)

A: cross section (mm^2)

Engineering strain (ϵ)

$$\epsilon = \frac{\Delta l}{l_0} \quad (3.2.)$$

Δl : extension (mm)

l_0 : original length (mm)

True stress (σ_T in Mpa)

$$\sigma_T = (1 + \epsilon)\sigma \quad (3.3.)$$

True strain (ϵ_T)

$$\epsilon_T = \ln(1 + \epsilon) \quad (3.4.)$$

The text files containing the data measured are opened with Microsoft Excel. The first three columns are copied from the text file containing the data measured by the tensile tester. Engineering stress and strain are then calculated using the data and finally, true strain and stress are calculated using engineering stress and strain. The different calculations are done and hardening curves are plotted.

Table 3.2 (next page) gives an example of values obtained for a specimen.

Width (mm)	0.045		Length (mm)	10		
Cross section area (mm ²)	0.004115					
Specimen 1						
Time (second)	Extension (mm)	Load (N)	E Strain	E Stress (Mpa)	True strain	True stress (Mpa)
0	0	0	0	0	0	0
0.38	0.015833	1.814629	0.001583	441.0005	0.001582	441.6987845
1.38	0.058333	2.770303	0.005833	673.2534	0.005816	677.1806831
2.38	0.101042	2.874283	0.010104	698.5231	0.010053	705.5811185
3.38	0.142708	2.928618	0.014271	711.7279	0.01417	721.8848428
4.38	0.185	2.977245	0.0185	723.5455	0.018331	736.9310643
5.38	0.227916	3.024031	0.022792	734.9157	0.022536	751.6655963
6.38	0.270416	3.049718	0.027042	741.1583	0.026682	761.200378
7.38	0.312708	3.077524	0.031271	747.9158	0.030792	771.303727
8.38	0.354791	3.104349	0.035479	754.435	0.034864	781.2016476
9.38	0.397083	3.126975	0.039708	759.9337	0.03894	790.1093048
10.38	0.439583	3.154027	0.043958	766.508	0.04302	800.2023279

Table 3.2. Example of table obtained using experimental results.

Using the two last columns (true stress and strain), a curve representing true stress versus true strain is plotted (Fig.3.22).

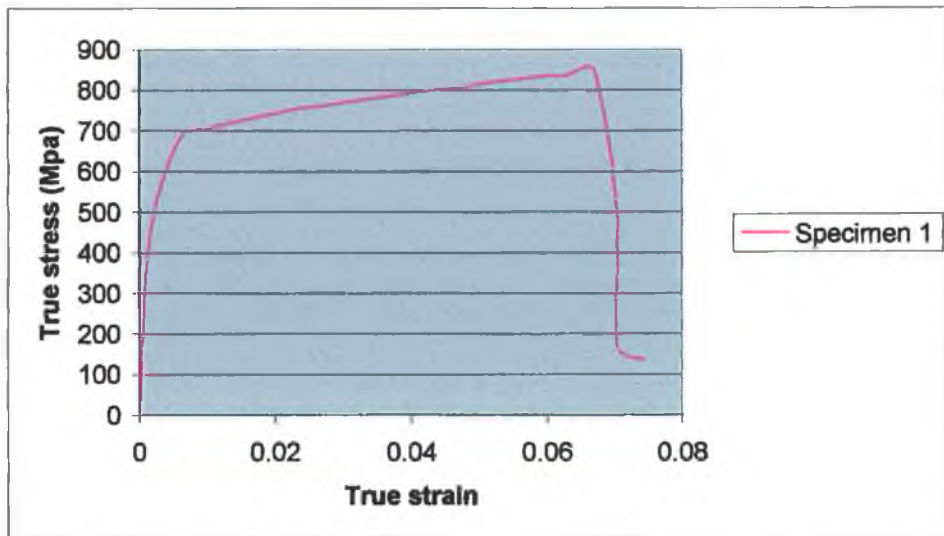


Fig.3.22 True stress versus true strain curve.

The same process is repeated for each specimen and all the curves are plotted on the same graph (Fig.3.23).

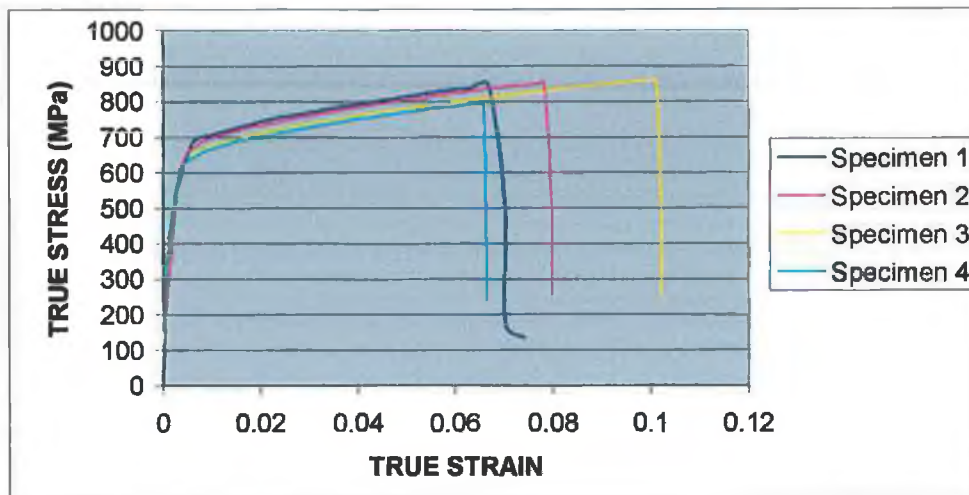


Fig.3.23 Curves obtained for four different specimens 0.0412 mm wide.

Fig.3.23 shows the curves plotted for the smaller width (0.0412 mm). Due to the small dimensions, a small variation of the force generates an important variation in stress. However, Fig.3.24 shows that the interval of confidence around the average hardening curve is never more than 8% in the plastic region. In the elastic region, as observed in Fig.3.14, the results are not repeatable enough to accurately calculate the Young's Modulus, but the variation of the average may be observed.

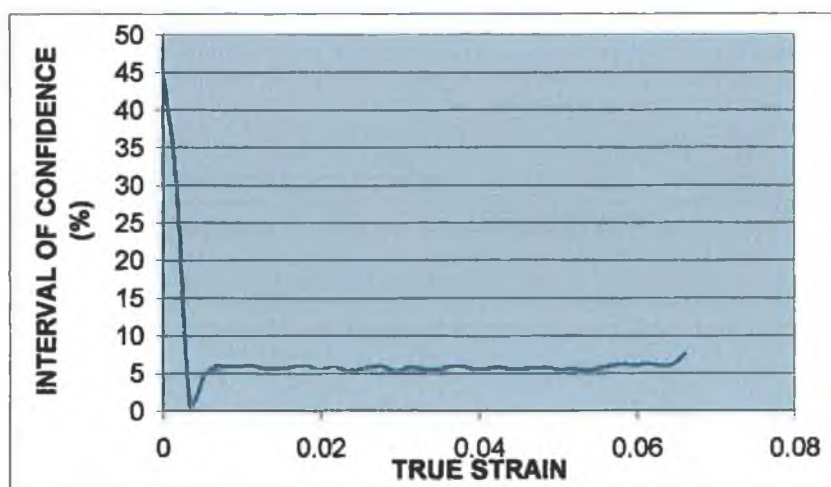


Fig.3.24 Interval of confidence versus strain for 0.0412 mm struts.

Likewise, the strain at breaking point varies between 0.065 and 0.1 which is less than 10% elongation in any case. Considering the accuracy of the equipment used and the accuracy of laser cutting (see paragraph II.6), closer results can not be expected. For larger specimens, as shown in paragraph II.5 of this chapter (Fig.3.14), the interval between the different strains at breaking obtained is reduced.

The aim of the study was to compare hardening curves obtained for different widths or manufacturing processes and not to identify the exact mechanical behaviour, therefore the curves obtained are acceptable. If the mechanical behaviour was to be identified another type of equipment and measurement method should be considered.

The results being acceptable, a curve representative of the width is then determined calculating an average stress (between the specimens measured) for each strain (Fig.3.25). All the true stress versus true strain curves obtained from tensile tests can be found in Appendix IV.

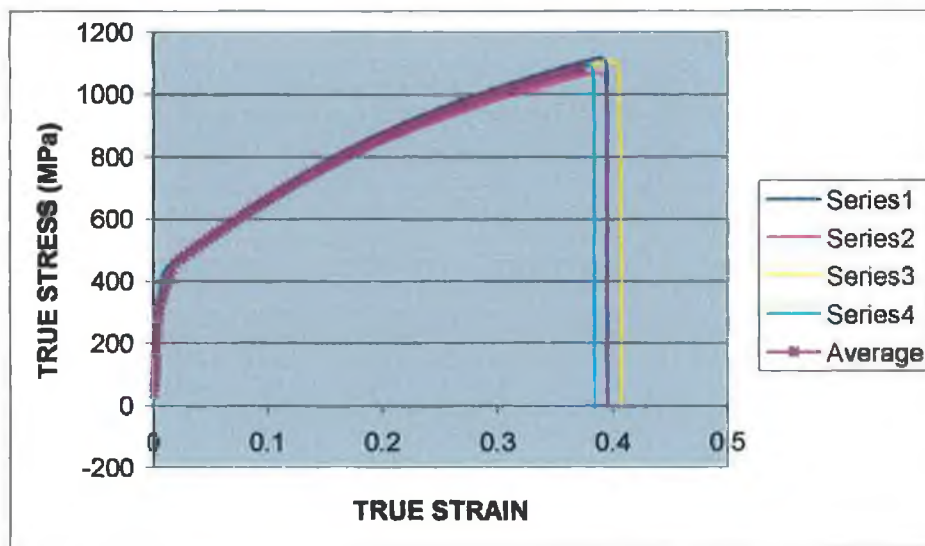


Fig.3.25 Hardening curves and average obtained for 0.78 mm.

IV INFLUENCE OF THE WIDTH

IV.1 INTRODUCTION

The purpose of this study was to show that the mechanical behaviour varies with the dimensions when they are very small. To confirm this point, specimens of different widths were tested.

The width X (Fig.3.26) of the different specimens tested varies from 0.05 mm to 8 mm. Thirty specimens of each width are laser cut and five of them are used for the tensile test, the others being kept for further tests.

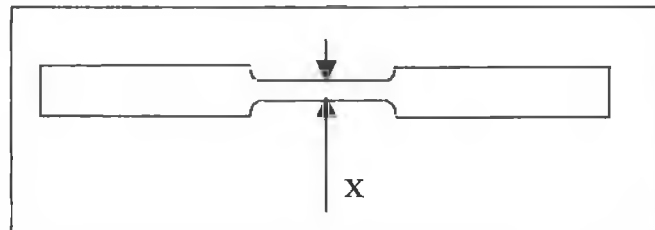


Fig.3.26 The width of the strut varies from 0.05 mm to 0.8 mm.

IV.2 EXPERIMENTAL RESULTS

In order to compare the mechanical behaviour of the different specimens, three properties have to be looked at. Firstly the Young's Modulus is important to characterise the elastic behaviour. Secondly the yield stress needs to be examined since it is the critical point between elastic and plastic behaviour. Finally, the strain and stress at breaking point need to be studied.

The hardening curves obtained for the first batch (batch 0) are presented in Fig.3.27 (next page).

The following changes are observed :

- The yield stress increases when the width decreases.
- The true strain at breaking point decreases when the width decreases.

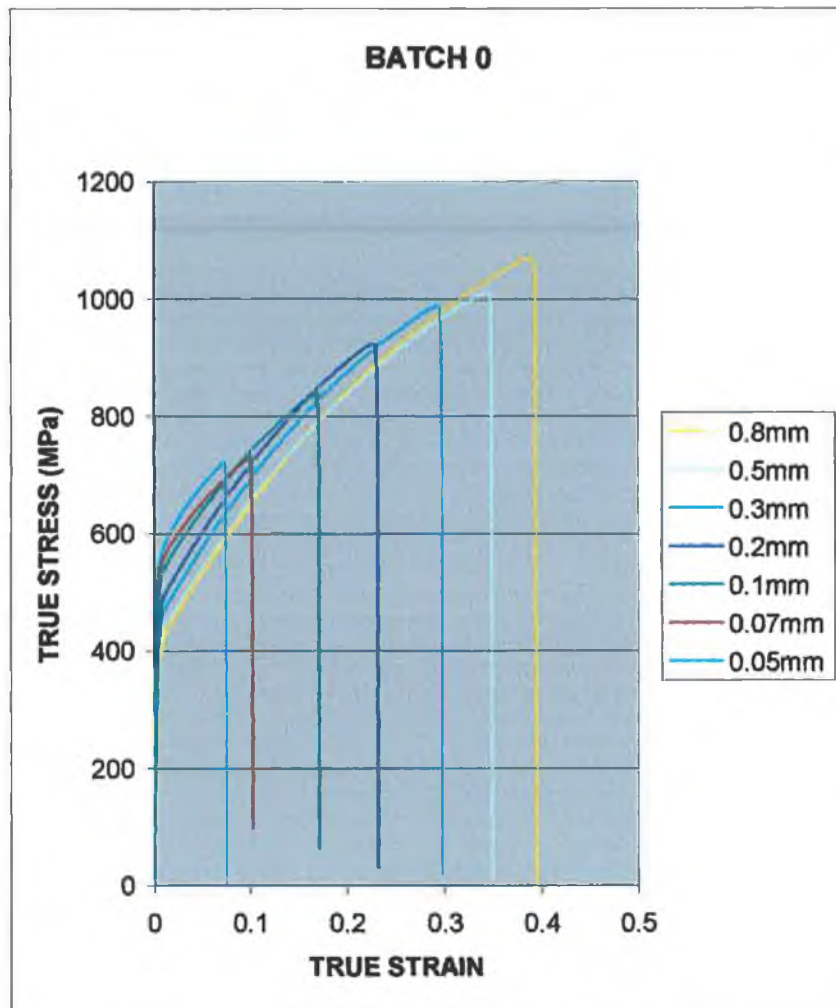


Fig.3.27 Hardening curves obtained by tensile tests of seven different widths.

In order to closely examine the phenomenon, Table 3.3 presents the approximate yield stress and strains at breaking point for the different widths and Fig.3.28 shows a zoom of the area concerned.

-Table 3.3 confirms the increase of the yield stress and decrease of the strain at breaking when the width decreases.

-Fig.3.28 presents a zoom on the yield stress which emphasises the increase of the yield stress, and shows an increase of the Young's Modulus as well. Tensile tests are known not to be accurate to calculate the Young's Modulus, therefore this last observation should be verified using further experimental tests.

	0.05 mm	0.07mm	0.10mm	0.20mm	0.30mm	0.50mm	0.80mm
Yield stress (Mpa)	500	480	460	420	400	370	360
Strain at breaking point	0.07	0.1	0.17	0.23	0.30	0.35	0.40

Table 3.3. Yield stress and breaking point for each width.

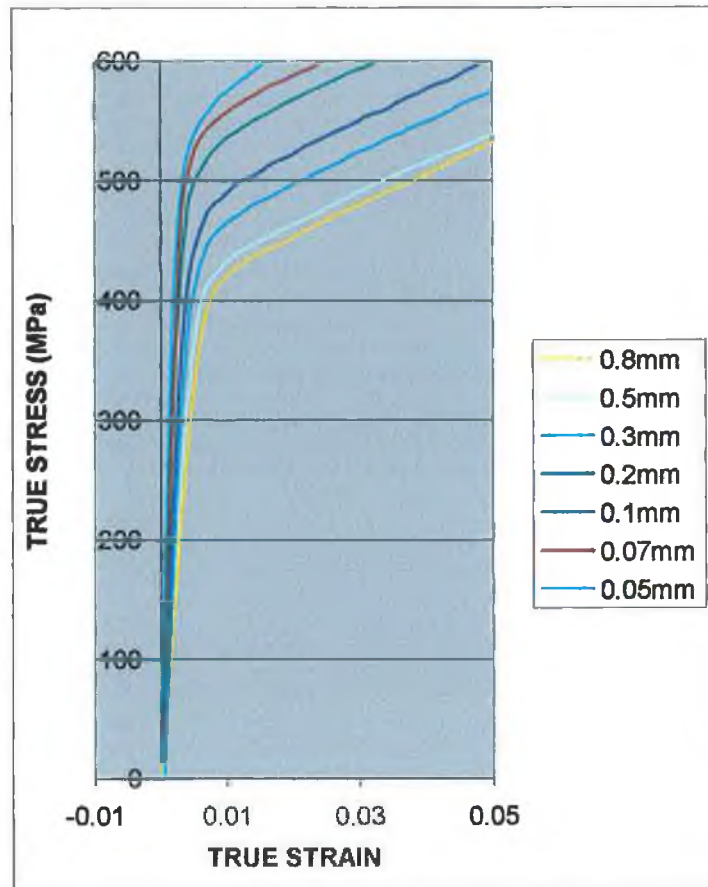


Fig.3.28 Zoom of the yield stress area.

IV.3 COMPARISON BETWEEN DIFFERENT BATCHES

The stent manufacturer receives the tubes by batches. The specifications given to the supplier allow the grain size of the material to vary from grade 8 to grade 10. In order to confirm the results obtained for Batch 0 and observe the influence of the grain size on the mechanical behaviour of the struts, more specimens were cut in two different batches.

Table 3.4 gives the mean intercept length L_3 calculated using the Heyn intercept method (Chapter 1) and the number of grains/mm for each of the batches. Chapter 5 shows the detail of the calculations.

	L_3	No. of grains/mm
Batch 0	0.013 mm	77
Batch 1	0.015 mm	67
Batch 2	0.012 mm	83



Table 3.4. Mean intercept length and number of grains/mm for each of the batches.

Fig.3.29 and Fig.3.30 shows the hardening curves obtained for batch 1 and 2 respectively.

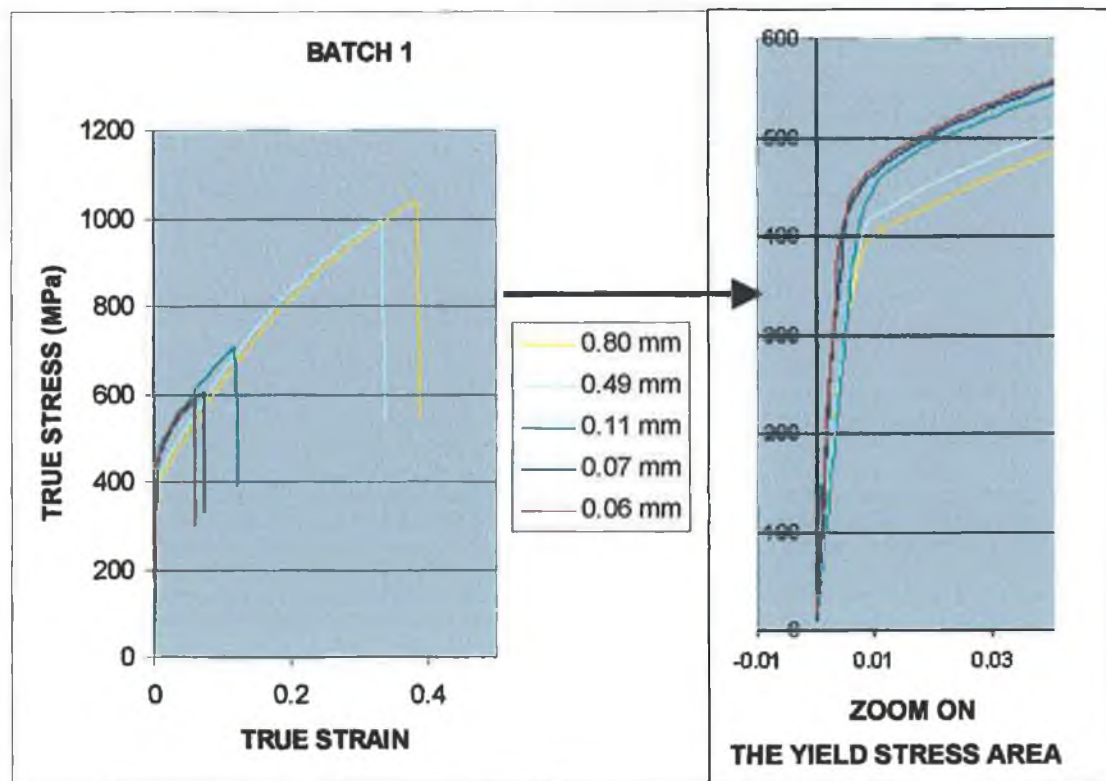


Fig.3.29 Hardening curves for batch 1 and zoom on the yield stress area.

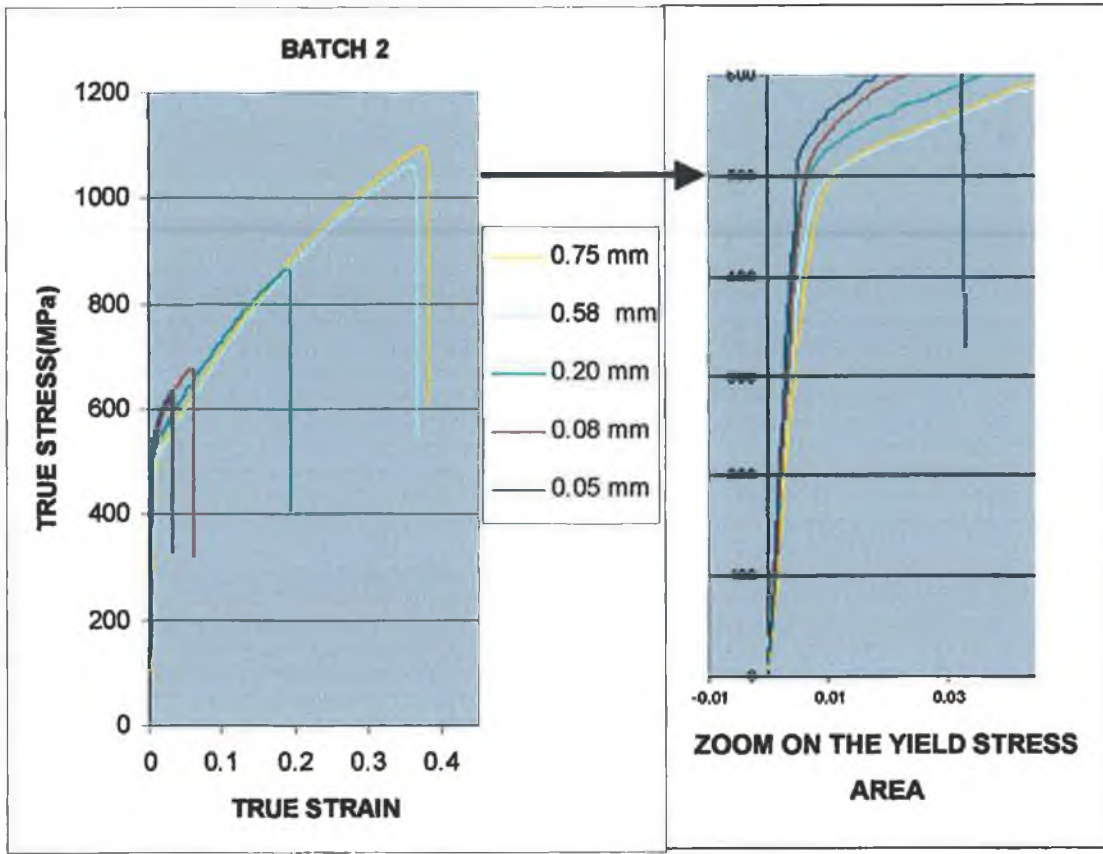


Fig.3.30 Hardening curves for batch 2 and zoom on the yield stress area.

Fig.3.31, Fig.3.32 and Fig.3.33 present the influence of the width of the strut on the yield stress, strain at breaking point and Young's Modulus (σ/ϵ) for the three batches.

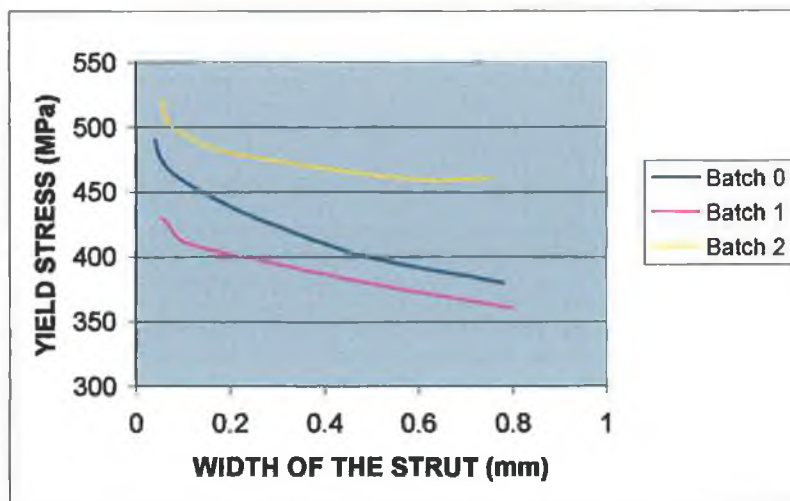


Fig.3.31 Yield stress versus width of the strut for three different batches.

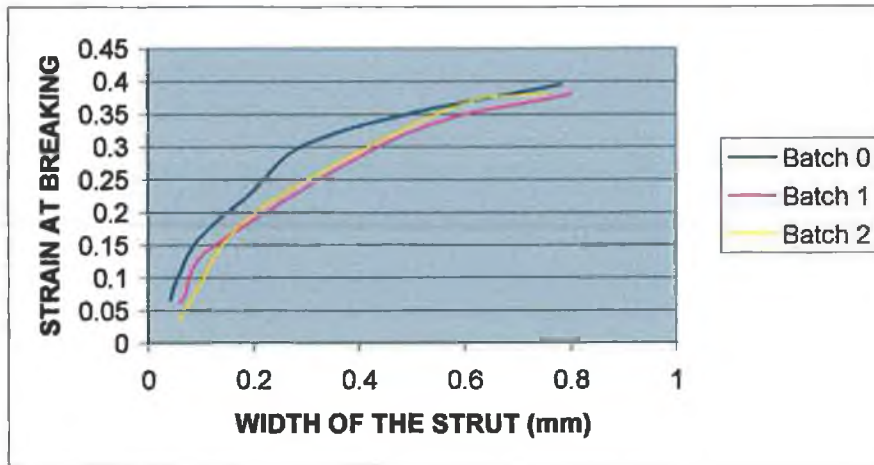


Fig.3.32 Strain at breaking versus width of the strut for three different batches.

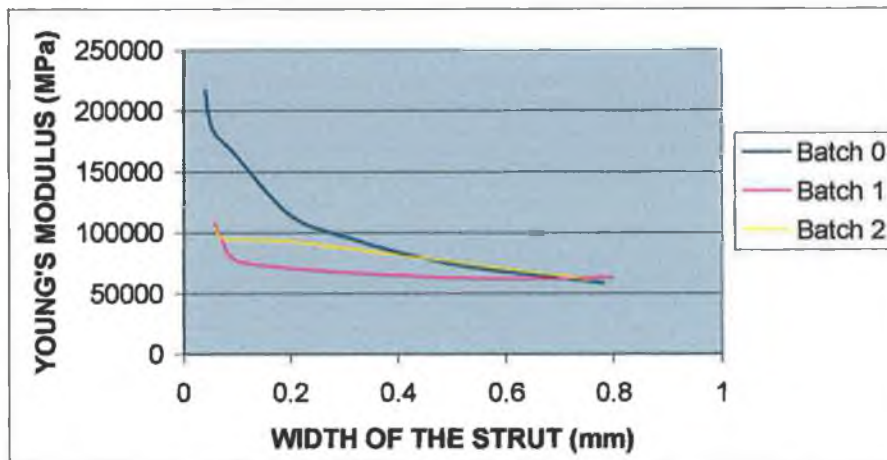


Fig.3.33 Young's Modulus versus the width of the strut for three different batches.

- The yield stress increases when the width of the strut decreases whereas the strain at breaking decreases with the width of the struts. Chapter 1 paragraph III.5.4 has explained that the strain at breaking decreases when the yield stress increases.
- The three batches have different yield stresses. This was to be expected since their grain sizes are different (see Chapter 5 for more details).
- The Young's Modulus increases when the width decreases. The three curves seem to converge for the larger specimens, however the values calculated are erroneous since the Young's Modulus of steel is known to be around 210000 Mpa.
- Batch 0 observes greater changes than the two other batches.

V INFLUENCE OF THE MANUFACTURING PATH

V.1 INTRODUCTION

Following laser cutting the struts are electro-polished, therefore it is important to study the changes resulting from this manufacturing process. Thirty specimens of each width were laser-cut in batch 0, the first ten were used without further processing.

The next ten were then electro-polished. Tensile tests were conducted on five of these, five were kept for further tests.

The last ten were annealed. This manufacturing process is not used by the company but is used by other manufacturers. Annealing softens the material and makes it more ductile, reducing the risk of cracks during deployment. It is therefore interesting to study the modifications resulting from this process.

V.2 EXPERIMENTAL RESULTS FOR ELECTRO-POLISHED SPECIMENS

Once electro polished, the specimen are narrower as shown on Table 3.5. The width of material removed varies between 0.020 and 0.035 mm, but when looking at the percentage of the width removed, it goes from 4.5% for the wider specimens to 50% for the smaller ones.

Width (mm) Laser-cut struts	0.0412	0.0548	0.0957	0.1953	0.2900	0.4963	0.7833
Width (mm) electro-polished struts	0.0204	0.0309	0.0660	0.1709	0.2682	0.4567	0.7488
Width (mm) removed	0.0208	0.0239	0.0297	0.0244	0.0218	0.0396	0.0345
% of the width removed	50.5 %	43.5 %	30 %	12.5 %	7.5 %	8 %	4.5 %

Table 3.5. Width of the struts after electro-polishing compared to their width before.

Fig.3.34 shows that the yield stress is constant when the width is greater than 0.2 mm then increases when the width decreases until the width become smaller than 0.05 mm, then the yield stress decreases. As observed after laser-cutting, the breaking point decreases with the width. The Young's Modulus (σ/ϵ) increases when the width decreases until the width is less than 0.1 mm and then decreases with the width. Chapter 5 will show that this results are explained by the relative grain size decreasing with the width.

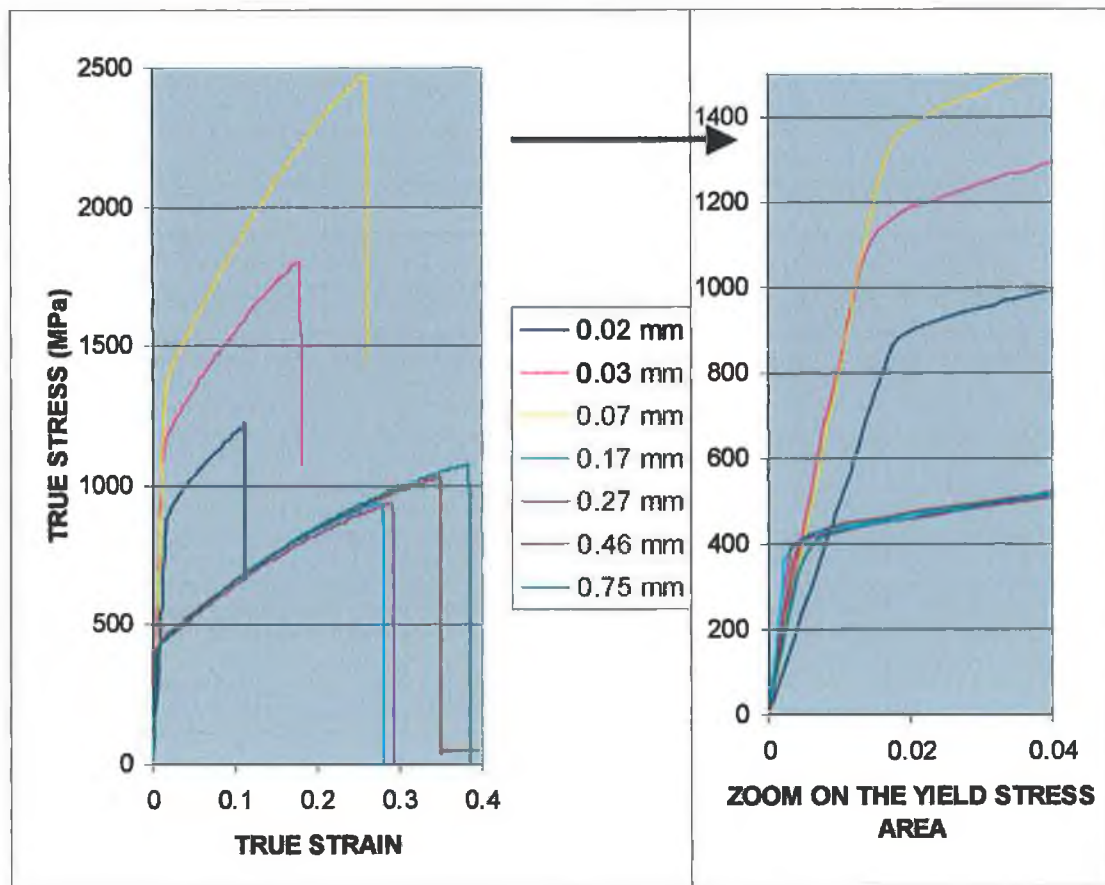


Fig.3.34 Hardening curves for polished specimens and zoom on the yield stress area.

V.3 INFLUENCE OF ELECTRO-POLISHING

In order to compare the mechanical behaviour of the material before and after electro-polishing, the main characteristics of the material are plotted versus the width of the strut before and after electro-polishing.

Fig.3.35 shows that the yield stress of the larger specimen is not significantly affected by this manufacturing process. However, when the width is smaller than 0.2 mm, the mechanical behaviour of the electro-polished strut follows a completely different pattern. It can be noted that this pattern is very similar to the Hall-Petch effect curve presented in Chapter 1. Chapter 5 will explore the factors responsible for this behaviour.

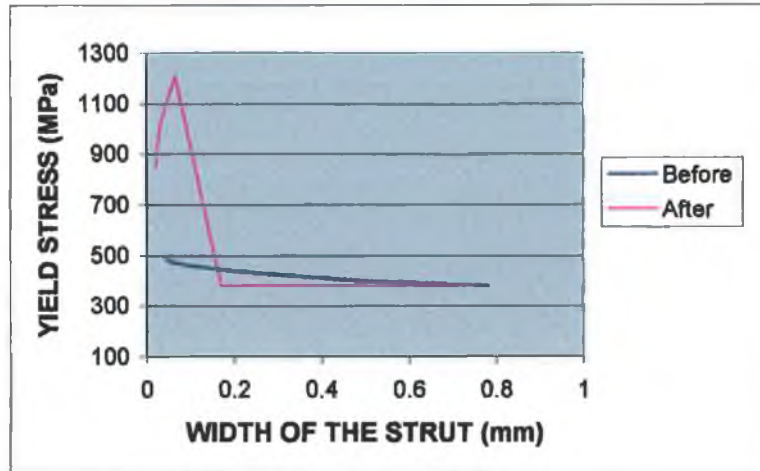


Fig.3.35 Yield stress versus the width of the struts before and after electro-polishing.

Fig.3.36 shows that electro-polishing does not affect the strain at breaking for the larger struts, but does when the width is smaller than 0.2 mm.

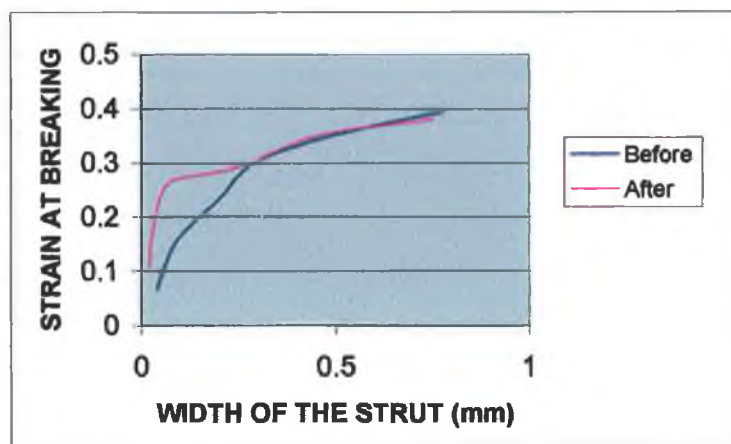


Fig.3.36 Strain at breaking versus the width of the struts before and after electro-polishing.

Fig.3.37 confirms that the process does not affect the maximum stress and strain when the width of the strut is greater than 0.2 mm but does when the strut is narrower.

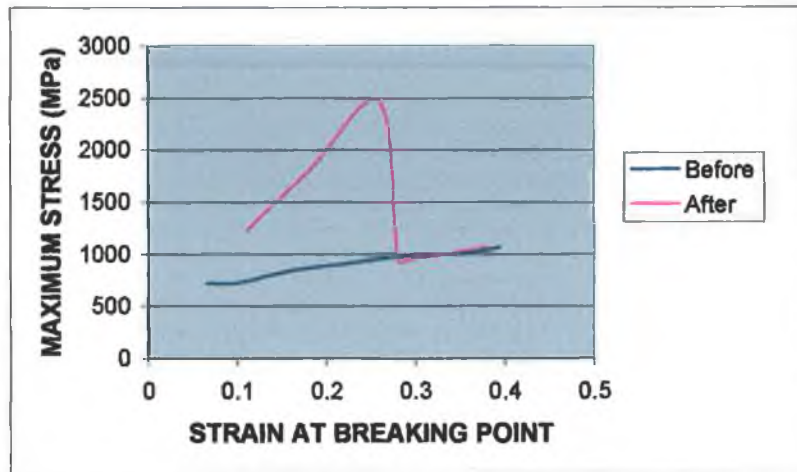


Fig.3.37 Maximum stress versus strain at breaking point before and after electro-polishing.

Fig.3.38 shows that the Young's Modulus follows the same pattern before and after electro-polishing for struts wider than 0.2 mm. It is, however, higher after electro-polishing. But, when the struts is smaller than 0.2 mm, as observed on the previous curves, the strut mechanical behaviour follows a completely different pattern.

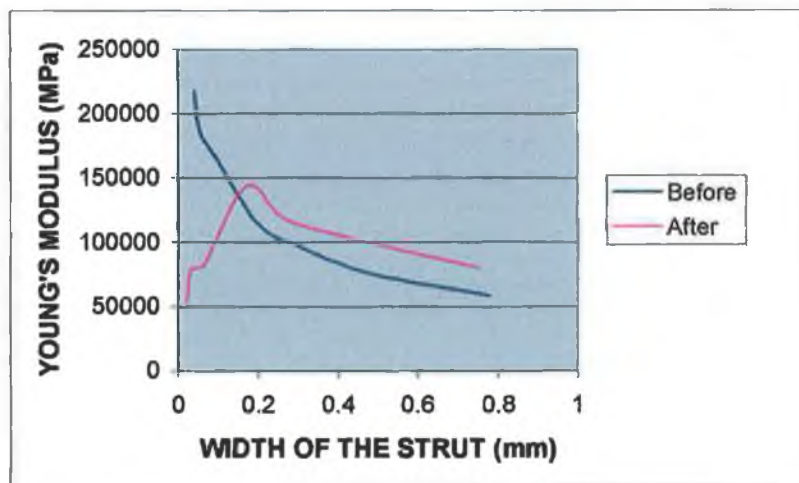


Fig.3.38 Young's Modulus versus the width of the struts before and after electro-polishing.

V.4 EXPERIMENTAL RESULTS FOR ANNEALED SPECIMENS

The specimens were preheated at 870°C for 60 minutes and then high-heated at 1025°C for 50 minutes. Finally, they were quenched in Nitrogen to 50°C. Referring to chapter one, this is a full annealing process, therefore the material becomes softer. This is due to the grain size increasing after annealing (see Chapter 5 for more detail).

Fig.3.39 shows the hardening curves obtained and a zoom on the yield stress area and the following observations can be made :

- The yield stress increases when the width decreases but when the width of the strut gets smaller than 0.1 mm the yield stress decreases suddenly, the hardening rule change and the amount of hardening increases when the width decreases.
- The breaking point decreases with the width.
- The Young's Modulus increases when the width decreases until a certain width where it starts decreasing.

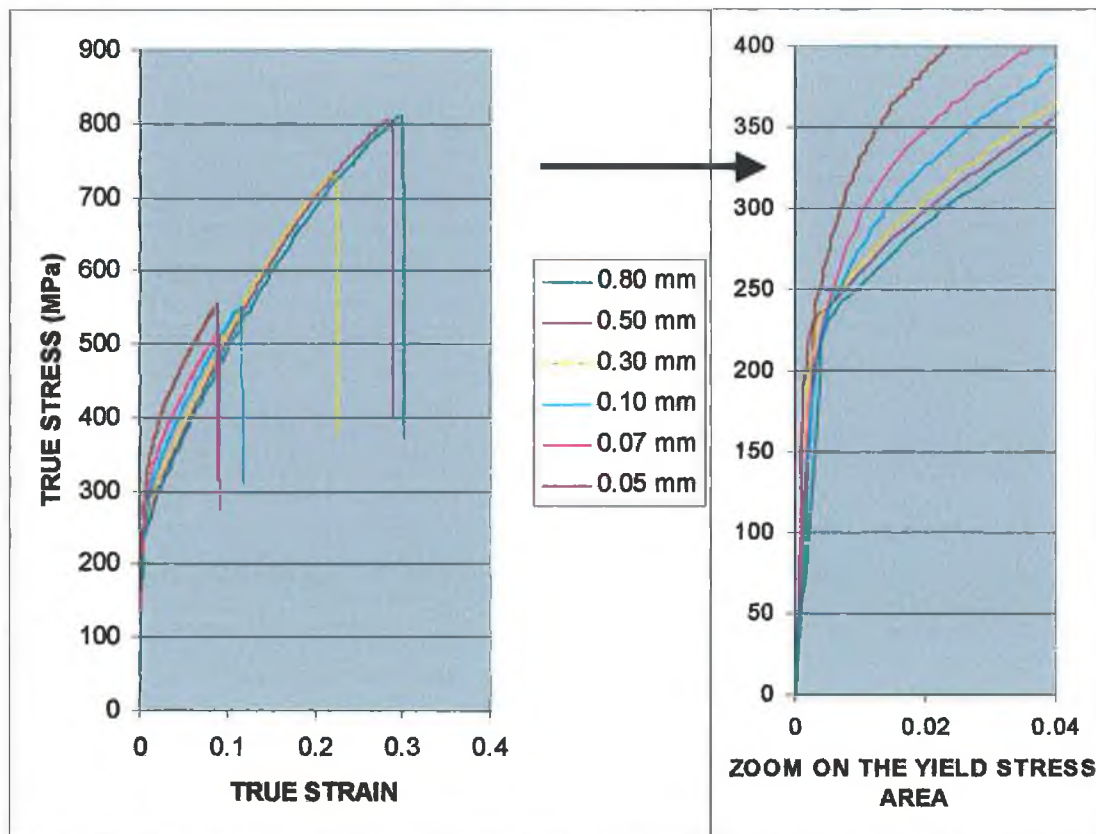


Fig.3.39 Hardening curves for annealed specimens and zoom on the yield stress area.

V.5 INFLUENCE OF ANNEALING

Fig.3.40 compares the yield stresses before annealing and after annealing. As expected the material becomes softer after annealing. Once annealed, the yield stress increases when the width decreases until the width reaches 0.1 mm then the yield stress decreases with the width until it reaches another limit and starts increasing again.

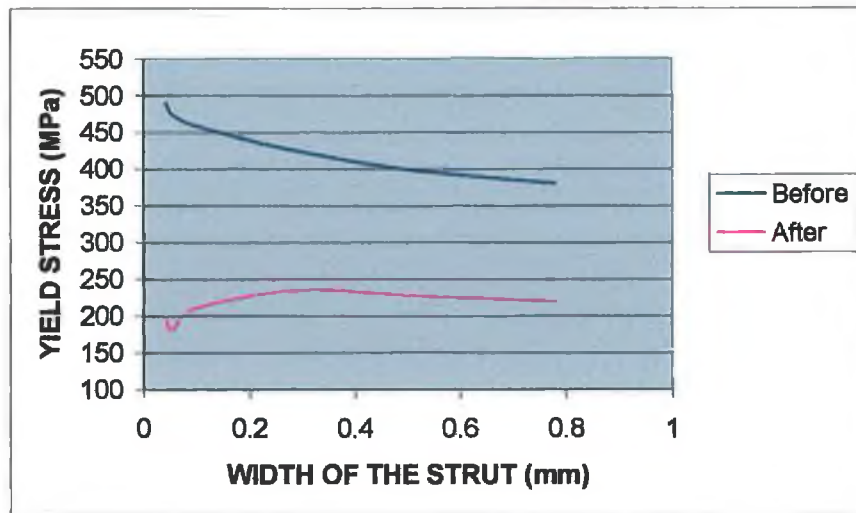


Fig.3.40 Yield stress versus the width of the strut before and after annealing.

Fig.3.41 shows that in both situations the strain at breaking point decreases with the width but the annealed struts break earlier than they did before being annealed.

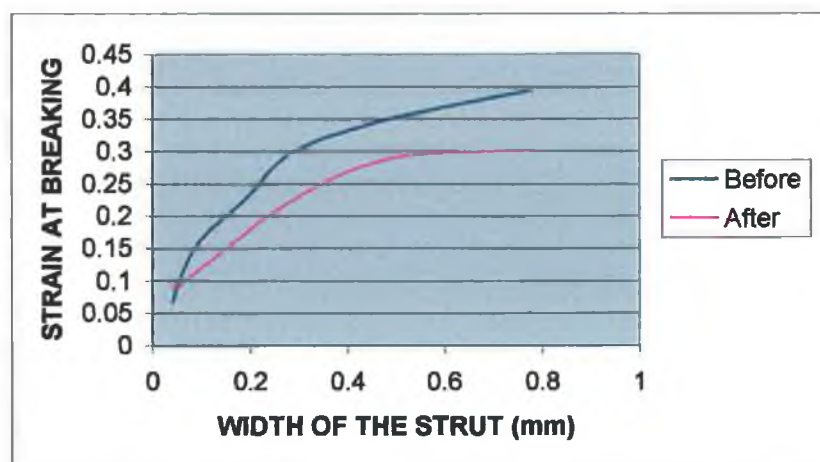


Fig.3.41 Strain at breaking versus the width of the strut before and after annealing.

Fig.3.42 shows that the maximum stress reached by the struts before breaking is lower after annealing than it was before.

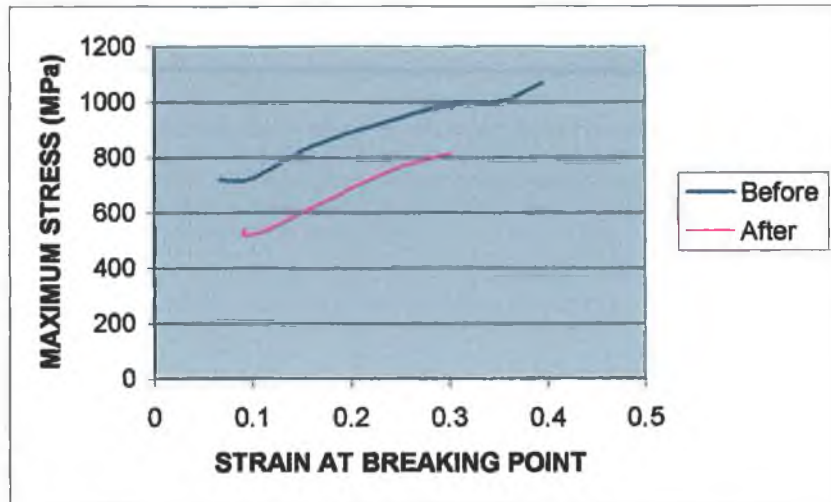


Fig.3.42 Maximum stress versus strain at breaking point before and after annealing.

Fig.3.43 shows that the Young's Modulus is not significantly influenced by the annealing process for the larger struts. However, before annealing, it keeps increasing when the width of the strut decreases whereas, after annealing it increases and then decreases.

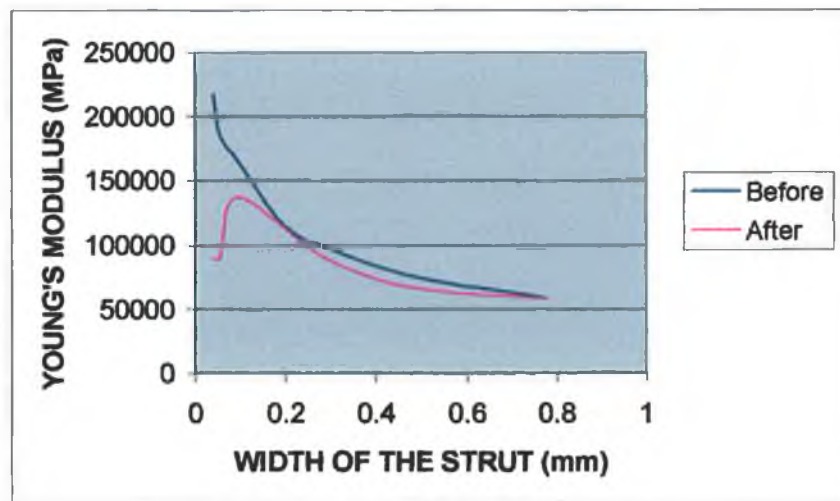


Fig.3.43 Young's Modulus versus the width of the struts before and after annealing.

VI INFLUENCE OF THE TRAPEZOIDAL SHAPE OF THE STRUTS ON THEIR MECHANICAL BEHAVIOUR

VI.1 INFLUENCE OF THE TRAPEZOIDAL SHAPE ON THE YIELD STRESS

In order to validate the results, Fig.3.44 compares curves obtained by experimentation and curves obtained by F.E.A for 0.05mm and 0.8mm width requested. The dimensions used to create the F.E.A. model are the ones presented in Table 3.1 page 85 and the hardening curve used is the one plotted using the data measured for the 0.8 mm wide strut. Observing Fig.3.44, the following points are noted:

- The slightly trapezoidal shape of the 0.8 mm does not have any influence on the behaviour since the 0.8 mm F.E.A curve and the material model curve are superimposed.
- The experimental curves for the 0.8 mm are close to the F.E.A. results which proves the validity of the model.
- The experimental curves from the 0.05 mm are far from the F.E.A results. Where the F.E.A results predicted a decrease of the yield stress, the experimental results show an increase and where the stress for a given strain was to decrease, the experimental results show an increase.

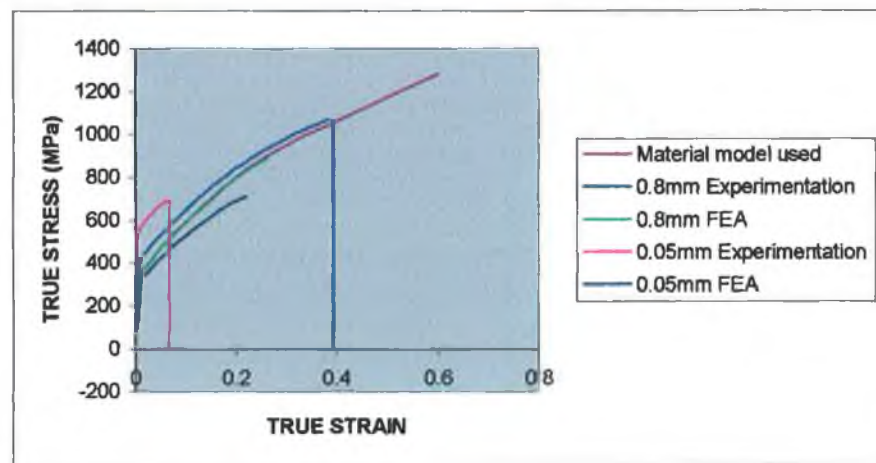


Fig.3.44 Comparison between experiment and F.E.A..

In conclusion the stress gradient created by the trapezoidal shape of the struts, according to the F.E.A., modifies the mechanical behaviour of the specimens by reducing their yield stress. However, the experimentation shows the yield stress increasing. Hence the inaccuracy of laser-cutting is not the reason for the increase of the yield stress when the width of the struts decreases.

VI.2 INFLUENCE OF THE TRAPEZOIDAL SHAPE ON THE BREAKING POINT

The trapezoidal shape creates a stress concentration at the smaller extremity of the strut. Fig.3.45 illustrates the stress concentration using F.E.A.

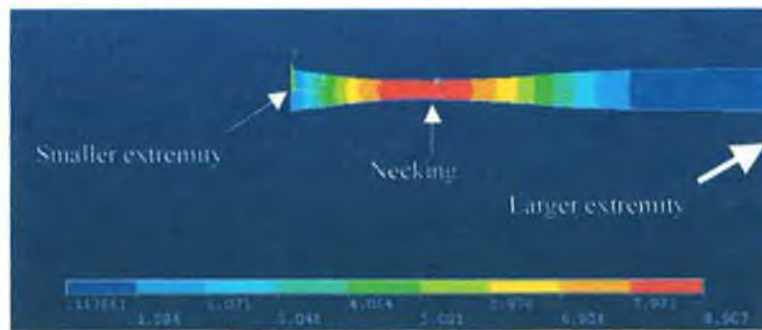


Fig.3.45 F.E.A representation of the necking at the smaller extremity of the strut.

Fig.3.46 shows the stress vs. time at three different points along the strut for the 0.05mm strut presented in Table 3.1. The smaller extremity being clamped the breaking point, (necking), is located slightly before the extremity. Whereas the stress at the larger extremity never get passed 700 Mpa, the stress at the smaller extremity reached 1000 Mpa. This is almost a 50% increase in stress and not the 17% expected from the calculation in Table 3.1. This is due to the elastic-plastic transition, which is reached at different times depending on the location along the strut. This implies that the maximum stress is attained earlier at the smaller extremity and therefore the strut breaks even if the global stress has not reached the maximum stress.

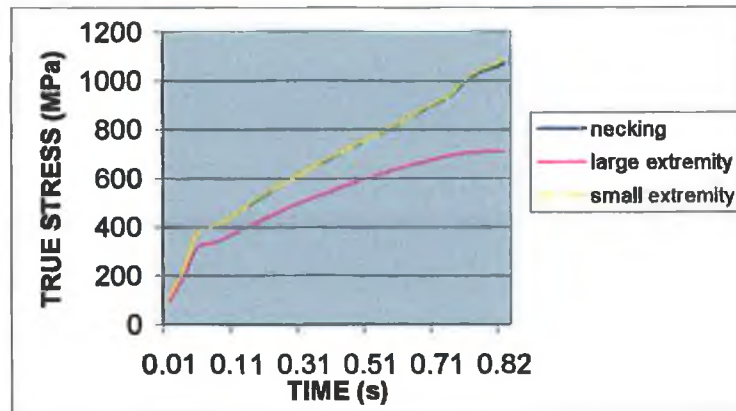


Fig.3.46 Stress vs. time at three different points along the strut.

In order to explain the breaking point decreasing with the width, Fig.3.47 shows the strain vs. time curve corresponding to the values shown in Fig.3.46. It is clear, from the curves, that when the strain measured by the machine (or global strain) is around 25%, the strain at necking is already around 40%. 40% is the strain at breaking point given by the supplier which explains why the strut breaks at this stage.

Table 3.1 showed how the width expansion along the strut, (due to inaccuracy), becomes progressively insignificant with the increase of the width. When the difference between the two extremities of the strut becomes progressively negligible, the global strain draws towards the strain at necking. This explains why the global strain at breaking point increases with the width of the strut.

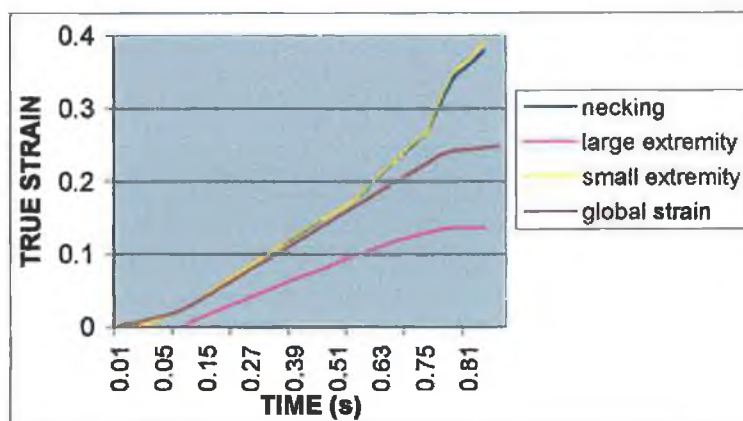


Fig.3.47 Strain vs. Time at three different points along the strut.

VII CONCLUSION

The influence of the width of laser-cut struts on the tensile behaviour has been identified :

- The Young's Modulus increases when the width decreases.
- The yield stress increases when the width decreases.
- The breaking point decreases when the width decreases.

The changes due to electro-polishing have also been studied :

- For the larger struts, the Young's Modulus is higher after electro-polishing but follows the same pattern as before electro-polishing. When the width of the strut gets smaller than 0.2 mm, the Young's Modulus increases and then decreases.
- The yield stress is not affected by the manufacturing process for wide struts. It is constant for the wider struts, but when the struts get narrower than 0.2 mm, as observed for the Young's Modulus, the yield stress increases and then decreases.
- The breaking point still decreases with the width. It is not affected by the manufacturing process for the wider struts but it is for the narrower ones

Finally, after annealing the following changes were observed :

- The Young's Modulus is not significantly influenced by annealing for the wider struts. However, before annealing, it keeps increasing when the width of the strut decreases whereas, after annealing, it increases and then decreases.
- The material becomes softer. The yield stress increases when the width decreases until the width reaches 0.1 mm then the yield stress decreases with the width until it reaches another limit and starts increasing again.
- The strain at breaking point still decreases with the width.

By measuring the specimen after laser cutting, it was noted that the specimens are not straight but have a trapezoidal shape. Failing to improve the accuracy of the cut, the consequences of this shape were studied. It was shown that the increase of the yield stress when the width decreases was not caused by the shape of the specimens. However, the shape of the specimen creates a stress concentration at one extremity, therefore the average stress and strain calculated at breaking are not representative of the material.

In order to better understand these results, a study of the microstructure will be conducted in Chapter 5.

CHAPTER 4 : BENDING BEHAVIOUR

I INTRODUCTION

The aim of this study is to identify the factors influencing the mechanical behaviour of small devices such as stents. Chapter 3 was dedicated to the tensile behaviour. The tensile test conducted on struts laser-cut in tubes used for the manufacturing of stents has led to the following conclusions :

- The yield stress and Young's Modulus increase when the width of the struts decreases.
- The strain at breaking decreases with the width but this could be a consequence of the trapezoidal shape of the struts (consequence of the inaccuracy of the laser cutting process).

A study of the effect of electro-polishing on the mechanical behaviour showed that :

- The mechanical behaviour is not significantly affected by electro-polishing when the struts are wider than 0.2 mm.
- For smaller struts, both Young's Modulus and yield stress increase and then decrease when the width decreases. The strain at breaking still decreases but follows a different pattern than before electro-polishing.

Finally, the influence of annealing was studied and it was shown that :

- After annealing, the material becomes softer and the yield stress increases when the width decreases until the width reaches 0.1 mm then the yield stress decreases with the width until it reaches another limit and starts increasing again. The strain at breaking still decreases with the width.
- As observed, after electro-polishing the Young's Modulus increases and then decreases.

This chapter deals with the bending behaviour which was shown to be of prime importance for the manufacturer.

- A three-point bending apparatus developed will be presented but shown to be inadequate for this study.

- The apparatus eventually used is described as well as the specimen design. The tensile test specimen are used after removing the parts of tube left-over after laser cutting.
- The method for the inverse identification of the mechanical properties of the struts is, then, explained.
- As in Chapter 3, the influence of the width and mechanical processes is studied.
- Tensile and flexure behaviour are also compared.

II EXPERIMENTATION

II.1 TEST DEVELOPED FOR THE MICRO TENSILE TESTER

The micro-tensile tester used for the tensile test being the only equipment available in G.M.I.T, an apparatus was developed by the author to test the specimen in bending (Fig.4.1).

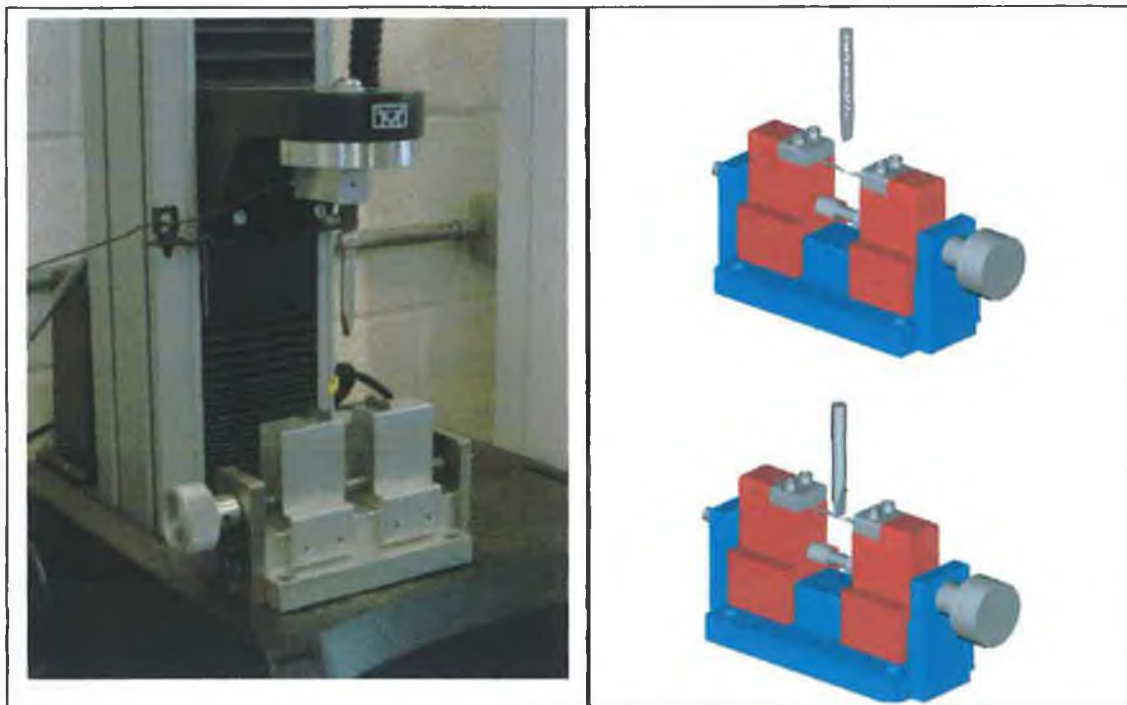


Fig.4.1 Bending apparatus developed for the micro-tensile tester.

The specimen can either be clamped as shown on Fig.4.2 (a) or just supported on each side by removing the grey parts clamping the tubes as shown on Fig.4.2 (b).

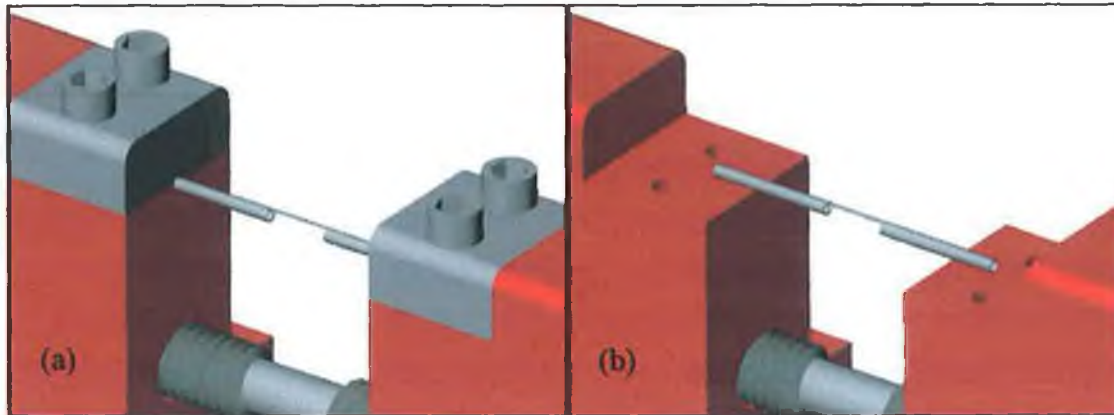


Fig.4.2 The apparatus is designed to (a) clamp the specimens or just (b) support them.

The distance between the supports is adjustable using the wheel (Fig.4.3). The wheel makes the screws inside the support turns. The threads of the screws are inversed such as the supports move in opposite directions, therefore staying at equal distance from the centre. This feature allows testing of specimen of different lengths.

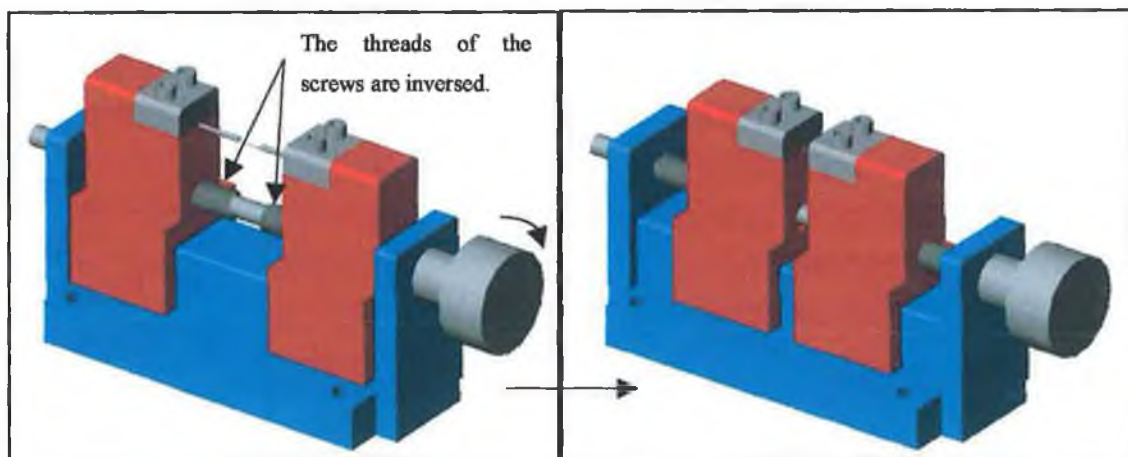


Fig.4.3 The supports move when rotating the wheel.

Firstly, specimens clamped each side (Fig.4.2 (a)) were tested and the curves on Fig.4.4 were obtained.

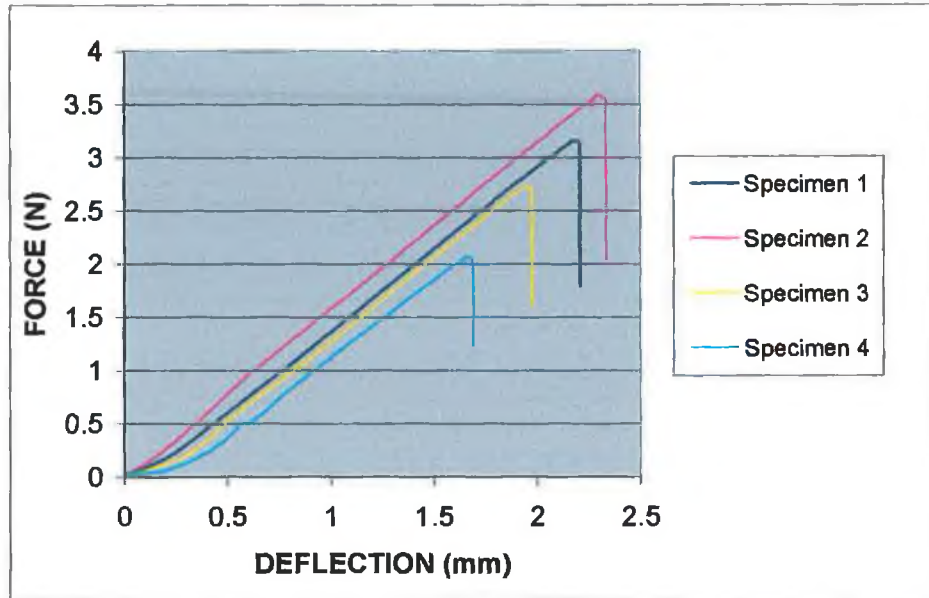


Fig.4.4 Force versus deflection curves obtained from bending a specimen clamped at both extremities.

The F.E.A simulation on Fig.4.5 shows that, the end tubes being clamped, the strut has to stretch in order to be able to bend. The strut is smaller before (a) than after bending (b). Therefore, the strut is subjected to tension as well as to bending.

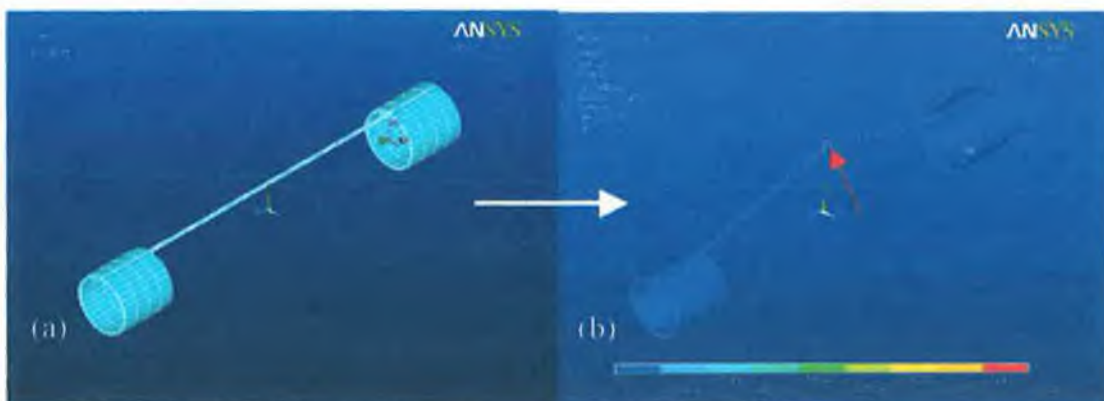


Fig.4.5 F.E.A simulation of the strut before bending (a), after bending (b).

The strain due to bending is negligible compare to the strain due to tension. It is therefore impossible to identify the bending behaviour from this test.

The next solution was to use the apparatus as a support, the test becoming a typical three-point bending test. Considering the small forces and deflection involved the accuracy of the results could not be guaranteed. Subsequently, we managed to get access to a Dynamic Mechanical Analyser (DMA) which is designed for this application, therefore the development of a bending apparatus for the micro tensile tester was abandoned.

II.2 DYNAMIC MECHANICAL ANALYSER

The machine used is the TA instruments DMA 2980 in the NCBES, NUIGalway. A DMA measures the mechanical properties of a material as a function of time and temperature. The DMA features an air bearing for frictionless motion, a high resolution optical encoder to detect low strain. The DMA was chosen for its ability to accurately measure very small forces and displacement. During the test, the apparatus is enclosed in a chamber avoiding any interference from the outside (Fig.4.6).



Fig.4.6 Picture of the Dynamic Mechanical Analyser DMA in NCBES, NUIGalway.

Fig.4.7 shows the three-points bending apparatus used. The distance between the supports is 5 mm.



Fig.4.7 Three-points bending apparatus

II.3 MEASUREMENTS

The DMA is linked to a computer (Fig.4.8) enabling the user to control the speed and frequency of the measurements.



Fig.4.8 Computer linked to the DMA.

Input

The software used is called Thermal Advantage. The different input available are shown in Fig.4.9. The interesting input here is the speed chosen to be 0.1 N/min, the temperature is constant and the test is stopped automatically at rupture.

The screenshot shows the 'Procedure Information' and 'Method' sections of the software. The 'Test' is set to 'Stress/Strain'. The 'Notes' field contains the text: 'Material is held isothermally and exposed to ramping (linearly increasing) force (stress) and the resultant deformation (strain) is'. The 'Method' section includes the following parameters:

Parameter	Value	Unit
Preload force:	0.010	N
Isothermal temperature:	20.00	°C
Soak time:	0.01	min
Force ramp rate:	0.100	N/min
Upper force limit:	18.000	N

Buttons for 'Advanced...', 'Post Test...', 'Run 1', 'Append Run', 'Apply', 'Undo', and 'Help' are also visible.

Fig.4.9 Input of the speed and criteria to end the test.

Measurements

The DMA measures the force applied and the displacement of the head. Data requested may be plotted simultaneously. Fig.4.10 shows stress and strain calculated by the software and plotted simultaneously as a function of time. The software is able to calculate stress and strain for basic geometries. In the context of this study, the geometry of the struts being complex, the data required are the load and deflection.

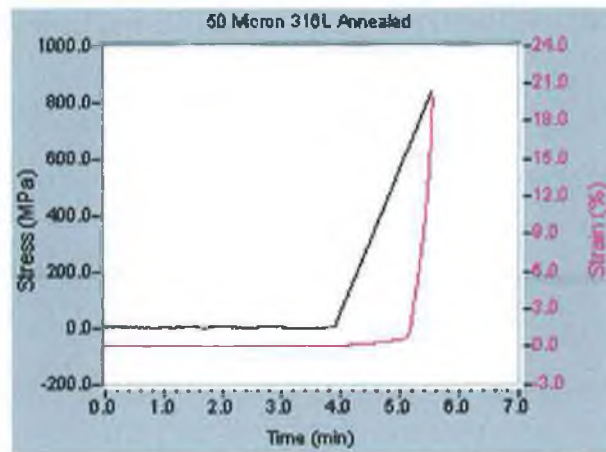


Fig.4.10 The software plots the stress and strain versus time for basic geometries.

The data measured are saved in a file readable by a software called Universal Analysis but not by Microsoft Excel. Universal Analysis allows the user to plot Static Force versus Displacement (dimension change) as shown on Fig.4.11 and save the data in a text file readable by Excel (Fig.4.12 next page).

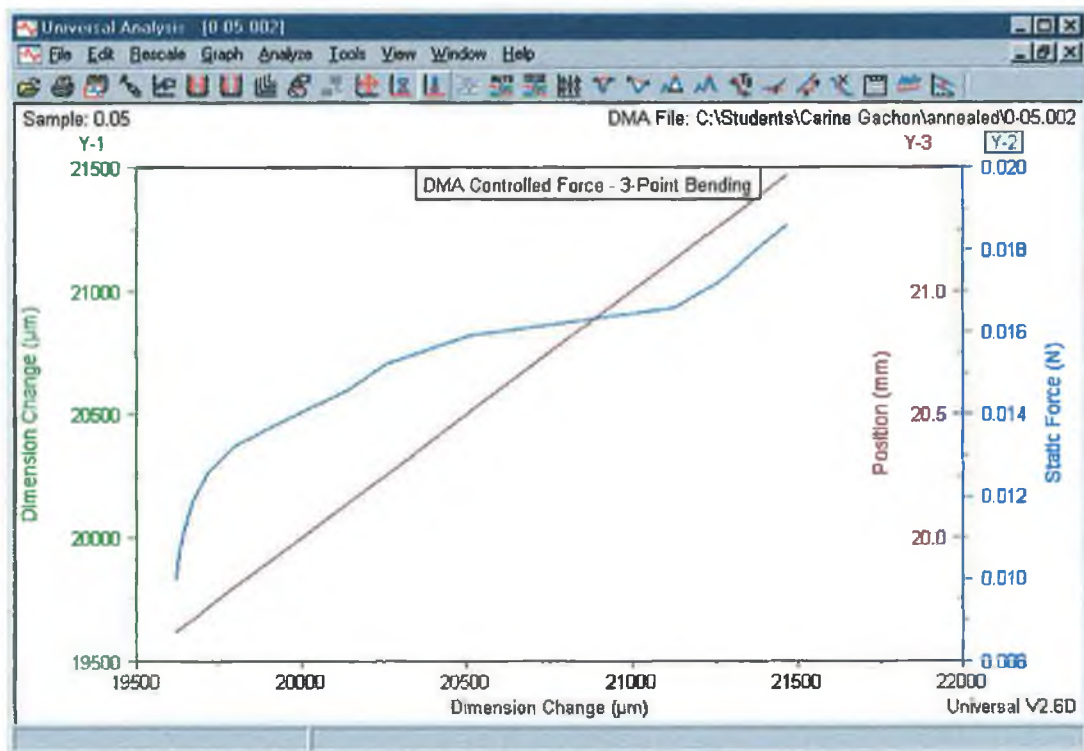


Fig.4.11 Universal Analysis converts the DMA file into a text file readable by Excel.

```

File: C:\...\Carine Gachon\annealed\0-05.002   Run Date: 4-Oct-02 14:44
Program: Universal V2.6D   Run Number: 1031

TA Instruments Thermal Analysis -- DMA Controlled Force - 3-Point Bending

Sample: 0.05
Size: 5.0000 x 0.0700 x 0.0900 mm
Operator: P.McDonnell
Method: Stress/Strain
Comment: Amplitude 10; Temp 25; Freq 1Hz; 0deg/min

Poisson's Ratio: 0.440

```

Dimension Change μm	Dimension Change μm	Static Force N	Position mm
19620.	19620.	0.01006	19.62
19630.	19630.	0.01062	19.63
19640.	19640.	0.01099	19.64
19650.	19650.	0.01133	19.65
19660.	19660.	0.01163	19.66
19670.	19670.	0.01192	19.67
19680.	19680.	0.01206	19.68
19690.	19690.	0.01220	19.69
19700.	19700.	0.01234	19.70
19710.	19710.	0.01248	19.71
19720.	19720.	0.01260	19.72
19730.	19730.	0.01268	19.73
19740.	19740.	0.01276	19.74
19750.	19750.	0.01284	19.75
19760.	19760.	0.01292	19.76
19770.	19770.	0.01300	19.77
19780.	19780.	0.01308	19.78
19790.	19790.	0.01316	19.79

Fig.4.12 Text file created by Universal Analysis.

II.4 SPECIMEN DESIGN

In order to compare tensile and bending behaviour, the specimens used for bending have to be the same as the ones used for the tensile tests. The part of tube left over each side of the strut has to be removed to stop the strut from bending under their weight (Fig.4.13).



Fig.4.13 Strut bending under the weight of the left over part of tubes.

Therefore, before positioning the specimen on the apparatus the pieces of tubes as well as the stiffening bars are cut out leaving only the strut.

II.5 POSITIONING OF THE SPECIMEN

The specimen is positioned manually on the apparatus. It is difficult to determine visually if the strut is perpendicular to the supports, as shown on the left part of Fig.4.14. If the strut is not perpendicular, as shown on the right part of Fig.4.14, the length of the strut in between the supports would be longer than 5 mm and consequently the results would be affected.

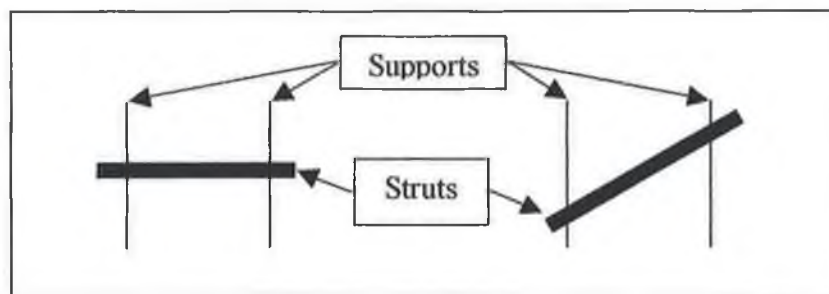


Fig.4.14 View from the top of the apparatus.

On the left, the strut is perpendicular to the supports, on the right, it is not.

The repeatability of the results shows that the method is acceptable: Fig.4.15 shows force versus deflection curves obtained for four struts of the same size and Fig.4.16 shows the interval of confidence versus deflection calculated for the results presented in Fig.4.15.

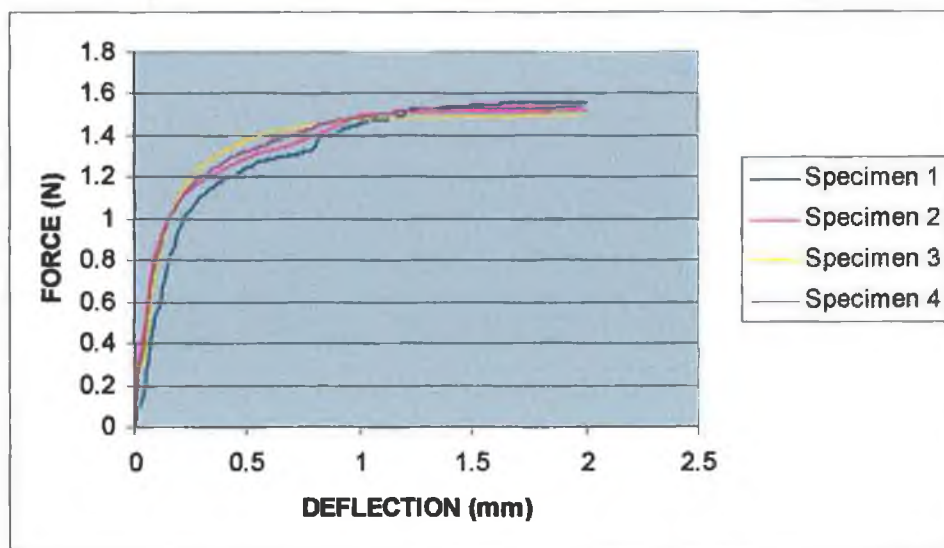


Fig.4.15 Force versus deflection curves obtained for four specimens of the same size.

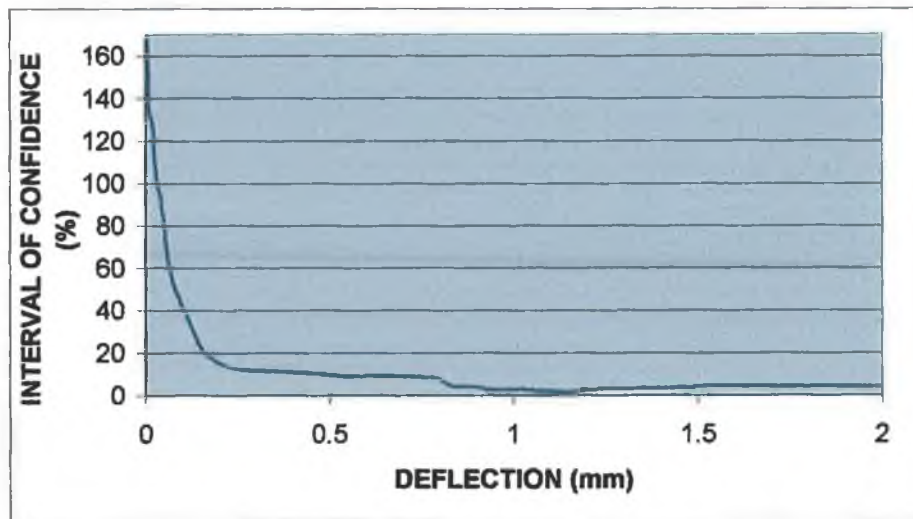


Fig.4.16 Interval of confidence versus deflection.

Fig.4.16 shows that, under 0.5 mm, the interval of confidence is over 10 % and reaches 170% for the smallest deflection read. This is in the elastic region (as shown in Fig.4.15), therefore the results are not repeatable enough to accurately calculate the Young's Modulus. However, as a first approach, the variation of the average Young's Modulus may be studied without considering its absolute value. A different method [90][91][92] should be used to confirm the results. For example, one method [90] uses a nano-indenter to apply the force and measure the displacement.

In the plastic region, the interval of confidence is less than 10%, therefore the curves are repeatable enough to study the plastic behaviour.

II.6 VALIDATION OF THE TEST

In order to validate the test an F.E.A analysis using ABAQUS/CAE was performed.

Modelling of the test

The first step is to create a model for the test. Due to the symmetry of the problem, only half of the test specimen is modelled (Fig.4.17). A symmetry is applied at one end of the strut and the other end (at 2.5 mm from the symmetry) the strut is in contact with the support. All the degrees of freedom of the support are suppressed and the strut is fixed on the X-axis. 3D hexahedra elasto-plastic elements are used.

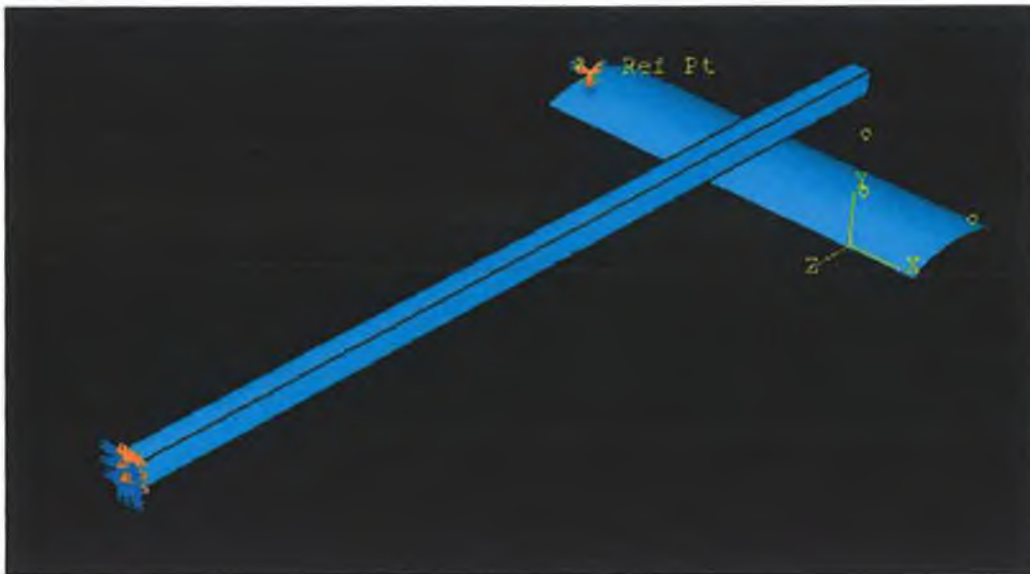


Fig.4.17 Modelling of the test.

A displacement is applied to the centre node of the symmetry (Fig.4.18). Due to their geometry, the strut and the head, applying the displacement, are only in contact at the centre node on top of the strut.

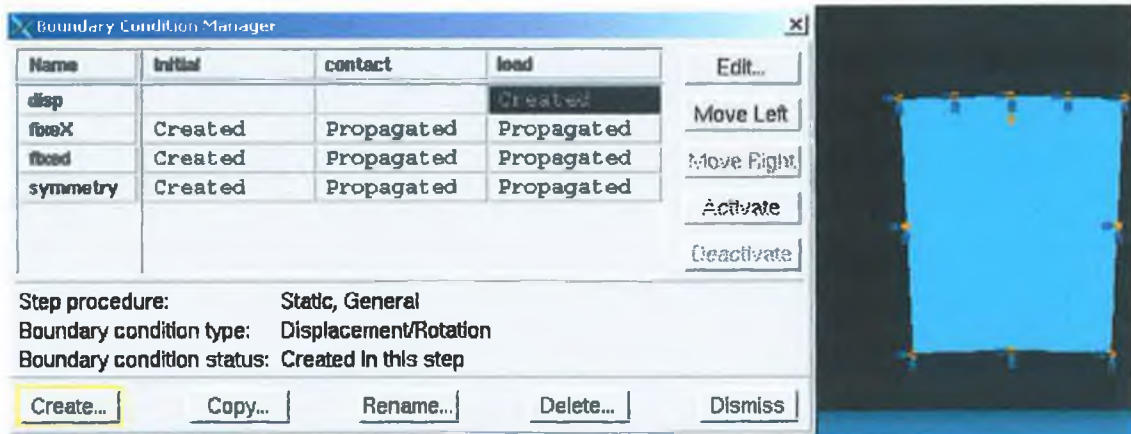


Fig.4.18 Displacement applied at the centre node on top of the strut.

Due to the geometry of the support the strut rolls on it and does not slide, therefore the contact is defined as frictionless.

Once the task is completed, the strain and stress in the strut are analysed.

Fig.4.19 shows the Von Mises stress along the strut and demonstrates that due to the geometry of the strut the stress is not only function of the position on the Z-axis but is also a function of the position on the X-axis. It is therefore difficult to measure the stress at a particular point on the strut as a function of the force applied.

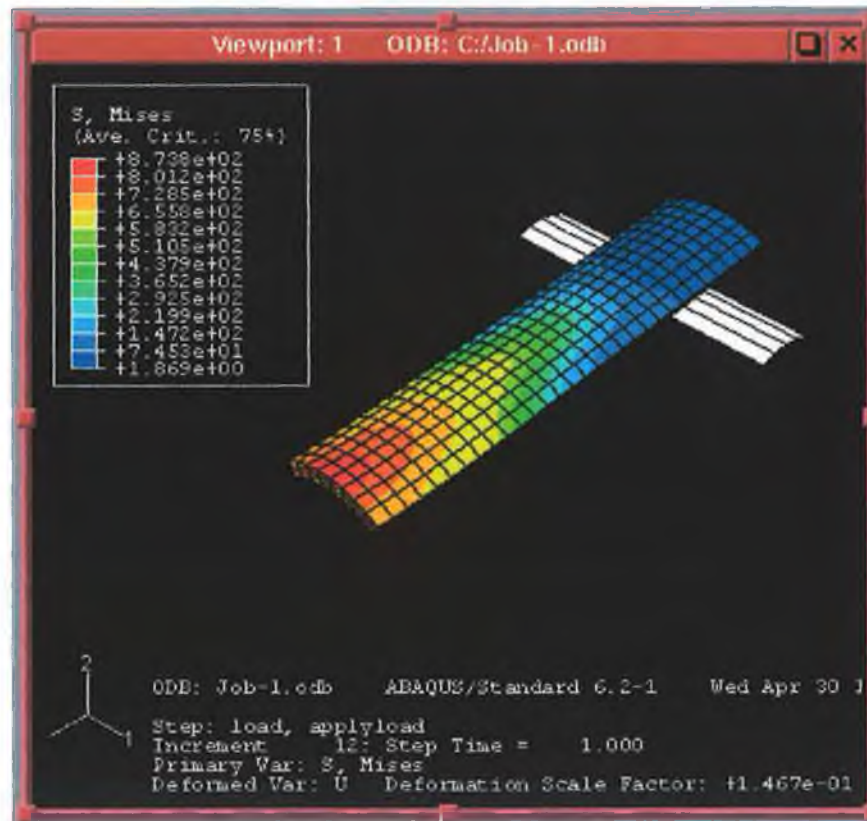


Fig.4.19 Von Mises Equivalent Stress.

Fig.4.20 (next page) shows the equivalent plastic strain and demonstrates that the plastic strain is very localised. Due to the size of the specimen it is not possible to use strain gauges and other methods of measurements such as optic methods (see Chapter 1) were not available, therefore the only way to determine the bending behaviour of the struts is to use an inverse identification as described in the next paragraph.

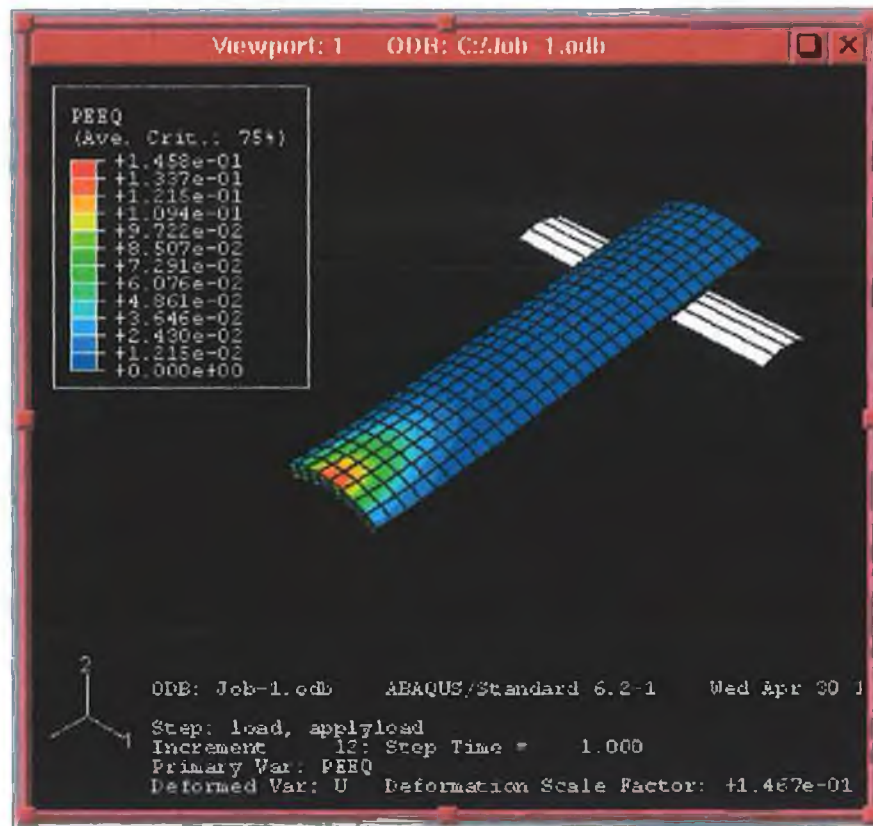


Fig.4.20 Equivalent plastic strain.

III INVERSE IDENTIFICATION

The machine records the load applied and the deflection of the beam. Due to the complexity of the plastic behaviour (Chapter 1 paragraph IV.2) and the geometry of the strut, the hardening curve has to be determined by inverse identification using F.E.A.

Algorithm of the method

Input the material properties determined from tensile test in the F.E.A model.

Compute using F.E.A package.

Extract data from F.E.A results.

Compare data to experimental results.

If the difference between F.E.A results and experimental results is smaller than 5% then stop.

If the difference is more than 5% then modify the input material properties .

Flow chart

Fig.4.21 shows the flow chart of the inverse identification method.

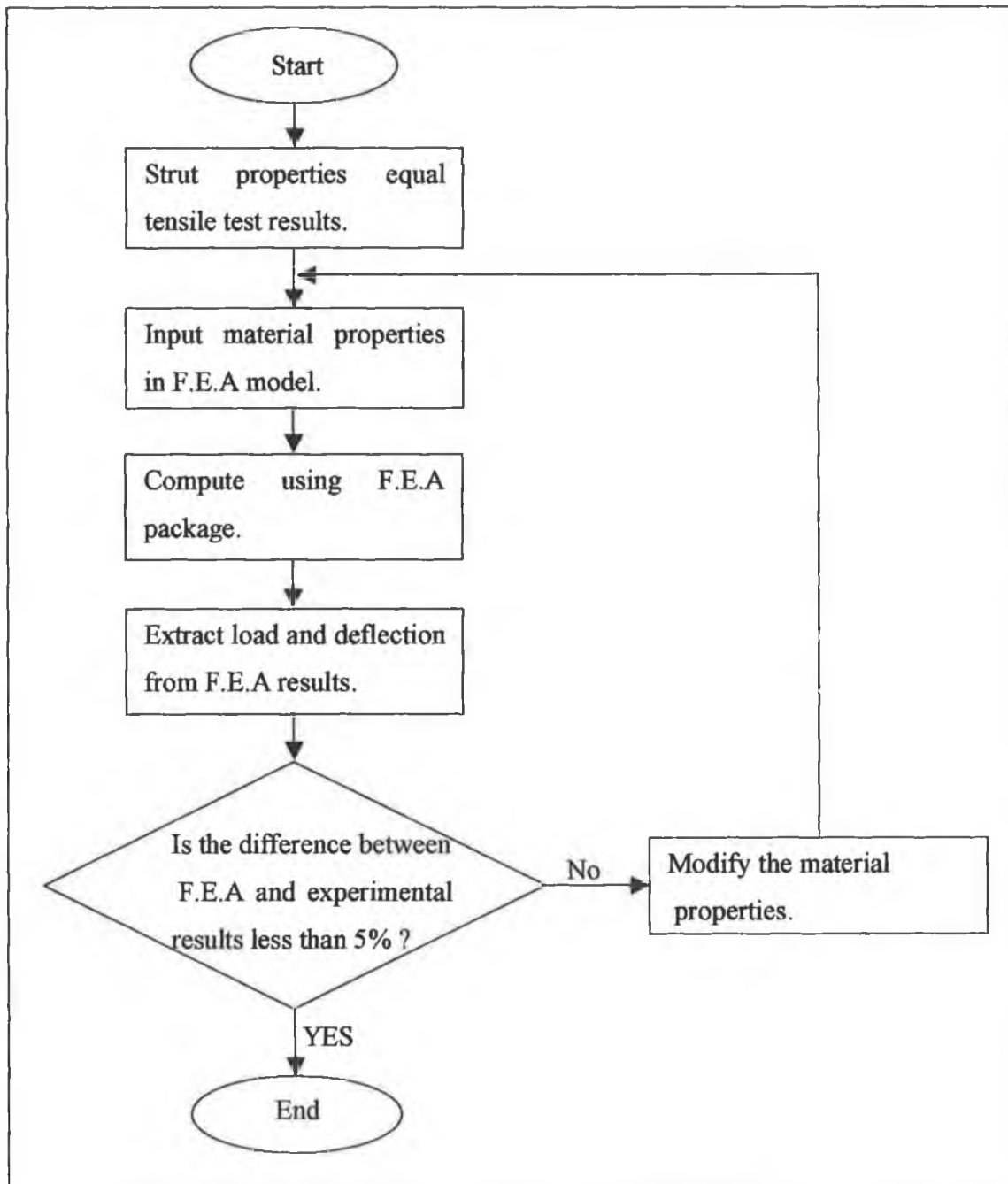


Fig.4.21 Flow chart of the inverse identification method.

Extraction of the data from the F.E.A results

Firstly, the node where the displacement was applied has to be picked in order to extract the displacement and reaction force. Fig.4.22 shows the displacement applied and Fig.4.23 shows the mesh of the strut and the same node being picked (small red circle).



Fig.4.22 Displacement applied.

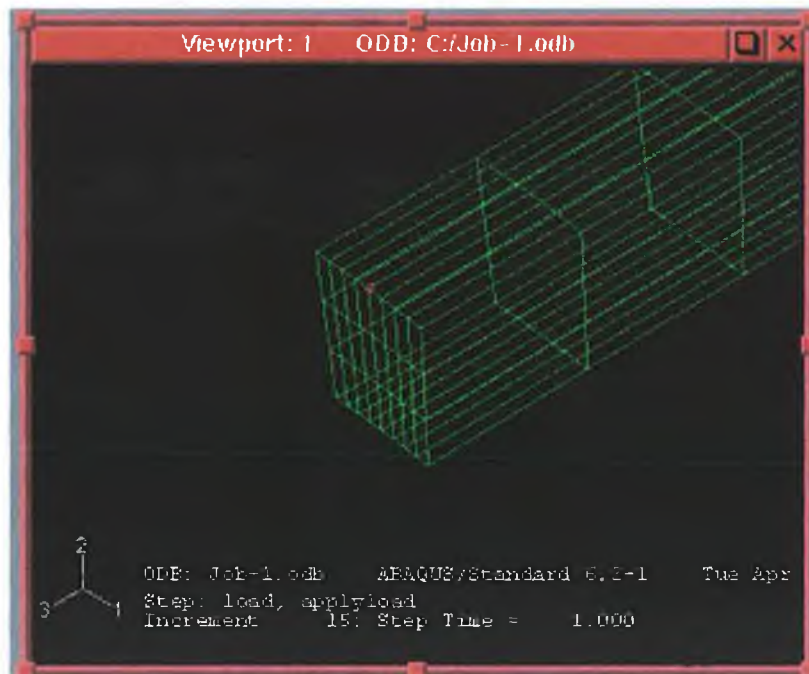


Fig.4.23 The node selected is the one where the displacement was applied.

Then, the force versus displacement on the Y axis (deflection) is plotted (Fig.4.24), the values are probed (Fig.4.25) and saved in a text file readable by Microsoft Excel.

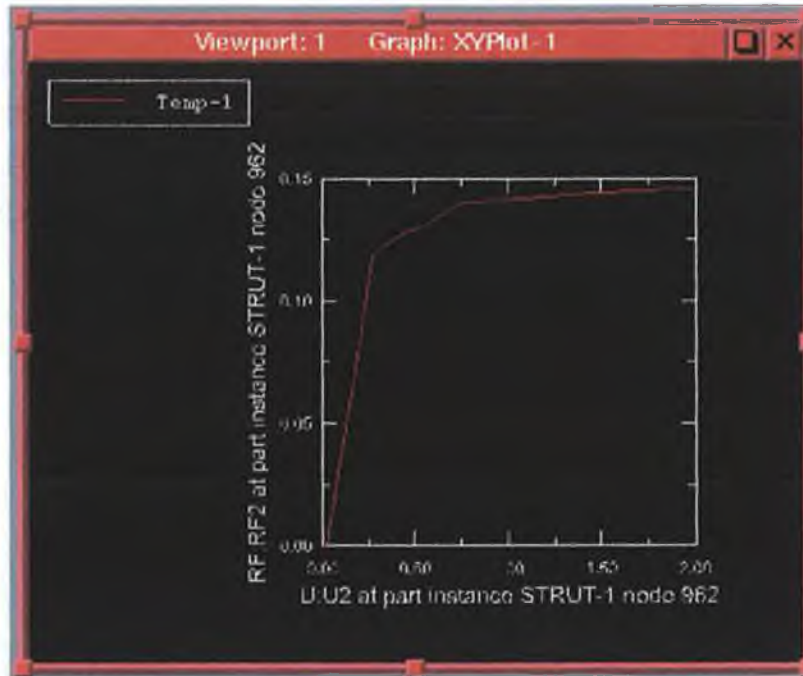


Fig.4.24 Force versus displacement on the Y axis (deflection of the beam).

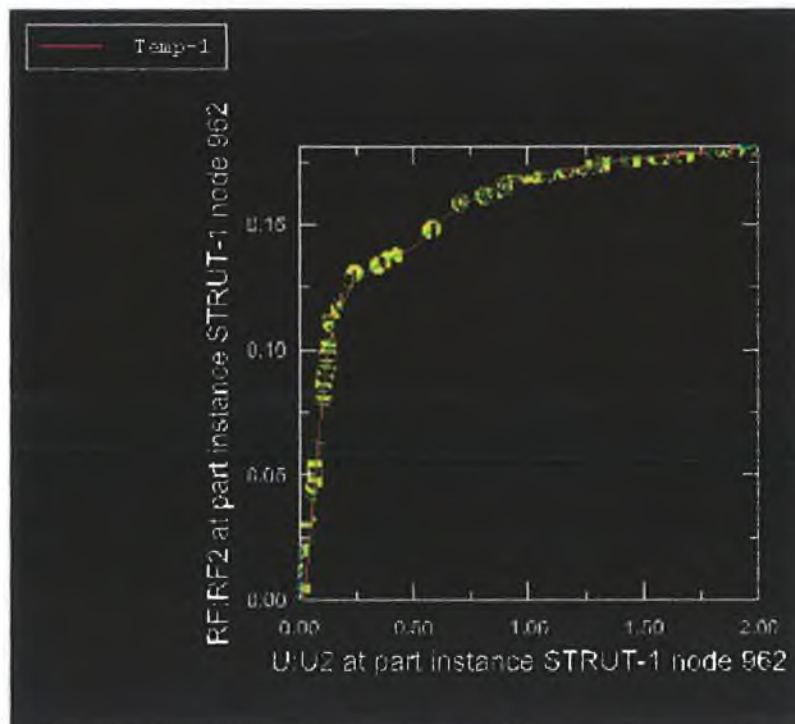


Fig.4.25 The data are probed (yellow spots on the curve).

The file is then opened with Excel and the curve is plotted on the same graph as the experimental results. The curves are compared and the material input in ABAQUS is then modified and the process is repeated until the curves match.

As an example, let's follow step by step, the inverse identification for batch 0.

The struts are 0.09 mm high, therefore the 0.07 mm and 0.05 mm wide struts are higher than wide causing them to tilt on their side (Fig.4.26). Therefore, only 0.8 mm down to 0.1 mm wide could be tested.

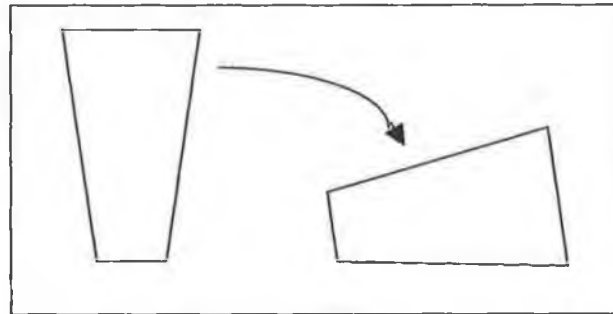


Fig.4.26 The struts tilt on their side when they are higher than wide.

0.8 mm wide struts

A hardening curve obtained from tensile testing (Table 4.1) is used as input .

Elasticity		
E=65000Mpa v =0.3	ϵ (plastic strain)	σ (stress in Mpa)
	0	386 (yield stress)
	0.031	510
	0.24	900
	0.28	1050

Table 4.1 Material identified from tensile test results.

Fig.4.27 shows the force versus deflection obtained by F.E.A compared to the experimental results. The difference between F.E.A and experimental results is more than 5%, therefore the material properties input are not correct. 65000 Mpa for the Young's Modulus is obviously erroneous and will be changed to 210000 Mpa at the next step.

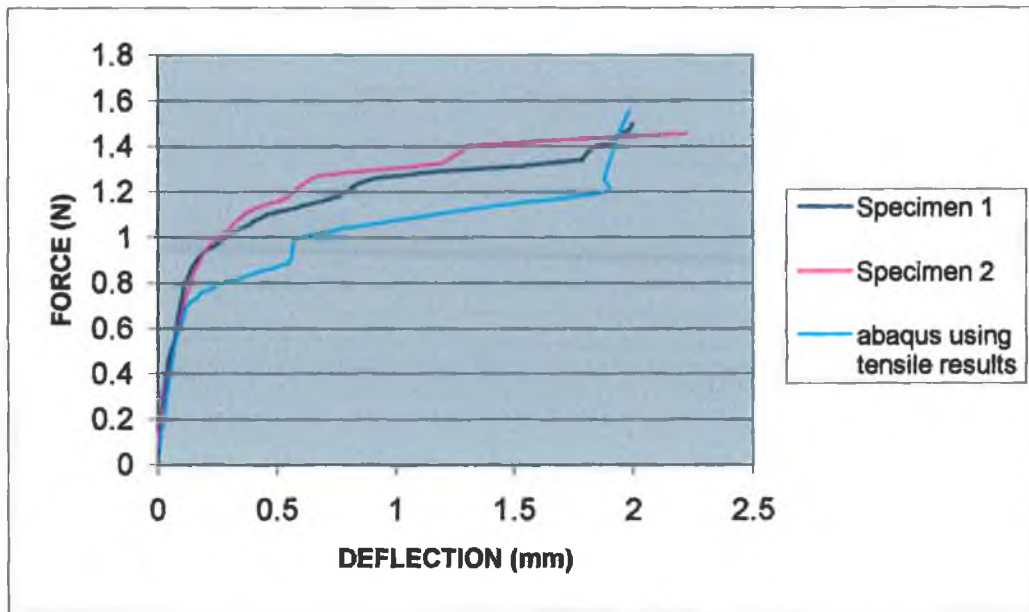


Fig.4.27 Comparison between F.E.A results, computed using tensile test results, and experimental results.

The material properties were therefore modified until a fitting curve was obtained. In the context of this study, only the Young's Modulus and yield stress are studied (the struts do not break), therefore only these two values and one value in the hardening region are modified. For larger strain the hardening is considered as insignificant. If the hardening curve was to be identified, more parameters would have to be introduced.

Fig.4.28 shows the three parameters on the hardening curve.

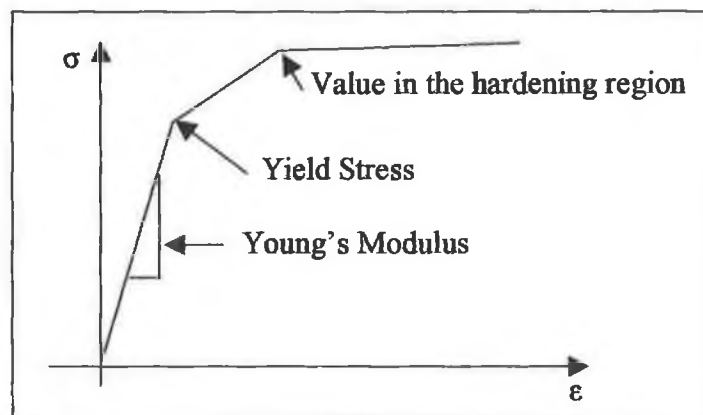


Fig.4.28 Parameters used for the inverse identification.

Table 4.2 gives the properties of the material obtained after three iterations.

Elasticity		
E=210000Mpa v =0.3	ϵ (plastic strain)	σ (stress in MPa)
	0	450 (yield stress)
	0.031	600
	0.24	601
	0.28	602

Table 4.2 Modified material properties.

Fig.4.29 shows the curve obtained. There is now less than 5% difference between experimental results and F.E.A results, therefore the process stops and the material presented in Table 4.2 is the result of the inverse identification.

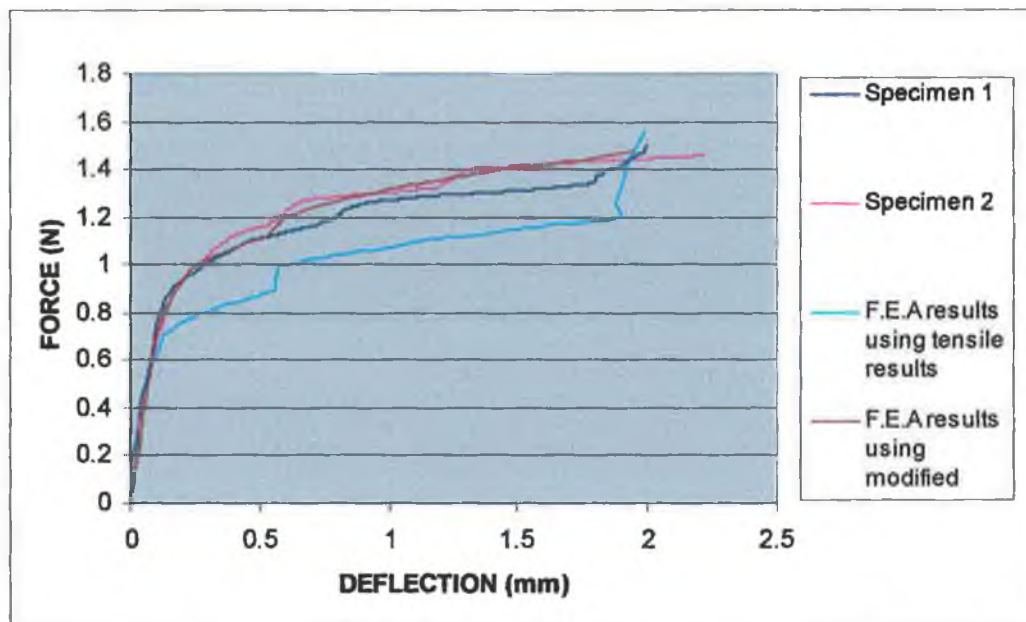


Fig.4.29 Graph showing the results obtained after modifying the material.

0.5 mm wide struts

The material determined for the 0.8 mm strut was used and the curve obtained perfectly fits the experimental results (Fig.4.30).

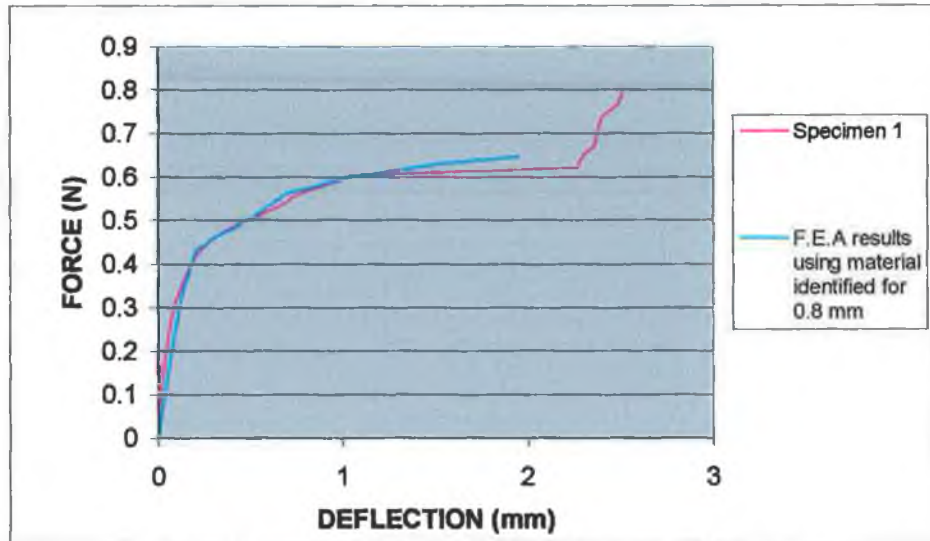


Fig.4.30 Curves obtained for 0.5 mm wide struts.

0.3 mm wide struts

The material determined for the previous width was input first and Fig.4.31 shows that the yield stress was a bit low and the maximal stress a bit high. The material was modified until the difference between F.E.A and experimental results was less than 5 %.

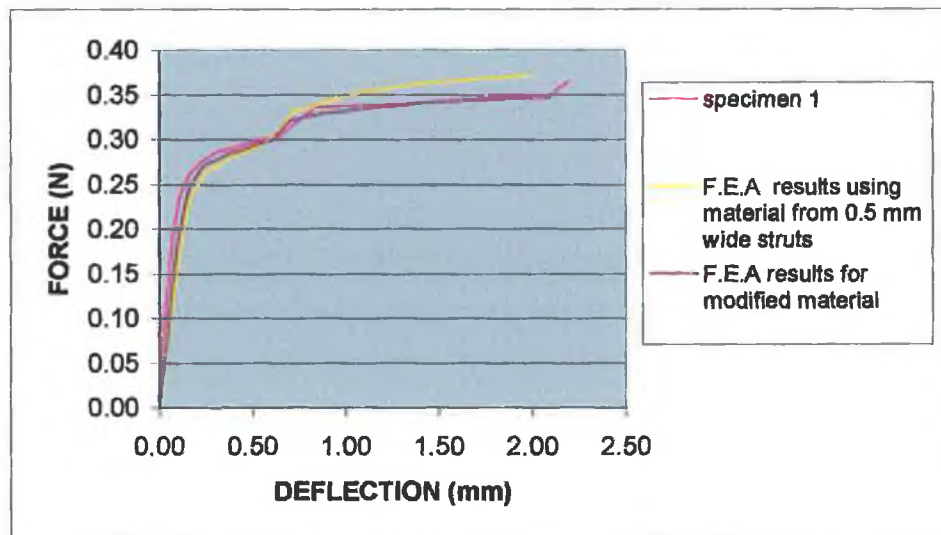


Fig.4.31 Curves obtained for 0.3 mm wide struts.

The modified material is presented in Table 4.3.

Elasticity		
E=250000Mpa v =0.3	ϵ (plastic strain)	σ (stress in MPa)
	0	475 (yield stress)
	0.031	610
	0.24	611
	0.28	612

Table 4.3 Material properties identified for 0.3 mm wide struts.

Note in Table 4.3 that the yield stress has increased as well as the Young's Modulus.

0.2 mm wide struts

Again the same process was used, the material determined for 0.3 mm was input. Fig.4.32 shows that the Yield stress and maximal stress were a bit too low, therefore the material was modified until the F.E.A results matched the experimental results.

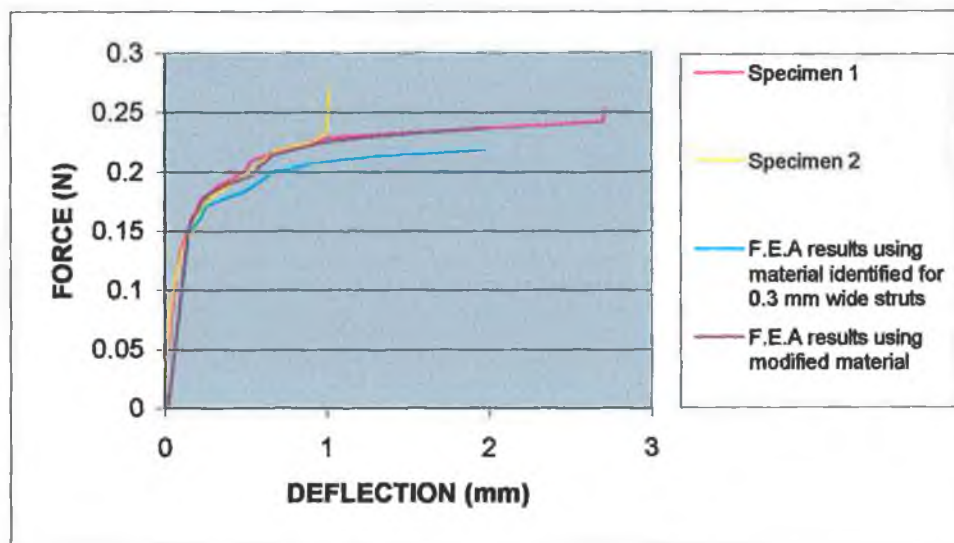


Fig.4.32 Curves obtained for 0.2 mm wide struts.

The material corresponding is presented in Table 4.4.

Elasticity		
E=250000Mpa v =0.3	ϵ (plastic strain)	σ (stressing MPa)
	0	500 (yield stress)
	0.031	615
	0.24	616
	0.28	617

Table 4.4 Material identified for 0.2 mm wide struts.

0.1 mm wide strut

Again for 0.1 mm, the material determined for 0.3 mm was input first in the F.E.A model. The yield stress once more is too low, therefore the material was modified until the F.E.A curve matched the experimental curves within 5% (Fig.4.33).

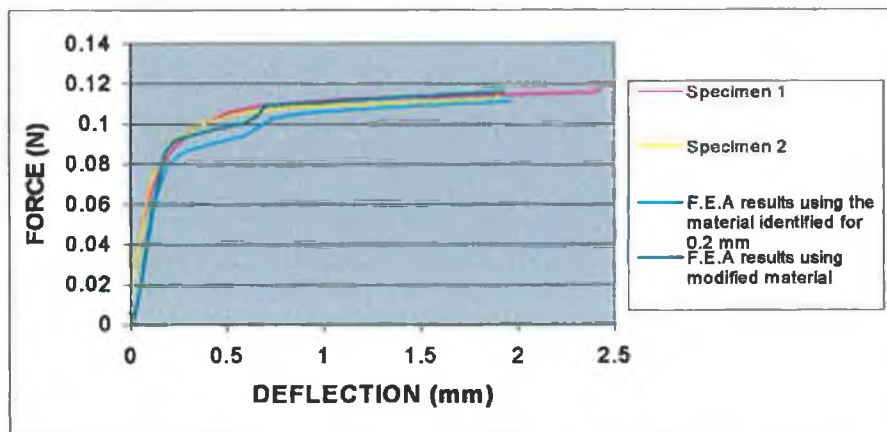


Fig.4.33 Curves obtained for 0.1 mm wide struts.

Table 4.5 shows the material obtained after modifications.

Elasticity		
E=280000Mpa v =0.3	ϵ (plastic strain)	σ (stress in MPa)
	0	550 (yield stress)
	0.031	620
	0.24	621
	0.28	622

Table 4.5 Material identified for 0.1 mm wide struts.

Hardening curves have been identified for five different widths, it is now possible to study the influence of the width of the struts on the mechanical behaviour.

IV INFLUENCE OF THE WIDTH

IV.1 INTRODUCTION

Chapter 3 showed that the width of the strut has an influence of the tensile behaviour of the material :

- The yield stress and Young's Modulus increases when the width of the struts decreases.
- The strain at breaking decreases with the width but this could be a consequence of the trapezoidal shape of the struts (consequence of the inaccuracy of the laser cutting process).

The next step is to study if the same observations can be made in bending.

The specimens used here are the ones that were kept at each stage of the tensile behaviour study, consequently the results can be compared to the hardening curves determined in tension.

IV.2 EXPERIMENTAL RESULTS FOR BATCH 0

The previous paragraph detailed how hardening curves were determined from the experimental results, here only graphs comparing the different widths will be presented (see Appendix V for all the force versus deflection curves). Fig.4.34 (next page) shows the hardening curves obtained in the previous paragraph plotted on the same graph in order to study the influence of the width.

As observed in tension, the yield stress and Young's Modulus increases when the width decreases. The strain at breaking can not be identified from this test since the struts slide from the supports before breaking.

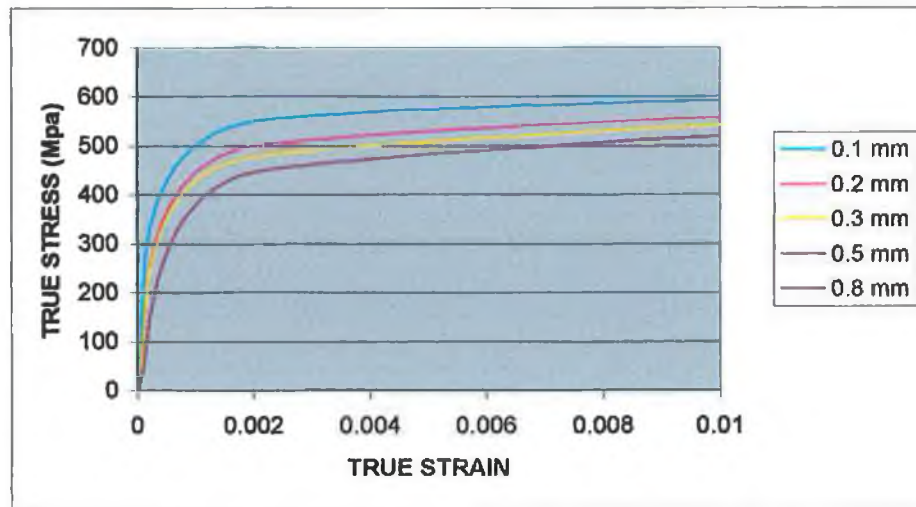


Fig.4.34 Hardening curves obtained for batch 0.

IV.3 TENSILE VERSUS BENDING BEHAVIOUR FOR BATCH 0

Fig.4.35 shows the yield stress versus the width of the strut in tension and bending.

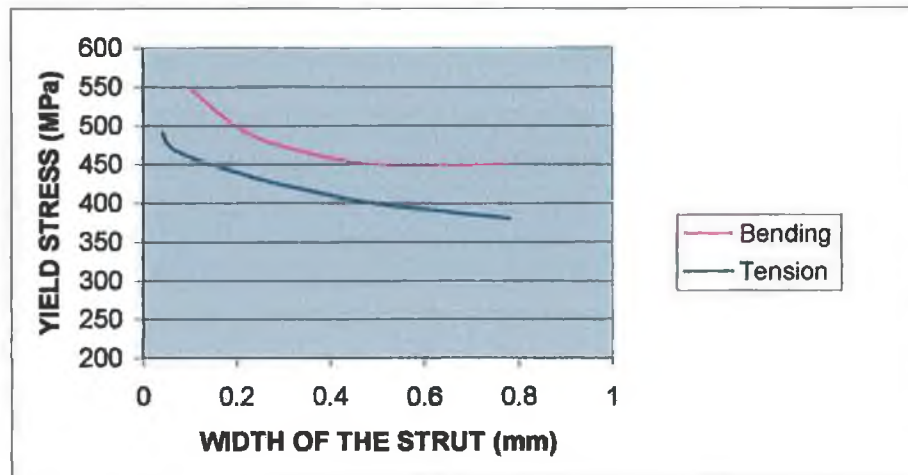


Fig.4.35 Yield stress versus the width of the strut in tension and bending.

Both in tension and bending, the yield stress increases when the width decreases. However, the yield stress is higher in bending. This could be explained by the strain gradient plasticity theory presented in Chapter 1 paragraph III.4. Bending creates a strain gradient in the width that was not present in tension. Due to the size of the struts this strain gradient could be significant and increase the yield stress in bending.

Fig.4.36 shows that the increase varies between 12 and 20 %.

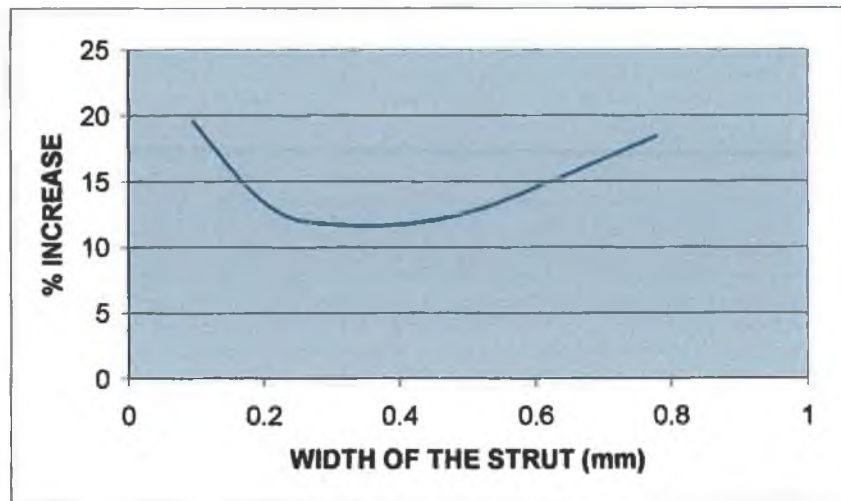


Fig.4.36 % increase of the yield stress from tension to bending versus the width of the strut for batch 0.

Fig.4.37 shows the Young's Modulus versus the width of the strut in tension and bending.

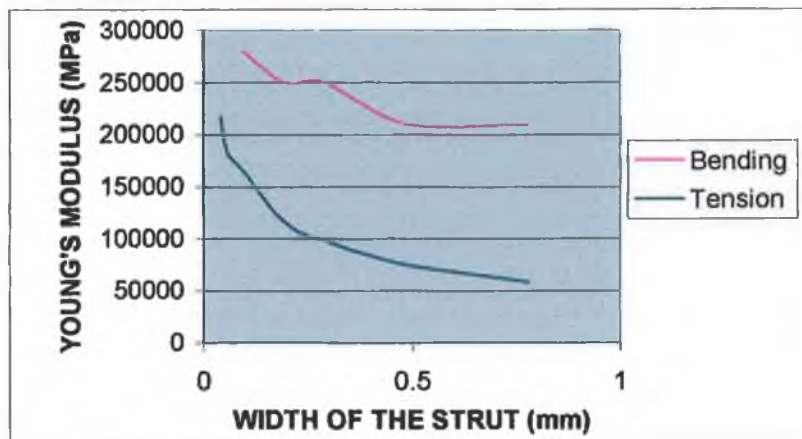


Fig.4.37 Young's Modulus versus the width of the strut in tension and bending.

Fig.4.37 shows that in both tension and bending the Young's Modulus increases when the width decreases. Due to lack of repeatability of the experimental results, the values obtained are not to be compared. However, the Young's Modulus calculated in bending are closer to the 210000 MPa expected for a steel than the values resulting from the tensile test.

IV.4 EXPERIMENTAL RESULTS FOR BATCH 2

Due to time constraint and limited access to the machine only batch 2 was tested in bending. Fig.4.38 shows the hardening curves obtained in bending for batch 2.

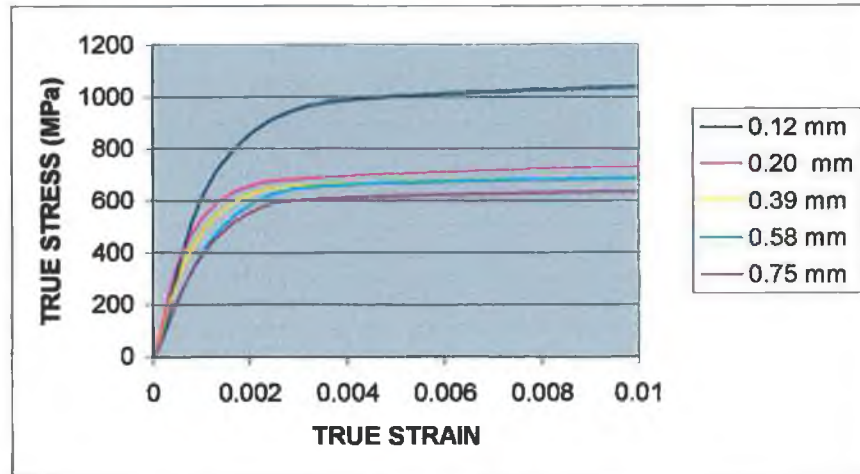


Fig.4.38 Hardening curves obtained for batch 2.

IV.5 TENSILE VERSUS BENDING BEHAVIOUR FOR BATCH 2

Fig.4.39 shows that, as for batch 0, the yield stress increases when the width decreases and is higher in bending than in tension.

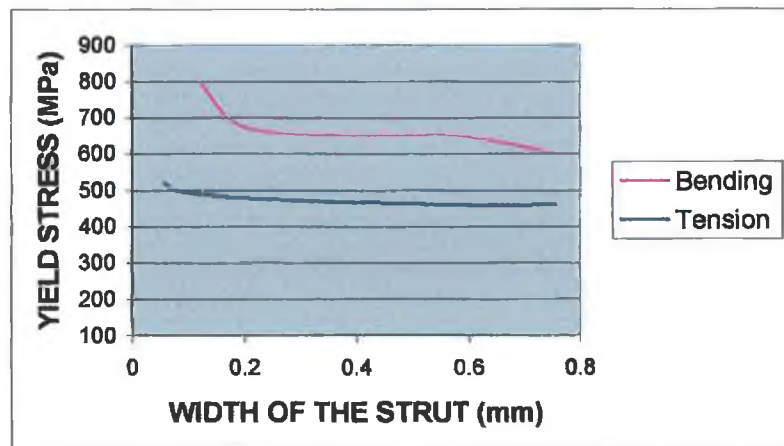


Fig.4.39 Yield stress versus the width of the strut in tension and bending for batch 2.

Fig.4.40 shows the Young's Modulus versus the width of the strut in tension and bending.

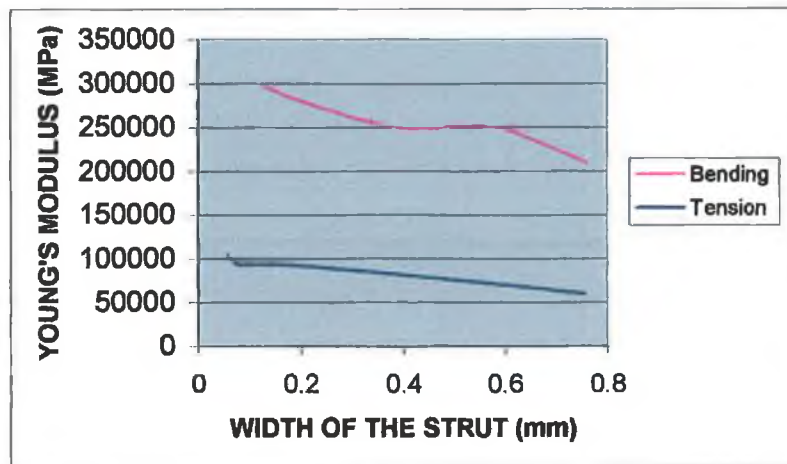


Fig.4.40 Young's Modulus versus width of the strut in tension and bending for batch 2.

As in tension, the Young's Modulus (σ/ϵ) increases when the width decreases but the Young's Modulus calculated in bending seems more realistic than in tension (Fig.4.40). It is important to remember that the values calculated are not accurate.

IV.6 COMPARISON BETWEEN BATCHES

For both batches, the yield stress increases when the width decreases but as observed in tension the yield stress of batch 2 is higher than the yield stress of batch 0 (Fig.4.41).

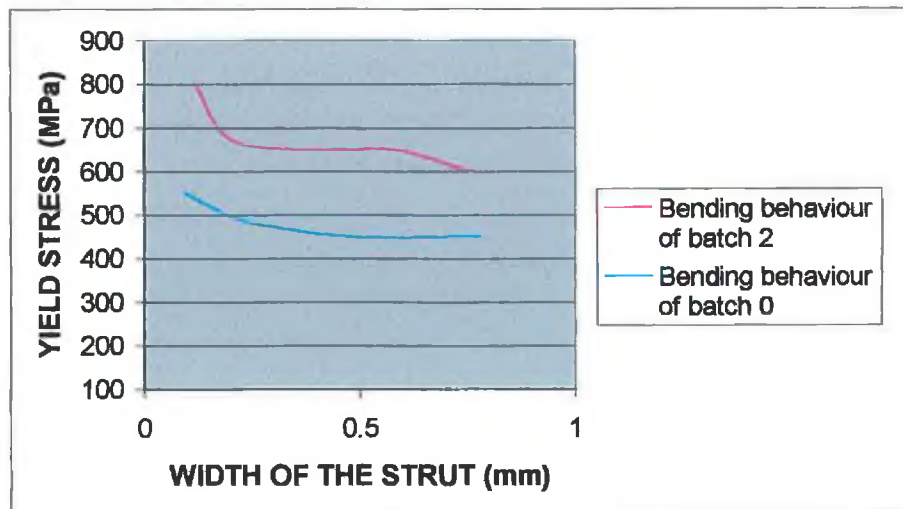


Fig.4.41 Yield stress versus width of the struts for batch 0 and 2.

For both batches, the yield stress is higher in bending than in tension, however, the increase of the yield stress from tensile to bending behaviour is greater for batch 2 than for batch 0 as shown in Fig.4.42.

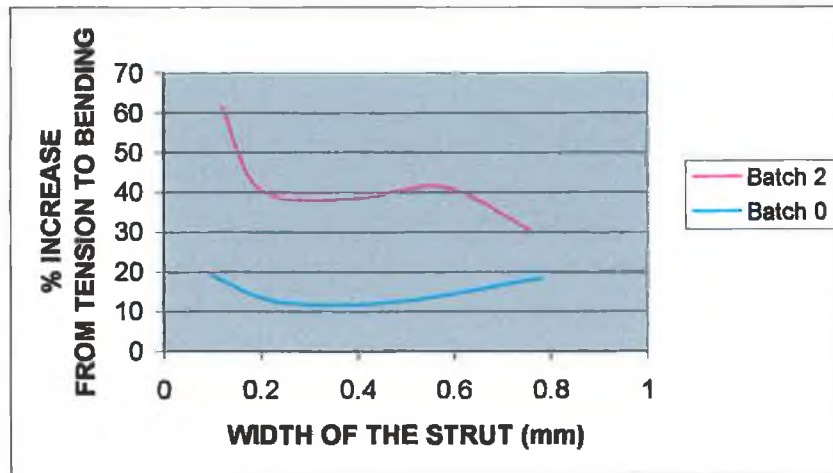


Fig.4.42 % increase of the yield stress from tension to bending versus the width of the strut for batch 0 and batch 2.

Fig.4.43 shows that for both batches the Young's Modulus increases when the width decreases, and as for the yield stress, the Young's Modulus is higher for batch 2 than for batch 0.

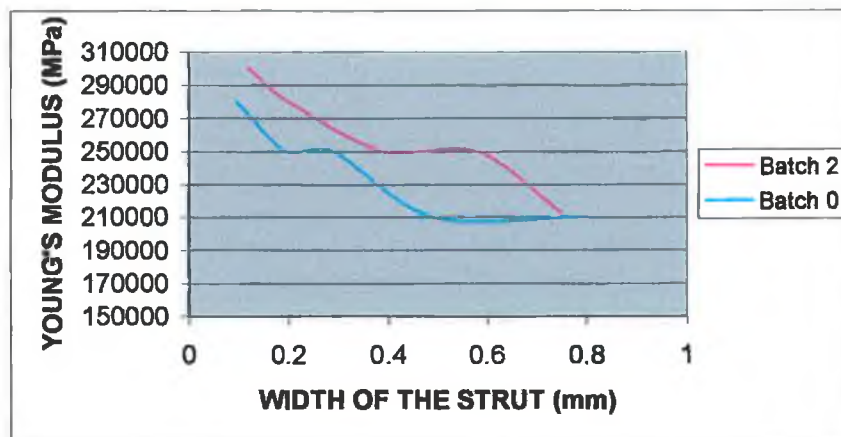


Fig.4.43 Young's Modulus versus width of the struts for batch 0 and 2.

In conclusion, after laser-cutting the tensile behaviour and bending behaviour follow the same pattern. However, yield stress and Young's Modulus are higher in bending.

V INFLUENCE OF THE MANUFACTURING PATH

V.1 INTRODUCTION

In Chapter 3, the results showed that :

After electro-polishing, the mechanical behaviour is not significantly affected by electro-polishing when the struts are wider than 0.2 mm.

For smaller struts, both Young's Modulus and yield stress increase and then decrease when the width decreases. The strain at breaking still decreases but follows a different pattern than before electro-polishing.

After annealing, the material becomes softer and the yield stress is independent of the width but the amount of hardening increases when the width decreases.

The strain at breaking still decreases with the width.

the Young's Modulus increases and then decreases.

The aim of this paragraph is to study if the same conclusions can be reached in bending.

V.2 RESULTS FOR ELECTRO-POLISHED SPECIMENS

Fig.4.44 shows the hardening curves obtained for electro-polished struts. 0.020 mm, 0.31 mm and 0.066 mm struts could not be tested since, as explained previously, being higher than wide they tilt on their side.

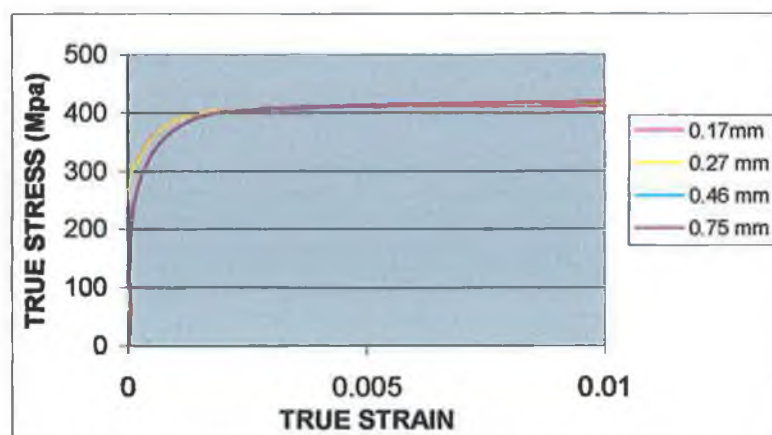


Fig.4.44 Hardening curves obtained for electro-polished struts.

V.3 TENSILE VERSUS BENDING BEHAVIOUR

Only the yield stress is studied since the Young's Modulus can not be calculated accurately and there is no breaking. As in tension, the yield stress is independent of the width for the wider struts (Fig.4.45). 0.020 mm, 0.031 mm and 0.066 mm struts, as mentioned previously, could not be tested, therefore the influence on the smaller struts can not be studied.

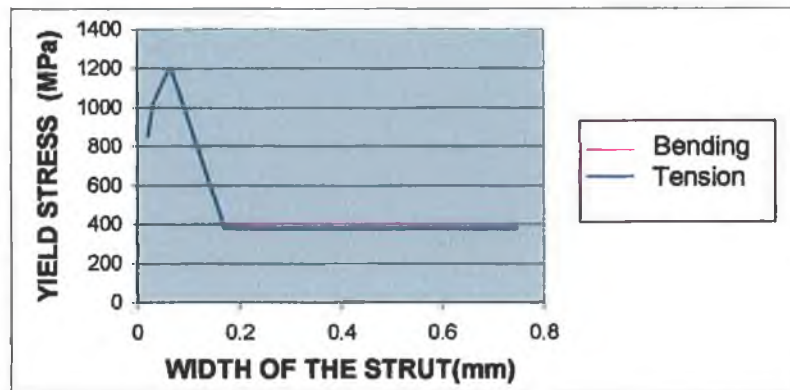


Fig.4.45 Yield stress versus width for electro-polished struts in tension and bending.

V.4 INFLUENCE OF ELECTRO-POLISHING IN BENDING

According to Fig.4.46, in bending, the yield stress after electro-polishing is lower than before. In tension no significant change was observed for these struts.

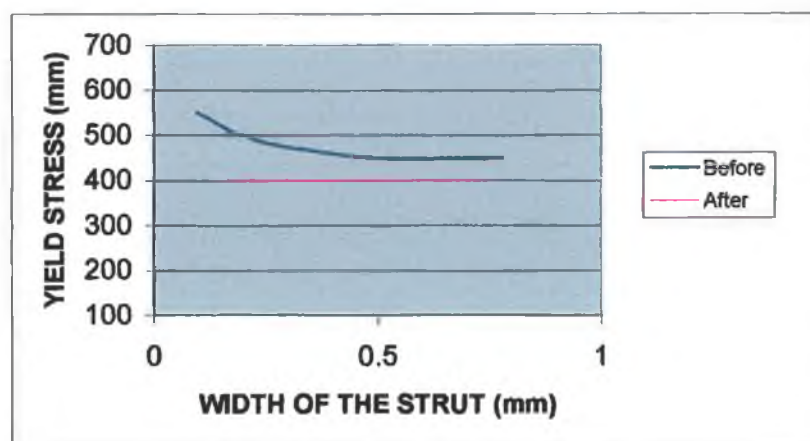


Fig.4.46 Yield stress versus width of the strut before and after electro-polishing.

V.5 RESULTS FOR ANNEALED SPECIMENS

Fig.4.47 shows the hardening curves obtained for annealing struts.

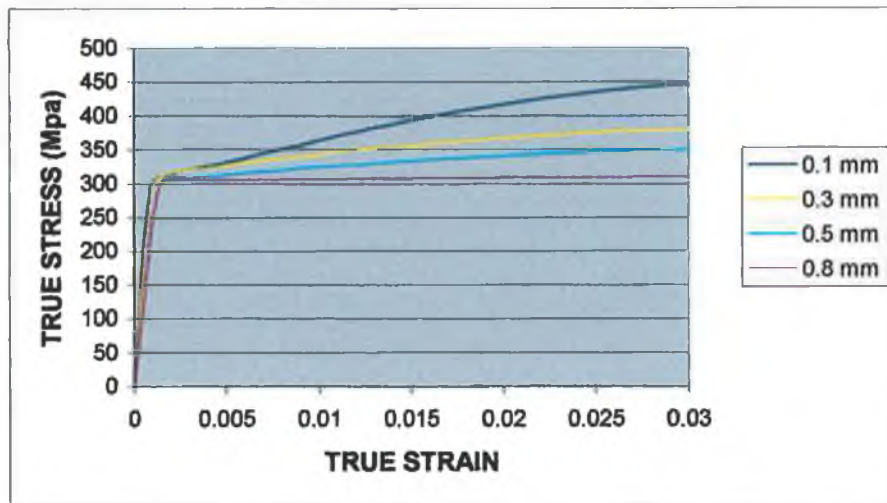


Fig.4.47 Hardening curves obtained for annealed struts.

V.6 TENSILE VERSUS BENDING BEHAVIOUR

The yield stress of annealed struts follows the same pattern in tension and bending (Fig.4.48). The yield stress is higher in bending than in tension.

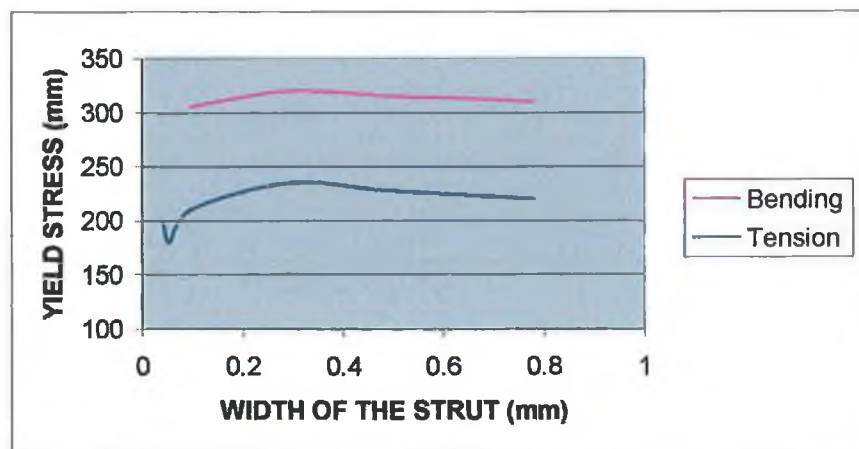


Fig.4.48 Yield stress versus width of the strut in tension and bending for annealed struts.

V.7 INFLUENCE OF ANNEALING IN BENDING

Fig.4.49 shows that the material is softer after annealing.

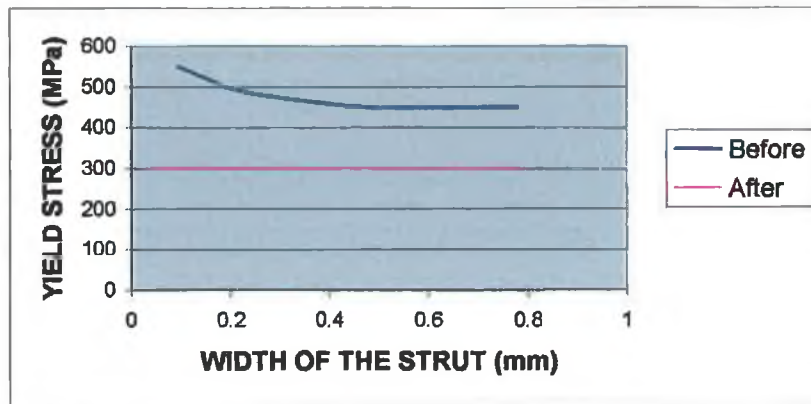


Fig.4.49 Yield stress versus the width of the strut before and after annealing.

Annealing does not change the geometry of the struts, therefore the load versus deflection curves obtained before annealing and after annealing (Fig.4.50) may be compared.

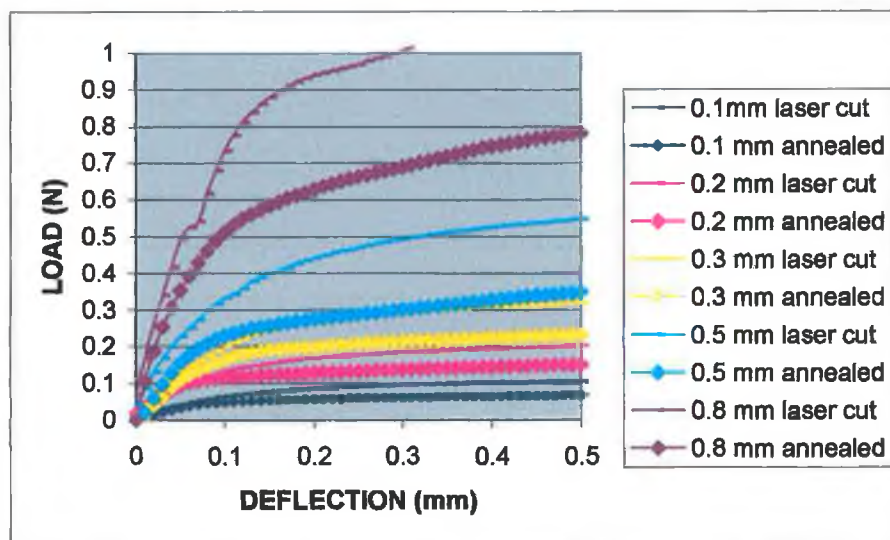


Fig.4.50 Load versus deflection curves before and after annealing.

Fig.4.50 shows again that the annealed struts are softer than the non annealed ones which is the normal consequence of annealing and was also observed in tension.

VI CONCLUSION

After studying the bending behaviour some observations made for the tensile behaviour have been confirmed :

Firstly, after laser-cutting :

- The Young's Modulus increases when the width decreases. This result would have to be confirmed by further tests since the test is not repeatable enough in the elasticity region to calculate the Young's Modulus accurately.
- The yield stress increases when the width decreases. However, the yield stress is higher in bending than in tension (this could be explained by the strain gradient plasticity theory).
- The strain at breaking could not be studied using this test since the struts slide from the supports before breaking.

After electro-polishing :

- The yield stress is independent of the width for the wider struts, the smaller struts could not be tested. But, in bending, the yield stress appears to be lower after electro-polishing

Finally, after annealing :

- The material becomes softer. The yield stress follows the same pattern in bending and tension.

The width of the struts and the manufacturing processes have an influence on both tensile and bending behaviour. In order to study what are the possible causes for these occurrences, a microstructure analysis needs to be conducted.

CHAPTER 5 : MICROSTRUCTURE ANALYSIS

I INTRODUCTION

In Chapter 3 and Chapter 4, experimental tests were conducted on struts laser-cut in tubes used for the manufacturing of stents, in order to study the influence of the width of the struts and manufacturing processes on their tensile and flexure behaviour. Observations have been made concerning :

Firstly, the influence of the width of the struts :

- The Young's Modulus increases when the width decreases.
- The yield stress increases when the width decreases.
- The breaking point decreases when the width decreases.

Secondly, the influence of electro-polishing :

- For the larger struts, the Young's Modulus is higher after electro-polishing but follows the same pattern as before electro-polishing. When the width of the strut gets smaller than 0.2 mm, the Young's Modulus increases and then decreases.
- The yield stress is not affected by the manufacturing process for wide struts. It is constant for the wider struts, but when the struts get narrower than 0.2 mm, as observed for the Young's Modulus, the yield stress increases and then decreases.
- The breaking point still decreases with the width. It is not affected by the manufacturing process for the wider struts but it is for the narrower ones.

Finally, the influence of annealing :

- The Young's Modulus is not significantly influenced by the annealing process for the wider struts. However, before annealing, it keeps increasing when the width of the strut decreases whereas, after annealing, it increases and then decreases.
- The material becomes softer. The yield stress increases when the width decreases until the width reaches 0.1 mm then the yield stress decreases with the width until it reaches another limit and starts increasing again..
- The strain at breaking point still decreases with the width.

The aim of the chapter is to try to explain these occurrences by observing the microstructure of the specimens.

- The procedure developed for the preparation of the samples is presented.
- Pictures of the grain structure of the different struts are observed to study the possible influence of the Heat Affected Zone resulting from laser cutting.
- And finally, the role of the number of grains in the width of the strut is studied.

II EXPERIMENTATION

As explained in Chapter 1, in order to observe the microstructure of a material the samples have to be mounted, ground, polished and then etched. Standard procedures exists, however due to the small dimension of the strut standard procedure for stainless steel could not be applied since the different grinding and polishing steps proposed would remove the entire strut. Therefore, a procedure was developed for this particular application. This procedure is presented in Appendix II.

II.1 ETCHING

The mechanical properties of a material depends on the grain size of the material as explained in Chapter 1 paragraph III.5. To determine the grain size, the grains have to be counted and therefore the grain boundaries have to be visible as shown on Fig.5.1.

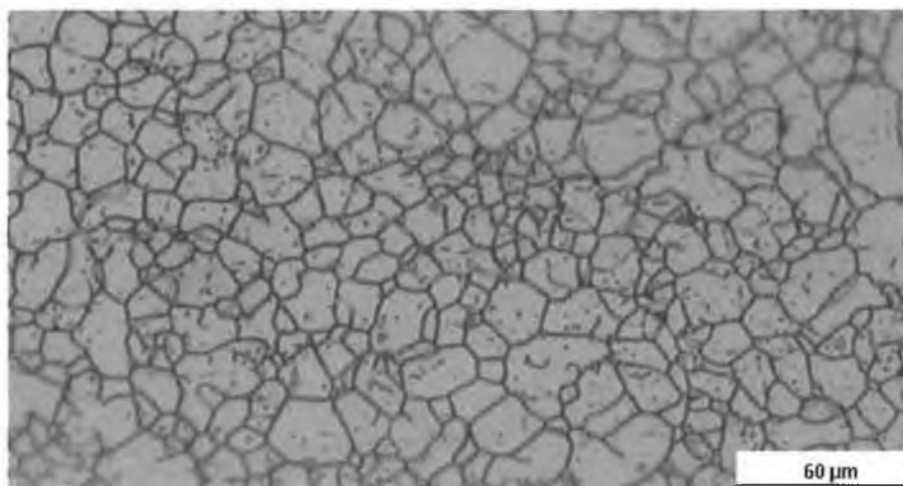


Fig.5.1 X200 Grain boundaries visible after etching.

II.1.1 Chemical Etching

In order to reveal the grain boundaries, once the surface is perfectly polished, the samples have to be etched. Chapter 1 presented a list of etchants. Chemical etching is more interesting since it does not involve much equipment. Stainless steels are the most difficult steels to etch due to their properties (high resistance to corrosion). Picral is known to be efficient, however, due to its explosive properties, it could not be used in our laboratory. Two other chemical etchants were used : Marble's reagent and the etchant made from equal part of HNO_3 , HCL and water.

Marble's reagent

The Marble's reagent is composed of 20 cm^3 of H_2O , 20 cm^3 of HCl and 4g of CuSO_4 . Both immersion (Fig.5.2 (a)) and swabbing (Fig.5.2 (b)) were used.

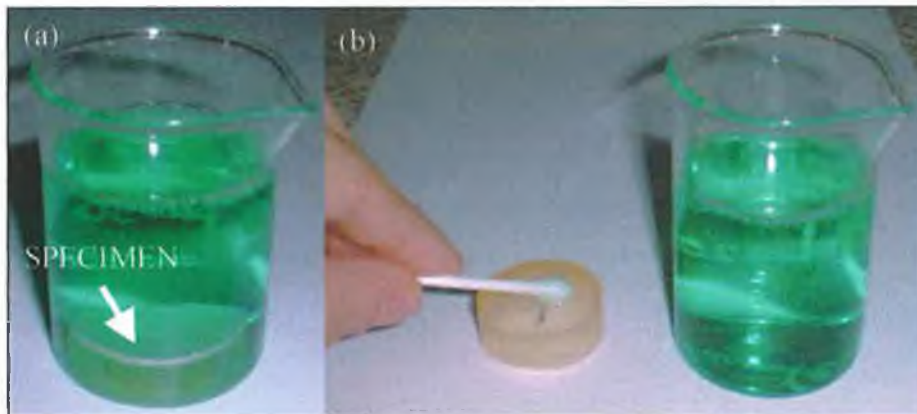


Fig.5.2 (a) Immersion of the sample, (b) swabbing.

In both cases, the sample was over etched as shown on Fig.5.3.

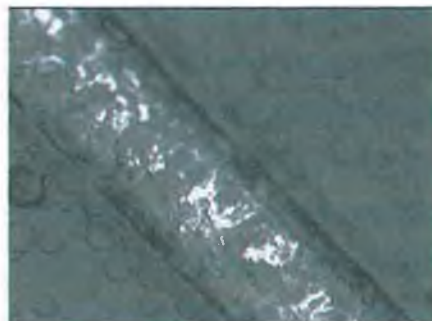


Fig.5.3 X200 Over-etched sample.

Equal part of H₂O, HCl and HNO₃

The composition of this etchant was found in the ASM Handbook [12]. Swabbing was the technique used. Depending on the quantity of etchant on the swab and the swabbing time, the quality of the etch obtained is variable. Fig.5.4 and Fig.5.5 show the different levels of etching obtained.

Fig.5.4 (a) shows a good etch, only the grain boundaries are etched. The grain boundaries are black because, once etched they do not reflect light. Few seconds later, the grains are getting darker (Fig.5.4 (b)) because they are etched and do not reflect light properly anymore.

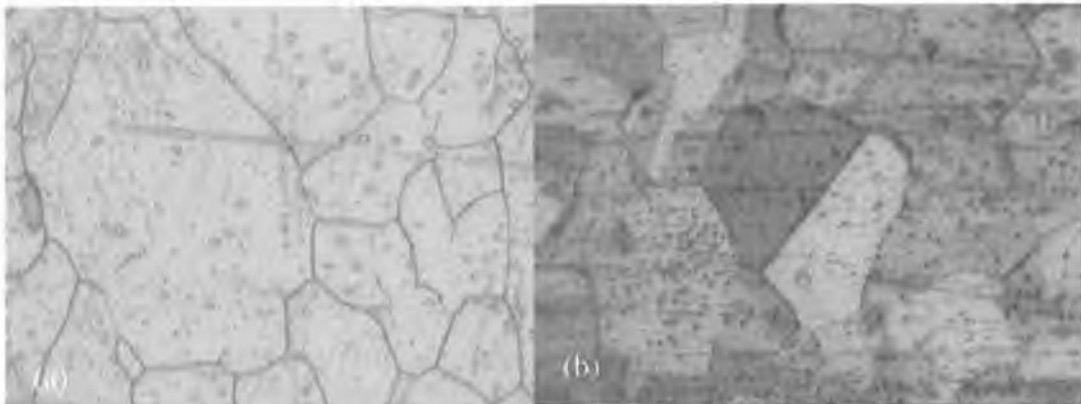


Fig.5.4 (a) X1000 Etched grain boundaries, (b) X500 Grains getting etched as well as the grain boundaries.

Fig.5.5 (a) and (b) show the grain getting progressively over-etched.

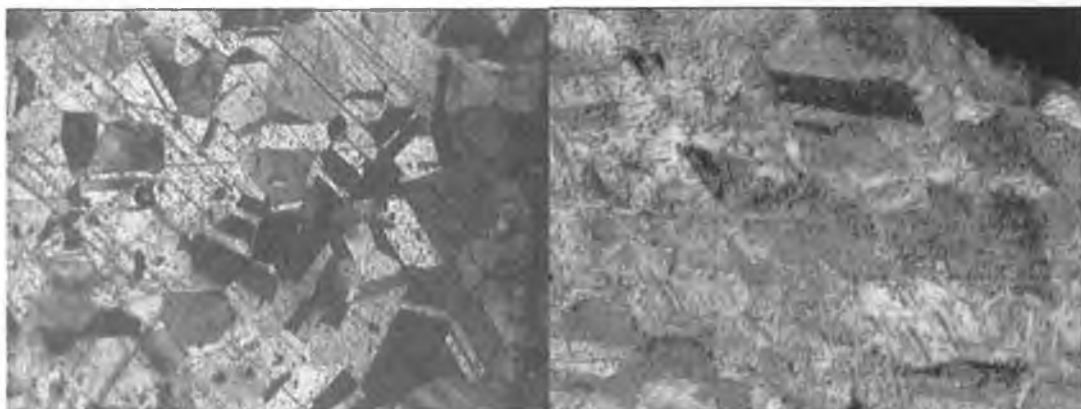


Fig.5.5 X500 (a) Colours of the grains getting darker, (b) Sample over-etched.

The sample goes through this different stages in the space of few seconds, and the time required varies from one sample to another. It is therefore very difficult to control the etching process and most of the time the samples end up being over etched.

Note that the scratches observable on the samples were made post-etching, during the time elapsed between etching and the capture of the images.

II.1.2 Electro-etching

Due to the difficulty encountered with chemical etching, an electro-etching apparatus was developed as part of the project (Fig.5.6). The base is in teflon and the anode and cathode are in titanium grade 2 (40 KSI-YS) which is 99.2 % commercially pure annealed titanium. The part of the sample to be etched is put in contact with the cathode.

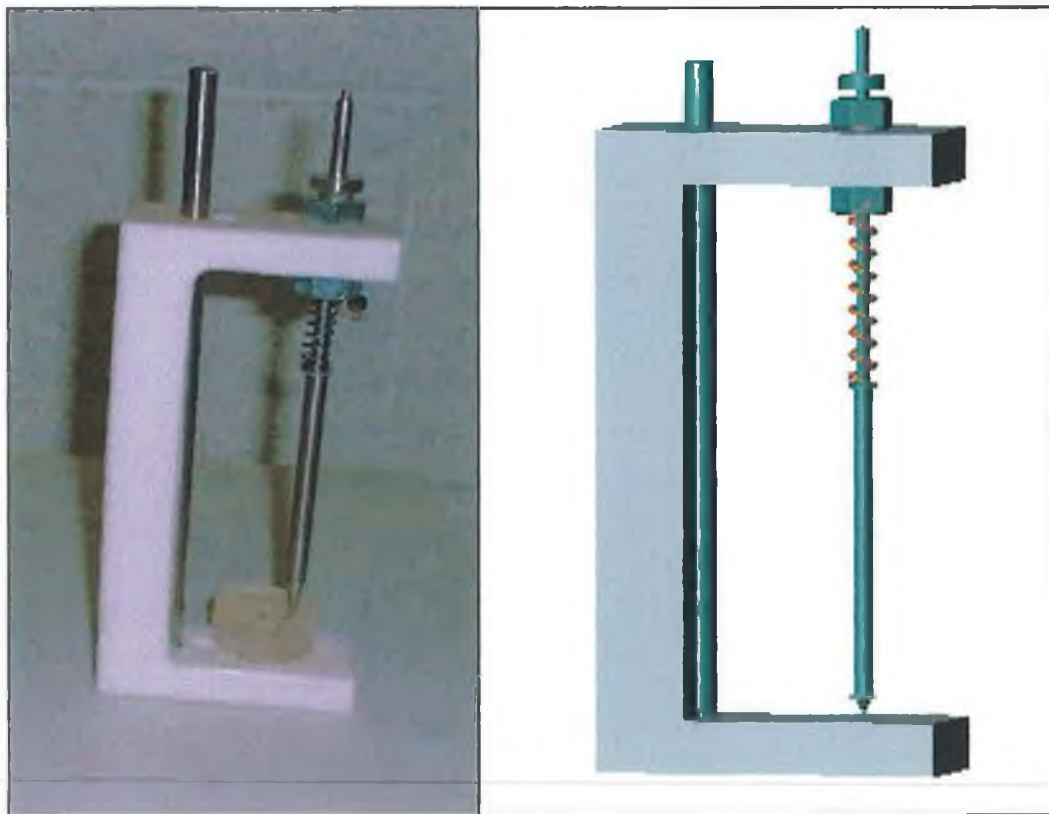


Fig.5.6 Electro-etching apparatus.

A 60% HNO_3 solution was then prepared and the apparatus immersed in it (Fig.5.7)



Fig.5.7 (a) preparation of the solution, (b) apparatus immersed in the solution.

Anode and cathode were then connected to a power supply and a continuous current was supplied to the apparatus with a voltage of 1 V during thirty seconds to one minute (Fig.5.8).



Fig 5.8 Apparatus connected to a power supply.

Fig.5.9 shows the etching obtained and this time only the grain boundaries have been etched.

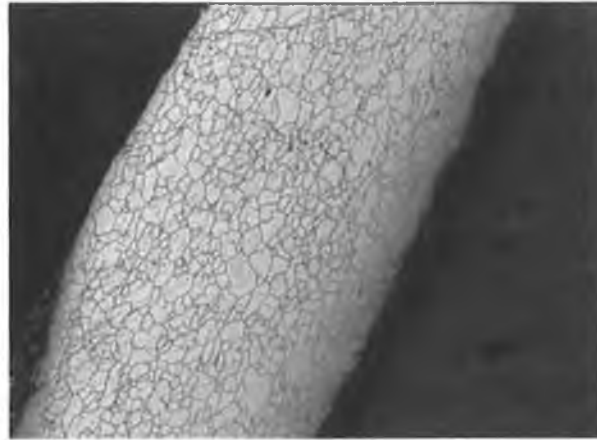


Fig.5.9 X200 Etch obtained by electro-etching.

In conclusion, electro-etching is easier to control than chemical etching and therefore gives better results.

II.2 IMAGE CAPTURE

The samples were now ready to be observed. Two types of microscopes were available to us : a Scanning Electron Microscope (SEM) and a stereo-microscope equipped with a digital camera linked to a computer.

II.2.1 Scanning Electron Microscope

A scanning electron microscope (SEM) has higher magnification (as high as X 300000) and greater depth of field than an optical microscope. At higher magnification more details are evident and the great depth of field is very important, because an optical microscope focus objects only in a shallow plane at higher magnification, which can make the examination of specimens difficult.

Fig.5.10 shows the SEM (LEICA 430) used in the G.M.I.T School of Sciences.



Fig.5.10 SEM LEICA 430.

The scanning electron microscopy technology is explained in Appendix III, but in order to understand why the samples have to be specially prepared for observation, a summarised description is given here.

An electron gun or virtual source (Fig.5.11) produces a beam of electrons and after various steps of condensing, constricting and focusing the beam of electrons strikes the sample.

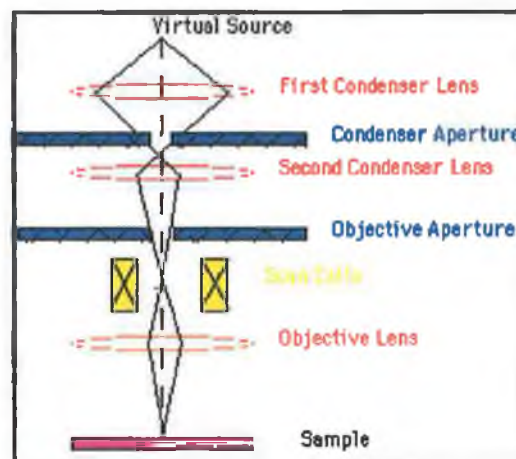


Fig.5.11 Diagram of the path followed by the electrons before striking the sample.

When the beam strikes the sample various reactions can occur as shown on Fig.5.12. The reactions noted on the top side of the diagram are utilised when examining thick or bulk specimens (SEM) while the reactions on the bottom side are those examined in thin or foil specimens (TEM).

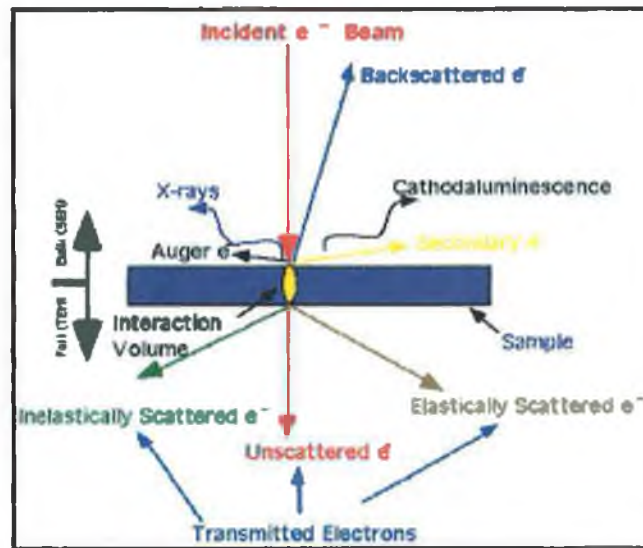


Fig.5.12 Reactions occurring when the beam strikes the sample.

Specimen interaction is what makes Electron Microscopy possible. In order to get a clear picture, the sample has to be conductor, a non conductor sample absorbs the electrons and the picture is blurred. The samples are therefore mounted on a metal support and the struts are linked to the support using a copper tape as shown on Fig.5.13.



Fig.5.13 Sample prepared for SEM examination.

The samples are then screwed to the S.E.M support (Fig.5.14) and enclosed in the air-tight chamber which is brought to a vacuum state necessary to the displacement of electrons.

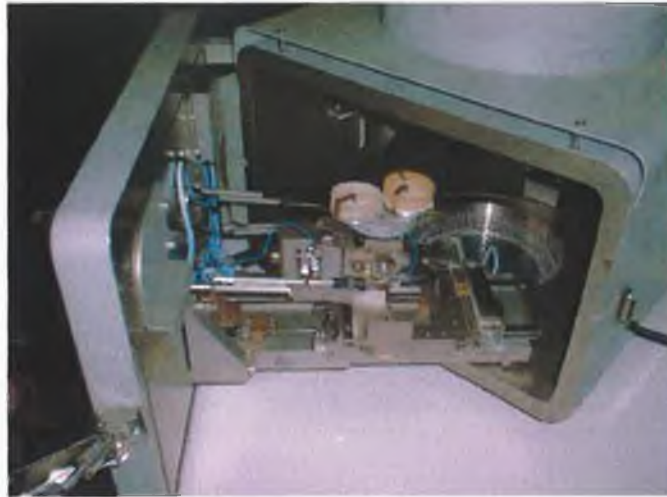


Fig.5.14 Sample screwed inside the air-tight chamber.

The SEM makes it possible to observe 3D features : Fig.5.15 shows the fracture of the strut and the cup shape characteristic of ductile material is noticeable.



Fig.5.15 X2500 SEM picture showing the cup shape characteristic of ductile fracture.

Fig.5.16 shows a magnification of a chemically etched strut. The grains have been etched as well as the grain boundaries, therefore the grain orientation are visible on this picture.

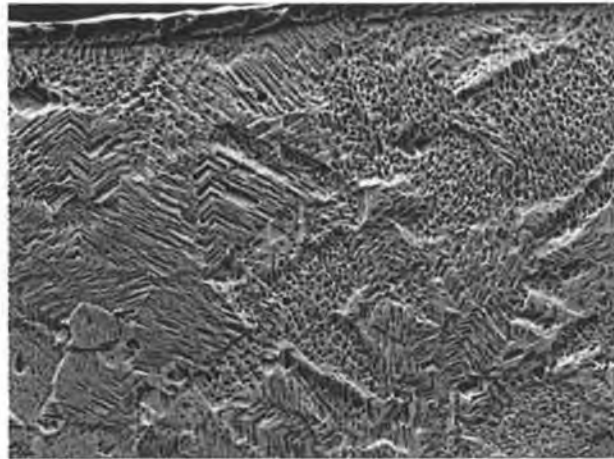


Fig.5.16 X3000 SEM picture of a chemically etched strut.

Fig.5.17 shows an electro-polished strut that has been electro-etched for grain count. Here, only the grain boundaries have been attacked by the chemicals and, therefore the grains are easier to count.

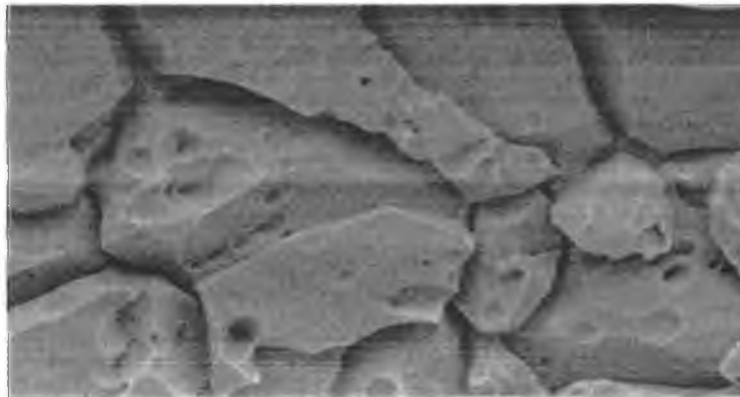


Fig.5.17 X5000 SEM picture of an electro-etched strut.

As shown on Fig.5.14 only two samples can be observed at a time and it takes around fifteen minutes to vacuum the chamber therefore the SEM is time consuming and a stereomicroscope is more appropriate to observe and take pictures of the samples.

II.2.2 Stereomicroscope linked to a computer

A stereomicroscope equipped with a digital camera linked to a computer (Fig.5.18) was used to take pictures of the samples (University of Limerick).



Fig.5.18 Stereomicroscope equipped with a digital camera linked to a computer.

Fig.5.19 shows a print screen of the software used. The screen on the right shows a live picture of the sample observed through the microscope.

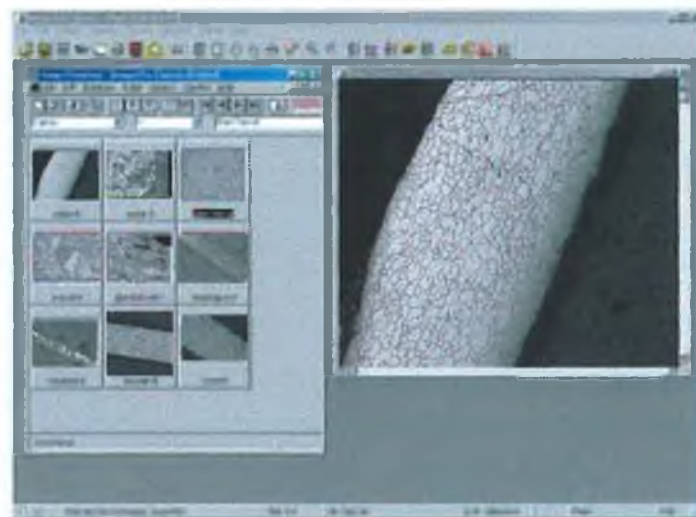


Fig.5.19 Software used for image capture.

The pictures (see Appendix VI for all the pictures that were taken but not included in the text) captured using the two kinds of microscope have to be examined and compared in order to understand the mechanical behaviour of the struts.

III INFLUENCE OF THE HEAT AFFECTED ZONE

III.1 INTRODUCTION

Chapter 1 paragraph III.5.5 presented studies done on the H.A.Z (heat affected zone) (Fig.5.20) consequence of laser cutting. According to these studies, the H.A.Z can result in the refinement of the grain and a precipitation of carbide. In both situations, the zone affected has a different microstructure and therefore different mechanical properties. When dealing with large devices, the size of the H.A.Z is relatively negligible, however, considering the size of the struts studied, the H.A.Z could be significant and the struts could behave as a sandwich material (Fig.5.20).

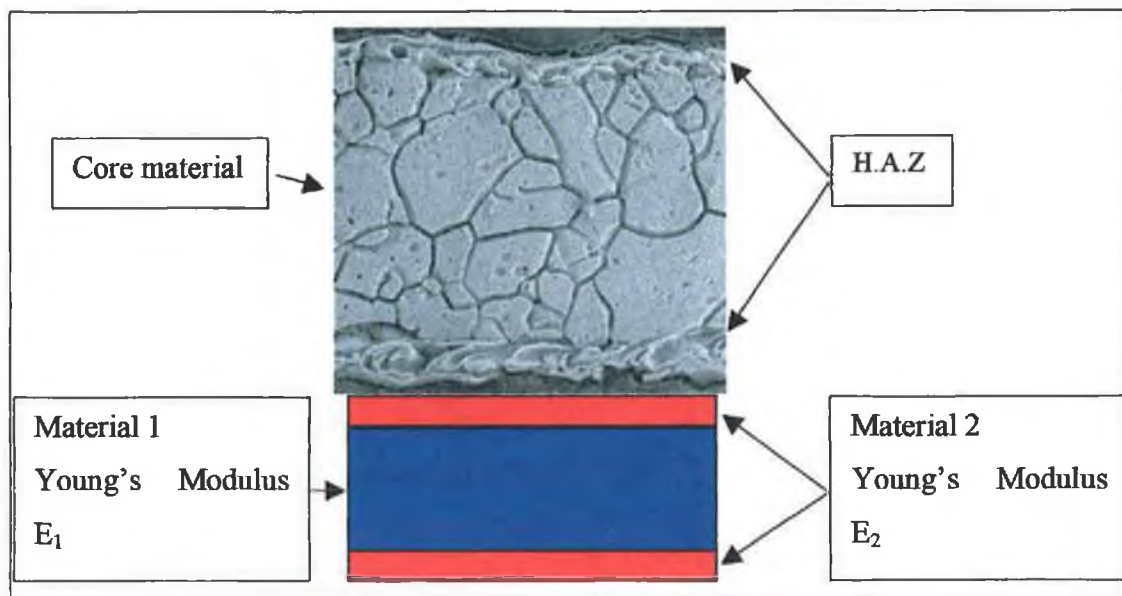


Fig.5.20 X2500 SEM picture of a laser cut strut compared to a sandwich material.

Young's Modulus and yield stress of a sandwich material are [18] :

$$E = \frac{E_1 V_1 + E_2 V_2}{V_1 + V_2} \quad (5.1)$$

$$\sigma_y = \frac{\sigma_{1y} V_1 + \sigma_{2y} V_2}{V_1 + V_2} \quad (5.2)$$

III.2 MICROSCOPE USED

Pictures taken with the S.E.M are used here since the H.A.Z is less visible on pictures taken with the stereomicroscope as shown on Fig.5.21. Fig.5.21 (a) shows a picture taken with the S.E.M of a 0.07 mm strut and Fig.5.21 (b) shows a picture of the same strut taken with the stereomicroscope. The H.A.Z is visible on both pictures but is easier to measure on the S.E.M one.

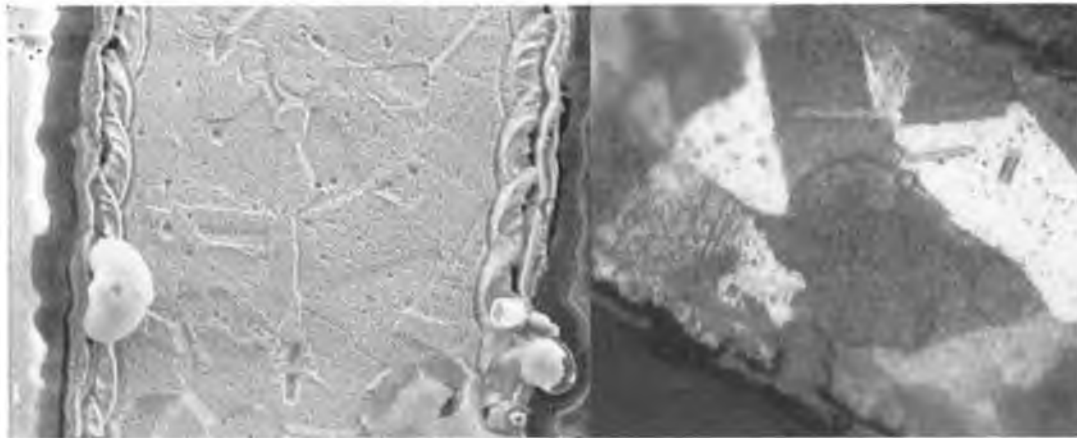


Fig.5.21 (a) X2500 SEM picture of a 0.07 mm strut,
(b) X500 Stereomicroscope picture of the same strut.

III.3 WIDTH OF THE H.A.Z

Fig.5.22 shows pictures of a 0.10 mm strut as well as a 0.07 mm strut.

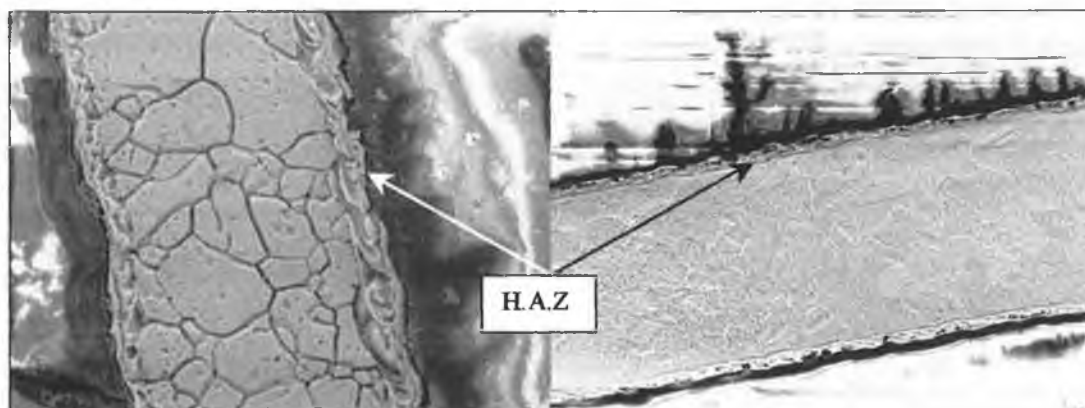


Fig.5.22 (a) X1250 0.07 mm strut, (b) X500 0.1 mm strut.

On Fig.5.22(b), the H.A.Z is around 1/10 of the width whereas on Fig.5.22 (a), the H.A.Z is around 1/5 of the width. The H.A.Z becomes relatively more important when the width of the strut decreases. It can be observed in Fig.5.22(a) that the grains of the H.A.Z are smaller than the one of the core. According to the Hall Petch Effect (Fig.5.23 and Chapter 1 paragraph III.5.3), the smaller the grain the higher the yield stress (until a certain limit d_c). Let assume that the yield stress of the H.A.Z is higher than the one of the core, the H.A.Z is therefore more brittle than the core (Chapter I paragraph III.5.4).

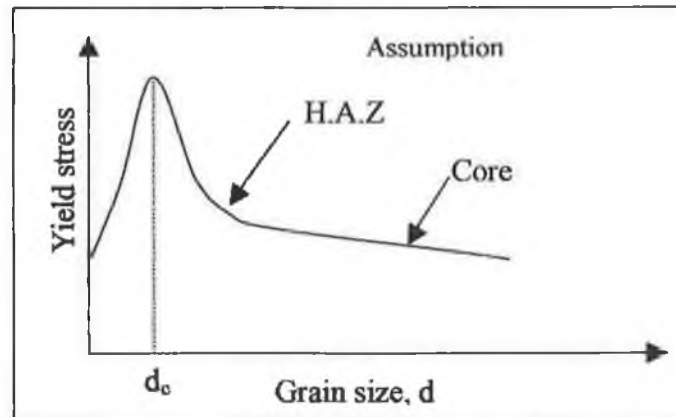


Fig.5.23 Hall-Petch Effect and assumption made concerning the grain sizes.

Fig.5.24 plotted using equation (5.2) shows that when the volume of H.A.Z becomes relatively more important the yield stress increase towards the yield stress of the H.A.Z.

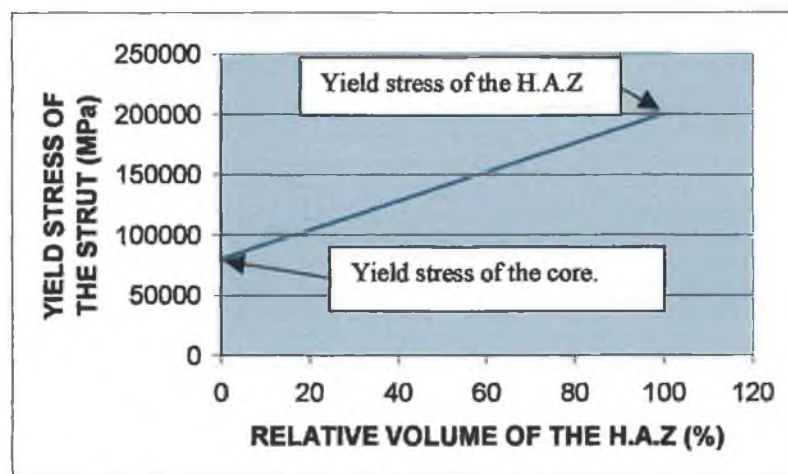


Fig.5.24 Yield stress of the strut versus relative volume of the H.A.Z.

The same analysis could be made for the strain at breaking. This could explain why the yield stress (Fig.5.25 (a)) increases when the width of the strut decreases and the strain at breaking point (Fig.5.25 (b)) increases with the width (Chapter 3 paragraph IV.3).

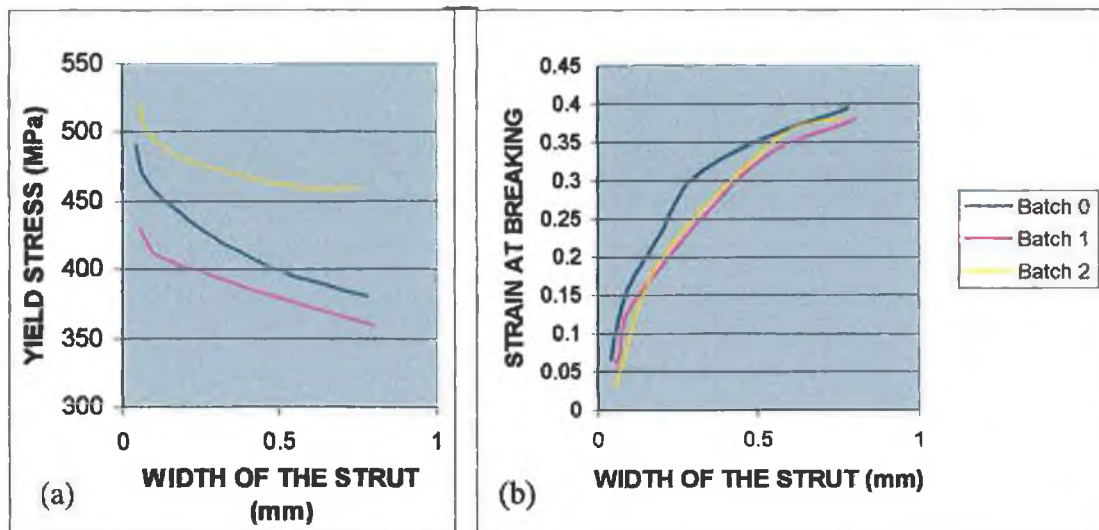


Fig.5.25 (a) Increase of the yield when the width decreases and (b) Increase of the strain at breaking point with the width of the strut.

Concerning that Young's Modulus and assuming that the Young's Modulus of the H.A.Z is higher than the one of the core, the analysis performed on the yield stress could also be applied for the Young's Modulus using equation (5.1) and this could explain why the Young's Modulus increases when the width of the strut decreases (Fig.5.26 and Chapter 3 paragraph IV.3).

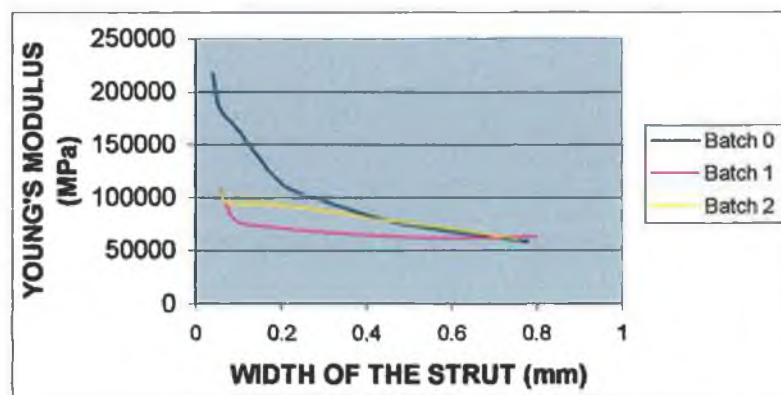


Fig.5.26 Young's Modulus increases when the width of the strut decreases.

A nano-indentation test would have to be conducted in order to prove that the Young's Modulus of the H.A.Z is higher than the one of the core.

According to Fig.5.24, the yield stress and Young's Modulus should increase linearly with the relative increase of the H.A.Z volume. Fig.5.25 and Fig.5.26 show that in both cases the increase could be considered linear for the larger struts, however, for struts smaller than 0.2 mm, the slope of both curves increase rapidly when the width decreases. Therefore, the H.A.Z is not the only factor influencing the mechanical behaviour of the small struts.

III.4 COMPARISON BETWEEN DIFFERENT BATCHES

Fig.5.27 shows the microstructure of 0.07 mm struts cut in three different batches.

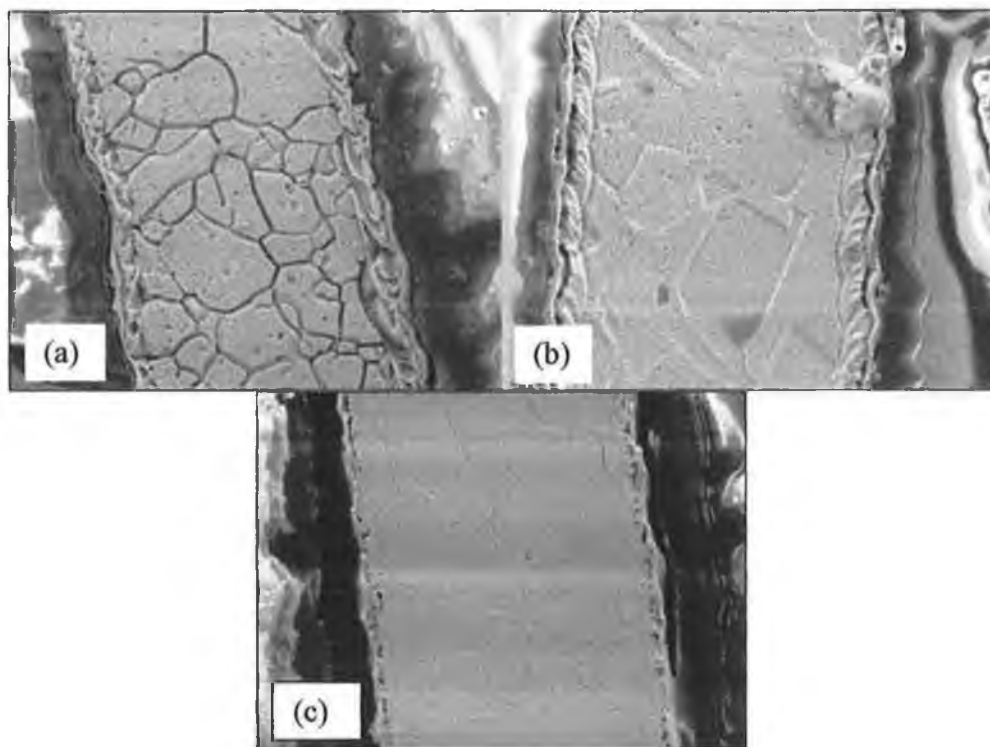


Fig.5.27 X2500 SEM pictures of 0.07 mm struts cut in (a) batch 0, (b) batch 1, (c) Batch 2.

Firstly, a few comments about the pictures: the grains look different from one batch to the other. This is due to the type of etching used. Batch 0 (Fig.5.27 (a)) and batch 2

(Fig.5.27 (c)) were electro-etched therefore only the grain boundaries are etched. Batch 1 (Fig.5.27 (b)) was etched with the equal part of H_2O , HCl and HNO_3 solution, therefore the grains are etched as well as the grain boundaries. It can also be observed that some of the pictures present some horizontal lines. This is due to the size of the struts. Even if the struts were linked to the support with copper tape, there is still a large volume of non conductive resin which absorbs electrons and creates this defect in the pictures.

Secondly, about the laser cut, it is noticeable that the H.A.Z is narrower in Batch 2 (1/10 of the width). Laser-cutter needs maintenance every few months for calibration. In between the laser beam becomes wider and the H.A.Z grows from the size observed in batch 2 to the size observed in batch 0. This could explain why the Yield stress of batch 2 does not increase as much as the yield stress of batch 0 (13% increase for batch 2 against 30% increase for batch 0). However, the H.A.Z of both batch 0 and batch 1 is around 1/5 of the width of the struts and the yield stress of batch 1 increases only of 20%. Other factors such as the grain size needs to be considered.

III.5 INFLUENCE OF THE MANUFACTURING PROCESSES ON THE H.A.Z.

III.5.1 Electro-polishing

Electro-polishing is used in the manufacturing of stents in order to smoothen the edges after laser-cutting. Fig.5.28 (a) shows the cut being rough before electro-polishing and Fig.5.28 (b) shows the cut being smooth after electro-polishing.

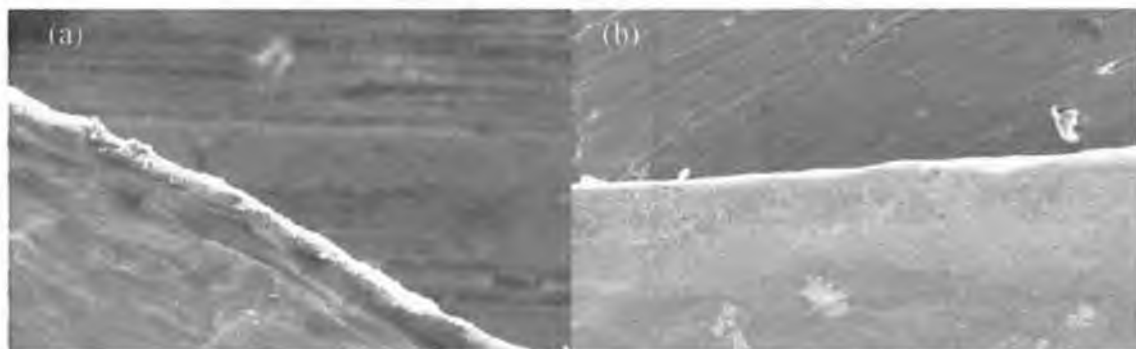


Fig.5.28 X1000 (a) cut before electro-polishing, (b) cut after electro-polishing.

When looking at the grain structure of the strut, Fig.5.29 shows that the electro-polishing removed the H.A.Z.

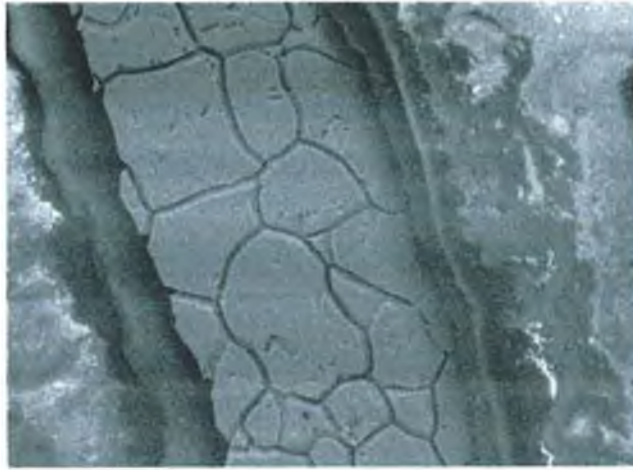


Fig.5.29 X3000 Grains structure of an electro-polished strut.

Since the H.A.Z. has been removed the mechanical behaviour should be independent of the width, which is confirmed by the tensile test results obtained for the larger struts. However this does not explain the behaviour for the struts smaller than 0.2 mm. This confirms the fact that the H.A.Z. has an influence on the mechanical behaviour but when the size of the struts becomes less than 0.2 mm, other factors have to be considered.

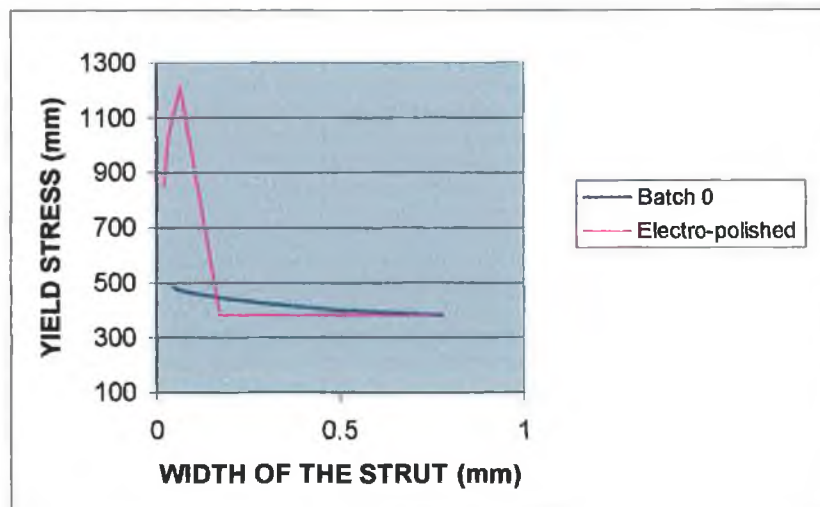


Fig.5.30 Yield stress versus the width of the struts before and after electro-polishing.

Fig.5.31 (a) and (b) show that after electro-polishing the edge of 0.05 mm and 0.07 mm struts are not straight and on (b) grains seem to have been removed.

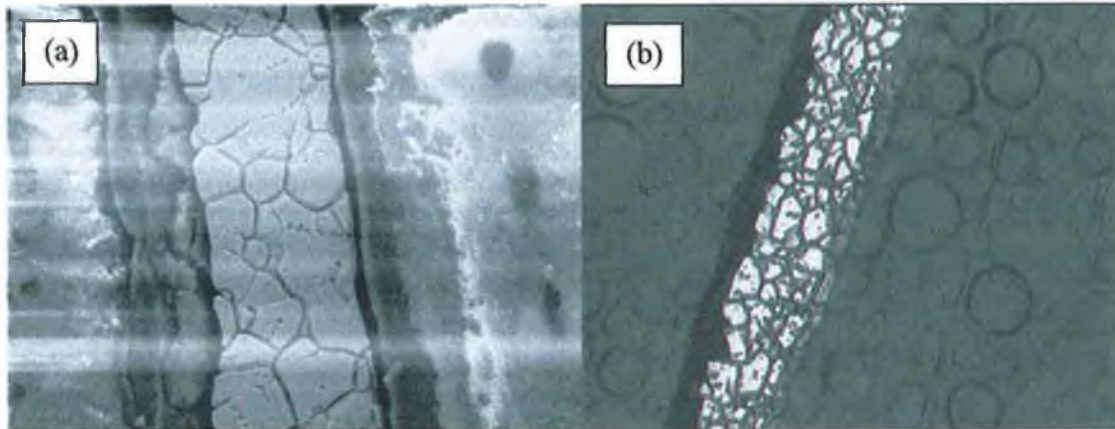


Fig.5.31 (a) X2500 S.E.M picture of an electro-polished 0.07 mm strut , (b) X200 stereomicroscope picture of a 0.05 mm strut (the face visible is the thickness of the tube).

Measurements taken along the struts before and after electro-polishing (Fig.5.32 (a)) show that for the larger strut the electro-polishing process seems to remove a constant amount of matter along the struts. However, Fig.5.32 (b) confirms that the smaller struts are not straight. This could explain the mechanical behaviour of the smaller struts (Fig.5.30).

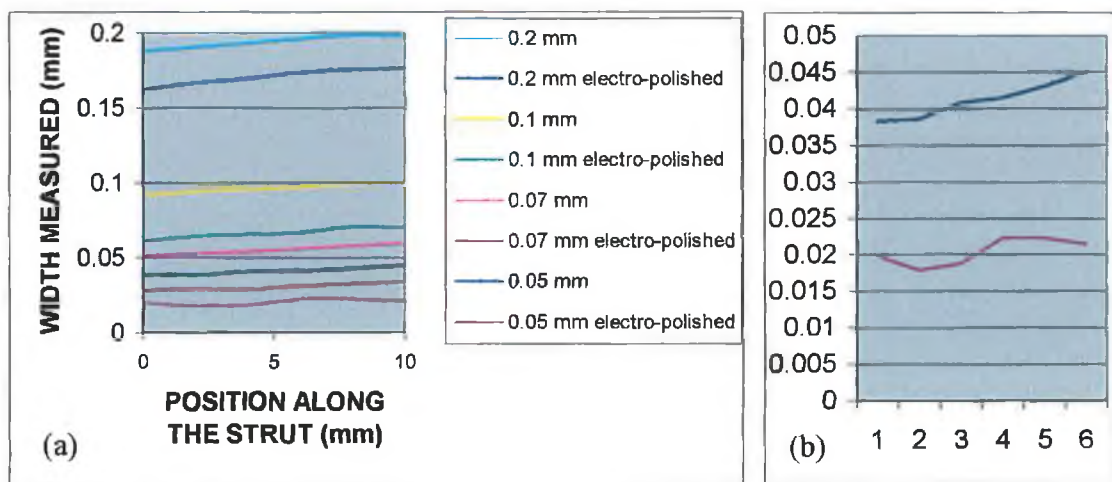


Fig.5.32 (a) Width of the strut versus position along the strut, (b) close up on the 0.05 mm strut.

III.5.2 Annealing

Here both SEM (Fig.5.33 (a)) and stereomicroscope (Fig.5.33 (b)) pictures are used. The strut (a) was chemically etched whereas strut (b) was electro-etched. On picture (a) the H.A.Z. appears as a black strip along the strut, on picture (b) confirms that the black strip is the H.A.Z. Therefore, annealing does not remove the H.A.Z.

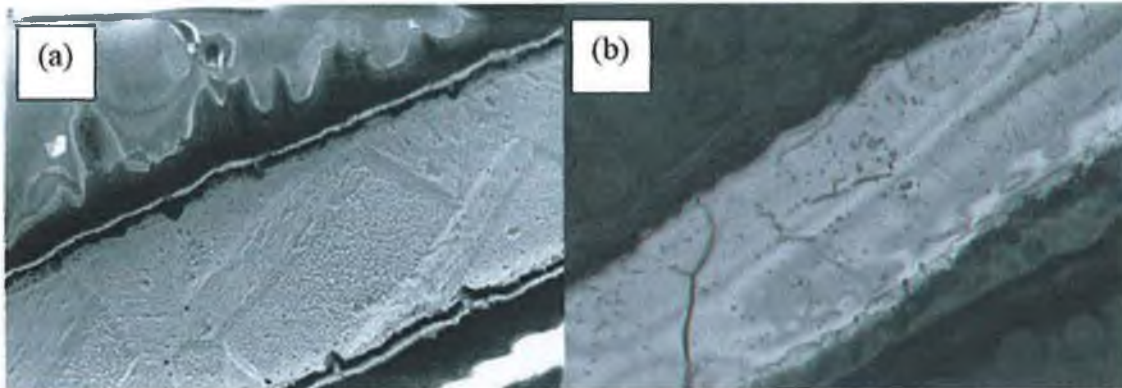


Fig.5.33 (a) X2500 SEM picture of a 0.07 mm annealed strut, (b) X200 Stereomicroscope picture of the same strut.

The tensile tests (Chapter 3 paragraph V.4 and Fig.5.34) showed that the yield stress increases when the width decreases until the width reaches 0.1 mm then the yield stress decreases with the width until it reaches another limit and starts increasing again. The presence of the H.A.Z. explains the increase of the yield stress for the wider struts but another factor must influence the behaviour of the smaller struts.

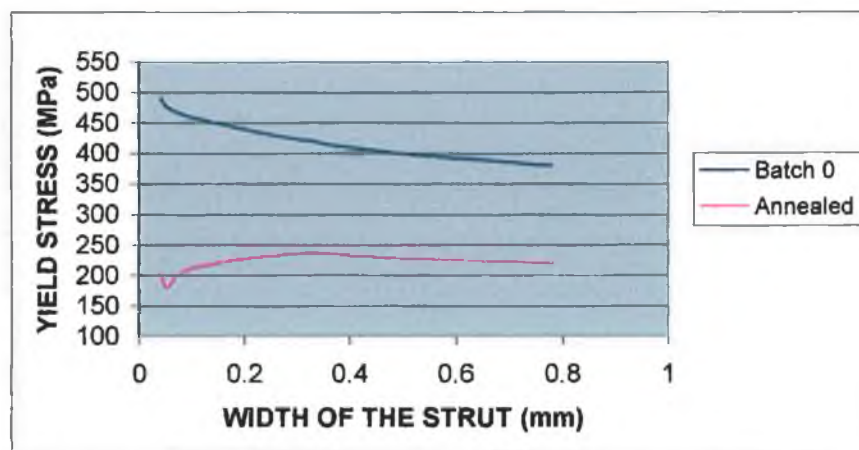


Fig.5.34 Yield stress versus true strain before and after annealing.

III.6 CONCLUSION

The size of the H.A.Z. becomes relatively larger when the width of the struts decreases. This explains why the yield stress and Young's Modulus increase when the width of the strut decreases and the strain at breaking decreases with the width. However, when the width of the strut is smaller than 0.2 mm, other factors have to be considered.

Electro-polishing remove the H.A.Z., therefore the tensile tests results confirm that when the struts are smaller than 0.2 mm, another factor influence the mechanical behaviour.

The H.A.Z. disappears with electro-polishing but not with annealing.

Annealing does not remove the H.A.Z., this explains the yield stress of the larger struts increasing when the width decreases but does not explain the behaviour of the smaller struts.

IV GRAIN SIZE

IV.1 INTRODUCTION

Austenitic stainless steel keep their FCC (Face Centred Cubic) austenitic structure (Fig.5.35) at room temperature because of the presence of Nickel. Therefore the grains observed are austenite grains.

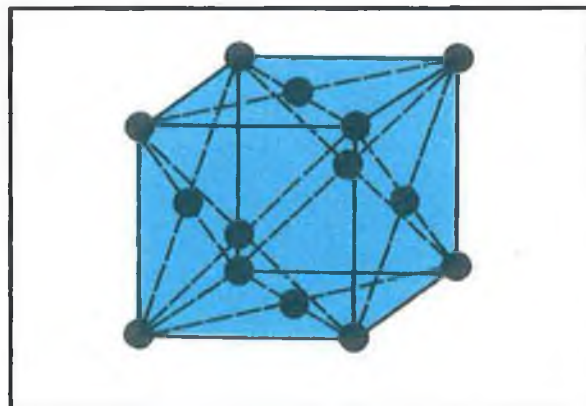


Fig.5.35 FCC structure [10]

The yield stress is a function of the grain size (Hall-Petch Effect (Fig.5.23)), therefore studying the grain size of the three different batches could explain their yield stresses being different.

IV.2 COMPARISON BETWEEN BATCHES

In order to compare the grain size of the batches, the Heyn intercept method, described in Chapter 1 paragraph V.3, is used.

Lines perpendicular to the edge of the strut are superimposed on the structure every 1 mm along the strut on the full size picture (Fig.5.36). Then the number of grains intercepting each line are counted (the H.A.Z. is excluded).

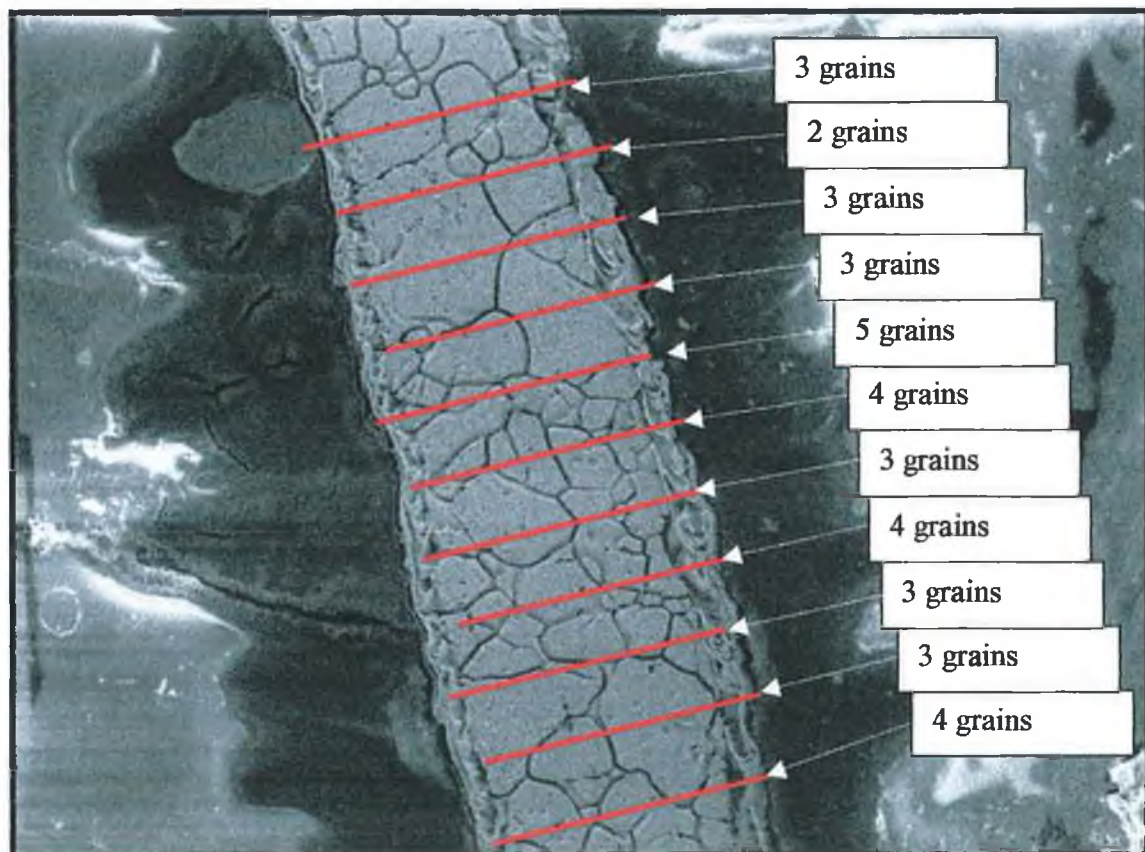


Fig.5.36 Grain count.

The average number along a line is 3.3636 (37/11). The length of a line is equal to the width of the strut (0.0548 mm) minus the width of the heat affected zone (0.011 mm).

The average size of the grain for batch 0 is :

$$L_3 = 0.0438/3.3636 = 0.0130 \text{ mm}$$

For batch 1, $L_3 = 0.0149$ and for batch 2, $L_3 = 0.0118$ mm.

According to the Hall-Petch effect the smaller the grain the higher the yield stress. This confirms the results obtained from the tensile test (Fig.5.37). According to Fig.5.37, the yield stress of batch 2 is higher than the yield stress of batch 0, which is higher than the yield stress of batch 1.

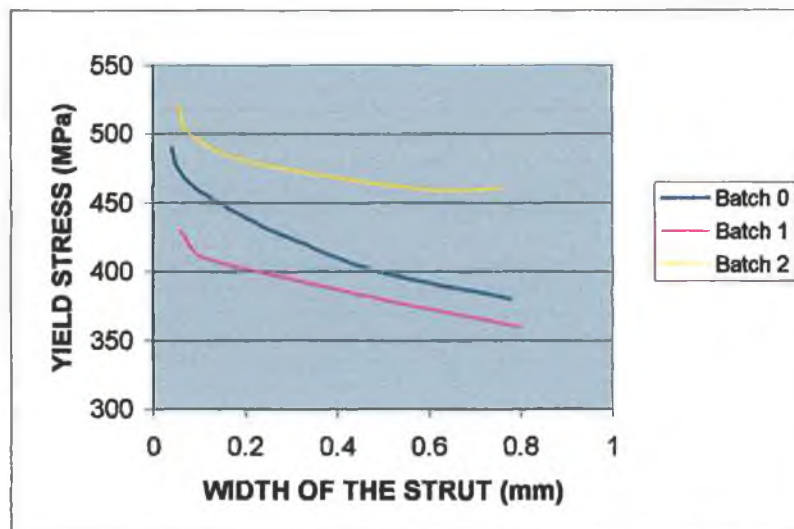


Fig.5.37 Yield stress versus width of the strut.

In conclusion, The three batches have different grain sizes, this explains why they have different yield stresses.

IV.3 INFLUENCE OF THE MANUFACTURING PATH

IV.3.1 Electro-polishing

Electro-polishing was shown to have no influence on the yield stress of the larger struts which were 0.8 mm wide (Chapter 3 paragraph V.3). Electro-polishing removes material at the surface of the struts and do not change the microstructure. Therefore, the measure of the grain size of electro-polished struts is not necessary, the grain size is equal to the grain size of the struts before polishing. However, after electro-polishing the struts are much narrower than before (the 0.05 mm strut is only 0.0204 mm and the 0.07 mm is only 0.0309 mm). Fig.5.38 shows that the number of grains in the width of the 0.0309 mm strut varies between 1 and 2. In the width of a 0.0204 mm strut the number of grains in the width tends to one.



Fig.5.38 X100 Electro-polished 0.0309 mm strut.

The consequence of having only one grain in the width needs, therefore, to be studied.

IV.3.2 Annealing

Fig.5.39 shows (a) an annealed 0.05 mm strut and (b) an annealed 0.07 mm strut. Comparing with the microstructure of the strut before annealing the size of the grain as increased. Both pictures show that there is only one grain in the width.

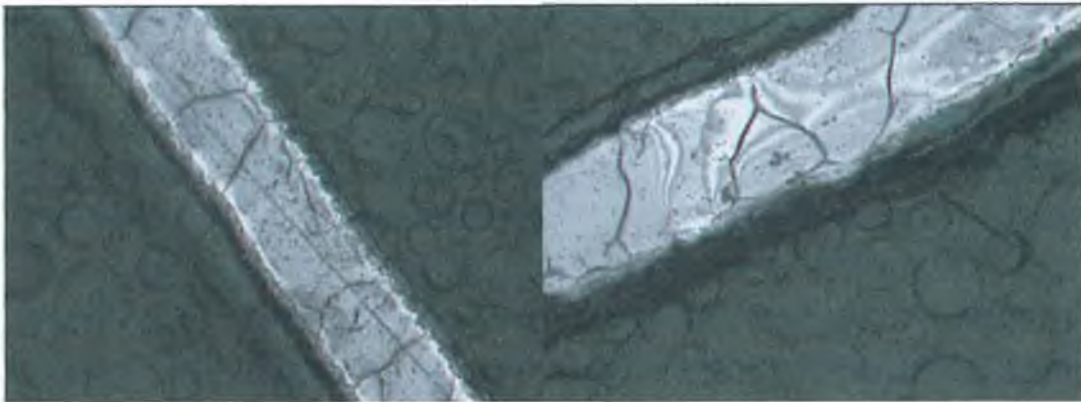


Fig.5.39 X200 (a) annealed 0.05 mm strut, (b) annealed 0.07 mm strut.

The struts, therefore, behave like a string of crystals (grains) as represented in Fig.5.40. The mechanical behaviour of such a strut needs to be studied.

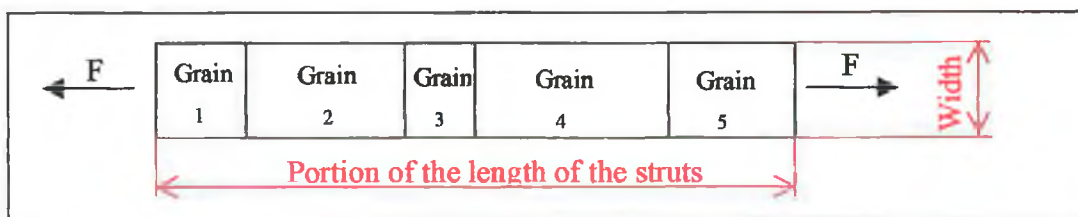


Fig.5.40 Sketch of a pile of crystals representing the strut.

IV.4 CONCLUSION

The three batches studied have different grain sizes explaining why they have different yield stresses.

After electro-polishing, the Heat Affected Zone has been removed therefore the struts are narrower and the smaller struts have only one grain in the width.

Annealing increases the grain size, consequently the smaller struts have only one grain in the width.

V NUMBER OF GRAINS IN THE WIDTH

V.1 INTRODUCTION

Both after annealing and after electro-polishing, the smaller struts are constituted of only one grain in the width. The influence of this occurrence on the mechanical behaviour of the strut needs, therefore, to be studied.

In paragraph IV.3 it was shown that the yield stress and Young's Modulus should increase linearly with the relative increase of the H.A.Z volume. However, experimental results showed that the increase could be considered linear for the larger struts but for struts smaller than 0.2 mm, the slope of both curves increase rapidly when the width decreases. Therefore, the H.A.Z. is not the only factor influencing the mechanical behaviour of the small struts. The number of grains needs to be considered.

V.2 ONE GRAIN IN THE WIDTH

Grain boundaries strengthen materials therefore single crystals have a lower yield stress than polycrystalline materials. The stress required to cause slip in a single crystal depends on the orientation of the active slip planes with respect to shear stresses. As an example, Fig.5.41 shows the orientation of the slip planes for a strut having only one grain in the width.

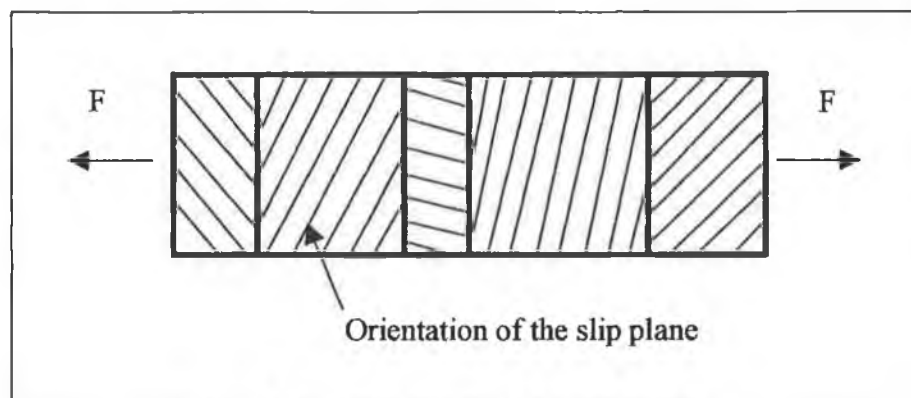


Fig.5.41 Orientation of the slip planes.

The Mohr circle shows that the shear stress is maximum at 45° from the force applied.

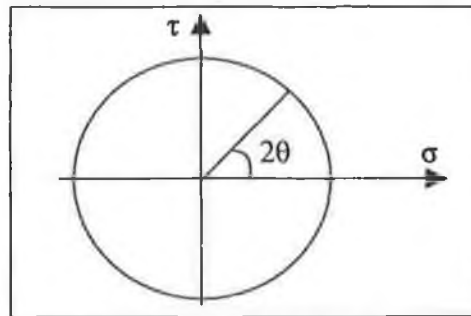


Fig.5.42 Mohr circle.

When the shear stress reaches the shear yield stress of the single crystal, the grains at a 45° angle enter in plasticity. The yield stress of a single crystal being lower than the yield stress of the polycrystalline material, the struts with only one grain in the width have a lower yield stress than the larger struts. This explains why the yield stress drops when electro-polished and annealed struts are smaller than 0.1 mm (Fig.5.30 and Fig.5.34).

The other grains that are not at a 45° angle do not enter in plasticity until the shear stress in their direction reaches the shear yield stress of the single crystal. This explains the small annealed struts entering progressively in plasticity and their hardening rule being different from the one of the larger struts as observed on Fig.5.43.

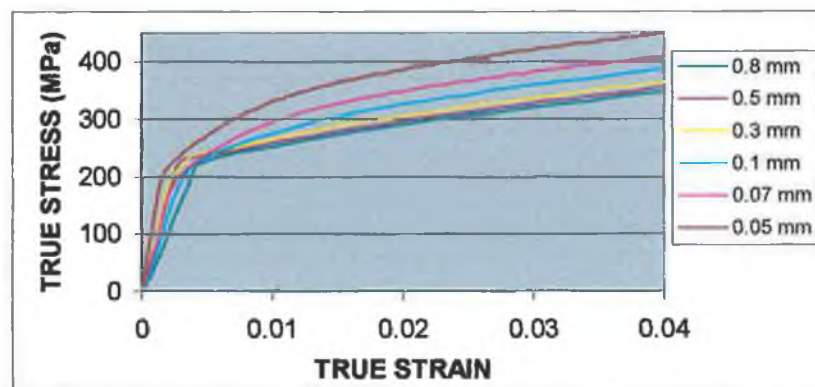


Fig.5.43 Hardening curves of annealed struts in tension.

V.3 FEW GRAINS IN THE WIDTH

Paragraph IV.3 showed that the yield stress and Young's Modulus should increase linearly with the relative increase of the H.A.Z. volume. This was verified for the larger struts, however, for struts smaller than 0.2 mm, the behaviour is not a linear function of the width. Therefore, the H.A.Z. is not the only factor influencing the mechanical behaviour of the small struts.

The only possible reason is the decreasing number of grains in the strut. As shown in paragraph VI.2, the grains are anisotropic since dislocations produce atomic displacements on specific crystallographic slip directions. When dealing with wide areas, the large amount of grains results in the material being homogeneous and isotropic. When the width considered is only few times the size of the grain, the material becomes non homogenous and anisotropic. This could explain why the mechanical behaviour of laser cut struts, narrower than 0.2 mm, does not vary linearly with the width. There is no obvious reason to explain this mechanism, however, some studies are currently in progress to model the grain behaviour and grain structure of materials [103][104][105]. This tool could allow the confirmation of this hypothesis.

V.4 CONCLUSION

When there is only one grain in the width of the strut, the yield stress is lower than the yield stress of a wider strut which has a large number of grains in the width.

When there is only few grains in the width of the strut, the hypothesis was made that the material is neither homogeneous nor isotropic anymore. This would explain why the mechanical behaviour of the smaller struts is not a linear function of the width.

VI CONCLUSION

The microstructure of the struts has been examined and conclusions have been reached concerning :

Firstly, the influence of the Heat Affected Zone (H.A.Z.)

- The H.A.Z. due to laser-cutting relatively increases when the width of the strut decreases. This explains why the yield stress and Young's Modulus increases when the width of the strut decreases and the strain at breaking decreasing when the width of the strut decreases. However, the theory implies that the three properties should vary linearly with the width and the experimental results showed that, when the struts are smaller than 0.1 mm, none of the three properties functions is linear. Therefore, the H.A.Z. is not the only factor influencing the smaller struts behaviour.
- Electro-polishing removes the H.A.Z., therefore the behaviour of the larger struts becomes independent of the H.A.Z. However, when the struts are smaller than 0.2 mm, the behaviour is function of the width, confirming that another factor than the H.A.Z. has to be considered for the smaller struts.
- Annealing does not remove the H.A.Z., this explains why the yield stress of the larger struts increases when the width decreases but does not explain the behaviour of the care of smaller struts.

Secondly, the influence of the grain structure

- The three batches studied each have a different grain size explaining why they have different yield stresses.
- After electro-polishing, the Heat Affected Zone has been removed therefore the 0.5 mm and 0.07 mm wide struts have only one or two grains in the width. Annealing increases the size of the grains. As a result, the smaller struts present only one grain in the width. It was shown that struts having only one grain in the width exhibit a lower yield stress and different hardening rule than struts having more grains in the width.
- When there are only few grains in the strut, the hypothesis was made that the material becomes anisotropic and non-homogeneous, explaining why the

mechanical behaviour of the laser-cut strut struts smaller than 0.2 mm does not increase linearly with the width.

The factors influencing the mechanical behaviour of the struts have been identified and Fig.5.44 summarises the influence of the H.A.Z. and the number of grains in the width. The pattern followed by this curve is similar to the Hall-Petch effect.

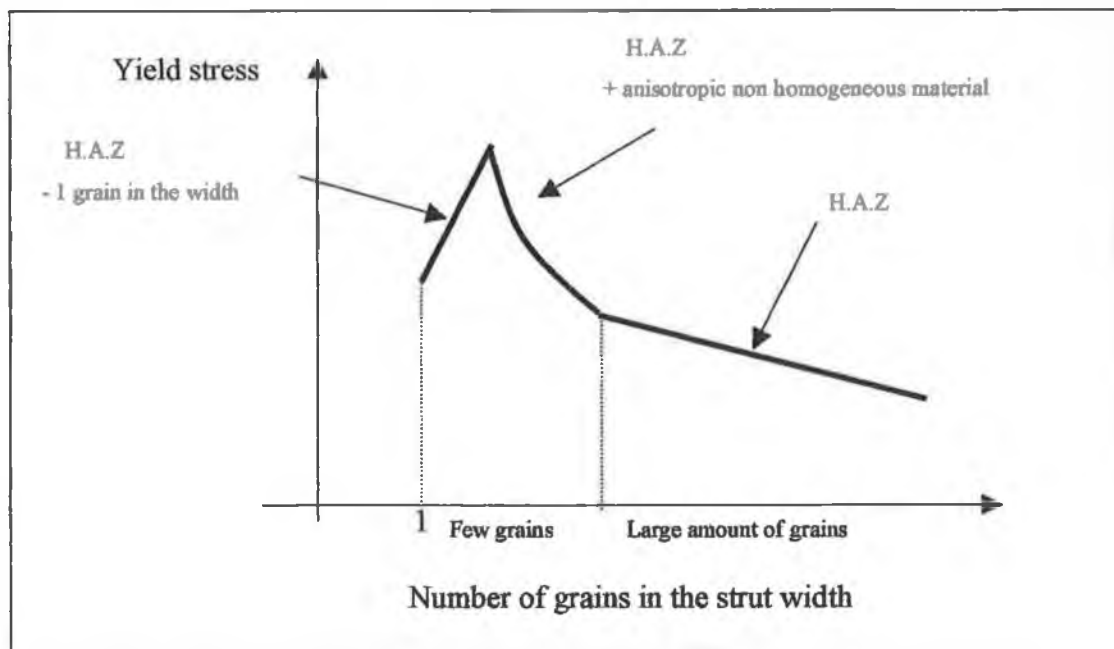


Fig.5.44 Summary of the factors influencing the mechanical behaviour of the struts.

CONCLUSION

The aim of this study was to show that both the size and the manufacturing path influence the mechanical behaviour of small devices such as stents. The study was conducted on struts laser-cut in tubes used for the manufacturing of stents. The struts were subjected to the same manufacturing processes as that used in the manufacturing of stents and they were tested in tension and bending after each of them. The microstructure of the different struts was then examined and the results of experimental tests interpreted.

CONCLUSIONS REACHED

Firstly, due to the inaccuracy of laser-cutting the struts are not straight :

- By measuring the specimen after laser cutting, it was noted that the specimen are not straight but have a trapezoidal shape.
- Failing to improve the accuracy of the cut, the consequences of this shape were studied. It was shown that the increase of the yield stress when the width decreases was not caused by the shape of the specimens.
- However, the shape of the specimen creates a stress concentration at one extremity, therefore the average stress and strain calculated at breaking are not representative of the material.

Secondly, the Heat Affected Zone (H.A.Z.) due to laser-cutting influences the behaviour.

This was proved by the following observations :

- The size of the H.A.Z. relatively increases when the width of the strut decreases and the material behaves like a sandwich material. This explains the yield stress and Young Modulus increasing when the width of the strut decreases and the strain at breaking decreasing when the width of the strut decreases. However, the theory implies that the three properties should vary linearly with the width and the experimental results showed that, when the struts are smaller than 0.1 mm, none of the three properties functions are linear. Therefore, the H.A.Z. is not the only factor influencing the smaller struts behaviour.

- Electro-polishing removes the H.A.Z., therefore the behaviour of the larger struts becomes independent of the width. However, when the struts are smaller than 0.2 mm, the behaviour is a function of the width, confirming that a factor other than the H.A.Z. has to be considered for the smaller struts.
- Annealing does not remove the H.A.Z., this explains why the yield stress of the larger struts increases when the width decreases but does not explain the behaviour of the smaller struts, again another factor needs to be considered.

Thirdly, the grain size influences the mechanical behaviour since :

- The three batches studied have different yield stresses because they have different grain size (Hall-Petch effect).
- Once annealed, the material becomes softer because its grain size increases.

Finally, the number of grain in the width influences the mechanical behaviour :

This was showed by the following observations :

- After electro-polishing, the Heat Affected Zone has been removed therefore the 0.5 mm and 0.07 mm wide struts have only one or two grains in the width. Annealing increases the size of the grains. As a result, the smaller struts present only one grain in the width. It was shown that struts having only one grain in the width exhibit a lower yield stress and different hardening rule than struts having more grains in the width.
- When there are only a few grains in the strut, the hypothesis was made that the material becomes anisotropic and non-homogeneous, explaining why the mechanical behaviour of the laser-cut strut struts smaller than 0.2 mm does not increase linearly with the width.
- By plotting the yield stress as a function of the number of grains in the width a curve similar to the Hall-Petch effect was obtained.

In conclusion, the Heat Affected Zone resulting from laser-cutting and the number of grains in the width of the strut both influence the mechanical behaviour when the struts are smaller than a millimetre.

FURTHER DEVELOPMENTS

This work was a first approach on the subject and some further experimentation would be necessary to corroborate the results :

- More repeatable tensile and bending tests could allow an accurate determination of the Young Modulus of the struts.
- As part of this project, a parallel study is being conducted to analyse the influence of the strain gradient in bending and confirm the difference between tensile and flexure behaviour
- A nano-indentation test should be conducted to determine the young modulus and yield stress of both affected and non affected zone in order to study further the strut behaving like a sandwich material.
- A microscopic observation of struts before and after electro-polishing should be done to examine the removal of grains by the manufacturing process.
- A modelling of the microstructure using F.E.A could confirm the hypothesis made on the influence of having only few grains in the width.
- Latest applications of stents include the delivery of drugs to the artery. This is achieved by coating the stent with the chosen drug. This will have to be included in the manufacturing path in order to identify the mechanical behaviour of stents before implantation.

The ultimate objective of further work should be the development of a procedure allowing manufacturers, knowing the grain size of the material and the manufacturing path, to determine the critical size at which the mechanical behaviour changes and the resulting mechanical properties.

This study concentrated only on the first part of the stents life span. After manufacturing the stent is implanted in the artery and is subjected to the pulsations of the artery. The studies currently in progress concerning the mechanical behaviour of stents in fatigue [106] will have to take into account the conclusions reached here when considering the material properties of the stent before implantation.

TO CONCLUDE

This work brings the study of the mechanical behaviour of stents a step further by showing the importance of the scale when dealing with such small devices. In a world where the smaller is the better, understanding mechanical behaviours at micro-scale is certainly becoming a priority.

REFERENCES

- [1] P.W Serruys: "Handbook of Coronary Stents", Dunitz limited, ISBN 1853178020.
- [2] E. Sverreborgersen, R.L. Sakagushi : "Using Marc Mentat to evaluate angioplasty balloon design parameters and their effects on stent expansion."
- [3] M.R. Jebwab, C.O. Clerc: "A study of the geometrical and mechanical properties of a self expanding metallic stent", Journal Of Applied Biomaterials, 1993, Vol.4 Part 1 Pages 77-85
- [4] J. Porte, A Aksan, D. Mulcahy, V. Sigwart: "Coronary Stents", Br.J.Hosp.Med, 1992. March. Vol.47 Part 6 Pages 411-419
- [5] C. Rogers, D.Y. Tseng, J.C. Squire, E.R. Edelman: "Balloon-artery interactions during stent placement"
- [6] S. Zhang, S. Tanaka and P.Rolfe: "Biomembrane mimicry : natural lipid layer adsorbed on a copolymer surface". Proceeding of the 20th Annual International Conference of the IEEE Engineering in Medicine and Biology Society, Vol 20, No 6, 1998, p2828-2829.
- [7] Y. M. Nenmakroha, S. Zhank, M. Wisman and P. Rolfe: "Cellular approach to improve the haemocompatibility of blood contacting medical devices". Proceeding of the 18th Annual International Conference of the IEEE Engineering in Medicine and Biology Society, 1996, p2063-2064.
- [8] M. Amon, S. Winkler, A. Dekler, A. Bolz, C. Mittermayer, M. Schaldach: "Introduction of a new coronary stent with enhanced radioopacity and haemocompatibility". Proceeding of the 17th Annual International Conference of the IEEE Engineering in Medicine and Biology Society, 1995, p107-108.
- [9] M. Amon , A. Bolz, B. Heublein, M. Schaldach: "Coating of Cardiovascular stents with amorphous silican carbide to reduce thrombogenicity". Proceeding of the 16th Annual International Conference of the IEEE Engineering in Medicine and Biology Society, 1994, p838-839.
- [10] W. F. Smith: "Principles of Materials Science and Engineering", International Edition. ISBN 0071147179.

- [11] "Metals Handbook, Atlas of Microstructures of Industrial Alloys", American Society for Metals.
- [12] American Society for Metals, "Metals Handbook : Atlas of Microstructures of Industrial Alloys".
- [13] A. Nayebi, O. Bartier, G. Mauvoisin, R. El Abdi: "New method to determine the mechanical properties of heat treated steels", International Journal of Mechanical Sciences 43 (2001) 2679-2697.
- [14] J. Lemaitre, J.L Chaboche: "Mechanics of Solid Materials", Cambridge University Press. ISBN 0521328535.
- [15] G. Verchery, T.S. Vong : "Une methode d'aide graphique a la conception des sequences d'empilement des stratifies", JNC5, Coptes rendus des cinquiemes Journess Nnationals sur les composites, C. Bathias and D.Menkes (1986) p 267-280.
- [16] C. Gachon : "Development of a method for the characterisation of the compliance and stiffness matrices of uncoupled material", Galway Mayo Institute of Technology, Galway, Republic of Ireland.
- [17] R. Hill: "The mathematical theory of plasticity", Clarendon Press, Oxford. ISBN 0198503679.
- [18] S.W. Tsai, "Composite Design", 4th ed., 1988, Think Composites, Dayton, OH.
- [19] A.S. Khan, S. Huang: "Continuum theory of plasticity", Wiley interscience publication. ISBN 047130433.
- [20] J. Lubliner: "Plasticity Theory", Collier Macmillan Publishers.
- [21] Q. Nguyen : "Probleme de Plasticite et de Rupture", Laboratory of Mechanics of Solids, Ecole Polytechnique, 91128 Palaiseau Cedex.
- [22] J.C. Gelin: " Structures Anelastiques" , University of Franche Comte, France.
- [23] M.X. Shi, Y. Huang, K.C Wang: "Plastic flow localisation in mechanism-based strain gradient plasticity", International Journal of Mechanical Sciences 42(2000) 2115-2131
- [24] M. Barney, G. Campbell, J.S. Stolken, W.E. King, R.O. Ritchie: "Experimental assessment of strain gradient plasticity theories".
- [25] Zervos, P. Papanastasiou, O. Vardoulakis: "A finite element displacement formulation for gradient plasticity".

- [26] D.M. Duan, N.Q. Wu, W.S. Slaughter, S.X. Mao: "Length scale effect on mechanical behavior due to strain gradient plasticity", *Materials Science and Engineering A303* (2001) 241-249.
- [27] A.H. Chen, T.C. Wang: "A new hardening law for strain gradient plasticity", *Acta. Mater.* 48 (2000)3997-4005.
- [28] A. Menzel, P.Steinmann: "On the continuum formulation of higher gradient plasticity for single and polycrystals", *Journal of the Mechanics and Physics of Solids* 48(2000) 1777-1796.
- [29] V.I.Levitas: "Plasticity theory of microinhomogeneous materials at large strain gradient", *Mechanics Research Communications*, Vol. 21 (1994), No.1, pp.11-17.
- [30] K. Shizawa, K. Kikuchi, H.M. Zbib: " A Stain gradient thermodynamic theory of plasticity based on dislocation density and incompatibility tensors", *Materials Science and Engineering A309-310* (2001) 416-419.
- [31] E.C. Aifantis: "The physics of plastic deformation", *Int. J. Plasticity* 3 (1987) p 211-247.
- [32] E.C. Aifantis: "Gradient aspects of crystal plasticity at micro and macro scales", *Key Engineering Materials* Vol. 177-180 (2000) pp 805-810.
- [33] V.P. Smyshlyaev, N.A. Fleck: "The role of strain gradients in the grain size effect for polycrystals", *J.Mech.Phys.Solids* 44(1996) 465-495.
- [34] W.J. Poole, M.F. Ashby, N.A. Fleck:"Micro-hardness of annealed and work-hardened copper polycrystals", *Scripta Materialia* 34(1996)559-564.
- [35] J.W. Hutchinson: "Plasticity at micron scale", *International Journal of solids and structures* 37 (2000) 225-238.
- [36] N.A Fleck, J.W. Hutchinson: "A reformulation of strain gradient plasticity", *Journal of the Mechanics and Physics of Solids* 49 (2001) 2245-2271.
- [37] N.A Fleck, J.W. Hutchinson: "Stain gradient plasticity", *Adv. Appl. Mech.* 33 (1997)
- [38] N.A Fleck, J.W. Hutchinson: "A phenomenological theory for strain gradient effects in plasticity.", *Journal of Mechanics and Physics of solids* 41 (1993) p 1825-57.

- [39] N.A. Fleck, G.M. Muller, M.F. Ashby, J.W. Hutchinson: "Strain gradient plasticity: theory and experiment." *Acta metall. Mater.* 42(1994) 475-487.
- [40] Z. C. Xia, J.W. Hutchinson: "Crack tip field in strain gradient plasticity", *J. Mech Phys. Solids.* 44(1996)1621-1648
- [41] Y. Wei, J. W. Hutchinson: "Steady-state crack growth and work of fracture for solids characterized by strain gradient plasticity", *J. Mech. Phys. Solids* 45(1997)1253-1273.
- [42] H.Gao, Y. Huang, W.D. Nix, J.W. Hutchinson: "Mechanism based strain gradient plasticity-I. Theory" *Journal of Mechanics and Physics of Solids* 47 (1999) p 1239-63
- [43] H.Gao, Y. Huang, W.D. Nix, J.W. Hutchinson: "Mechanism based strain gradient plasticity-II. Analysis" *Journal of Mechanics and Physics of Solids* 48 (2000) p 99-128.
- [44] K.C. Hwang, Y. Huang: "Mechanism-based strain gradient (MSG) plasticity and the associated asymptotic crack-tip fields", *Key Engineering Materials* Vol. 183-187 (2000) pp 9-18.
- [45] Y. Huang, J. Chen: " Analysis of size effects based on a symmetric lower-order gradient plasticity model", *Computational Materials Science* 19(2000)143-157.
- [46] H. Gao, Y. Huang, W.D. Nix: "Modeling plasticity at the micrometer scale", *Naturwissenschaften* 86 (1999),507-515.
- [47] E. H. Lee, T.S. Byun, J.D. Hunn, M.H Yoo, K. Farrell, L.K. Mansur: "On the origin of deformation microstructures in austenitic steel: Part I-Microstructures", *Acta. Mater.* 49(2001) 3269-3276.
- [48] X.F. Fang, W. Dahl: "Microstructure and strain hardening of steels", *Key Engineering Materials* Vol. 97-98 (1994) p 329-334.
- [49] M.W. Jessel, P.D. Bons: "Vieps/Mainz Microstructure course". Volume 2, *Journal of the virtual explorer.*
- [50] F. Cleri : "Multi-scale simulations of complex materials"
http://hammurabi.casaccia.enea.it/music_HTML/music.htm,
- [51] J. Schiøtz, T. Leffers and B. N. Singh." Modelling of dislocation generation and interaction during high-speed deformation of metals", to be published.

- [52] J. Schiøtz, T. Leffers and B. N. Singh: "Dislocation nucleation and vacancy formation during high-speed deformation of fcc metals", *Phil. Mag. Lett.* 81, 301-309 (2001).
- [53] J. Schiøtz, K. W. Jacobsen, and O. H. Nielsen: "Kinematic generation of dislocations", *Phil. Mag. Lett.* 72, 245-250 (1995).
- [54] J. Schiøtz, L. M. Canel, and A. E. Carlsson: "Effects of crack tip geometry on dislocation emission and cleavage: A possible path to enhanced ductility", *Phys. Rev. B* 55, 6211-6221 (1997).
- [55] D. Sherman, D. Brandon: "Mechanical properties of hard materials and their relation to microstructure", *Advanced Engineering Materials* 1999,1, No. 3-4 p 161-181.
- [56] H.H. Fu, D.J. Benson, M.A. Meyers: "Analytical and computational description of effect of grain size on yield stress of metals", *Acta Materialia* 49 (2001) 2567-2582.
- [57] J. Schiøtz, F. D. Di Tolla and K. W. Jacobsen: "Softening of nanocrystalline metals at very small grain sizes", *Nature* 391, 561-563 (1998).
- [58] J. Schiøtz, T. Rasmussen, K. W. Jacobsen, and O. H. Nielsen: "Mechanical deformation of nanocrystalline materials", *Phil. Mag. Lett.* 74, 339-344 (1996).
- [59] J. Schiøtz, T. Vegge, F. D. Di Tolla and K. W. Jacobsen: "Simulations of mechanics and structure of nanomaterials - from nanoscale to coarser scales".
- [60] J. Schiøtz, T. Vegge and K. W. Jacobsen: "Atomic-scale modeling of the deformation of nanocrystalline metals", in "Multiscale Modelling of Materials", edited by V. V. Bulatov, T. Diaz de la Rubia, R. Phillips, E. Kaxiras and N. Ghoniem, *Mater. Res. Soc. Symp. Proc.* 538, 299-308 (1999).
- [61] J. Schiøtz, T. Vegge, F. D. Di Tolla and K. W. Jacobsen: "Atomic-scale simulations of the mechanical deformation of nanocrystalline metals", *Phys. Rev. B* 60, 11971-11983 (1999)
- [62] E.O.Hall: *Proc. Roy. Soc (london)*, B64 (1951) 474.
- [63] N.J.Petch: *J. iron steel inst.*, 1953, 174, 25.
- [64] H. Huang, F. Spaepen: "Tensile testing of free-standing Cu, Ag and Al thin films and Ag/Cu multilayers", *Acta Materialia* 48(2000) 3261-3269

- [65] G.T. Gray III, S.R. Chen, K.S. Vecchio, *Met. and Mat. Trans.*, 30A (1999) 1235.
- [66] L.E. Murr, S.S. Hekker, *Scripta Metall.*, 13 (1979) 667
- [67] B.L. Adams, W.E. King, *Phyl. Mag*, A(2000)80,9
- [68] M.A. Meyers, E. Ashworth, *Phil. Mag. A*(1982) 46,737
- [69] R.W. Hertzberg: "Deformation and Fracture Mechanics of Engineering Materials", John Wiley & Sons, Inc. ISBN 0471012149.
- [70] T.L. Andersson: "Fracture mechanics", CRC-Press
- [71] D. Chae, J.P. Bandstra, D.A. Koss: "The effect of pre-strain and strain-path changes on ductile fracture: experiment and computational modeling", *Materials Science and Engineering A285* (2000) 165-171
- [72] M. Zheng, G. Zhou, D.A. Zacharopoulos, M. Kuna: "Crack initiation behavior in StE690 steel characterised by strain energy density criterion", *Theoretical and Applied Fracture Mechanics* 36 (2001) 141-145.
- [73] G.E. Beltz, D.M. Lipkin, L.L. Fischer: "Role of crack blunting in ductile versus brittle response of crystalline materials", *Physical Review Letters*, Vol. 82, No.22, p 4468-4471.
- [74] S.J. Zhou, D.M. Beazley: "Large-scale molecular dynamic simulations of three-dimensional ductile failure", *Physical Review Letters*, Vol. 78, No.3, p 479-482.
- [75] J. Schiøtz, A. E. Carlsson, L. M. Canel, and Robb Thomson: "Effect of crack blunting on subsequent crack propagation", *Mater. Res. Soc. Symp. Proc.* 409, 95-100 (1996).
- [76] J. Grum, Zulman.: "Analysis of heat effects in laser cutting of steels". *Journal Of Materials Engineering And Performance* Aug 1996, Vol 5 Part 4 Pages 256
- [77] P. Sheng and V. Joshi: "A numerical model to predict heat affected zone in laser cutting of steels", [Http://greenmfg.me.berkeley.edu/lml/research/haz/](http://greenmfg.me.berkeley.edu/lml/research/haz/)
- [78] P.S. Sheng, V.S. Joshi: "Analysis of heat affected zone formation for laser cutting of stainless steel", *Journal of Materials Processing technology*, Sept.1995 Vol 53. Part 3 / 4 Pages 879.
- [79] J.H. Kim, Y. J. Oh, I. S. Hwang, D. J. Kim, J. T. Kim: "Fracture behaviour of heat affected zone in low alloy steels", *Journal of Nuclear* 299(2001)132-139

- [80] D. Butorin, D. Gerasimov: "The influence of structural components size on the abrasion resistance of steel".
- [81] ASTM Standards Section 3, Metals Test Methods and Analytical Procedures, Volume 3.01, Mechanical Testing; Elevated and Low-Temperature Tests; Metallography.
- [82] J. M. Whitney, I. M. Daniel and R. Byron Pipes, "Experimental mechanics of fiber reinforced composite materials", revised edition, published by the Society of Experimental Mechanics, Brookfield Center, Connecticut.
- [83] M.E. Tuttle, "Fundamental Strain-gage Technology", from the "Manual on experimental methods for mechanical testing of composites", edited by Richard L.Pendleton and Mark E.Tuttle, published by the Society of Experimental Mechanics, Brookfield Center, Connecticut.
- [84] C. W. Bert, "Liquid-Metal Strain Gages", from the "Manual on experimental methods for mechanical testing of composites", edited by Richard L.Pendleton and Mark E.Tuttle, published by the Society of Experimental Mechanics, Brookfield Center, Connecticut.
- [85] V.J. Parks, "Geometric Moire", from the "Manual on experimental methods for mechanical testing of composites", edited by Richard L.Pendleton and Mark E.Tuttle, published by the Society of Experimental Mechanics, Brookfield Center, Connecticut.
- [86] Y.Y.Hung, "Shearography : A New Strain-Measurement Technique and a Practical Approach to Nondestructive Testing", from the "Manual on experimental methods for mechanical testing of composites", edited by Richard L.Pendleton and Mark E.Tuttle, published by the Society of Experimental Mechanics, Brookfield Center, Connecticut.
- [87] R.A Higgins, "Materials for the Engineering Technician", Third Edition, ISBN 0470 23626 4
- [88] T.S. Byun, E.H. Lee, J.D. Hunn, K. Farrell, L.K. Mansur: "Characterization of plastic deformation in a disk bend test", *Journal of Nuclear Materials* 294 (2001) 256-266.
- [89] I. Beltrami, A. Bertholds, D. Dauw: "A simplified post process for wire cut EDM", *Journal of Materials Processing Technology* 58 (1996) 385-389

- [90] O. Kraft, R.Schwaiger, W.D. Nix: "Measurement of mechanical properties in small dimensions by microbeam deflection".
- [91] T. Lube, M. Manner: "Development of a bending-test device for small samples", Key Engineering Materials Vol. 132-136 (1997) p 488-491.
- [92] J.S. Stolken, A.G. Evans: "A microbend test method for measuring the plasticity length scale", Acta, Mater. 46(1998)519-5115.
- [93] F.Krompholz, D. Kalkhof, E. Groth: "Size effects studies on Geometrically scaled three point bend type specimen with U-notches", PSI-Bericht-(2001) No.01-03
- [94] G. F. Vander Voort, "Handbook of Applied Metallography". ASIN: 0317456156.
- [95] W. Rostoker, J. R. Dvorak, "Interpretation of Metallographic Structure.", ISBN: 0125982550.
- [96] J. Newby, "Metals Handbook : Metallography and Microstructure". ISBN: 0871700158.
- [97] G. Petzow, "Metallographic Etching", ISBN 0-87170-002-6.
- [98] R. H. Greaves, H. Wrighton, "Practical Microscopical Metallography", ISBN 412-20400.
- [99] G. F. Vander Voort, "Metallography: Principles and Practice". ISBN: 0871706725.
- [100] Ma, "Metallography: "A Practical Tool for Correlating the Structure and Properties of Materials", ISBN: 080310510X.
- [101] J. Krzystof , B.R. Kurzydowski : "The Quantitative Description of the Microstructure of Materials", CRC press, Inc.
- [102] B.P Murphy, P. Savage, B.P O'Donnell, P.E. McHugh : "Computational modelling and experimental testing to determine the constitutive and failure behaviour of 316L stainless steel for stent applications.", Acta Bioengineering and Biomechanics, Vol. 4, Sup. 1 (2002).
- [103] J. Schiøtz and T. Vegge: "Computer simulations of the mechanical properties of metals", Science Progress 82, 313-325 (1999).
- [104] A. Paquin, S. Berbenni, V. Favier, X. Lemoine, M. Berveiller: "Micromechanical modelling of the elasto-viscoplastic behaviour of polycrystalline steels", International Journal of Plasticity 17(2001) 1267-1302.

- [105] T.A. Venkatesh, K.J. Van Vliet, A.E. Giannakopoulos, S. Suresh: "Determination of elasto-plastic properties by instrumented sharp indentation : guidelines for property extraction", *Scripta Materialia* 42 (2000) 833-839.
- [106] G.N. O'Donnell, C.F. Ciobanu : "A comparison study on 2D and 3D finite element models for the fatigue of stents", *Acta Bioengineering and Biomechanics*, Vol. 4, Sup. 1 (2002).
- [107] H.G.Paris: "Metallurgy, Processing and Applications of metal wires-A review", *Journal of Technology*, Georgia Tech Research Institute.
- [108] M.E. Kassner, M.T. Perez-Prado: "Fire-power-law creep in single phase metals and alloys" *Progress in Materials Science* 45 (2000) 1-102.
- [109] L. Keller, P. Stanek: "Nondestructive determination of the transition from the elastic into microplastic state", *Materials Science Forum* Vol. 210-213 (1996) pp. 63-68.
- [110] J. V. Carstensen, T. Leffers, T. Lorentzen, O. B. Pedersen, B. F. Sørensen and G. Winther: "Modelling of Structure and Mechanics of Materials from Microscale to Product", *Proceedings of the 19th Risø International Symposium on Materials Science*, pp. 133-148 (1998).
- [111] K. Kyung-Suk, J. A. Hurtado: "Length-scale effects in nano- and micro-mechanics of solids", *Key Engineering Materials* Vol. 183-187 (2000) pp 1-8.
- [112] M. Kuroda, V. Tvergaard: "Shear band development predicted by a non-normality theory of plasticity and comparison to crystal predictions.", *International Journal of Solids and Structures* 38 (2001)8945-8960.
- [113] J.T. Gau, G.L. Kinzel: "An experimental investigation of the influence of the Bauschinger effect on springback predictions", *Journal of /materials Processing Technology* 108 (2001) 369-375.
- [114] G. Brecht, P.D. Bons, M.W. Jessel: " Domain boundary migration at multiple scales in experiment and nature". Volume 2, *Journal of the virtual explorer*.

WEBSITES

- [web 1] www.hgcardio.com/heart_disease.htm
- [web 2] www.guidant.com/
- [web 3] www.bae.ncsu.edu/bae/courses/bae465/1995_projects/dill/
- [web 4] www.zipmall.com/mpm-art-coronary.htm
- [web 5] www.angiodynamics.com
- [web 6] www.bostonscientific.com/
- [web 7] www.medtronicave.com
- [web 8] www.jomed.com
- [web 9] www.biocompatibles.co.uk/
- [web 10] www.steel.sandvik.com/
- [web 11] www.matweb.com
- [web 12] www.lasermade.com.au/
- [web 13] www.lasermachining.com/applications/processes/cutting.htm
- [web 14] www.rofin-baasel.com/
- [web 15] www.ableelectropolishing.com/electrop.htm
- [web 16] www.celcoinc.com/electro.htm
- [web 17] physics.uwstout.edu/strength/special/spec85.htm
- [web 18] www.efunda.com
- [web 19] spiff.mech.uwa.edu.au/sarndt/wps/wps2.html
- [web 20] www.metallography.com
- [web 21] www.metallographic.com
- [web 22] www.struers.com
- [web 23] www.buehler.com
- [web 24] www.chem.ufl.edu
- [web 25] www.mos.org/sln/SEM
- [web 26] www.unl.edu/CMRAcfem.semoptic.htm

APPENDIX I

SUPPLIER'S SPECIFICATIONS OF THE 316L TUBES

Certification of Analyses and Tests			
Cert Number : 15842		P.O.# : 715546 ITEM 1	Prep Date : 09/28/2001
Customer : BIOCOMPATIBLES CARDIOVASCULAR		UT SO #: CT010495	Qty : 3001.00 FT
Specifications: ASTM F-139 REV 00, CHEM ONLY, LESS YIELD STRENGTH			
Description: OD .0615/.0621 WA .0042/.0048 LT 35/37 IN DWG CM-0056 REV 2 P/N CM-0056-02 MADE IN USA			
Chemical Composition		Mechanical Properties	
Alloy : STAINLESS 316L MEDICAL		Test Number(s) : 75170	
Lot No : 1967B Heat: 515070		Test Date : 09/24/2001	
Material : WELDED & DRAWN TUBE			
C	0.017	WP	Temper U.T.S. (PSI) Elongation (%) in 2" Y.S (PSI)
Cr	17.51	WP	
Cu	0.03	WP	1 - Annealed 91960 - 92840 49 - 57 -
Fe	BAL	WP	
Mn	1.85	WP	Hardness Avg Grain Size Micro
Mo	2.85	WP	
N	0.035	WP	HRB 88.60 ASTM 8.5 SATISFACTORY
Ni	14.75	WP	
P	0.017	WP	Flare Test Flatten Test Hydrostatic Test Pressure Test
S	0.002	WP	
Si	0.33	WP	Aged U.T.S. (PSI) Aged Elongation (%) Aged Y.S. (PSI)
			Surface RA Concentricity Corrosion Test Embrittlement Test
			Surface Check / par.
0 past 3rd decimal is insignificant WP = Weight %, PPM = Parts/million Bal = Balance, ND = Not Detected			OD 16.7/ID 9.7 SATISFACTORY
			FASSIVATION SATISFACTORY

Fig.I.1 Supplier's Specifications of the 316L tube.

APPENDIX II

SAMPLE PREPARATION

MOUNTING

Cold Mounting

Cold mounting requires no pressure and little heat, and is a means of mounting large numbers of specimens more rapidly than by compression mounting.

Materials for cold mounting are classified as polyesters, epoxides and acrylics. Polyesters are transparent and usually water clear; epoxies are almost transparent and straw color; acrylics are opaque. Cold mounting materials of all three classifications are two component systems that consist of resin and a hardener; both the resin and the hardener can be liquid, both can be solids, or one can be liquid and the other a solid. Mixing of the resin and the hardener produces exothermic polymerisation, and therefore this operation is critical in producing a satisfactory cure and limiting the temperature to a permissible level. The temperature rise may be reduced at the expense of longer curing time.

Epoxy resins are the most widely used cold mounting materials. They are hard and adhere tenaciously to most metallurgical, mineral and ceramic specimen. They also exhibit lower volume shrinkage than either polyesters or acrylics and are very useful for impregnating porous structures or cracks by vacuum method. Epoxy resin mounts may be cured in a low-temperature or placed in a low temperature oven for fast curing, depending on the mixture ratio of resin to hardener.

Polyester resins have greater volume shrinkage than epoxies. They provide water-clear or slightly coloured transparent mounts, which strip readily from glass casting surfaces and metal moulds.

Acrylic materials are fast curing, and the mixing and casting process for the acrylics is quick and simple. The fast curing rate results from the relatively high rate heat evolution during exothermic polymerisation, but some control of the exothermal temperature rise can be accomplished by varying the sizes of the specimen and the mount. Stripping acrylic mounts from metal or glass moulds is not difficult.

GRINDING

Grinding is a most important operation in specimen preparation. During grinding the operator has the opportunity of minimizing mechanical surface damage that must be removed by subsequent polishing operations. Even if sectioning is done in a careless manner, resulting in severe surface damage, the damage can be eliminated by prolonged grinding. However, prolonged polishing will do little toward eliminating severe surface damage introduced by grinding.

Grinding is accomplished by abrading the specimen surface through a sequence of operations using progressively finer abrasive grit. Grit sizes from 40 mesh through 150 mesh are usually regarded as coarse abrasives and grit sizes from 180 mesh through 600 mesh as fine abrasives.

Grinding should commence with coarse grit size that will establish an initial flat surface and remove the effects of sectioning within a few minutes. An abrasive grit size 150 or 180 mesh is coarse enough to use on specimen surfaces sectioned by an abrasive cut off wheel. The abrasive used for each succeeding grinding operation should be one or two grit size smaller than that used in the preceding operation. A satisfactory grinding sequence might involve grit sizes of 180, 240, 400 and 600 mesh.

All grinding should be done wet, provided water has no adverse effects on any constituents of the microstructure. Wet grinding minimizes loading of the abrasive with metal removed from the specimen being prepared. Water flushes away most of the surface removal products before they become embedded between adjacent abrasive particles. Thus, the sharp edges of the abrasive particle remain exposed to the surface of the specimen throughout the operation. If the sharp edges are unexposed the result is smearing of the abraded surface rather than removal of surface metal. The operator must determine, by examining the specimen throughout the sequence of grinding steps, that the abrasive is actually cutting and not merely smearing or burnishing. Burnishing results primarily from using an abrasive beyond its effective limit. Use of worn-out abrasives and dulled cutting edges is detrimental to good preparation.

Another advantage of the wet grinding is the cooling effect of the water. Considerable frictional heat can develop at the surface of a specimen during grinding and can cause alterations of the true microstructure - for example, tempering of martensite in steel - that

cannot be removed during polishing. Wet grinding provides effective control of overheating.

The purpose of grinding is to lessen the depth of deformed metal to the point where the last vestiges of damage can be removed by series of polishing steps. The scratch depth and the depth of cold worked metal underneath the scratches decrease with decreasing particle size of abrasive. However the depth of cold worked metal is roughly inversely proportional to the hardness of the specimen and may be 10 to 50 times the depth of penetration of the abrasive particle. It is imperative that each grinding steps completely remove the deformed metal produced by the previous step. The operator usually can assume this is accomplished if he or she grinds more than twice as long as the time required to remove the scratches incurred by the previous step. To ensure the complete elimination of the previous grinding scratches found by visual inspection, the direction of grinding must be changed 45 to 90 degrees between successive grit sizes. In addition, microscopic examination of the various ground surfaces during the grinding sequence may be worthwhile in evaluating the effect of grinding. Each ground surface should have scratches that are clean-cut and uniform in size, with no evidence of previous grinding scratches.

Success in grinding depends in part on the pressure applied to the specimen. A very light pressure removes insufficient metal. Somewhat heavier pressure produce polishing, while still heavier pressure brings about the desired grinding action. Very heavy pressure results in non-uniform scratch size, deep gouges, and embedded abrasive particles. Generally, a medium to moderately heavy pressure applied firmly gives the best results.

Grinding Mediums

The grinding abrasives commonly used in the preparation of specimens are silicon carbide (SiC), aluminium oxide (Al_2O_3), emery ($Al_2O_3 - Fe_3O_4$), diamond particles, etc. They are generally bonded to paper or cloth backing material of various weights in the form of sheets, disks and belts of various sizes. Limited use is made of grinding wheels consisting of abrasives embedded in a bonding material. The abrasive may be also used in powder form by charging the grinding surfaces with loose abrasive particles.

Silicon carbide has a hardness of 9.5 on the Mohs scale, which is near the hardness of diamond. Silicon carbide abrasive particles are angular and jagged in shape and have very sharp edges and corners. Because of these characteristics, silicon carbide is a very effective grinding abrasive and is preferred to other abrasives for metallographic grinding of almost all types of metal.

Aluminium oxide abrasive material has a trigonal crystal structure and a hardness of 9.1 on the Mohs scale.

Emery is an impure, fine-grained variety of natural corundum containing 25 to 45 admixed iron oxide. The hardness of emery is Mohs 8.0. Emery abrasive particles have much smoother surfaces than either silicon carbide or aluminium oxide abrasive particles. For this reason, emery particles do not feel as coarse as silicon carbide or aluminium oxide particles of equivalent grit size and the cutting rate of emery is inferior to that of either of the two other abrasives.

Another abrasive material used occasionally for grinding specimens is boron carbide, which has a hardness of nearly 10 on Mohs scale. Boron carbide is used primarily for grinding ceramic and other extremely hard materials.

Increasing use is being made of diamond as a grinding medium as well as a polishing medium. Carefully sized diamond abrasive particles are available from 280 microns (about 60 mesh) to 0.25 microns in size. The coarser grades of diamond are used in the form of resin-bonded cloth-backed disks, metal bonded lapping surfaces, and loose particles for charging of grinding surfaces. Diamond abrasives of all sizes are available as suspensions in oil-soluble and water-soluble paste vehicles known as diamond compounds. The extreme hardness (Mohs 10) and sharp cutting edges of diamond particles impart at high cutting rate to diamond abrasives. Diamond abrasives are particularly suitable for grinding the harder alloys and refractory materials.

Hand Grinding

A simple set-up for hand grinding can be provided by a piece of plate glass, or other material with a hard, flat surface, on which an abrasive sheet rests. The specimen is held by hand against the abrasive sheet as the operator moves specimen in a rhythmic style away from and toward them in a straight line. Heavier pressure should be applied on the

forward stroke than on the return stroke. The grinding can be done wet by sloping the plate glass surface toward the operator and providing a copious flow of water over the abrasive sheet. Fig.II.1 shows a hand belt grinder.



Fig.II.1 Hand belt grinder

Belt, Disk and Surface Grinders

The most common types of motor-driven grinding equipment are the belt grinder and the disk grinder. In using either, the metallographic specimen is held by hand against a moving, fixed-abrasive grinding material supported by a platen. Belt grinders and disk grinders may be used in either a horizontal or vertical position.

Specimens can be belt or disk ground successfully through all grinding sequences.

POLISHING

Polishing is the final step in producing a surface that is flat, scratch free, and mirror like in appearance. Such a surface is necessary for subsequent accurate metallographic interpretation, both qualitative and quantitative. The polishing technique used should not introduce extraneous structure such as disturbed metal, pitting, dragging out of inclusions, comet tails and staining.

Before final polishing is started, the surface condition should be at least as good as that obtained by grinding with a 400-grit (25 microns) abrasive.

Polishing should be done in a relatively dust-free area, preferably removed from the area for sectioning, mounting and rough grinding. Any contamination of a polishing lap by abrasive particles carried over from a preceding operation or by dust, dirt or other foreign matter in the air cannot be tolerated. Carryover as a result of improper cleaning between final polishing steps is another prime source of contamination. The specimen can be cleaned ultrasonically or by careful washing under running water and swabbing with cotton. In automatic equipment in which holding fixtures for the specimens are also transferred through successive polishing steps, proper cleaning of the assembly can be accomplished only by using an ultrasonic cleaner.

If a polishing lap becomes contaminated, it is virtually impossible to remove all of the contaminant by washing the polishing cloth. Instead, the operator should replace the cloth and use fresh polishing solution. Cleanness cannot be overemphasized. It takes only one particle of grit on a final polishing lap to ruin all prior preparation.

Hand Polishing

Specimen Movement

The specimen is held with one or both hands, depending on the operator's preference, and is rotated in a direction counter to the rotation of the polishing wheel. In addition, the specimen is continually moved back and forth between the centre and the edge of the wheel, thereby ensuring even distribution of the abrasive and uniform wear of the polishing cloth. The main reason for rotating the specimen is to prevent the formation of "comet tails".

Polishing Pressure

The correct amount of applied pressure must be determined by experience; in general, firm hand pressure is applied to the specimen in the initial polishing step and is proportionally decreased with successively finer polishing steps. For very soft materials, pressure other than that from the weight of the specimen itself may be eliminated entirely in the last polishing operation.

Automatic Polishing

High quality preparation of most metallographic specimens often can be expedited by the use of automatic polishers. Automatic polishing equipment usually allows the preparation

of several specimens simultaneously. Some methods of specimen preparation can be done only with automatic polishers, such as remote polishing of radioactive materials, chemical-mechanical polishing, and polishing in special atmospheres. There is no ideal automatic polisher; each has its merits and shortcomings and each metallographer must determine which is best for their particular requirements.

Polishing Cloths

The requirements of any good polishing cloth include the ability to hold an abrasive, long life, absence of any foreign material that may cause scratches, and absence of any processing chemicals that may react with the specimen.

A cloth without nap or with a very low nap is preferred for the preliminary or rough polishing operation. The absence of nap ensures maximum contact with the polishing abrasive, and results in fast cutting with minimum of relief. The cloths most frequently used are canvas, low-nap, cotton, nylon, silk and Pelon. These cloths are stretched tight on the laps and fastened securely, usually by a band-type clamp. Some cloths are available with a contact adhesive on the back, which greatly simplifies installation on the wheel. After installation, the cloths are charged with the appropriate abrasive (usually in sizes from 15 microns down to 1 microns) and carrier. Rough polishing is usually done with the laps rotating at 500 to 600 rpm. Cloths with a medium or high nap are ordinarily used on slow rotating laps (less than 300 rpm) for intermediate and final polishing. Felt or billiard cloths (100% virgin wool), used with 0.3 micron aluminium oxide or other comparable abrasive, are excellent for intermediate polishing of soft metals (most nonferrous alloys and low carbon steels) and final polishing of hard materials (such as hardened alloy steels). One of the most popular cloths for final polishing of most metals is composed of densely packed, vertically aligned, synthetic fibres bonded to a suitable backing. For some metals or for particular types of polishing, other cloths, such as velvets, satins, cashmeres or cottons, may be required. The ability to select the proper combination of cloth, abrasive, carrier, polishing speed (rotational speed of the polishing wheel), and pressure applied can be acquired only by experience.

Polishing Abrasives

Polishing usually involves the use one or more of five types of abrasive: aluminium oxide (Al_2O_3), magnesium oxide (MgO), chromic oxide (Cr_2O_3), iron oxide (Fe_2O_3), and diamond compound. With the exception of diamond compound these abrasives are normally used in a distilled water suspension, but if the metal to be polished is not compatible with water, other suspensions, such as ethylene glycol, alcohol, kerosene or glycerine, may be required. The diamond compounds should be extended only with the carrier recommended by the manufacturer.

Aluminium oxide (aluminia) is the polishing abrasive most widely used for general metallographic polishing. The alpha grade aluminium oxide is used in a range of particle sizes from 15 microns to 0.3 micron. For some hard materials the 0.3 micron size is sufficient for a final polish. The gamma grade of aluminium oxide is available in a 0.05 micron particle size for final polishing.

Magnesium oxide (magnesia) is recommended for final polishing, especially for the preparation of magnesium and aluminium, and their alloys. Only the metallographic grades, which contain no water soluble alkalis, should be used; otherwise, any free alkalis present could stain and chemically attack the specimen. Magnesium oxide also reacts slowly with water to form magnesium hydroxide. This in turn reacts with carbon dioxide present in the atmosphere and in tap water to form magnesium carbonate, which can contaminate the polishing lap. If carbonate is present, the polishing cloth must be replaced or treated in acidified distilled water (2% HCl solution) to convert the carbonate to water-soluble magnesium chloride. If the polishing cloth is to be retained for future polishing, it should be removed from the wheel immediately after use, washed in running water and stored in the 2% hydrochloric acid solution.

Chromic oxide, available in a range of particle size down to 0.05 micron, is used for rough and final polishing of steel and cast iron.

Iron oxide, known as jeweler's rouge is available as a powder of approximately 3 micron particle size. It may be used for rough and final polishing of steel and cast iron, depending on the finish required.

Diamond polishing compounds are becoming increasingly popular for preparing metallographic specimen. Diamond is the only substance hard enough and with good

enough cutting qualities to be used for mechanical polishing of materials such as boron carbide and sintered tungsten. Specimens that have both hard and soft constituents, such as graphite in cast iron and silicon in aluminium, can be polished without causing relief, with diamond compounds on an appropriate lap. These polishing compounds are available either in water soluble and oil soluble carriers or in the form of dry diamond powder in particle size down to 0.25 microns.

ETCHING

The purpose of etching is to optically enhance microstructural features such as grain size and phase features. Etching selectively alters these microstructural features based on composition, stress, or crystal structure. The most common technique for etching is selective chemical etching. Other techniques such as molten salt, electrolytic, thermal and plasma etching have also found specialized applications.

Chemical etching

Chemical etching selectively attacks specific microstructural features. It generally consists of a mixture of acids or bases with oxidizing or reducing agents. Etching may be done either by immersion of the sample in the etchant or by swabbing, depending on the etchant strength. Table II.1 gives a list of the common chemical etchants.

Etchant	Composition	Conc.	Conditions	Comments
Kellers Etch	Distilled water	190 ml	10-30 second immersion. Use only fresh etchant	
	Nitric acid	5 ml		
	Hydrochloric acid	3 ml		
	Hydrofluoric acid	2 ml		
Kroll's Reagent	Distilled water	92 ml	15 seconds	
	Nitric acid	6 ml		
	Hydrofluoric acid	2 ml		

Nital	Ethanol Nitric acid	100 ml 1-10 ml	Seconds to minutes	
Kallings Reagent	Distilled water Copper chloride (CuCl ₂) Hydrochloric acid Ethanol (85%) or Methanol (95%)	40 ml 2 grams 40 ml 40-80 ml	Immerse or swab for few seconds to a few minutes	
Kallings Reagent Number 2	ethanol, HCl, CuCl ₂	100 mL 100 mL 5 g		
Lepito's Reagent	Acetic acid Nitric acid	50 ml 50 ml	Swab	
Marble's Reagent	Distilled Water Hydrochloric acid Copper sulfate	50 ml 50 ml 10 grams	Immersion or swab etching for a few seconds	
Murakami Reagent	Distilled Water K ₃ Fe(CN) ₆ NaOH or KOH	100 ml 10 grams 10 grams	Immerse or swab for seconds to minutes	Use fresh
Picral	Ethanol Picric acid	100 ml 2-4 grams	Seconds to minutes	Do not let crystallize or dry - explosive

Vilella's Reagent	Glycerol Nitric acid Hydrochloric acid	45 ml 15 ml 30 ml	Seconds to minutes	
No name	Equal part of : HCL HNO ₃ Water		Seconds	

Table II.1. Common chemical etchants.

Electrolytic etching

Electrolytic is another fairly common etching technique. It is similar to chemical etching in that acids and bases are used for modifying the pH, however the electrochemical potential is controlled electrically by varying the voltage and current externally as opposed to chemically. Electrolytic etching is often used for harder to etch specimens that do not respond well to basic chemical etching techniques. Electrolytic techniques require that the specimen be conductive and is therefore limited primarily to metals. Table II.2 gives a list of the common electro-chemical etchants.

Application	Etchant	Conditions	Comments
Wrought stainless steel	Concentrated NH ₄ OH	Stainless steel cathode 6 volts DC Room temperature 30-60 seconds	General structure
Austenitic stainless steels	100 ml Distilled water 10 gram CrO ₃	3-6 volts DC 5-60 seconds	Attacks carbides and sigma phase
stainless steels	60 ml Nitric acid 40 ml Distilled water	Seconds to a minute 1 V	

Steels	10 grams Chromic acid 100 ml Distilled water	Pt or stainless steel cathode 3-6 volts DC 5-60 seconds	Carbide and cementite etching
Stainless Steels	100 ml Distilled water 10 grams oxalic acid	Stainless steel cathode 6 volts DC Room temperature	General structure

Table II.2. Common electro-chemical etchants.

PROCEDURE DEVELOPED FOR THIS STUDY

MOUNTING

The struts have to be mounted on a resin, there are different kind of resins available depending on the material studied (see Chapter 1 paragraph V.2.1). An epoxy resin was chosen for its adherence to metal and low shrinkage. The resin (powder in Fig.II.2 (b)) and a liquid hardener (Fig.II.2(a)) are mixed to form a liquid.



Fig.II.2 (a) Hardener, (b) Epoxy resin.

Mounting of the specimen is done in three steps :

Step 1 : Due to the small dimensions of the strut, sectioning would create too much damage, therefore the entire struts are mounted. The further the struts are from the surface of the sample, the more grinding is necessary to reveal the surface of the struts. Therefore, to limit the grinding time, the struts have to stay at the bottom of the sample. To stop them from floating in the resin, the struts are glued to the bottom of the sample cups (Fig.II.3 (a)).

Step 2 : The resin and hardener are then mixed and the liquid obtained is poured in the sample cup (Fig.II.3 (b)).

Step 3 : After allowing around 8 hours to set, the resin is cured (Fig.II.3 (c)) and the samples are ready (Fig.II.3 (d)).

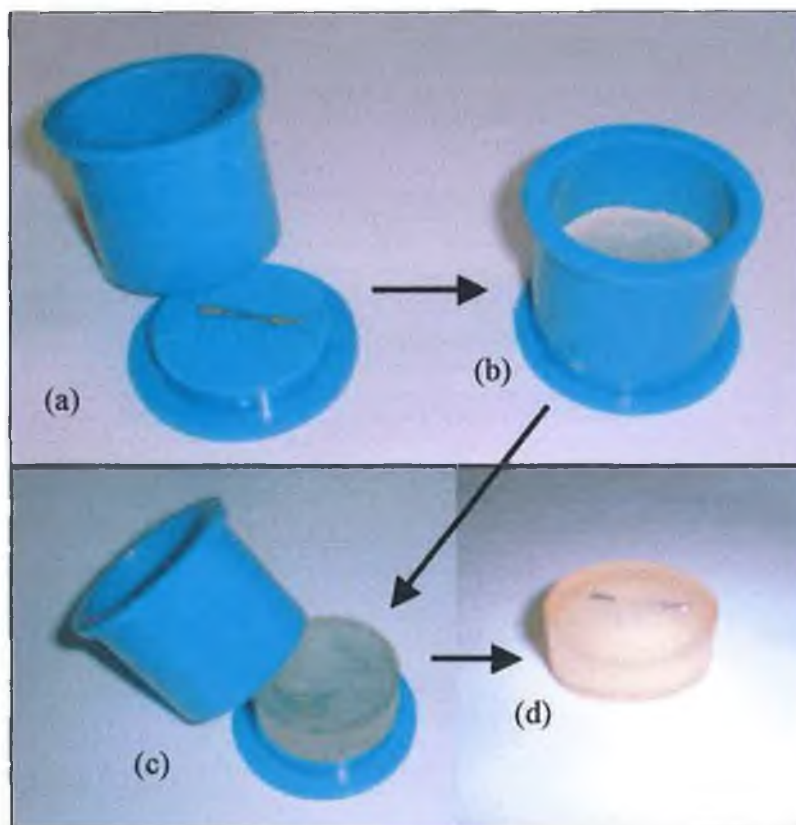


Fig.II.3 (a) strut glued on the bottom of the cup, (b) resin poured in the cup, (c) resin after curing, (d) sample ready for polishing.

GRINDING AND POLISHING

Grinder Polisher

The equipment used for grinding and polishing is a Metaserv 2000 Grinder Polisher (Fig.II.4 (a)). This is a manual procedure (Fig.II.4 (b)), the speed of the revolving disk may be adjusted to control how fast the matter is removed. The pressure applied on the sample determines the quantity of matter removed at each revolution. Considering the small dimensions of the specimen, the quantity of material removed has to be controlled carefully.

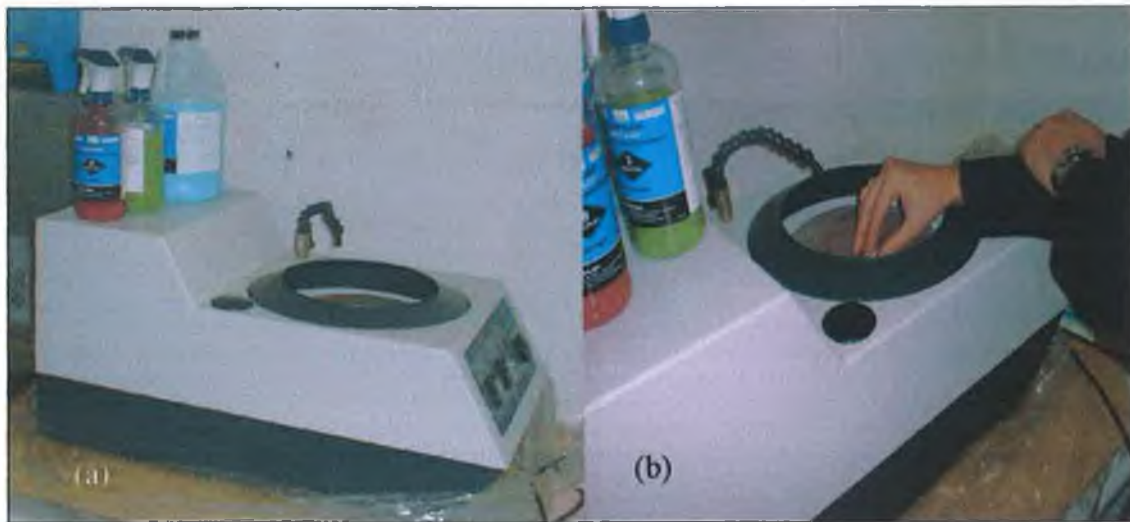


Fig.II.4 (a) Metaserv 2000 Grinder Polisher, (b) manual grinding.

In order to obtain a scratch free surface different polishing disks have to be used successively. The number and sort of disks needed are function of the material and geometry of the sample. Here, the most appropriate is to use four steps :

- Rough grinding (600 grit),
- Fine grinding (9 μm),
- Finer grinding (3 μm),
- Polishing.

Step one : Rough grinding

To remove the resin that might be on top of the strut and flatten the sample, a Silicon Carbide Grinding Paper 600 grit (Fig.II.5) is used. Lower grits exist but the strut being very thin a lower grit would remove too much matter and create too much damage. The coolant is water.



Fig.II.5 Carbide Grinding Paper 600 grit.

After each step the sample has to be examined through the microscope to confirm that the scratches from the previous step have been eliminated.

The microscope used is a Meiji stereomicroscope (Fig.II.6).



Fig.II.6 Meiji stereomicroscope.

The procedure being manual, the speed of the revolving disks and the duration of the step are difficult to set since the manual pressure applied on the sample is not measurable. Therefore, the sample has to be observed regularly and the procedure is stopped when the strut is no longer covered by the resin. Fig.II.7 shows the scratches observed after rough grinding.

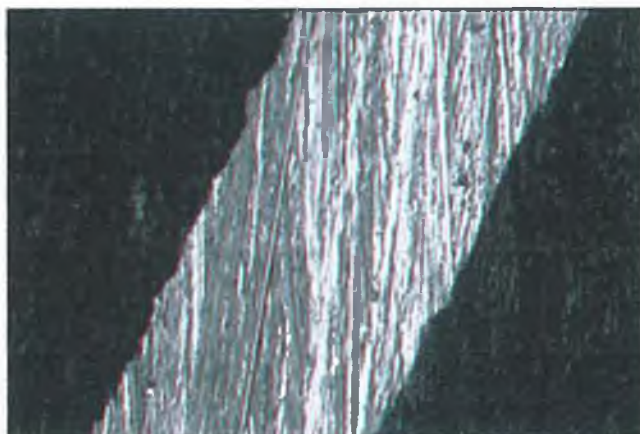


Fig.II.7 X200 Scratches resulting from rough grinding.

Step two : Fine grinding

The first fine grinding is performed using a rough cloth (Ultrapad) (Fig.II.8(a)) and a Metadi Diamond suspension of 9 μm (Fig.II.8 (b)).



Fig.II.8 (a) Ultrapad, (b) Metadi Diamond Suspension 9 μm .

Fig.II.9 shows the structure of the Ultrapad which is three dimensional plastic sheet. The cloth has to be rough in order to retain the 9 μm diamond crystals which would roll on a finer cloth. Depending on the degree of grinding required the supplier advice on the cloth and suspension to combine for best results.



Fig.II.9 Structure of the Ultrapad.

Fig.II.10 shows the scratches resulting from fine grinding. Again the sample needs to be examined regularly until the scratches created by the previous step have disappeared . It can be observed on Fig.II.10 that all the scratches are in the same direction, proving that the scratches created by the previous step have been removed.

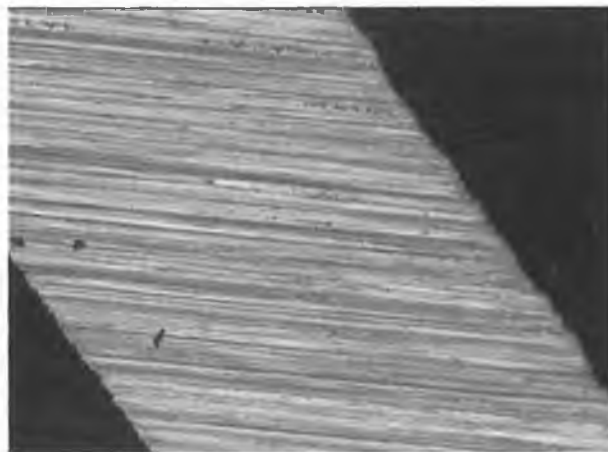


Fig.II.10 X200 Surface obtained after grinding with a 9 μm diamond suspension.

Step three : Finer grinding

A finer cloth (Trident) (Fig.II.11 (a)) and 3 μm diamond suspension (Fig.II.11 (b)) are used. Fig.II.11 (c) shows the structure of the Trident. The cloth is a again plastic sheet but the structure is much finer than the Ultrapad one.

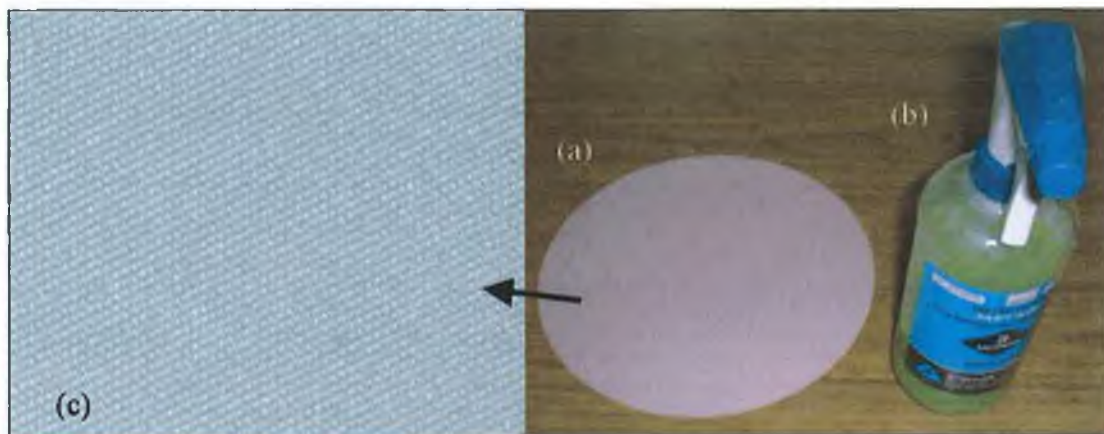


Fig.II.11 (a) Trident cloth, (b) Metadi 3 μm diamond suspension, (c) close-up on the structure of the Trident cloth.

Fig.II.12 shows that the scratches resulting from this step are much smaller than the ones observed after the 9 μm suspension. Few scratches from the previous step are still visible (Fig.II.12). For a perfect preparation, this step should be prolonged until there is no scratches left from step four, however, due to the dimensions of the strut, extra grinding could result in the removal of the entire strut.

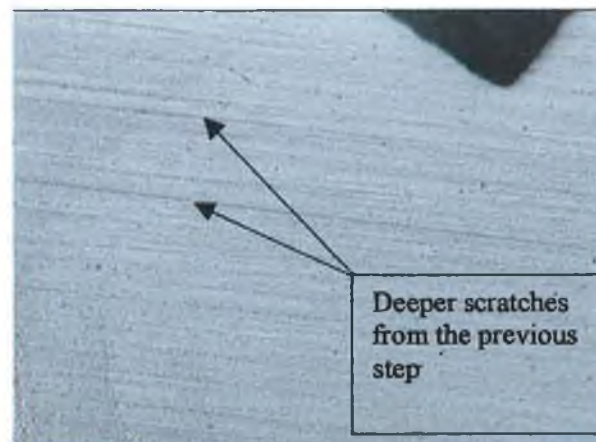


Fig.II.12 X 200 Surface obtained after grinding with a 3 μm diamond suspension.

Step four : Polishing

This is the final step and on completion of polishing the surface should be scratch free. A polishing cloth (Microcloth, Fig.II.13(a)) and a Colloidal Silica Polishing Suspension (Mastermet, Fig.II.13(b)), Fig.II.13 (c) shows a detail of the polishing cloth structure. The cloth is soft and has a woollen texture.

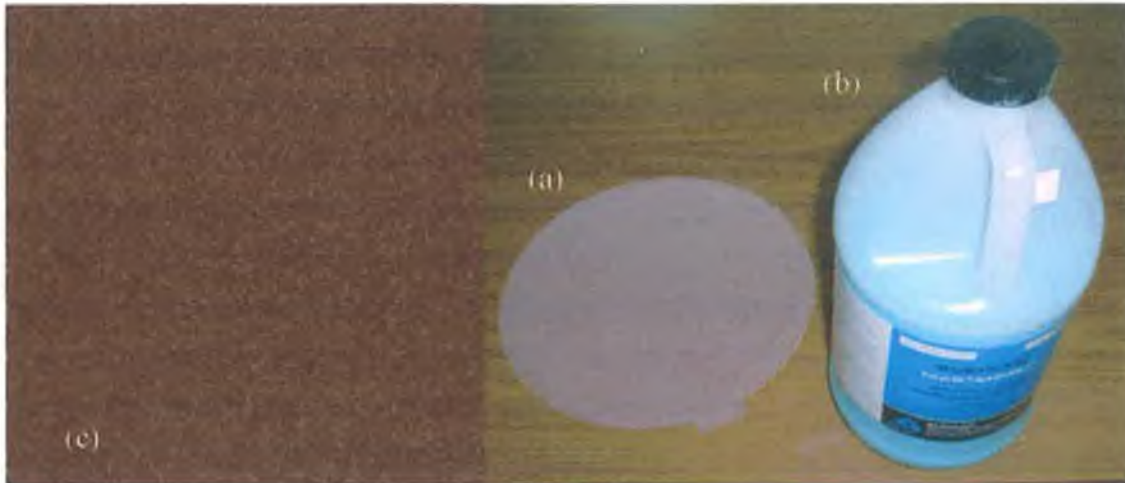


Fig.II.13 (a) Microcloth, (b) Mastermet, (c) Microcloth structure.

Fig.II.14 shows the scratch free surface obtained after final polishing.



Fig.II.14 X200 Surface obtained after polishing.

The sample has been ground and polished. The surface of the sample is now scratch free and ready for etching.

APPENDIX III SCANNING ELECTRON MICROSCOPE TECHNOLOGY

1. An electron gun (virtual source) produces a stream of electrons (Fig.III.1).

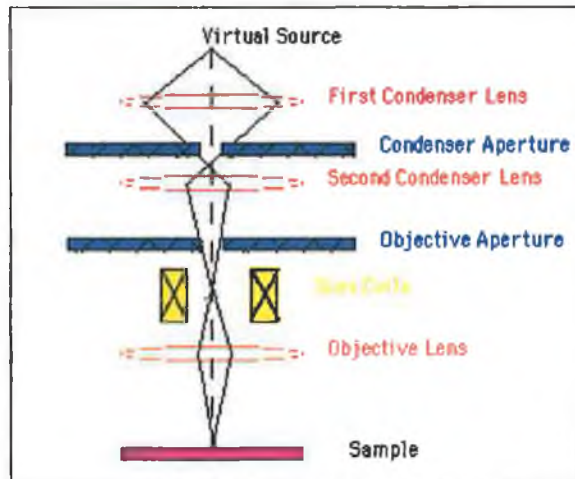


Fig.III.1 S.E.M mechanism.

2. The stream is condensed by the first condenser lens (usually controlled by the "coarse probe current knob"). This lens is used to both form the beam and limit the amount of current in the beam. It works in conjunction with the condenser aperture to eliminate the high-angle electrons from the beam.
3. The beam is then constricted by the condenser aperture (usually not user selectable), eliminating some high-angle electrons.
4. The second condenser lens forms the electrons into a thin, tight, coherent beam and is usually controlled by the "fine probe current knob"
5. A user selectable objective aperture further eliminates high-angle electrons from the beam.
6. A set of coils then "scan" or "sweep" the beam in a grid fashion (like a television), dwelling on points for a period of time determined by the scan speed (usually in the microsecond range).
7. The final lens, the Objective, focuses the scanning beam onto the part of the specimen desired.

8. When the beam strikes the sample (and dwells for a few microseconds) interactions occur inside the sample and are detected with various instruments.
9. Before the beam moves to its next dwell point these instruments count the number of interactions and display a pixel on the computer screen whose intensity is determined by this number (the more reactions the brighter the pixel).
10. This process is repeated until the grid scan is finished, the entire pattern can be scanned 30 times per second.

Specimen interaction (Fig.III.2) is what makes Electron Microscopy possible. The energetic electrons in the microscope strike the sample and various reactions can occur. The reactions noted on the top side of the diagram are utilised when examining thick or bulk specimens(SEM) while the reactions on the bottom side are those examined in thin or foil specimens (TEM).

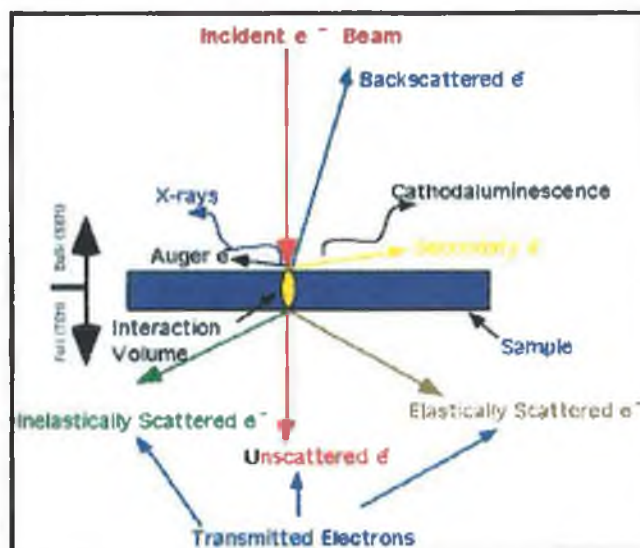


Fig.III.2 Specimen interaction.

Backscattered Electrons

Caused by an incident electron colliding with an atom in the specimen which is nearly normal to the incident's path. The incident electron is then scattered "backward" 180 degrees.

The production of backscattered electrons varies directly with the specimen's atomic number. This differing production rates causes higher atomic number elements to appear brighter than lower atomic number elements.

Secondary Electrons

Caused by an incident electron passing "near" an atom in the specimen, near enough to impart some of its energy to a lower energy electron (usually in the K-shell). This causes a slight energy loss and path change in the incident electron and the ionization of the electron in the specimen atom. This ionized electron then leaves the atom with a very small kinetic energy (5eV) and is then termed a "secondary electron". Each incident electron can produce several secondary electrons.

Production of secondary electrons is very topography related. Due to their low energy, 5eV, only secondaries that are very near the surface (<10nm) can exit the sample and be examined. Any changes in topography in the sample that are larger than this sampling depth will change the yield of secondaries due to collection efficiencies.

Auger Electrons

Caused by the de-energization of the specimen atom after a secondary electron is produced. Since a lower (usually K-shell) electron was emitted from the atom during the secondary electron process an inner (lower energy) shell now has a vacancy. A higher energy electron from the same atom can "fall" to a lower energy, filling the vacancy. As the electron "falls" it emits energy, usually X-rays. This creates an energy surplus in the atom which can be corrected by emitting an outer (lower energy) electron; an Auger Electron.

Auger Electrons have a characteristic energy, unique to each element from which it was emitted from. These electrons are collected and sorted according to energy to give compositional information about the specimen.

X-rays or Light emitted from the atom will have a characteristic energy which is unique to the element from which it originated.

Unscattered Electrons

Incident electrons which are transmitted through the thin specimen without any interaction occurring inside the specimen.

The transmission of unscattered electrons is inversely proportional to the specimen thickness. Areas of the specimen that are thicker will have fewer transmitted unscattered electrons and so will appear darker, conversely the thinner areas will have more transmitted and thus will appear lighter.

Elastically Scattered electrons

Incident electrons that are scattered (deflected from their original path) by atoms in the specimen in an elastic fashion (no loss of energy). These scattered electrons are then transmitted through the remaining portions of the specimen.

All incident electrons have the same energy (thus wavelength) and enter the specimen normal to its surface. All incidents that are scattered by the same atomic spacing will be scattered by the same angle. These "similar angle" scattered electrons can be collated using magnetic lenses to form a pattern of spots; each spot corresponding to a specific atomic spacing (a plane). This pattern can then yield information about the orientation, atomic arrangements and phases present in the area being examined.

Inelastically Scattered Electrons

Incident electrons that interact with specimen atoms in an inelastic fashion, losing energy during the interaction. These electrons are then transmitted through the rest of the specimen.

The inelastic loss of energy by the incident electrons is characteristic of the elements that were interacted with. These energies are unique to each bonding state of each element and thus can be used to extract both compositional and bonding (i.e. oxidation state) information on the specimen region being examined.

Bands of alternating light and dark lines that are formed by inelastic scattering interactions are related to atomic spacing in the specimen. These bands can be either measured (their width is inversely proportional to atomic spacing) or "followed" like a roadmap to the "real" elasticity scattered electron pattern.

APPENDIX IV CURVES OBTAINED FROM TENSILE TESTS

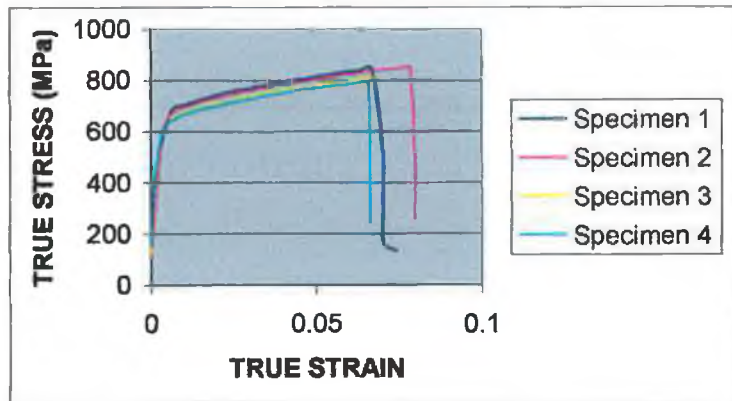


Fig.IV.1 Batch 0 0.05 mm wide laser-cut struts

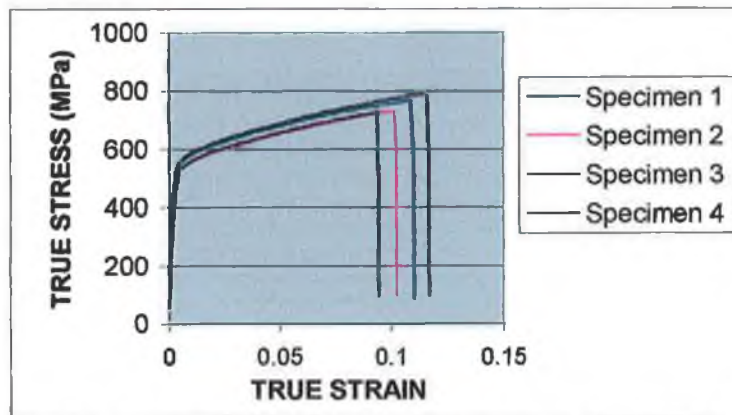


Fig.IV.2 Tensile Batch 0 0.07 mm wide laser-cut struts.

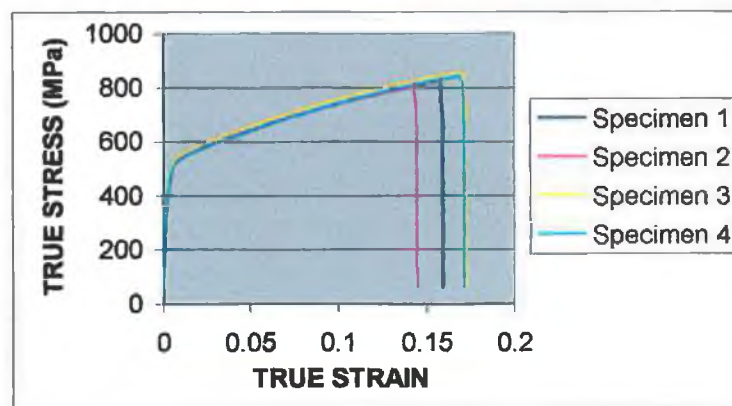


Fig.IV.3 Tensile Batch 0 0.1 mm wide laser-cut struts.

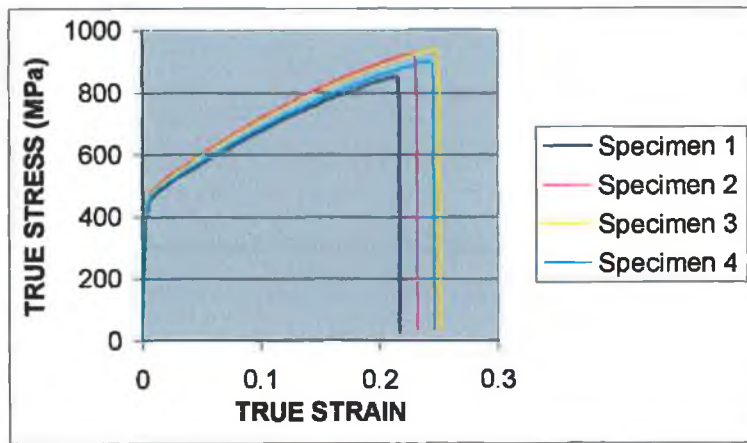


Fig.IV.4 Tensile Batch 0 0.2 mm wide laser-cut struts.

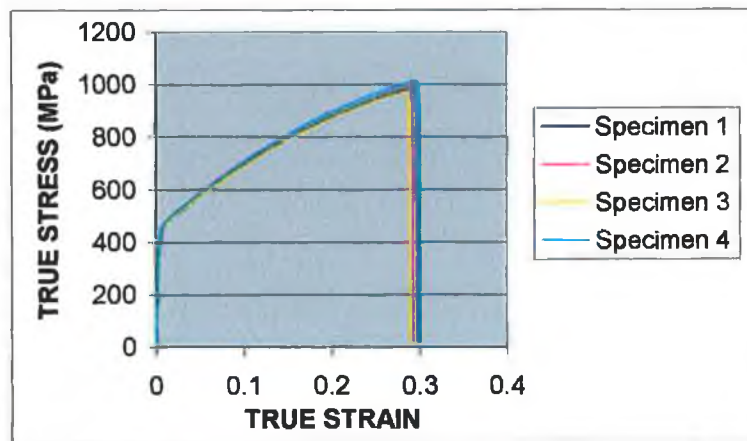


Fig.IV.5 Tensile Batch 0 0.3 mm wide laser-cut struts.

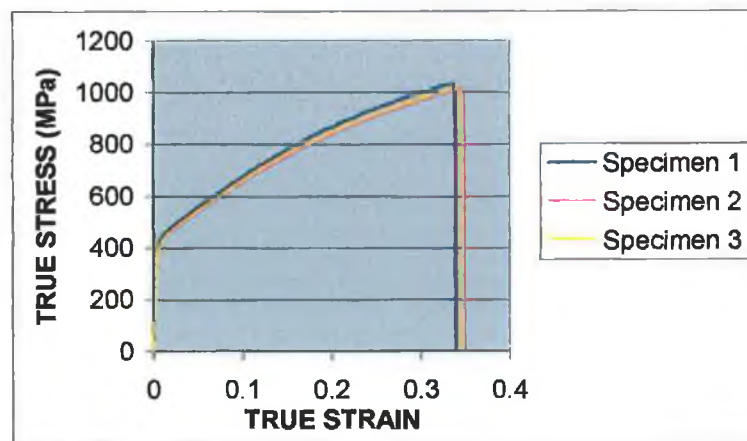


Fig.IV.6 Tensile Batch 0 0.5 mm wide laser-cut struts.

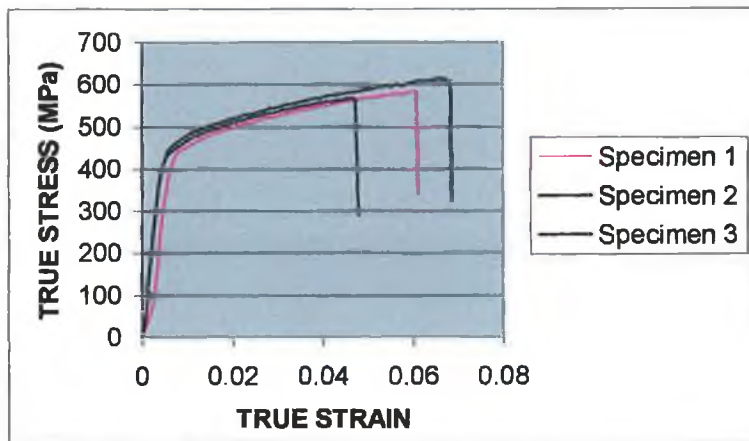


Fig.IV.7 Tensile Batch 1 0.06 mm laser-cut wide struts.

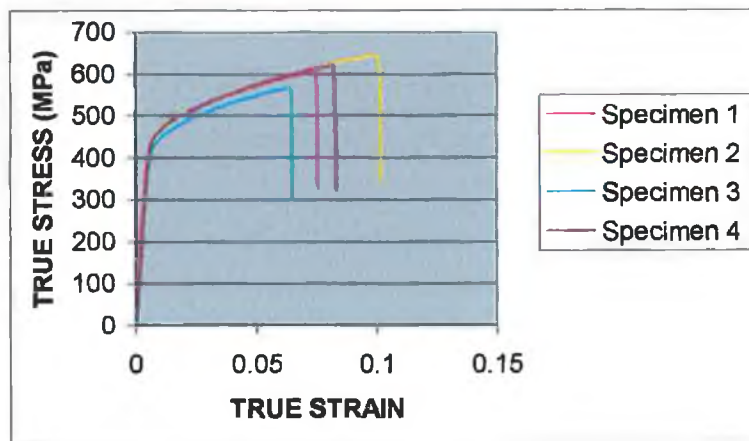


Fig.IV.8 Tensile Batch 1 0.07 mm laser-cut wide struts.

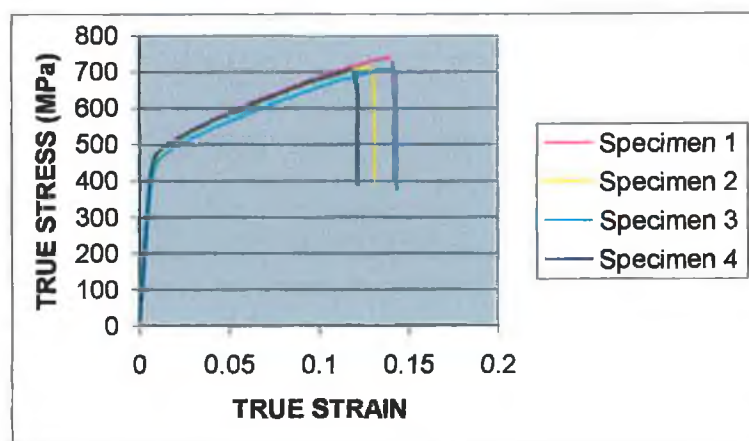


Fig.IV.9 Tensile Batch 1 0.11 mm wide laser-cut struts.

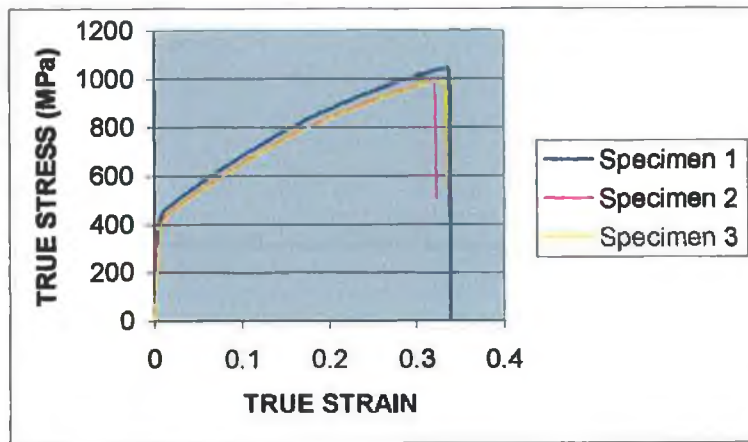


Fig.IV.10 Tensile Batch 1 0.49 mm wide laser-cut struts.

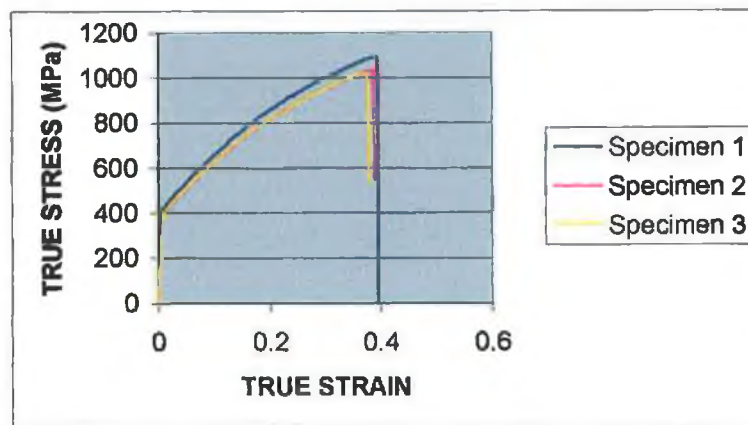


Fig.IV.11 Tensile Batch 1 0.80 mm wide laser-cut struts.

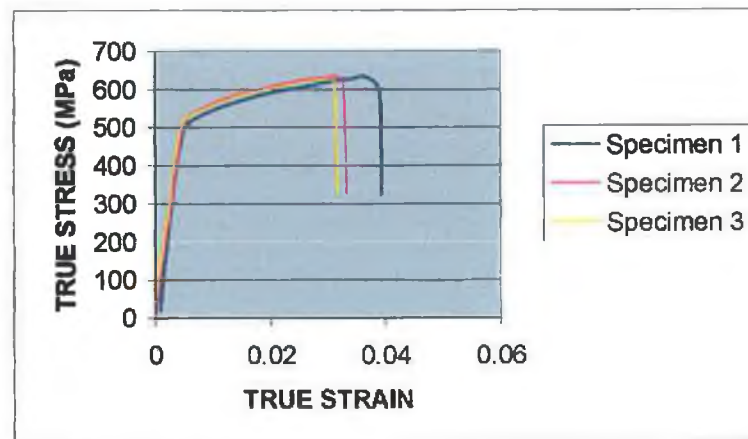


Fig.IV.12 Tensile Batch 2 0.05 mm wide laser-cut struts.

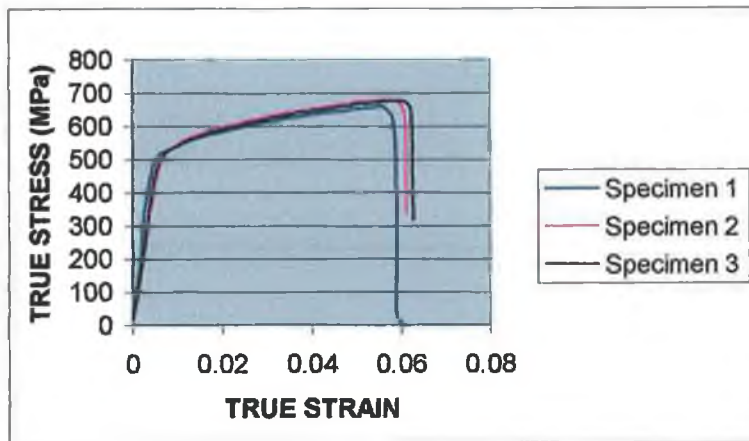


Fig.IV.13 Tensile Batch 2 0.08 mm wide laser-cut struts.

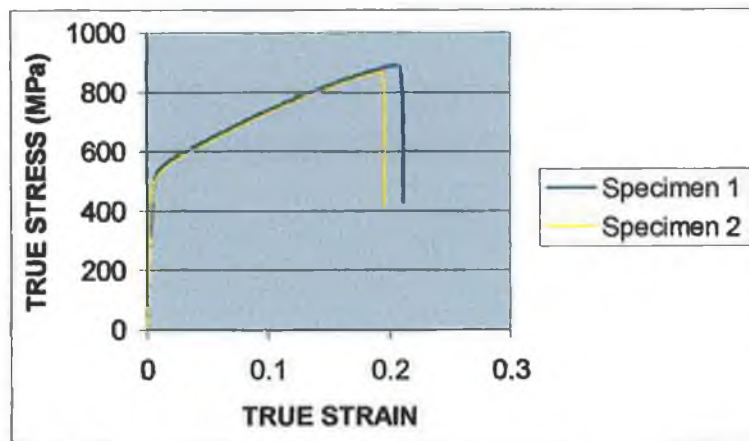


Fig.IV.14 Tensile Batch 2 0.2 mm wide laser-cut struts.

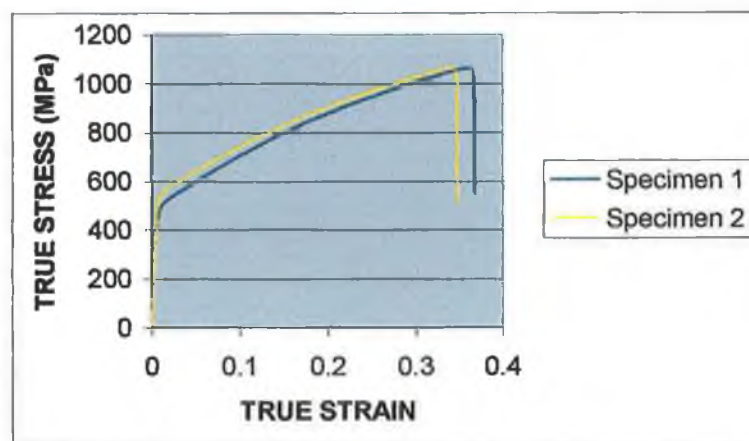


Fig.IV.15 Tensile Batch 2 0.58 mm wide laser-cut struts.

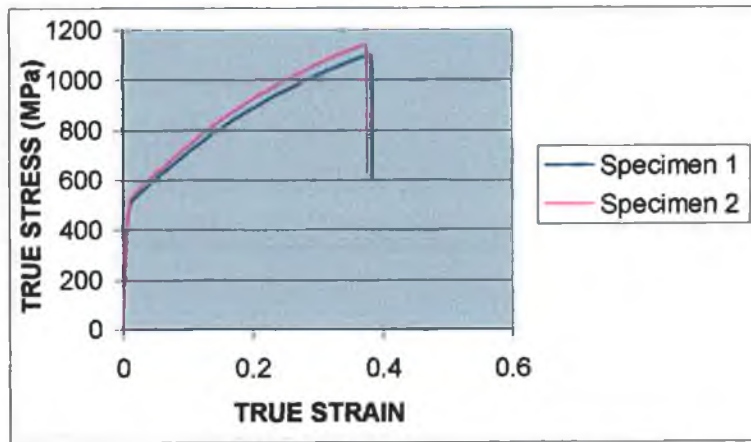


Fig.IV.16 Tensile Batch 2 0.75 mm wide laser cut struts.

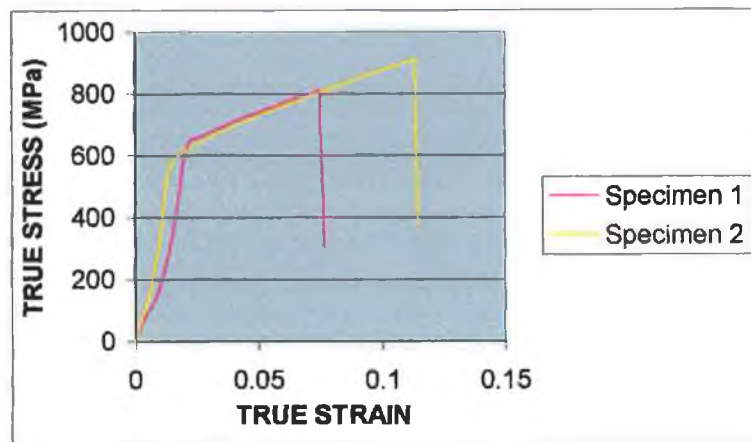


Fig.IV.17 Tensile Batch 0 0.02 mm electro-polished struts.

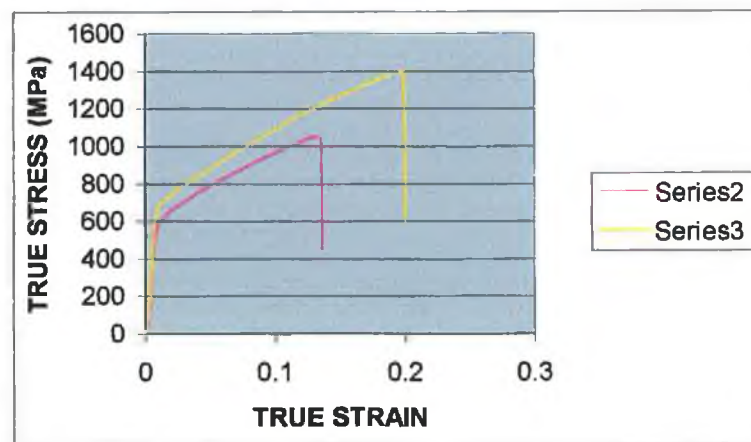


Fig.IV.18 Tensile Batch 0 0.07 mm electro-polished struts.

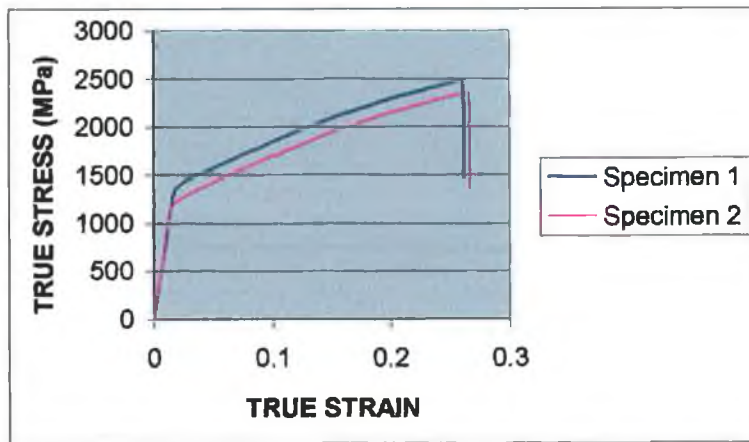


Fig.IV.19 Tensile Batch 0 0.07 mm electro-polished struts.

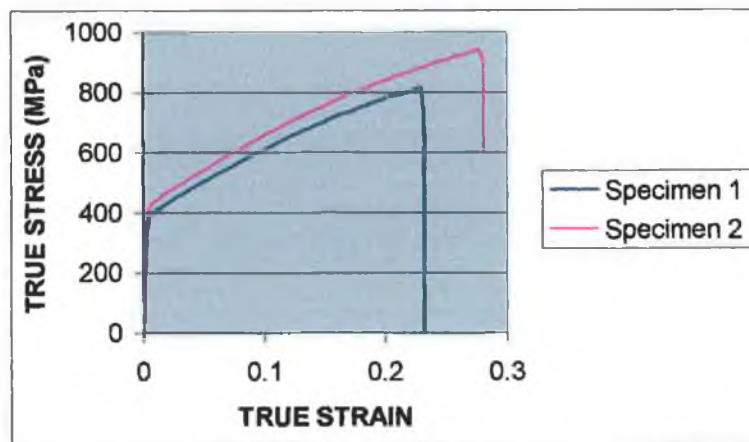


Fig.IV.20 Tensile Batch 0 0.17 mm electro-polished struts.

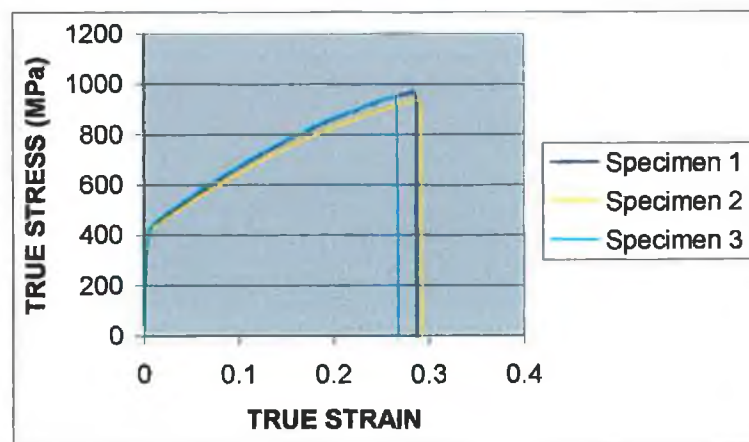


Fig.IV.21 Tensile Batch 0 0.27 mm electro-polished struts.

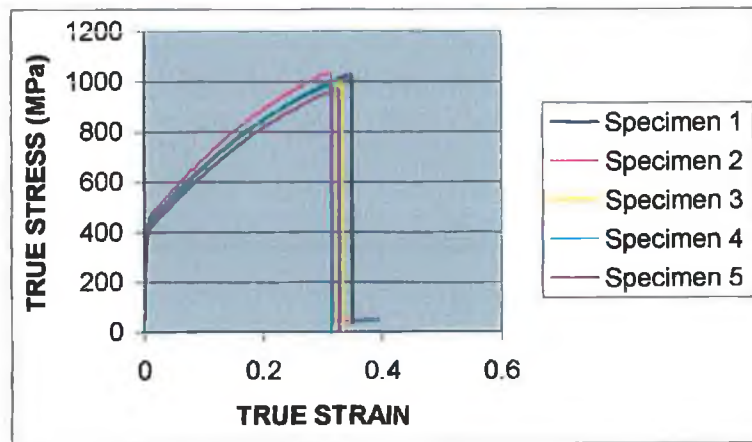


Fig.IV.22 Tensile Batch 0 0.46 mm electro-polished struts.

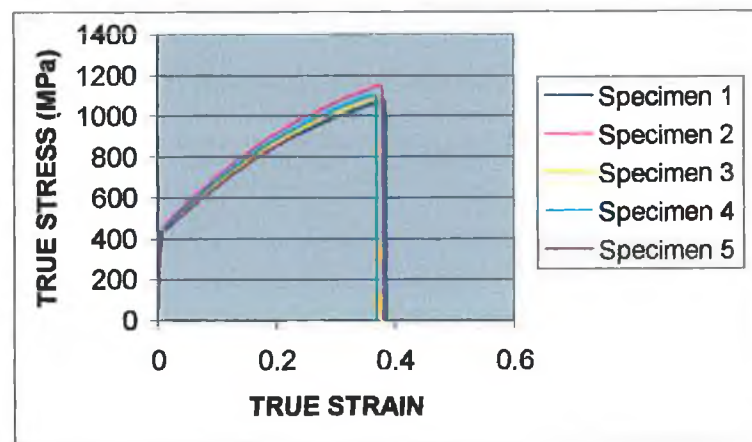


Fig.IV.23 Tensile Batch 0 0.75 mm electro-polished struts.

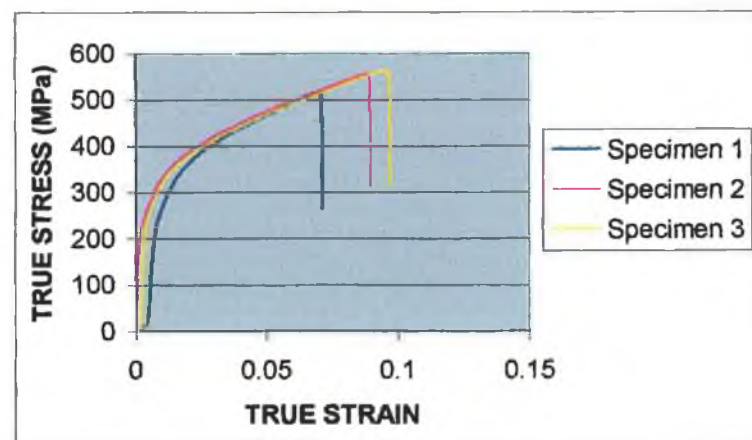


Fig.IV.24 Tensile Batch 0 0.05 mm annealed struts.

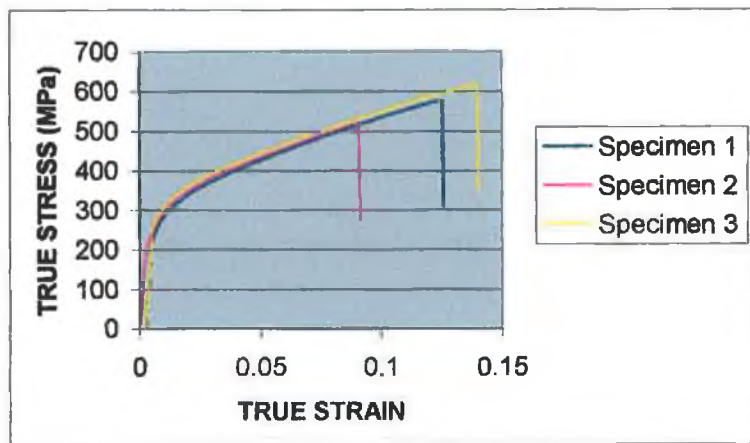


Fig.IV.25 Tensile Batch 0 0.07 mm annealed struts.

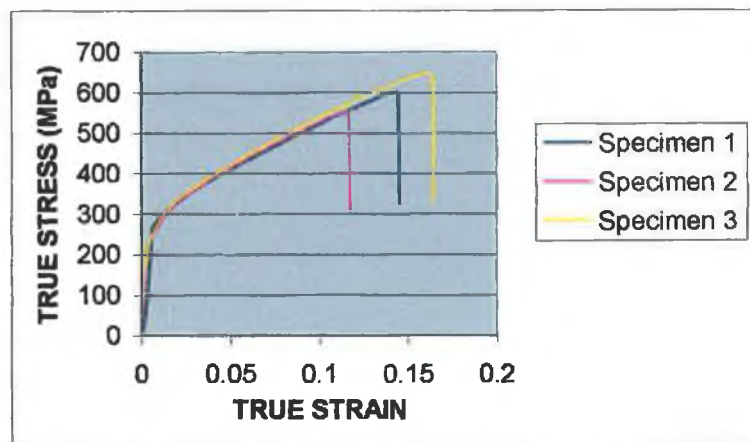


Fig.IV.26 Tensile Batch 0 0.10 mm annealed struts.

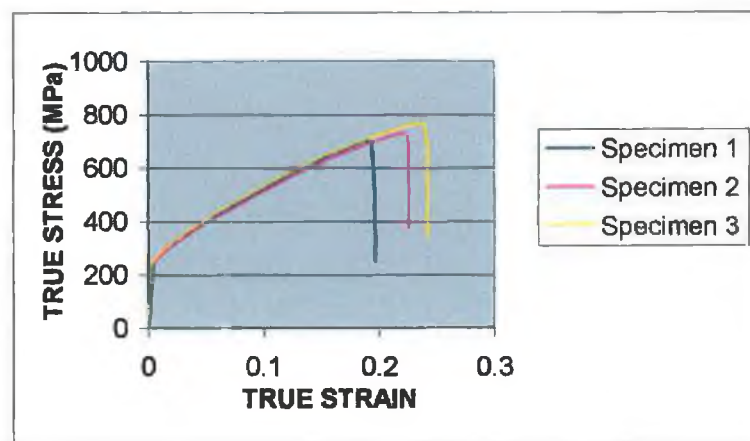


Fig.IV.27 Tensile Batch 0 0.30 mm annealed struts.

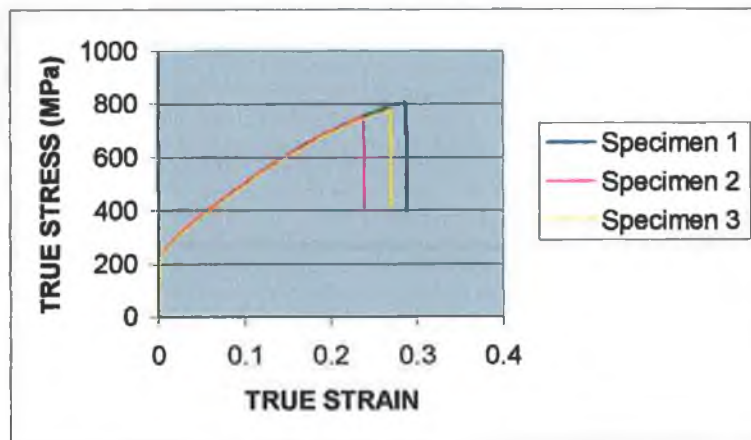


Fig.IV.28 Tensile Batch 0 0.80 mm annealed struts.

APPENDIX V INVERSE IDENTIFICATION

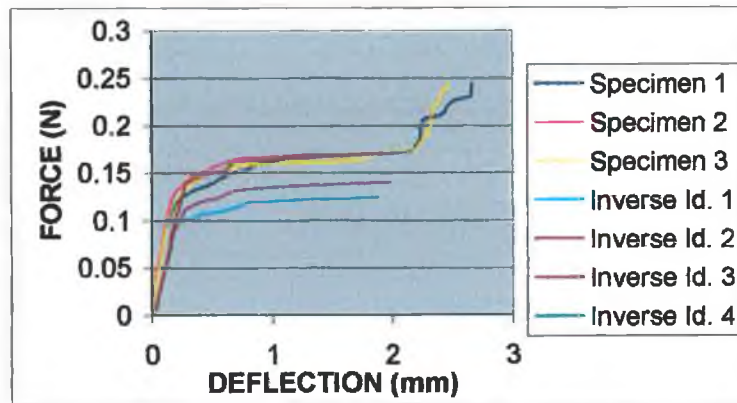


Fig. V.1 Bending Batch 2 0.12 mm laser-cut struts.

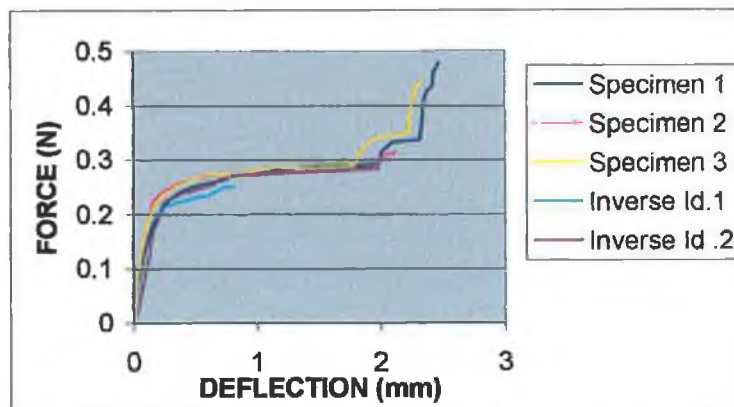


Fig. V.2 Bending Batch 2 0.20 mm laser-cut struts.

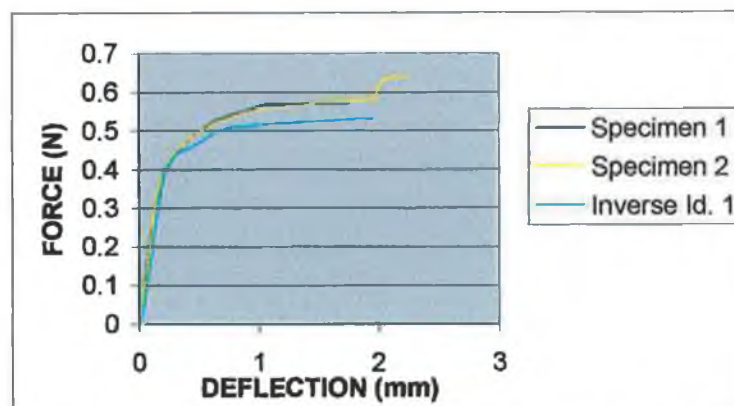


Fig. V.3 Bending Batch 2 0.39 mm laser-cut struts.

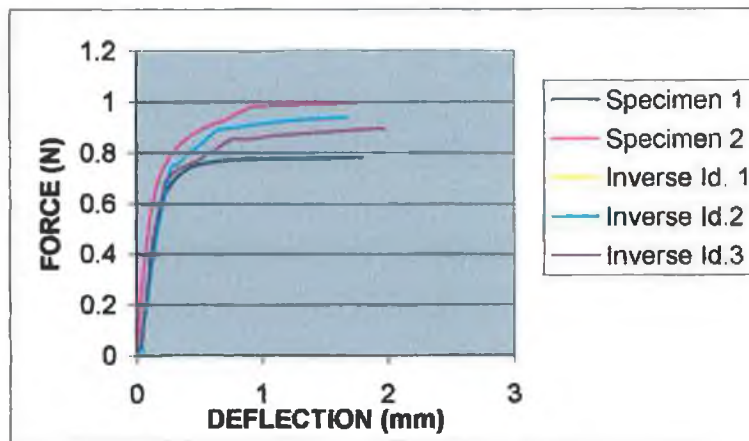


Fig. V.4 Bending Batch 2 0.58 mm laser-cut struts.

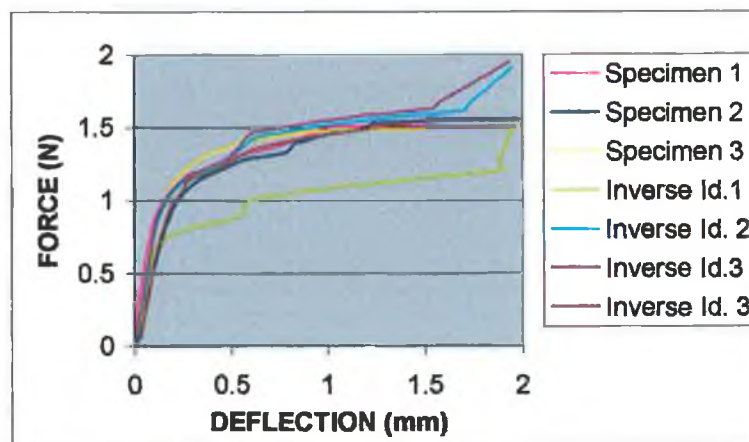


Fig. V.5 Bending Batch 2 0.75 mm laser-cut struts.

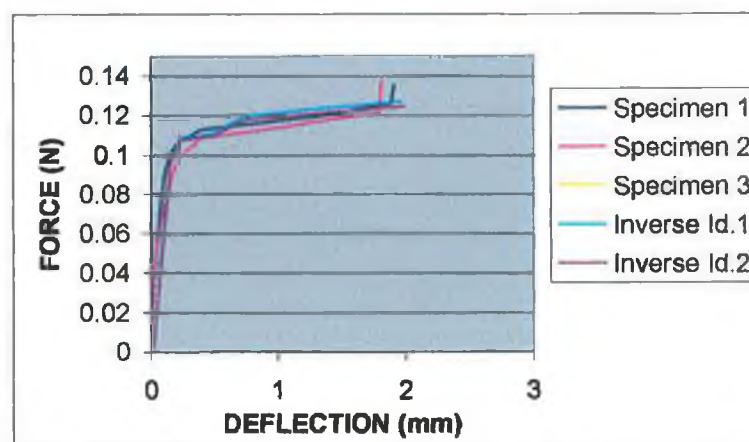


Fig. V.6 Bending Batch 0 electro-polished 0.17 mm laser-cut struts.

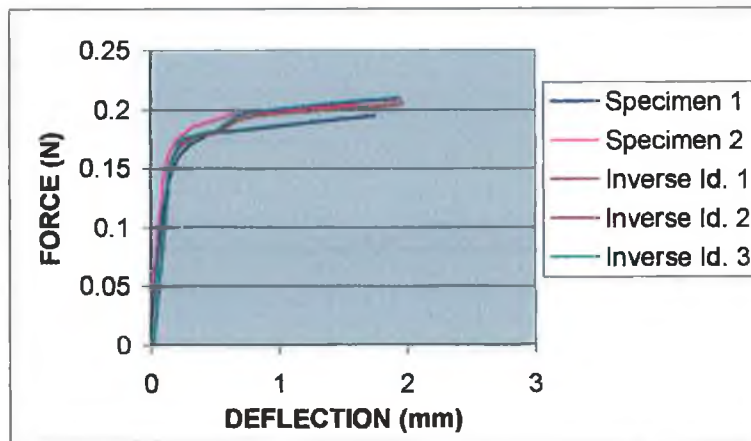


Fig. V.7 Bending Batch 0 electro-polished 0.27 mm struts.

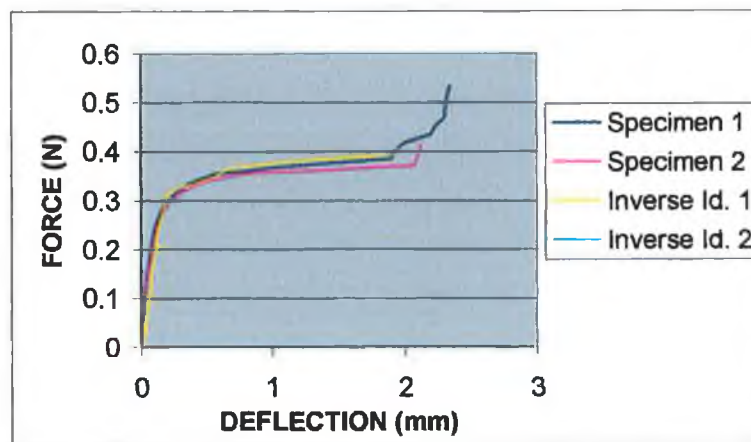


Fig. V.8 Bending Batch 0 electro-polished 0.46 mm struts.

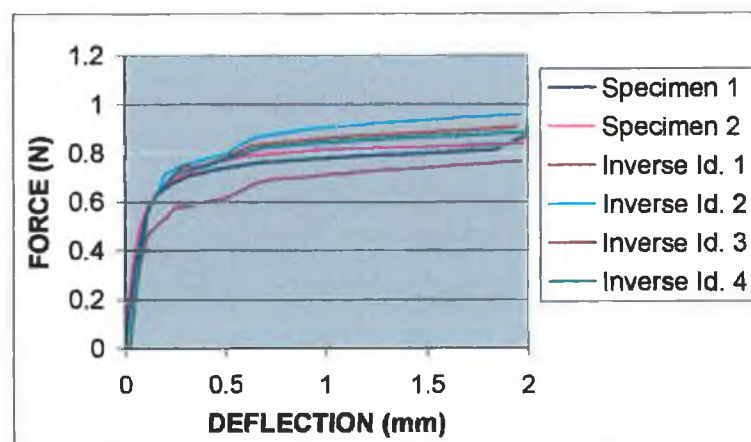


Fig. V.9 Bending Batch 0 electro-polished 0.75 mm struts.

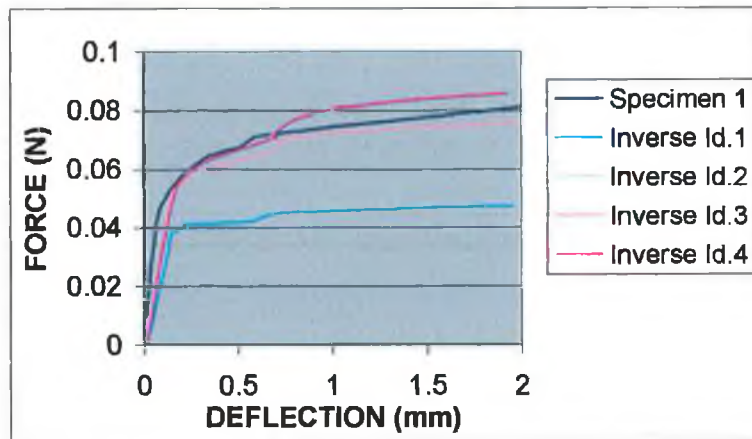


Fig. V.10 Bending Batch 0 0.1 mm annealed struts.

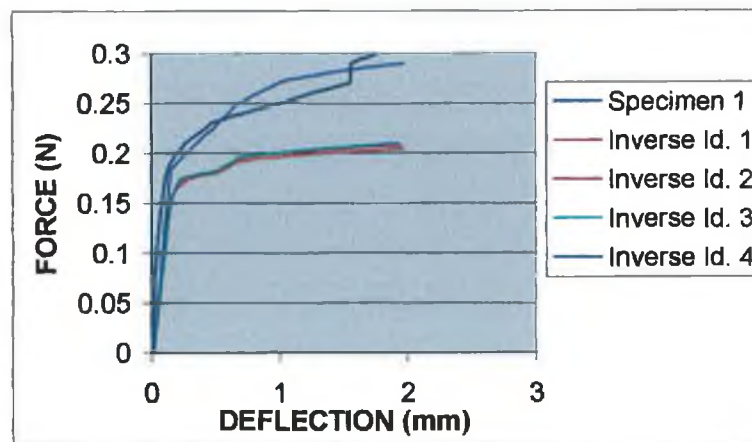


Fig. V.11 Bending Batch 0 0.3 mm annealed struts.

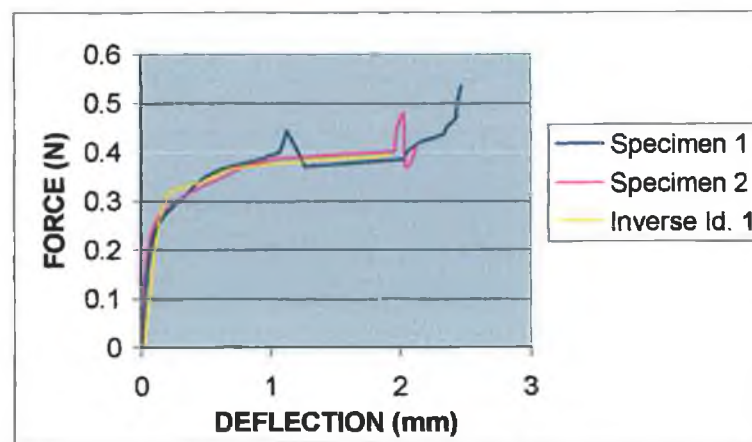


Fig. V.12 Bending Batch 0 0.5 mm annealed struts.

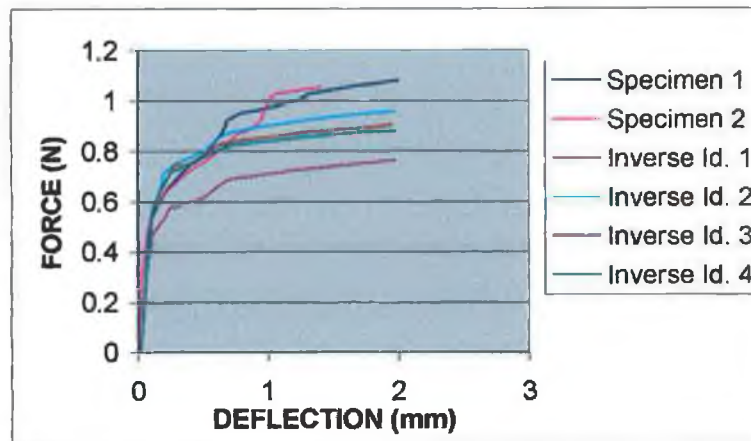


Fig. V.13 Bending Batch 0 0.8 mm annealed struts.

APPENDIX VI MICROSTRUCTURE OBSERVATION

Batch 0 0.07 mm

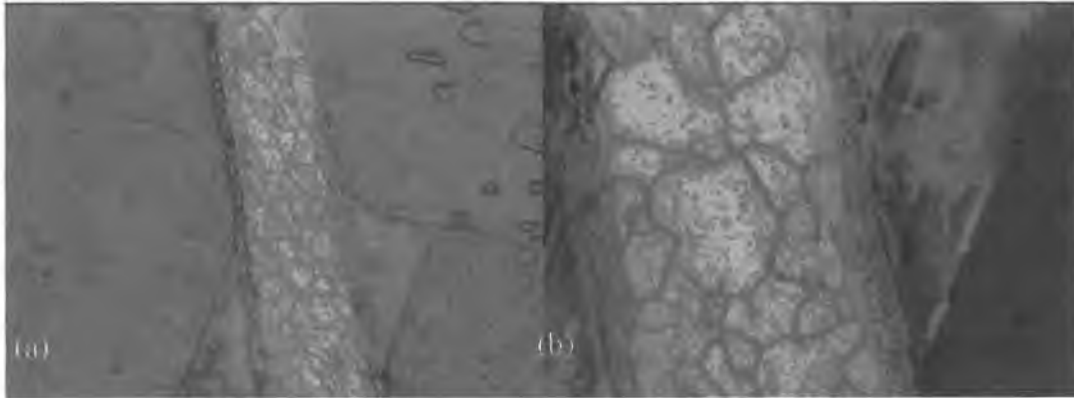


Fig.VI.1 Batch 0 0.07 mm struts (a) X200, (b) X500.

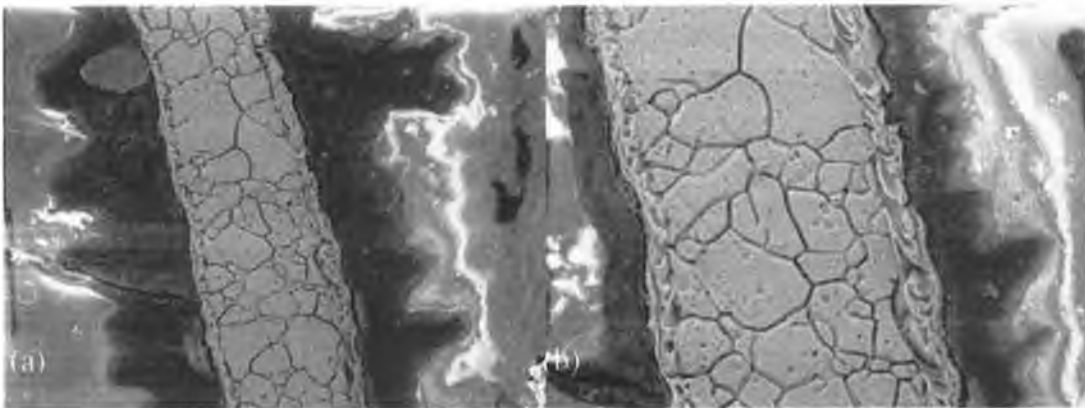


Fig.VI.2 Batch 0 SEM 0.07 mm laser-cut (a) X1250, (a) 2500.

Batch 0 0.1 mm

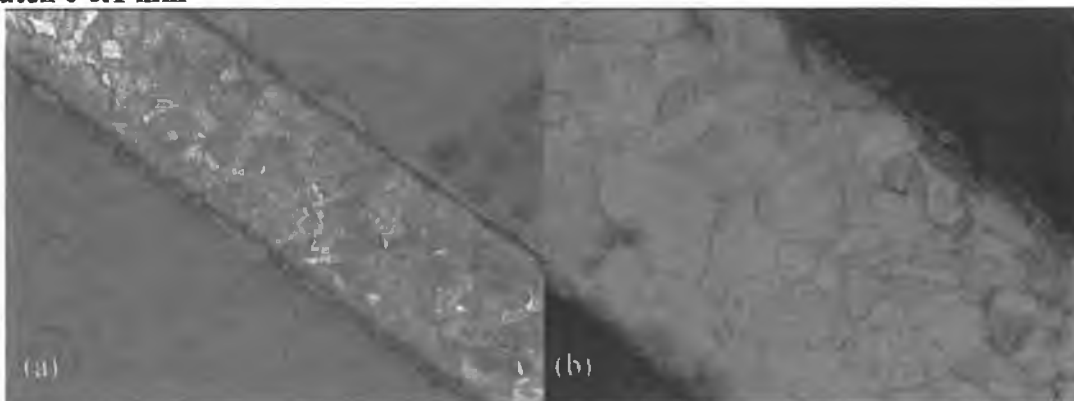


Fig.VI.3 Batch 0 0.1 mm struts (a) X200, (b) X500.

Batch 0 0.3 mm

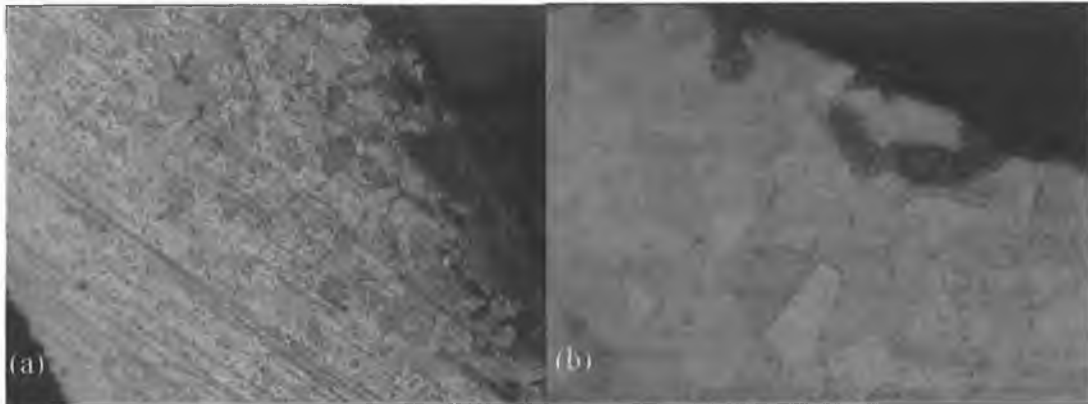


Fig.VI.4 Batch 0 0.3 mm struts (a)X200, (b)x500.

Batch 0 0.5 mm



Fig.VI.5 Batch 0 0.5 mm struts (a) X500, (b) SEM X1250.

Batch 0 0.8 mm

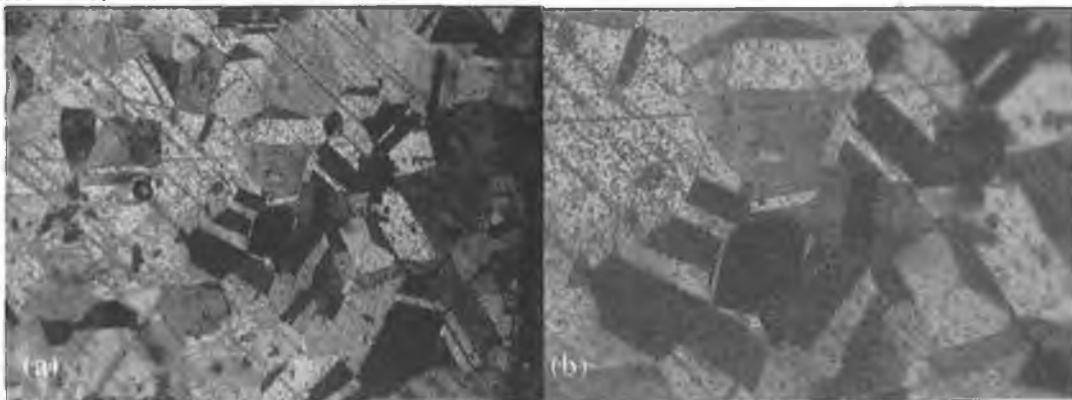


Fig.VI.6 Batch 0 0.8 mm struts (a) X500,(b) X1000.

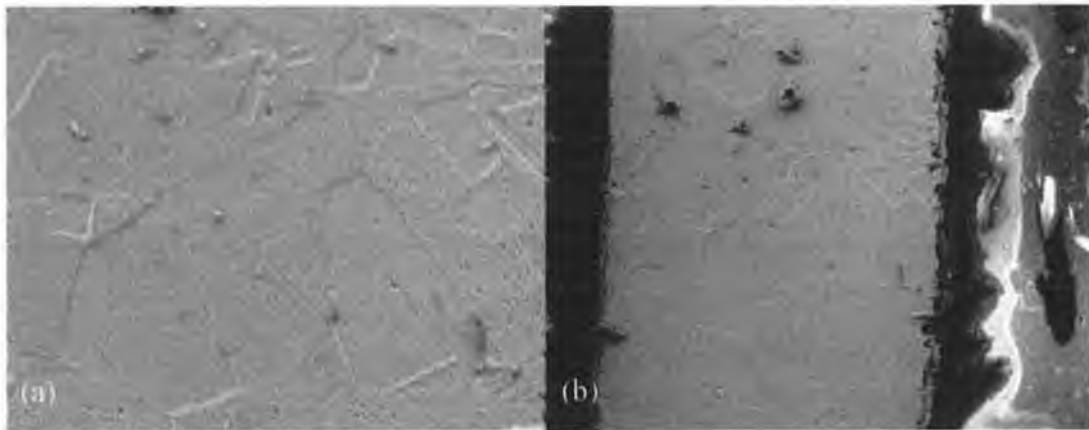


Fig. VI.7 Batch 0 0.8 mm struts SEM (a) X2500 (b) X800.

Batch 1 0.07 mm

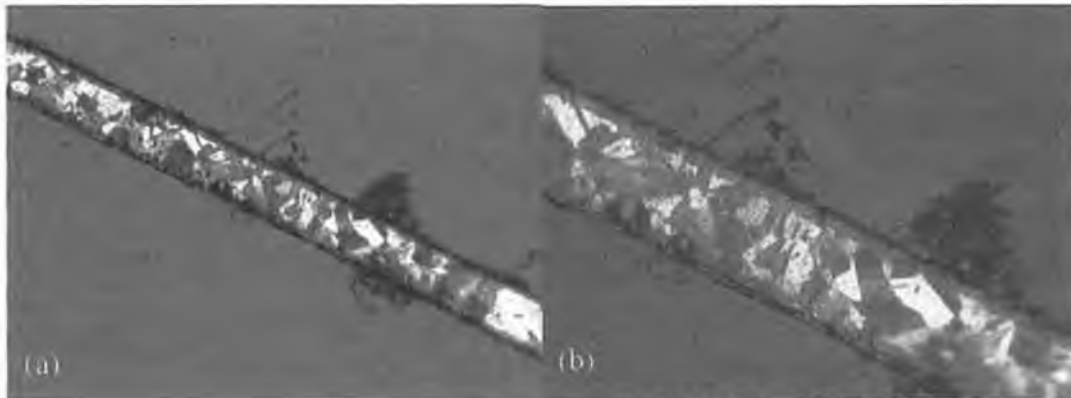


Fig. VI.8 Batch 1 0.07 mm (a) X100, (b) X200.

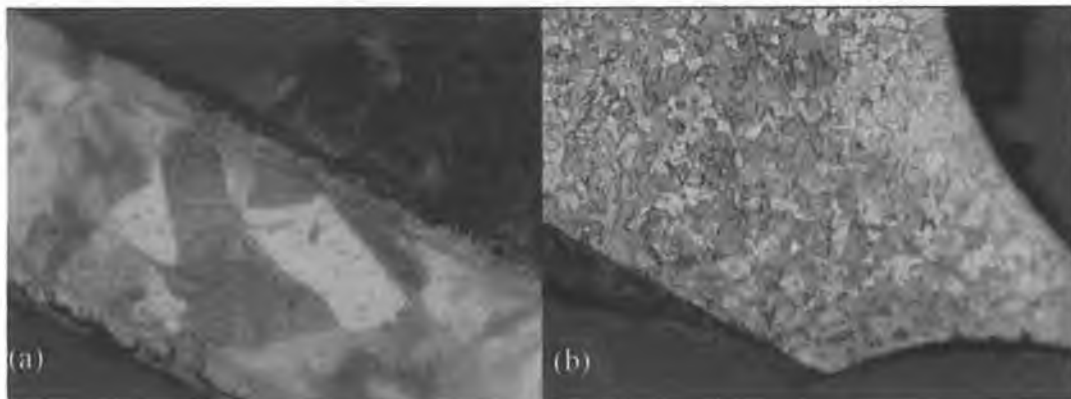


Fig. VI.9 Batch 1 0.07 mm (a) X500, (b) X100.

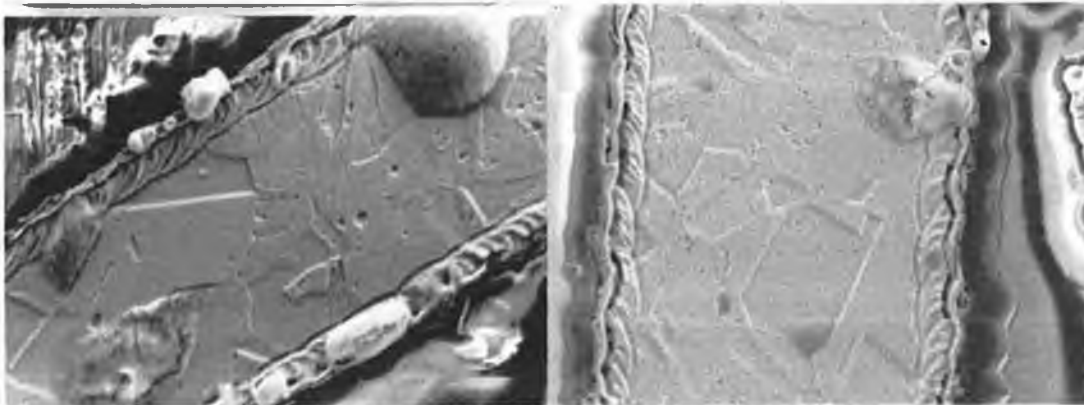


Fig.VI.10 Batch 1 0.07 mm struts SEM X2500.

Batch 1 0.5 mm

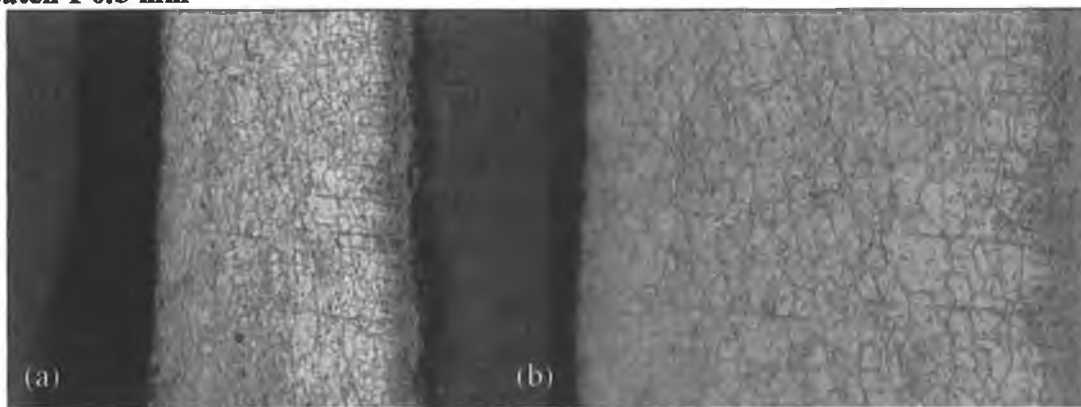


Fig.VI.11 Batch 1 0.5 mm struts (a) X100, (b) X200.

Batch 2 0.05 mm

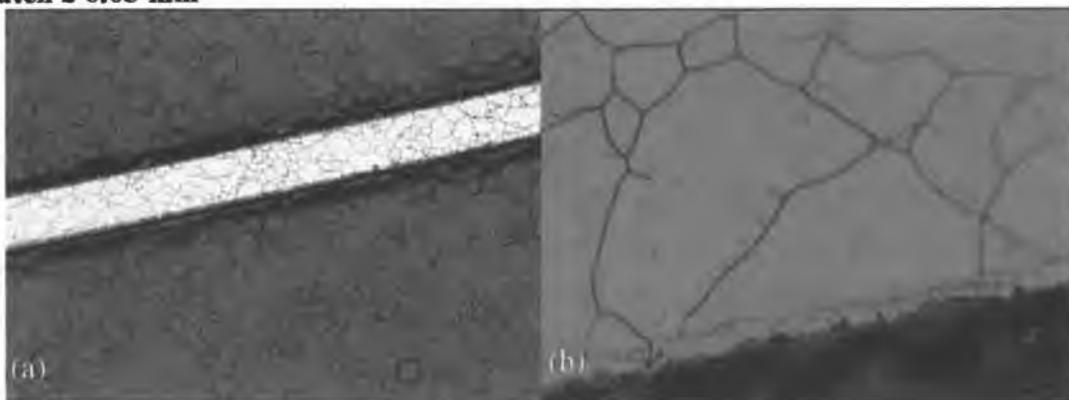


Fig.VI.12 Batch 2 0.05 mm struts (a) X100, (b) X1000.

Batch 2 0.07 mm

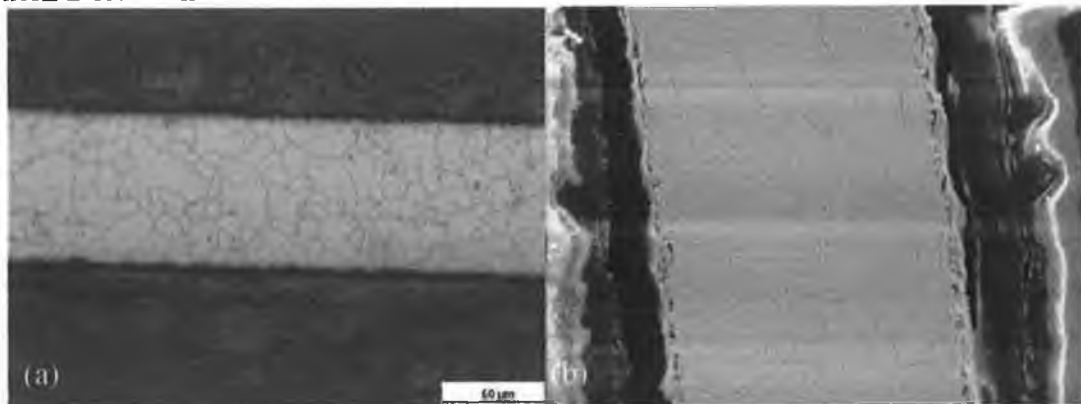


Fig.VI.13 Batch 2 0.07 mm struts (a)X200, (b) SEM X2500.

Batch 2 0.1 mm

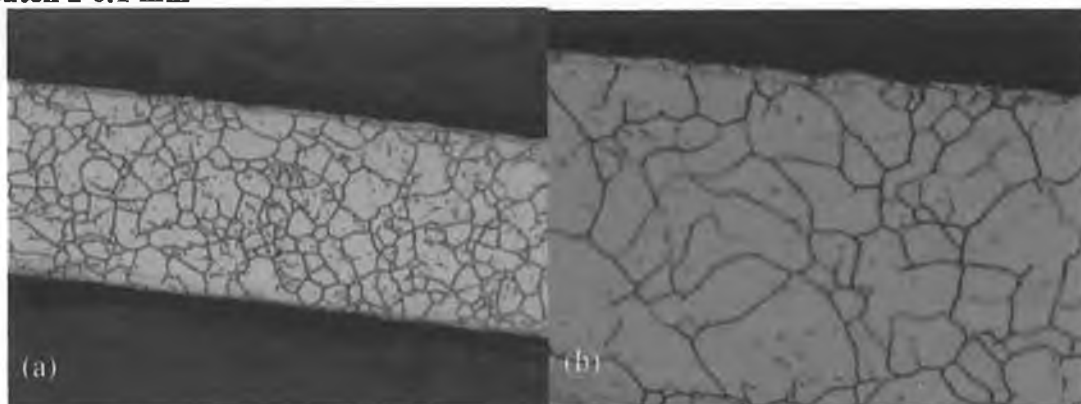


Fig.VI.14 Batch 2 0.1 mm struts (a) X200, (b) X500.

Batch 2 0.2 mm

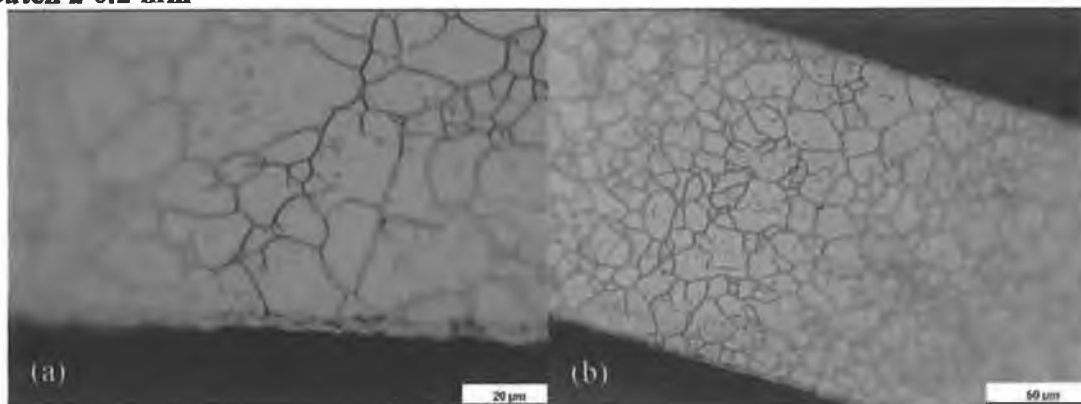


Fig.VI.15 Batch 2 0.2 mm struts (a) X500, (b) X200.

Batch 2 0.4 mm

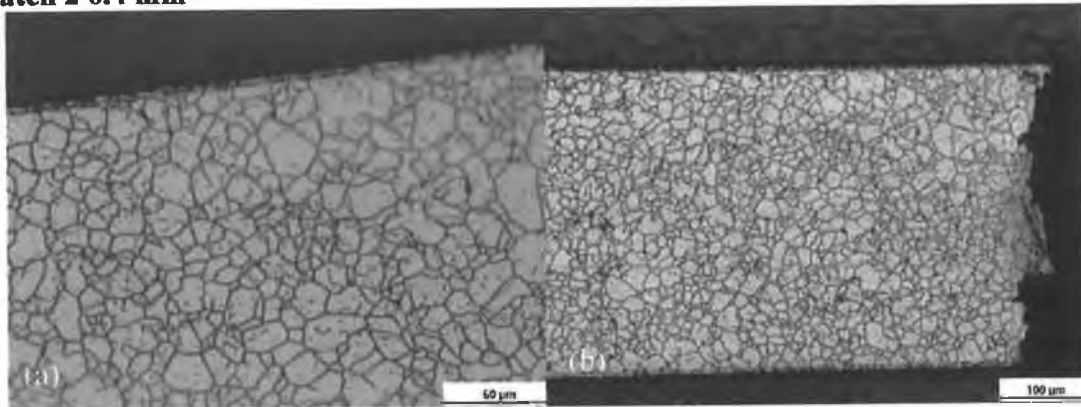


Fig.VI.16 Batch 2 0.4 mm struts (a) X200, (b) X100.

Batch 2 0.8 mm

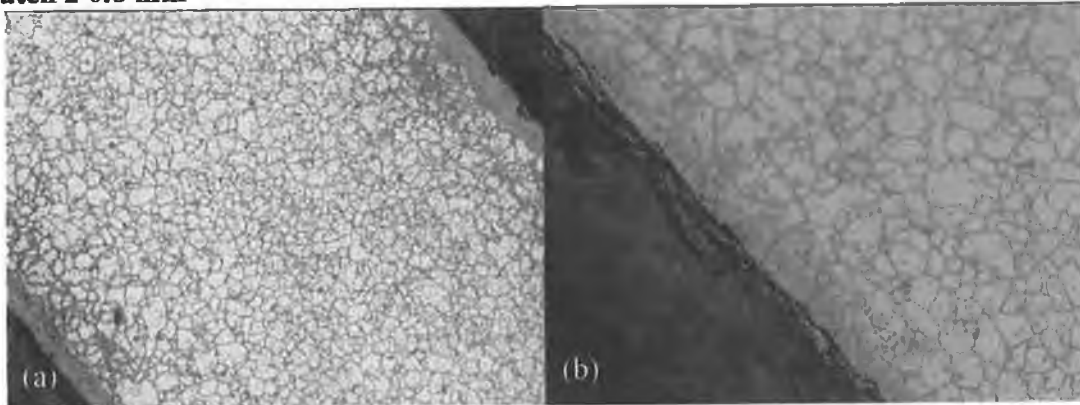


Fig.VI.17 Batch 2 0.8 mm struts (a) X100, (b) X200.

Electro-polished 0.8 mm

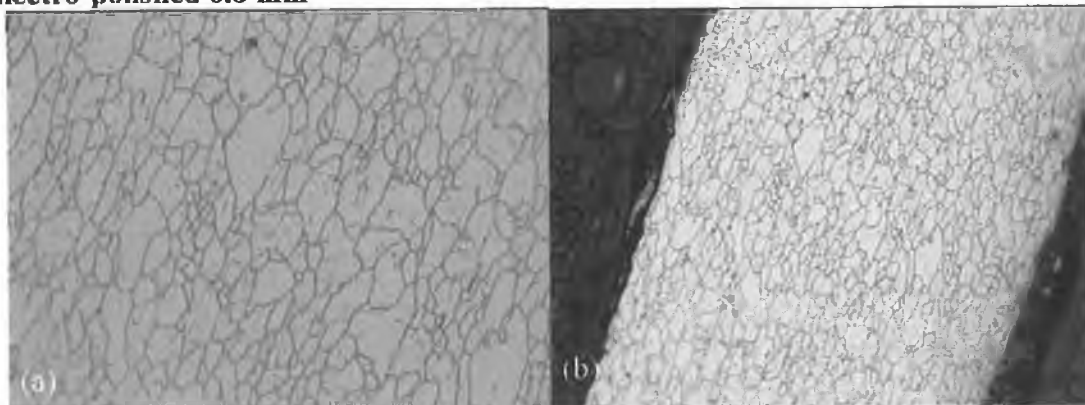


Fig.VI.18 Batch 0 0.8 mm electro-polished strut (a) X200, (b) X100.

Annealed 0.05 mm

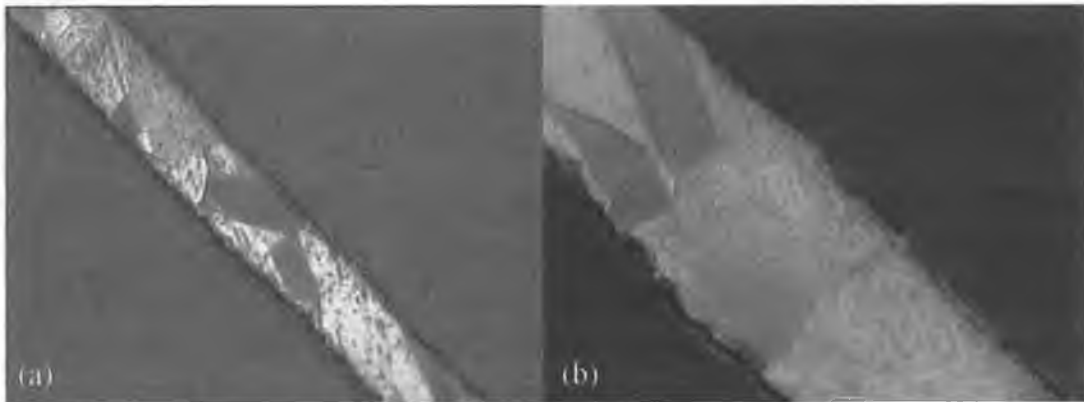


Fig. VI.19 Batch 0 0.05 mm annealed struts (a) X100, (b) X200.

Annealed 0.07 mm

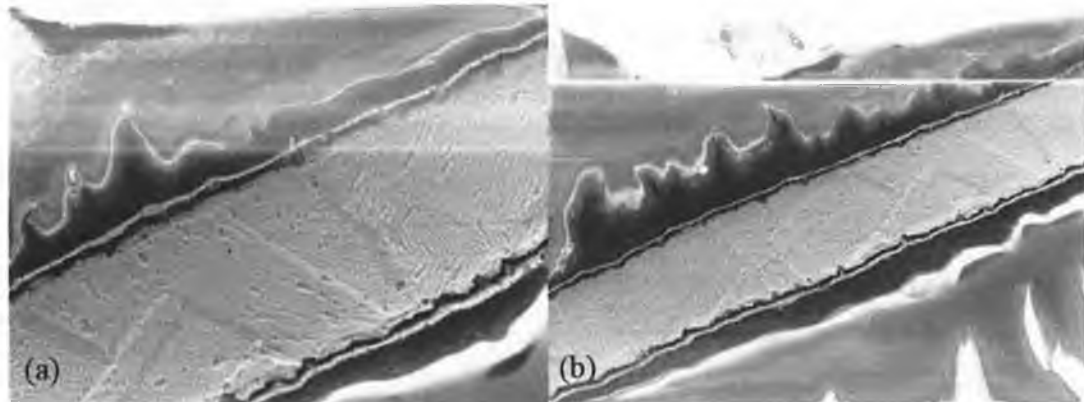


Fig. VI.20 Batch 0 0.07 mm annealed struts SEM (a) X1250, (b) X2500.

Annealed 0.8 mm

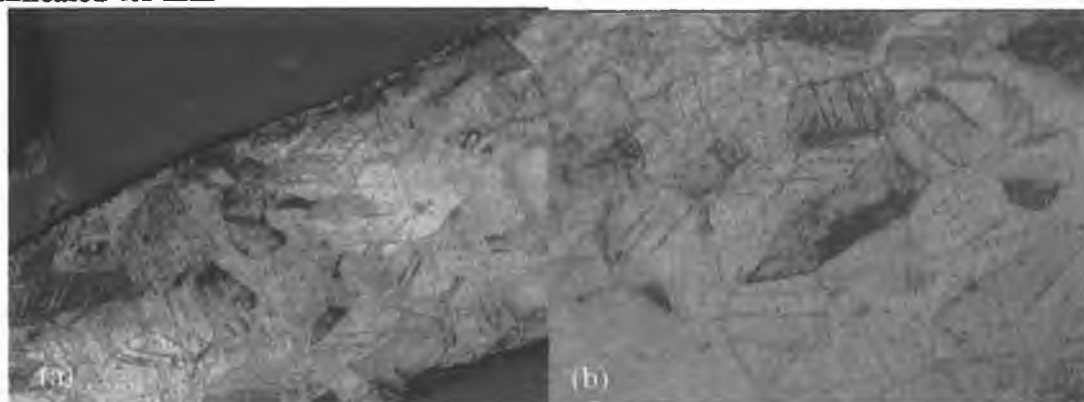


Fig. VI.21 Batch 0 0.8 mm annealed struts (a) X100, (b) X200.